Arsenic Trisulfide Inorganic Photoresist for Three-Dimensional Photolithography

Zur Erlangung des akademischen Grades eines

DOKTORS DER NATURWISSENSCHAFTEN

(Dr. rer. nat.)

der Fakultät für Chemie und Biowissenschaften der Universität Karlsruhe (TH) vorgelegte

DISSERTATION

von

M.Sc. Sean Hang Edmond Wong

aus Hong Kong, China

Table of Contents

Zusammenfassung

Bis heute sind die anspruchvollsten Architekturen für dreidimensionale photonische Strukturen photonische Kristalle. Diese bieten unübertroffene Möglichkeiten, Licht auf der Skala seiner Wellenlänge zu führen und zu manipulieren. Insbesondere die Kombination einer vollständigen photonischen Bandlücke mit optisch aktivem Material hat zur Entwicklung von theoretischen Blaupausen geführt, die z.B. schwellenlose Laser und ultra-schnelle, rein optische Schalter realisieren sollen. Gerade letztere basieren auf einer Heterostruktur aus photonischen Kristallen, in der ein zweidimensionaler photonischer Kristall von zwei dreidimensionalen photonischen Kristallen in einer Art Sandwich eingeschlossen wird und auf diese Weise eine vollständige photonische Bandlücke zur Verfügung stellt, die Verluste aus der Ebene des zweidimensionalen photonischen Kristalls vermeiden soll. Eine Herausforderung dabei ist die Maßgabe, dass nur in der zweidimensionalen Schicht optisch aktives (z.B. Quantenpunkte) oder nichtlineares Material verwendet werden soll. Momentan gibt es nur zwei experimentelle Zugänge, eine derartige Geometrie zu realisieren, nämliche die direkte Halbleiterfabrikation oder das direkte Laserschreiben (DLW, *direct laser writing*). Die direkte Halbleiterfabrikation realisiert dreidimensionale Strukturen durch Wafer-Fusion von entsprechend strukturierten zweidimensionalen Wafern. Der hohe Brechzahlkontrast, der für eine vollständige photonische Bandlücke benötigt wird, kann auf diese Weise relative einfach realisiert werden und auch das gezielte Einbringen optisch aktiven Materials in nur einer einzigen Lage wurde bereits experimentell demonstriert. Trotz dieser offensichtlichen Vorteile bedarf diese Technk einer hochqualitativen Halbleiter-Mikrofabrikationsanlage und technologisch extrem anspruchvoller

Positioniertechniken, um die relative Lage der einzelnen Schichten vor und während der Wafer-Fusion beizubehalten.

Diese Strukturen können mittels DLW prinzipiell ebenfalls hergestellt werden. Dabei startet man mit einem polymeren Photolack als Templat mit anschließender Konversion bzw. Inversion in entsprechend hochbrechende Materialien. Das ungelöste Problem ist die Einbringung photolumineszierendem Spezies in einer genau definierten Lage innerhalb der Struktur. Während kürzlich die Kombination von photolumineszierenden Material mit einem Photolack demonstriert wurde, geht dieses bei den anschließenden Konversionsschritten unweigerlich verloren. Eine spätere Infiltration der hochbrechenden Struktur mit z.B. Quantenpunkten kann eine gezielte Positionierung innerhalb des hochbrechenden Materials nicht gewährleisten.

Das Ziel dieser Arbeit ist es, ein Materialsystem zu identifizieren bzw. zu entwickeln, das sowohl einen hohen Brechungsindex aufweist, als auch die Möhlichkeit bietet, räumlich präzise positionierte Photolumineszenz zu zeigen. Zu dem sollte das System so einfach wie ein Photolack handhabbar sein, um mittels DLW strukturiert zu werden.

Dazu wird eine thermische Verdampfungstechnik entwickelt, die die Transformation von glasartigem Arsensulfid (As_2S_3) in einen photoempfindlichen Film ermöglicht, der für das DLW geeignet ist und dort ein Verhalten wie ein Negativlack zeigt. Eine detaillierte chemische und physikalische Charakterisierung dieser photoempfindlichen Filme wird vorgenommen.

Nach der Etablierung einer reproduzierbaren Methode wird im Detail auf das direkte Laserschreiben in diesen Filmen eingegangen. Insbesondere wird auf die während dieser Untersuchung zu Tage getretenen optischen Herausforderungen hingewiesen, die eine direkte Folge des hohen Brechzahlkontrastes sind.

Lösungsvorschläge werden vorgestellt und diskutiert sowie teilweise sehr erfolgreich in die Praxis umgesetzt. Dies führt zu einer ersten Demonstration von nahezu perfekten 3D-Strukturen in Arsensulfid. Ein wesentlicher Punkt der Arbeit beschäftigt sich mit der Entwicklung einer Ätzflüssigkeit, die sehr hohe Aspektverhältnisse in diesem Photolacksystem erlaubt. Um die Effekte zu untersuchen, die die Ätzselektivität bestimmen, wurde eine Bibliothek von Aminen synthetisiert, um die Zusammenhänge zwischen den molekularen Modifikationen der Ätzmoleküle und ihrem makroskopischen Ätzverhalten herauszuarbeiten. Das so gewonnene Wissen erlaubt die Synthese eines neuen Amins (4-methoxybenzyl-pyren-1-yl-amine), das extrem hohe Ätzselektivität zeigt. Dazu wird eine detaillierte Analyse des Ätzmechanismus mit dieser Substanz durchgeführt. Mit einer DMSO/CP-Lösung des Amins können eine Vielzahl von 3D-photonischen Strukturen hergestellt werden, die die einwandfreie Funktionsweise als Photolacksystem unter Beweis stellen.

Als letzter Schritt wird das Dotierverhalten dieses Photolacksystems bei Dotierung mit Erbium untersucht, um einen bei Raumtemperatur photolumineszierenden, hochbrechenden Film zu erhalten. Dies wird mittels einer direkten Gasphasen-Dotiertechnik erreicht, die wir hiermit einführen und im Detail diskutieren. Auch hier werden die chemischen und physikalischen Eigenschaften der Filme mittels einer Vielzahl von Methoden analysiert. Die Einsetzbarkeit dieses Photolacksystems zur Herstellung von Mikro- und Nanostrukturen wird demonstriert. Zusammenfassend gesagt, wird in dieser Arbeit die Entwicklung von As_2S_3 und mit Erbium dotierten Abwandlungen als Photolacksystem dokumentiert und anhand von aktiven und passiven 3D-Strukturen, die mittels DLW hergestellt werden, demonstriert.

Introduction

To date, the most demanding three-dimensional (3D) architectures for photonics are photonic crystals, providing unsurpassed opportunities for guiding and manipulating light on a scale of the wavelength of light[1,2]. Especially the combination of a complete photonic bandgap with optically active materials stimulated the development of theoretical blueprints for, e.g., threshold-less lasers[3] and ultra-fast all-optical switches[4]. The latter designs are based on a photonic crystal hetero-structure in which a two-dimensional photonic crystal layer containing functional elements like waveguides and resonators is clad between two 3D photonic crystals, providing a complete photonic bandgap to eliminate out-of-plane losses. To challenge matters further, the blueprint requires optically active materials, e.g., quantum dots, to be placed only inside the two-dimensional layer. Currently, there are only two experimental approaches, which could in principle achieve the realization of these blueprints, namely direct semiconductor microfabrication and direct laser writing. Direct semiconductor microfabrication realizes 3D structures by wafer fusion of suitable structured 2D layers. The high index of refraction required for a complete photonic band-gap can easily be achieved and even the inclusion of only one optically active layer has recently been demonstrated[5]. Despite these obvious advantages, this technique requires a fully equipped semiconductor microfabrication facility and technological extremely demanding positioning accuracy prior to wafer fusion for maintaining the orientation between the different layers. On the other hand, direct laser writing is capable of fabricating the required structures in principle, starting with a polymeric photoresist as a template and converting it in subsequent steps into high index of refraction materials like silicon *via* a double-inversion[6] or single-inversion[7] scheme. The remaining and to date unsolved problem is the precise placement of

photoluminescent material inside the required layer. While recent photoresist development demonstrated the inclusion or generation of photoluminescent species inside the bulk photoresist[8,9], they will inevitably be lost during the following conversion steps. Subsequent infiltration of the high index structures with, e.g., quantum dot solutions fails the requirement of precise placement inside the high index material[10].

The aim of this thesis is to investigate and develop a material that has both a high refractive index and spatially localizable photoluminescence while being processable like a conventional photoresist, so that it can be used with the 3D direct laser writing (3D DLW) technique. Reducing this idea to practice will enable the creation of 3D photonic crystals with full-photonic bandgaps, and the opportunity to incorporate photoluminescent guests at specific locations in the photonic crystal lattice.

Outline of this Thesis

In chapter 1, a brief introduction to the theoretical concepts of a 3D photonic crystal is provided. Based on these theoretical concepts, a set of design requirements are identified, and the state-of-the-art fabrication techniques used to make such structures are scrutinized based on their ability to implement these design requirements. From this analysis, we will provide justification that the 3D DLW technique is the most promising fabrication technique, and conduct a review of its current materials limitations. From this review, a materials solution which would allow the 3D DLW technique to directly fabricate functional 3D photonic crystal nanostructures is revealed, and steps for its implementation are outlined in detail.

In chapter 2, the method to transform arsenic trisulfide into a negative-tone photoresist suitable for 3D direct laser writing is detailed. The chapter begins with an

introduction of the thin film deposition methods that are currently available for fabricating thin films of As_2S_3. Then we provide a detailed analysis of the high-vacuum thermal evaporation technique that is used to form the photosensitive thin films used in this work. This is followed by a detailed chemical and physical characterization of the photosensitive thin films produced using this process. By clearly analyzing and defining the arsenic trisulfide photoresist in this chapter, it builds the foundation for all of the subsequent chapters of this thesis.

In chapter 3, a detailed description of the 3D direct laser writing technique and its application to arsenic trisulfide based photoresist is provided. This is followed by a discussion of the optical aberrations that are encountered when 3D DLW is performed in this material. Possible remedies to these optical aberrations are discussed, and some of these counter-measures were implemented. At the conclusion of this chapter we use concrete examples to demonstrate that near perfect 3D structures in As_2S_3 can be fabricated by controlling these optical aberrations.

In chapter 4, the important aspect of etch selectivity in this photoresist system is addressed. The chapter begins with an in-depth analysis of the etching chemistry of this material. Then a library of amine molecules is synthesized in order to explore the relationship between molecular modifications of the etchant molecule and its macroscopic etching behavior. The knowledge obtained from this detailed analysis enabled the rational synthesis of a novel amine etchant *N*-(4-methoxybenzyl)-(pyren-1-yl)amine that demonstrates high etch-selectivity. Furthermore, a detailed analysis into the reaction mechanism of this highly selective molecule is conducted. Finally, we show that 3D PBG structures, and other interesting 3D nanostructures, can be effectively produced using an etchant containing the *N*-(4-methoxybenzyl)-(pyren-1-yl)amine molecule.

In chapter 5, the doping of the element erbium into the As_2S_3 host, to form a photoresist exhibiting both a high-refractive index and room-temperature photoluminescence is described in detail. A justification of the necessity to include a photoluminescence species into an otherwise inactive host material is first discussed. This is followed by an introduction and demonstration of the technique that is used to achieve this controlled doping. The optical and physical properties of this photoluminescent photoresist are then fully characterized. The chapter concludes by providing a discussion and actual demonstration of the applications of this Er doped As_2S_3 material for fabricating micro- and nano-photonic structures.

In chapter 6, we provide a summary of the results obtained in this thesis, and provide an outlook into the future prospects of this photoresist system as a whole.

Due to the breath and complexity of the characterization techniques used in this thesis, the details of the material and experimental methods are separately documented in chapter 7. Furthermore, tables of the key optical data for As_2S_3, Er doped As_2S_3, as well as other tabulated data are provided in the Appendix section of this thesis.

Chapter 1 – Design and Implementation of 3D Photonic Crystals

1.1 Theoretical Concepts of Photonic Crystals

Here we give a brief discussion into the theoretical background of the photonic band gap effect. A rigorous derivation will not be given here, but we only state that the Maxwell's equation can be re-written to yield an eigenvalue equation in the frequency domain for the magnetic field, and for non-magnetic materials with magnetic permeability $\mu = 1$ [11,12]:

Equation 1.1 $\quad \nabla \times (\varepsilon^{-1}(\vec{r}) \nabla \times \vec{H}(\vec{r})) = \dfrac{\omega^2}{c_o^2} \vec{H}(\vec{r})$

Here, $c_o = 1/\sqrt{\varepsilon_o \mu_o} = 2.9979 \times 10^8$ m/s is the vacuum speed of light and the effects from free charges and currents are absent.

In periodically structured dielectric media, waves can propagate without scattering, and their behavior is governed by a plane wave multiplied by a periodic envelope function. This is the central theme of the Floquet-Bloch theorem. Since the photonic crystals that we are considering here are strictly periodic dielectric media, we can use the Floquet-Bloch theorem to write an eigenfunction $\vec{H}(\vec{r})$ which satisfies the eigenvalue in equation 1, where $\vec{H}(\vec{r})$ should be represented as a plane wave travelling through the periodic lattice of a photonic crystal. Therefore, $\vec{H}(\vec{r})$ is defined in the form of a plane wave multiplied by vectorial function with the periodicity of the Bravais lattice of the photonic crystal, where there is a periodic dielectric function for some primitive lattice vectors, $\vec{R}$.

Equation 1.2 $\quad \vec{H}_{n\vec{k}}(\vec{r}) = \exp(i\vec{k} \cdot \vec{r}) \vec{u}_{n\vec{k}}(\vec{r})$

Equation 1.3 $\quad \vec{u}_{n\vec{k}}(\vec{r}) = \vec{u}_{n\vec{k}}(\vec{r} + \vec{R}), \ \vec{R} \in \boldsymbol{R}$

Once we have defined these eigenfunctions to represent the photonic crystal lattice, we can use equation 1.1 to solve the discrete eigenvalues for each of the different Bloch wavevectors inside the Brillion zone of the 3D photonic crystal. (The first Brillouin zone is the reciprocal lattice of the Bravais lattice.) The periodic boundary conditions of the k-vectors that lie inside the Brillouin zone indicate that as a k-vector approaches the edge of the Brillouin zone, it folds back on itself. The back-folding of the Bloch vector creates the discrete bands that are observed in the band structure of the photonic crystal. The entire eigenproblem presented in equation 1.1, can be solved numerically using a plane-wave expansion or finite-difference time domain technique to obtain the eigenvalues (ω^2 / c_o^2) for each Bloch wavevector $\vec{k}$. Since the eigenvalues are a continuous function of the Bloch wavevector, when ω is plotted against $\vec{k}$, a band structure, or dispersion diagram, is obtained. The results of this calculation, for a 3D woodpile photonic crystal with diamond symmetry are presented in Figure 1.1.

This woodpile structure can be built up with layers of dielectric rods with a stacking sequence that repeats itself every four layers with a repeat distance of c. Within each layer, the rods are arranged with their axes parallel and separated by a distance a. The orientation of the axes is rotated by 90 degrees between adjacent layers. To obtain a periodicity of four layers in the direction of stacking, the rods of second neighbor layers are shifted by a distance of $0.5a$ in the direction perpendicular to the rod axes. For $c / a = \sqrt{2}$ the lattice can be considered as an fcc primitive unit cell with a basis of two rods. This layered structure can be derived from the diamond lattice by replacing the (110) chains in the diamond structure with these rods.
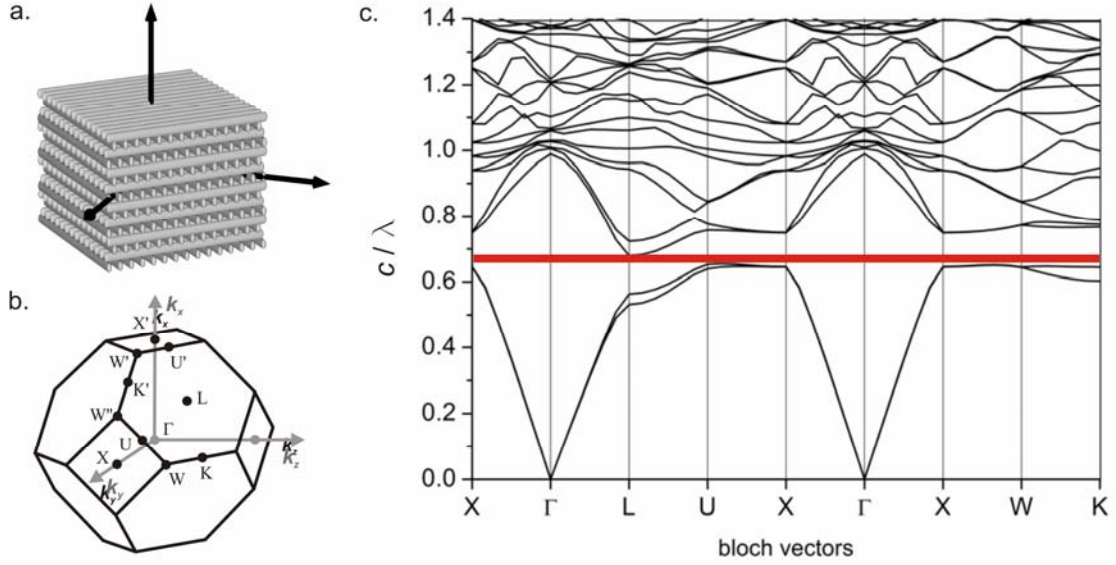
Figure 1.1 a. A woodpile photonic crystal with FCC symmetry. **b.** The first Brillouin zone of such an FCC structure. **c.** The band-structure calculation of such a woodpile photonic crystal structure ($\varepsilon = 6.0025$) exhibiting a full-photonic band gap.

The band-structure maps out all the possible interactions in the 3D photonic crystal system that is under study. From inspecting the band-structure in Figure 1.1 c., one can see that there is a certain frequency window in the dispersion relation $\omega(\vec{k})$, where electromagnetic wave propagation is forbidden over all directions of the 3D structure. In this case, the frequency gap is called a full-photonic band-gap (full-PBG). In all other cases where only some directions of the structure exhibit this frequency window, the resulting gap is called a stop-gap.

From this analysis it becomes clear that one of the prerequisites for fabricating a 3D structure which can demonstrate a full-photonic band-gap, is that it must be perfectly periodic (so as to satisfy the condition of periodicity that is stated in the Floquet-Bloch theorem). Furthermore, the dielectric contrast between the dielectric of the material used to construct the 3D structure, and the background dielectric (usually air), must be sufficiently large to sustain a full-photonic band gap. When the dielectric

13
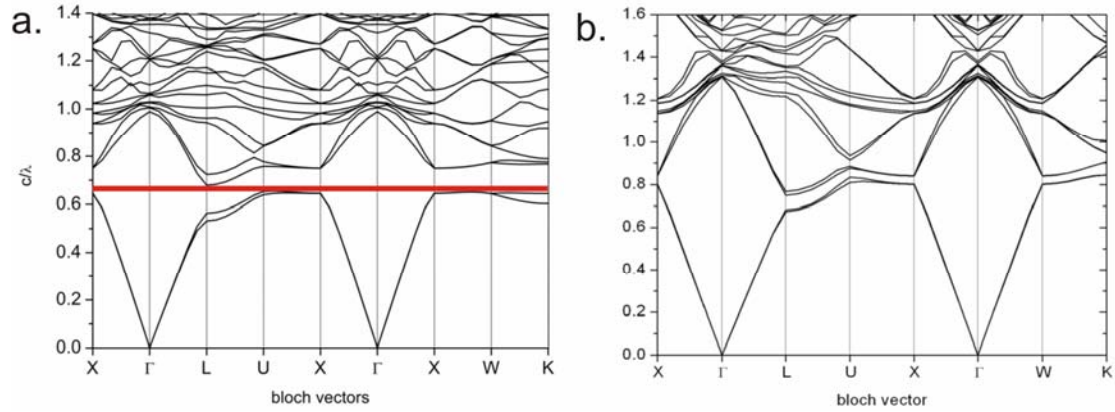
Figure 1.2 The band structure diagram for a 3D woodpile photonic crystal made with a material with a) a dielectric constant (ε) equal to 6.002 (or a refractive index (n) equal to 2.45) a full-photonic band gap is present. b) When the material that is used has a lower dielectric constant $\varepsilon = 2.464$ ($n = 1.57$), only certain directions posses a photonic stop gap, and a full-photonic band-gap is absent.

contrast is too low, the band separation decreases, and the photonic band-gap is closed. In general, the width of the band-gap tends to increase as the dielectric contrast between the material and the background is increased. The effect of the change in the dielectric contrast on the photonic band gap is shown in Figure 1.2. We should note that since the dielectric constant ε, is related to the refractive index n, via the relation $n^2 = \varepsilon\mu$ ($\mu = 1$ for non-magnetic materials) the two values are used interchangeably and describe the same effect.

Furthermore, the eigenvalue equation (equation 1.1) is linearly scalable and as a result the calculated band structure is also linearly scalable. This means that the band-structure that is calculated for one range of frequencies can be directly shifted to another range of frequency by multiplying a scaling factor to the resulting band-structure.

In order to scale the 3D photonic crystal so that it exhibits a photonic band gap at optical telecommunication frequencies, which is centered at a wavelength of 1550 nm, the physical features that constitute such a 3D structure must contain individual features that fall in the nanometer regime.

👆	• Ease and speed of large-scale fabrication. • Very well defined surfaces.	• Material with large index of refraction can be used. • Functional defects can be incorporated.	• Ease and speed. • Large area possible. • Simple incorporation of functional defects. • Defect-free periodicity.
👎	• Intrinsic defects and disorder difficult to control. • Incorporation of functional defect is very difficult. • Inversion required.	• Slow, ultra-high precision alignment • Complicated preparation. • Only layer by layer geometries possible. • Limited to very few layers.	• Organic photoresist material has a low index of refraction. • Structures produced lacks the refractive index contrast. • Inversion required.

Figure 1.3 A comparison of the major fabrication techniques for producing 3D photonic crystals. These four major techniques are (from left to right), colloidal self-assembly, semiconductor fabrication technique, and holography and three-dimensional direct laser writing 3D DLW.

It is due to the stringent design criteria which require perfect nano-scale periodicity in three-dimensions and the use of materials having a high index of refraction, that fabrication of high-quality 3D nanostructures for the optical regime still remains a challenge today.

In the next section, we will elaborate more on the required fabrication parameters and also some of the current techniques that are used to address these requirements in order to enable the experimental realization of 3D photonic crystal structures that operates at optical frequencies.

1.2 Current Methods for Fabricating Three-dimensional Photonic Crystals

The theoretical concepts that are used to describe 3D photonic crystals yield some design rules for fabricating 3D photonic crystal samples. If one was to construct a 3D PBG structure that operates at the optical telecommunications region centered at 1550 nm wavelength, the fabrication technique of such a structure must allow for:

1. The generation of perfectly periodic structures in three-dimensions,

2. the use of a material that has a sufficiently large refractive index to provide a full photonic band-gap (*n* typically more than 2),

3. generation of structural features in the nanometer regime, and

4. the ability to generate precisely positioned defects in three dimensions.

Only when the first 3 important criteria are met, can such a 3D structure exhibit a full-PBG in a manner that is predicted by theory. Although satisfying criteria number 4 is not essential for a structure to possess a full-PBG, it is of vital importance if such a structure is to exhibit the functional behaviors that have been predicted for 3D structures with complex geometries[13,14]. These functional behaviors include the inclusion of line defects to provide a possible means to use such engineered defects as a waveguide to guide light around bends with radii on the wavelength-scale.

Developing a fabrication method that can simultaneously satisfy all four design criteria presents a very demanding challenge to both experimental physicists and chemists alike. Although many fabrication methods have been investigated for the fabrication of these 3D PBG structures, four fabrication methods stand out in this field. These are: colloidal self-assembly[15], semiconductor micro-fabrication[5], holography[16], and three-dimensional direct laser writing (3D DLW)[17]. Although each of the four methods has proven beneficial in the fabrication of 3D PBG

structures, they also have their drawbacks. A comparison of the different methods is provided in Figure 1.3.

For the colloidal self-assembly technique, a colloidal suspension of spherical nano-particles is dried in a controlled manner so that they self-assemble into an ordered crystal lattice. Although this technique provides a simple method to produce photonic crystals covering large areas, there are two main drawbacks to using this method. First, the intrinsic stacking faults that are generated in the crystal structure during the self-assembly procedure cannot be easily controlled[18]. The presence of such intrinsic defects reduces the prospects of this system to exhibit a full-PBG. Furthermore, the incorporation of properly designed defects, which are functional, has proven to be very difficult in this system[19]. Second, since the actual self-assembled photonic crystal structure itself cannot support a full-PBG, it must be post-processed by inverting the structure with silicon[20]. This extra post-processing step adds complexity and introduces the possibilities for error into the fabrication process.

In the semiconductor micro-fabrication technique, the 3D structure is built by stacking individual layers on top of each other in a layer-by-layer fashion. Each layer must be aligned relative to each other with nanometer precision. Although high-refractive materials such as silicon or gallium arsenide can be used in this method, the precision alignment that is required can be very difficult to achieve in practice. Therefore, to this date, only structures that are a few layers thick have been successfully demonstrated.

Another two techniques that are particularly promising, are multi-beam holography and three-dimensional direct laser writing (3D DLW). In the multi-beam holography technique, an interference pattern created by the constructive interference of three or more beams result in the creation of a 3D pattern, which can be recorded in an

17
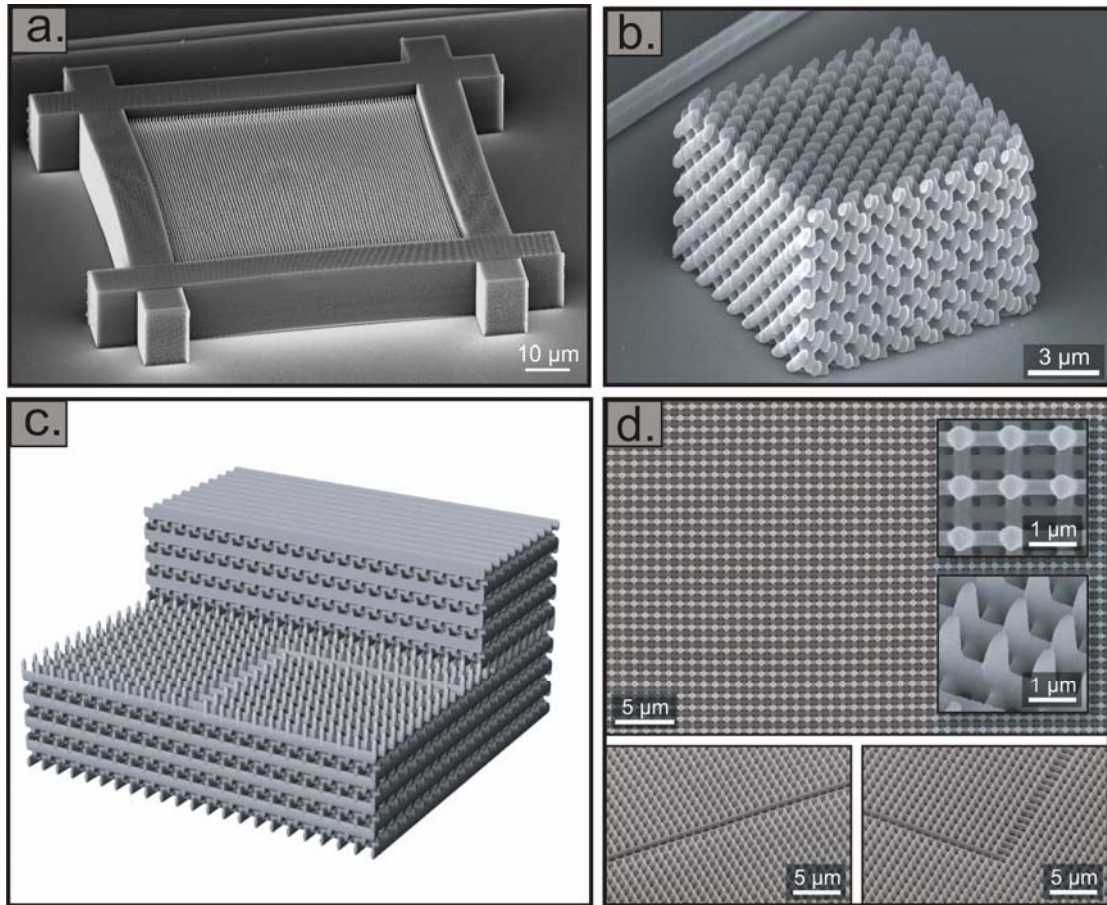
Figure 1.4 3D structures that were fabricated using 3D DLW in the organic photoresist SU-8. **a.** SEM image of a woodpile photonic crystal **b.** SEM image of an SP$_2$ photonic crystal **c.** Schematic depiction of a 3D-2D-3D photonic crystal hetero-structure. The line-defect present in the 2D layer was envisioned to provide lossless wave-guiding around sharp bends. **d.** SEM images of the hetero-structure depicted in **c.**

organic photoresist material. The benefit of this technique is that large areas of photoresist can be exposed via a single exposure of the interference pattern, thus enabling highly ordered photonic crystal structures to be fabricated over large areas. However, since this method only allows for photo-patterning of periodic structures, it is not possible to directly incorporate defects into this structure during this exposure step. Therefore, extra photolithography steps will have to be added subsequently to allow for the placement of defects.

With the 3D DLW technique, a photoresist exhibiting an intensity threshold for exposure is illuminated by laser light whose photon energy is insufficient to expose it by a one-photon polymerization process. If this laser light is tightly focused into the resist, however, the light intensity inside a small volume element ("voxel") enclosing the focus may become sufficiently high to exceed the phtoto-exposure threshold by a multi-photon processes. By scanning the focus relative to the photoresist, in principle, any 3D connected structure consisting of these voxels maybe written directly into the photoresist. This technique has enabled 3D PBG structures with highly complex geometries to be fabricated with high quality. The 3D DLW method has shown that it allows for the fabrication of complex structures with a quality and complexity that cannot be achieved with any other fabrication techniques. However, since the organic photopolymers (e.g. SU-8, n $\approx$ 1.57) that are used in this process exhibit a low refractive index, the final structures produced using this material are not capable of sustaining a full-PBG.

Despite the short-comings of the organic photopolymers that are used as the photo-resist material, the 3D DLW technique itself is the most promising photolithographic technique for the fabrication of 3D PBG structures. The reason is that this method provides an infinite design flexibility to create any connected 3D structure of arbitrary geometry. This flexibility enables highly complex theoretical 3D structures to be experimentally realized. For example, 3D woodpile photonic crystals with and without defects[21,22], as well as other more sophisticated 3D structures such as the SP$_2$ structure, have already been realized in organic photopolymers using the 3D DLW method[23,24]. (Figure 1.4) Due to the promising potential of this technique, we have decided to employ it as the photolithographic tool of choice in this thesis work.

As we have mentioned before, despite the utility and versatility of the 3D DLW technique, the structures that are produced from organic photopolymers are not capable of exhibiting a full-PBG. A remedy that is currently used to solve this problem is to use a post-fabrication process which uses the original 3D structure, made with organic photopolymers, as a template and replace it with a material such as silicon which has a large index of refraction to achieve a full-PBG. This post-fabrication method is called "silicon double-inversion", and it is an intricate process where high-quality results can be achieved by skilled operators[25,26].

Another approach that could provide a solution to the problem of low index of refractions that are experienced with organic photoresist, is to change the photoresist entirely and replace it with one that possesses an intrinsically high-index of refraction. Intuitively, by using a photoresist with a sufficiently large index of refraction, a suitable 3D structure can exhibit a full-PBG immediately after the 3D DLW process.

1.3 Arsenic Trisulfide (As_2S_3) as a Photoresist for 3D DLW

However, not all materials with a high refractive index can be used directly as a photoresist. The most important consideration when choosing the correct material is that it should exhibit photo-inducible changes in its chemical or structural properties. Furthermore, in order to easily adapt it for use with the 3D DLW technique, the potential photoresist material should act in a negative-tone behavior. These criteria mean that such a material must exhibit photo-polymerization behavior, and also the ability for the removal of the un-polymerized areas after the photolithography step. One class of material that has been shown to simultaneously possess both a high refractive-index and the ability to be photo-patterned are the chalcogenide glasses. These glasses have been known for their photo-induced meta-stabilities[27], which

have led to their widespread use in optical storage media like compact disk ROMs (CDRs) and digital versatile disks (DVDs)[28,29]. These glasses not only change their optical properties under photo-exposure, but also their chemical properties. This allows for selective chemical etching, making them suitable candidates for lithographic techniques.

Due to these favorable materials properties, various chalcogenide glasses, have already been used for the fabrication of 3D PCs. However, these previous works have been limited to opal infiltration[22–24] or layer-by-layer fabrication techniques[30,31], where two- or three-beam holographic laser lithography was combined with selective etching to build each layer successively. As above-gap radiation and thus one-photon absorption was used in these experiments the lithographic step could only be used to fabricate a single layer at a time. Consecutive layers had to be stacked on top of each other and PCs with a maximum of four layers have been reported.

One particularly well studied chalcogenide glass that exhibits the aforementioned materials properties is arsenic trisulfide, As_2S_3, an amorphous semiconductor with high transparency throughout the near-infrared and infrared spectral region[32]. The index of refraction of this material lies between 2.45 and 2.53[33], which is sufficient to open a full-PBG. In As_2S_3, the position of the absorption edge is found at 530 nm, this leaves a broad part of the visible and NIR spectrum accessible for the placement of a full-PBG. Furthermore, this absorption characteristic makes this material compatible with most 3D DLW systems that operate with femtosecond lasers at the wavelength near 800 nm[34,35,36].

Therefore, in this thesis work the objective is to develop As_2S_3 into a photoresist system for 3D DLW. Through the use of this chalcogenide glass, one could create a photoresist system which combines the flexibility of 3D DLW with the intrinsically
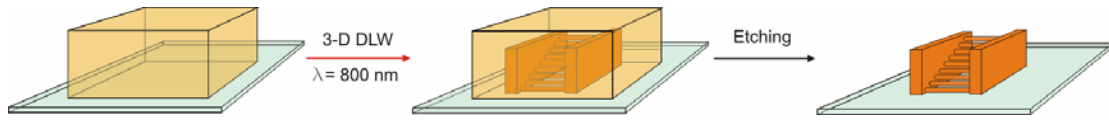
Figure 1.5 A schematic of the 2-step all-inorganic photoresist system that is based on the inorganic glass As_2S_3. In the first step of this system, the As_2S_3 precursor glass is to be formed into a photosensitive thin-film using a high-vacuum thermal evaporation technique. Such a thin-film will have to demonstrate photosensitivity towards the 3D DLW method. In the second step, the photo-polymerized structure will have to be etched out with high-selectivity so as to allow a free-standing 3D structure to be produced in one single etching step.

high index of refraction and the possibilities of selective chemical etching of this material, to directly produce 3D PBG structures with a full-PBG.

This novel approach entails the rendering of As_2S_3 into a 2-step photoresist system that is suitable for use with the 3D DLW technique, a schematic of which is presented in Figure 1.5. In this photoresist system, the first step is to fabricate a photosensitive thin film that can be photo-polymerized using 3D DLW. Then in the second-step, the 3D structure should be freed by removing the un-polymerized material. This step is called etching, and for the sake of simplicity, it should be done in a single-step. Such a photoresist system would allow the 3D DLW technique to directly produce 3D structures which possess a full-photonic band-gap.

Although the basic techniques that are used for the photoresist preparation, as well as the mechanism of the chemical etching reaction are documented in the literature[37,38,39], it is still unclear how one should adapt this material as a photoresist for fabricating three-dimensional structures using the 3D DLW technique. The reason is two-fold. First, the methods to produce a photosensitive thin film of As_2S_3 differ widely in the literature. It is well documented that As_2S_3 can be formed into a thin film using many different techniques. However, a gas-phase technique which can produce a total fragmentation of the polymeric As_2S_3 into individual molecules of S_8, As_4S_4 and As_4S_6, is required to produce a photoresist film with the highest

photosensitivity[38]. Although it has been documented that the complete fragmentation of the precursor material can only be obtained using a purely thermal technique, the exact deposition conditions for this technique vary greatly in the published literature. Due to these inconsistencies in the literature, a direct comparison of the results from different deposition parameters is impossible. Therefore, a thorough investigation into the thermal deposition conditions must be performed in this work, to determine the deposition conditions which can provide the desired gas-phase species.

Second, while As_2S_3 has been previously investigated for use both as a positive and negative-tone photoresist, those investigations are confined to producing thin, solid, 3D structures less than 500 nm in height[30,31,38]. For these thin structures, etchants with quick etch times and low selectivity are sufficient. However, those etchants documented in the literature for this purpose are not suitable for the fabrication of large and intricate 3D PBG nanostructures. The reason for this unsuitability is two-fold. First, because 3D PBG nanostructures are nanoporous, it requires increased etch times over a solid 3D structure due to the slower diffusion of the liquid etchant though the more tortuous architectures of the porous nano-scale voids of a 3D PBG structure. The need for increased etch times leads to the need for longer periods of immersion. A further challenge relates to the higher reaction rate in the volumes that have already been developed by the etchant in 3D nanostructures. The difference in the reaction rates is a result of the larger surface area per unit volume of a 3D porous material over that of a solid 3D structure. To overcome these long etch times in structures which have an inherently high reaction rate, the etchant that is used must possess a high etch selectivity. Since currently available etchants cannot provide the necessary selectivity to etch 3D PBG structures, a new highly selective etchant must be developed for this work.

Furthermore, although the As_2S_3 photoresist possesses an intrinsically high refractive index, this material does not provide any intrinsic room temperature photoluminescence. Therefore, structures that are fabricated with this material remain passive, and lack the ability to provide any optical activity. The ability for structures to possess optical activity is desirable since this would allow them to exhibit properties such as lasing[5] and all-optical signal amplification[40]. If the As_2S_3 photoresist was able to provide intrinsic room-temperature photoluminescence, it could also simultaneously serve as a gain medium for the investigation of these desirable behaviors in 3D PBG structures[41]. Since there is no current demonstration of a deposition method which provides photoluminescence to As_2S_3 photoresist which is suitable for 3D DLW, it is important to investigate and develop such a method.

In this thesis work, we will address and provide solutions to the chemical as well as the technical challenges that are present when formulating As_2S_3 into a 2-step photoresist used for 3D DLW. First, we present the investigations into the thermal deposition method, which allows a photosensitive thin film of As_2S_3 to be fabricated. Second, we will provide the details of an investigation, which leads to the synthesis of a highly selective etchant that allows the etching to be performed in one simple step. Furthermore, we provide an in-depth study into the inclusion, or doping, of photoluminescent erbium atoms (Er) into As_2S_3, in order to provide intrinsic photoluminescence to this material, while retaining all of its properties as a photoresist.

The results of these investigations described in this thesis allow As_2S_3 to be made into a functional and reliable 2-step photoresist system, which can also demonstrate photoluminescence, and is compatible with the 3D DLW technique. Using this

photoresist system, we demonstrate the fabrication of 3D PBG structures as well as other 3D nanostructures with interesting optical properties.

Chapter 2 - Thin Film Fabrication

2.1 Introduction

The initial overview of the optical and chemical characteristics of As_2S_3 in chapter 1 indicates that this material could become a very attractive candidate for use as a high refractive index photoresist for the 3D DLW method if it can be made into a photoresist system. Furthermore, in that chapter we also mentioned that if As_2S_3 is to be made into a photoresist system, the simplest way to implementation would be to formulate it into a two-step, negative-tone photoresist according to the scheme outlined in Figure 1.5. In this chapter, we will provide a technique which allows this material to be transformed into a photoresist material that is suitable for the 3D DLW method.

2.2 Thin Film Fabrication Concepts

In the bulk form, As_2S_3 is usually found as a glassy, amorphous solid. In this glassy, amorphous form, the atoms in this material are highly cross-linked and randomly arranged with no long-range order being present[33]. Although various photo-induced behaviors can be observed in this glassy form, the photo-polymerization behavior that is sought after in this current work does not occur in this form because the material is already highly cross-linked. Therefore, in order to transform the highly cross-linked As_2S_3 glass into a form that exhibits photo-polymerization, we must first de-polymerize the precursor into individual arsenic-sulfide molecules, which could then be photo-polymerized back into the highly cross-linked glass[42].

In order to aid in the understanding of this polymerization process, one could draw an analogy to organic polymers. An organic polymer would not undergo further

$$2(m+n)\,As_2S_3 \leftrightarrow n(As_4S_4 + \tfrac{1}{4}S_8) + m\,As_4S_6$$
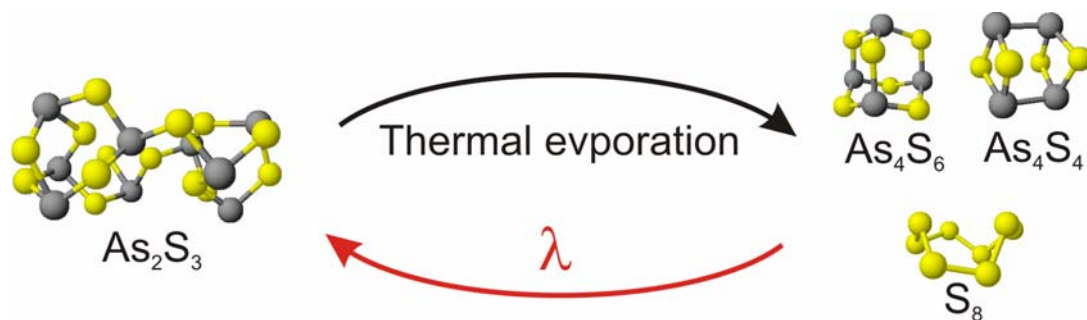
Figure 2.1 The process of thermal evaporation and photo-polymerization. The cross-linked As_2S_3 glass can be fragmented into molecules of S_8, As_4S_4 and As_4S_6 using a high vacuum thermal evaporation technique. These individual molecules can be collected on the surface of a thin film and then be photo-polymerized and cross-linked back into the As_2S_3 form using light with the suitable energy and intensity. The reversible reaction is depicted in the equation above.

polymerization if there is no more monomer present. The polymerization reaction can only proceed when monomers are present in the reaction. The physical state of the solid amorphous As_2S_3 is similar to that of the fully-polymerized organic polymer. No polymerization can proceed since "monomers" of the As_2S_3 glass are not present in this fully polymerized form. Therefore, in order to allow As_2S_3 to exhibit photo-polymerization behavior, "monomers" of this material must first be generated. Furthermore, the majority of these "monomers" that are to be generated from the As_2S_3 precursor should largely consists of S_8, As_4S_4 and As_4S_6 molecular species, since it had been reported that a thin film, which contained these molecular species exhibits the highest photosensitivity towards photo-polymerization[28,43,44]. Therefore, the first step in implementing As_2S_3 into a two-step photoresist system was to find a method which can allow for the generation of arsenic-sulfide molecular species or

"monomers" and also their subsequent collection onto the surface of a substrate to form a photosensitive thin film.

Currently available thin-film deposition methods for fabricating arsenic-sulfur thin film involves the use of a vaporization technique, which first evaporates the precursor material into the gas-phase, and then subsequently collects this vapor on a substrate to form a thin film. It has been shown previously that different vaporization techniques will result in the generation of different types of gas-phase species[45,46]. These various types of vaporization techniques currently used can be divided into two main categories that depend on the gas-phase species that are generated. The first category consists of vaporization methods that retain the structure and stochiometry of the precursor material, and the second category consists of methods that produce a high degree of fragmentation of the precursor during the vaporization process.

The first category of vaporization techniques uses a highly intense energy source that interacts with the As_2S_3 precursor for a very short time. Due to the short interaction time between the incident energy source and the precursor material, local heating is dominant and the even thermal heating that is required to obtain complete thermal fragmentation of the material cannot be achieved. Therefore, these vaporization techniques do not cause any significant bond dissociation or rearrangement in the material that is emitted or ejected from the precursor source. A type of evaporation technique that exhibits this behavior is physical vapor deposition or sputtering. (e.g. argon ion sputtering [47].) Here, fast ion-bombardment impacts and dislodges material into the gas-phase, with a chemical composition and structure that is similar to that of the precursor at the source. Another technique that exhibits this behavior is the use of highly energetic electron beams to generate a vapor from the source[46]. The electron beam is capable of generating very high temperatures at the

28

precursor. However, because the temperatures that are instantaneously generated in the precursor are so high, the low melting As_2S_3 glass tends to vaporize so quickly that it explodes locally and becomes ejected as large un-fragmented particles. Yet another technique that employs a rapid local heating and causes thermal ablation of the precursor source is laser-assisted deposition (or laser ablation)[48,49]. This technique also causes an instantaneous vaporization of the precursor and has the same drawbacks as the electron beam technique. Overall, the films produced using these techniques exhibit poor photo-polymerization behavior because the fragments that are ejected into the gas-phase contain large portions of polymerized material. The presence of these large polymerized fragments introduces discontinuities in the as-deposited photoresist film, which tend to reduce the resolution of the photoresist and generate roughness in the final structure[50,51].

The only known vaporization technique that is capable of producing photosensitive thin films of As_2S_3, that are significantly different both chemically and structurally from the precursor, is the thermal evaporation technique[52]. This vaporization technique involves the use of an oven which allows the precursor at the source to be thermally heated in a slow and controllable manner, thus enabling a more complete fragmentation of the precursor glass to take place. In this process, the As_2S_3 glass precursor is thermally heated in a high-vacuum environment until it evaporates into the gas-phase. During the evaporation process, the precursor glass defragments and rearranges in the gas-phase to yield individual molecular fragments or "monomers"[43]. Due to the random gas-phase fragmentation process, a host of arsenic and sulfur molecules can be identified in the gas-phase. However, the most abundant molecular fragments that have been identified in the gas-phase, and collected on the substrate, are the molecules of S_8, As_4S_4 and As_4S_6[43,53,54]. Once the As_2S_3 precursor has been

fragmented into this monomer form, it can then be re-polymerized via the use of light sources with sufficient photon energies, such as a laser. The entire thermal evaporation process takes place in a high vacuum chamber to reduce contamination from oxygen and water, and also serves to lower the boiling point of the As_2S_3 precursor thus allowing lower heating temperatures to be used. Using this method, it is possible to produce thin films composed of molecules that are chemically and structurally different from the As_2S_3 precursor[55,56]. A schematic of the generation and photo-polymerization of these molecular species or "monomers" during the de-polymerization process is shown in Figure 2.1.

Such a high-vacuum thermal evaporation thin film fabrication method was used to produce the photosensitive thin films that are used in this thesis work. Throughout this thesis we shall describe the As_2S_3 precursor glass, when it is in the polymerized state, as the "photo-polymerized material", and when it is in the fragmented molecular or monomer form, we will describe it as being in the "as-deposited" state.

From Figure 2.1, one may also notice that the photo-polymerized form and the as-deposited form have different morphologies. The photopolymerized form is a highly cross-linked polymer whereas the as-deposited form contains highly fragmented molecules. The morphological difference between these two forms enables selective chemistry to be performed on these different areas and thus allows for the removal of one form over the other. (cf. Chapter 3) The ability to remove individual areas selectively also satisfies the second criteria of the two-step photoresist system that we have proposed in Chapter 1, which is the ability for selective etching.

In the rest of this chapter we will present the high-vacuum thermal evaporation method that is used to generate photosensitive As_2S_3 thin films that are suitable for the 3D DLW process. Then we will provide an analysis of the gas-phase species that are

30
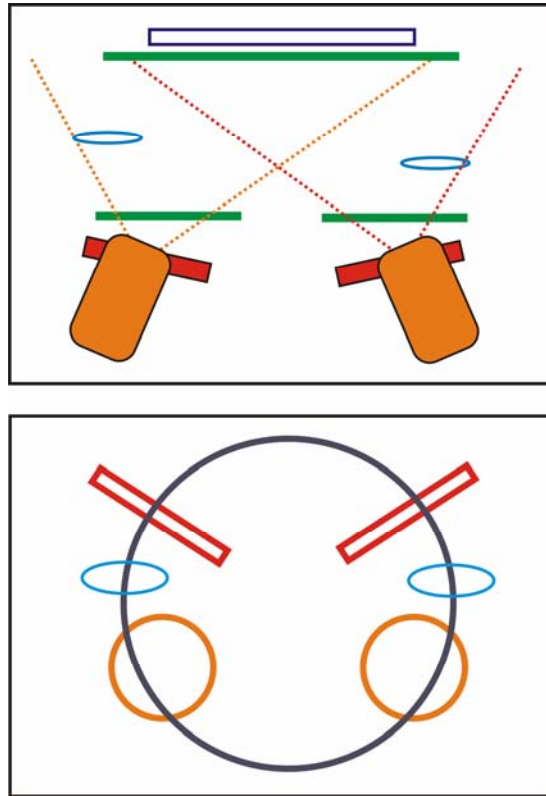
Figure 2.2 A schematic of the arrangement of the interior of the high-vacuum thermal evaporation chamber. The orange circles represent the crucible oven sources, the red-boxes represent the tungsten thermal filaments, the purple box represents the substrate holder, and the blue ovals represent the quartz micro-balances that are used to sample the rate of the deposition during computer controlled closed-loop operation. (Upper image) A side view of the arrangement of each of the components in the chamber. The sources are positioned so that their vapor cones provide an overlap at the substrate holder. The quartz microbalances are staggered so as to prevent cross-sampling of the different vapor cones. (Lower image) The positions of the thermal sources inside the deposition chamber, viewed from a top-down perspective. The sources are arranged symmetrically so as to allow the vapor cones of the 4 sources to provide even overlap at the substrate holder.

generated in this process using a mass spectrometric analysis technique. Furthermore, we provide an analysis of the chemical and optical properties of the photo-resistive thin films that are fabricated using this method.

2.3 Experimental Results and Discussion

To generate the photosensitive thin films that were required in our study we introduced a setup, based on the high-vacuum thermal evaporation method, which allowed for the generation of a vapor of molecular fragments of the As_2S_3 precursor and the collection of this vapor to form a photosensitive thin film. It had been well documented in the literature that the photosensitivity of the as-deposited thin films, that were fabricated using this method, was highly sensitive to the experimental deposition conditions used[35,46,51]. However, since the deposition parameters cited in the literature varied widely or were simply poorly documented, it was necessary to develop our own set of deposition parameters for this work. Therefore, to optimize the deposition conditions that were necessary to generate the desired molecular fragments, we used a temperature resolved gas-phase analysis technique to simulate the deposition process. Using this simulation we could determine the optimum deposition parameters that should be used in the actual high-vacuum thermal evaporation method. The results of this investigation are presented in the following section.

2.3.1 High Temperature Thermal Evaporation

The high vacuum apparatus that was employed to produce all of the As_2S_3 thin film samples used throughout this thesis work was a commercially available high-vacuum thin film deposition system from BOC Edwards. (BOC Edwards Auto 500). The setup consisted of 4 thermal evaporation sources. Two of the sources were crucible ovens with a capacity of 5 cc and a maximum temperature of 500 ºC. The oven sources were used exclusively for the evaporation of As_2S_3. The other two sources employed

removable tungsten thermal filaments, with a capacity between 0.5 to 1 cc of material, and a maximum heating temperature of 1530 ºC. These filament sources were used to evaporate materials where high vaporization temperatures are required, such as pure metals. A schematic of the arrangement of these deposition sources is illustrated in Figure 2.2.

Solid As_2S_3 glass of >99.99% purity (Amorphous Materials, Garland, Texas) was used as the precursor material. Silica glass cover-slips (Menzel Gläser, 170 ($\pm$ 10 μm) were used as substrates. The chalcogenide glass was first crushed, then placed in the high vacuum system and thermally evaporated onto the glass substrates which are mounted onto a water-cooled, rotating substrate holder directly opposite to the source. The chamber was operated at high vacuum ($P < 2x10^{-6}$ mbar) and the evaporation temperature of the source containing the As_2S_3 precursor was maintained between 370 to 390 °C. The evaporation rate of the material was monitored using a quartz crystal microbalance. The entire process was computer controlled to ensure reproducibility.

2.3.2 TGA-MS and Thermal MS Analysis of Gas-Phase Species

Using the system as described above, it was possible to simply evaporate the precursor material and obtain a thin film of unknown composition and morphology. However, in order to produce a vapor which contains the suitable species that yielded the highest photosensitivity, we need to determine the optimum thermal evaporation conditions and parameters. In the ideal scenario, a complete fragmentation of the As_2S_3 precursor into S_8, As_4S_4, and As_4S_6 should provide the optimum photoresist behavior, which will yield high resolution and good photo-polymerization behavior.

Therefore, in order to determine these optimum conditions for generating the suitable gas-phase species, and to determine which types of gas-phase species were
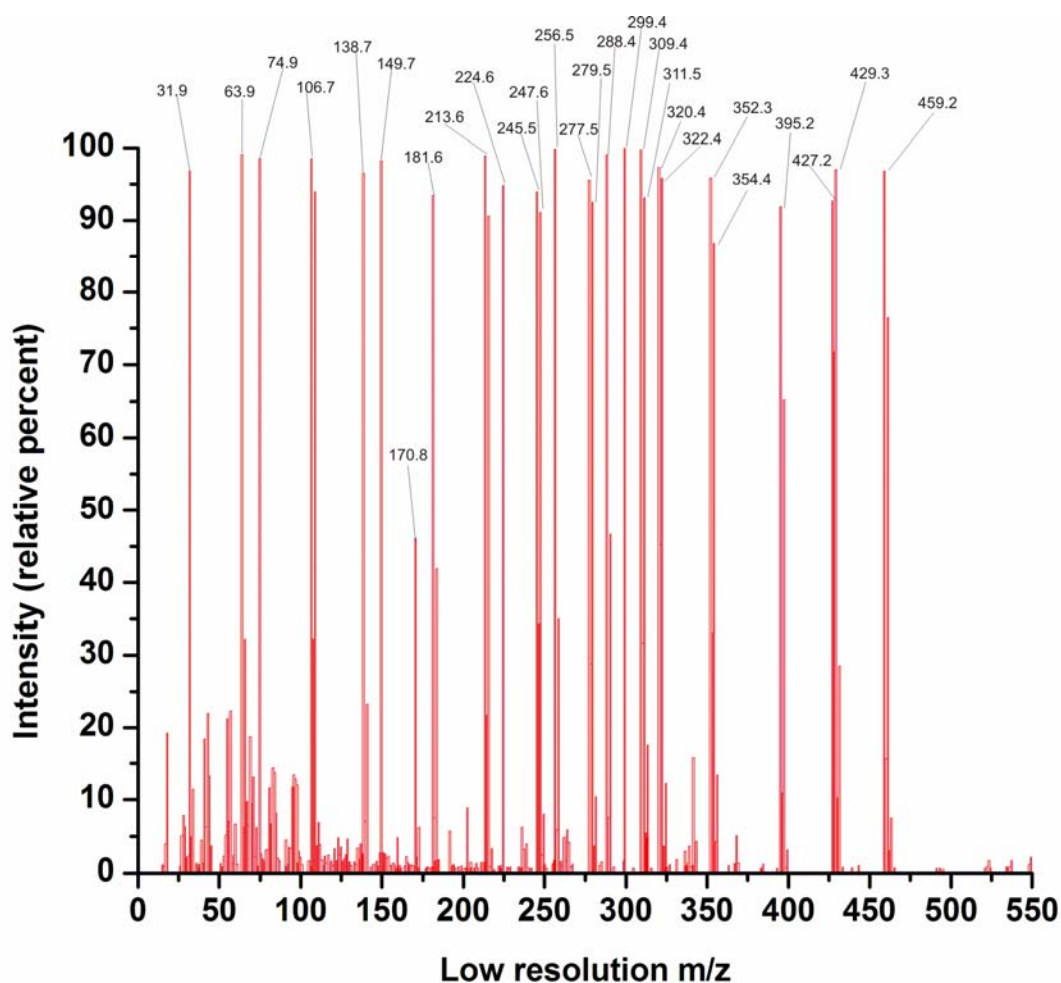
Figure 2.3 A mass spectrum of the As_2S_3 precursor as obtained from the MS2 mass spectrometer. The masses of the important fragments are assigned. A discussion of the fragments is provided in the text and in Figure 2.4.

being generated, we employed the analysis techniques of thermal mass spectroscopy (MS) and a thermogravimetric analysis-mass spectrometry (TGA-MS), which is a coupled analytical technique, to simulate various deposition conditions and characterized the molecular mass of the species that were present in the vapor as they were being generated from the As_2S_3 precursor.

The molecular mass of the individual fragments that are generated in the gas-phase was analyzed using two different mass spectroscopic setups because each setup has its unique benefits as well as drawbacks. In the case of the TGA-MS setup, the mass loss
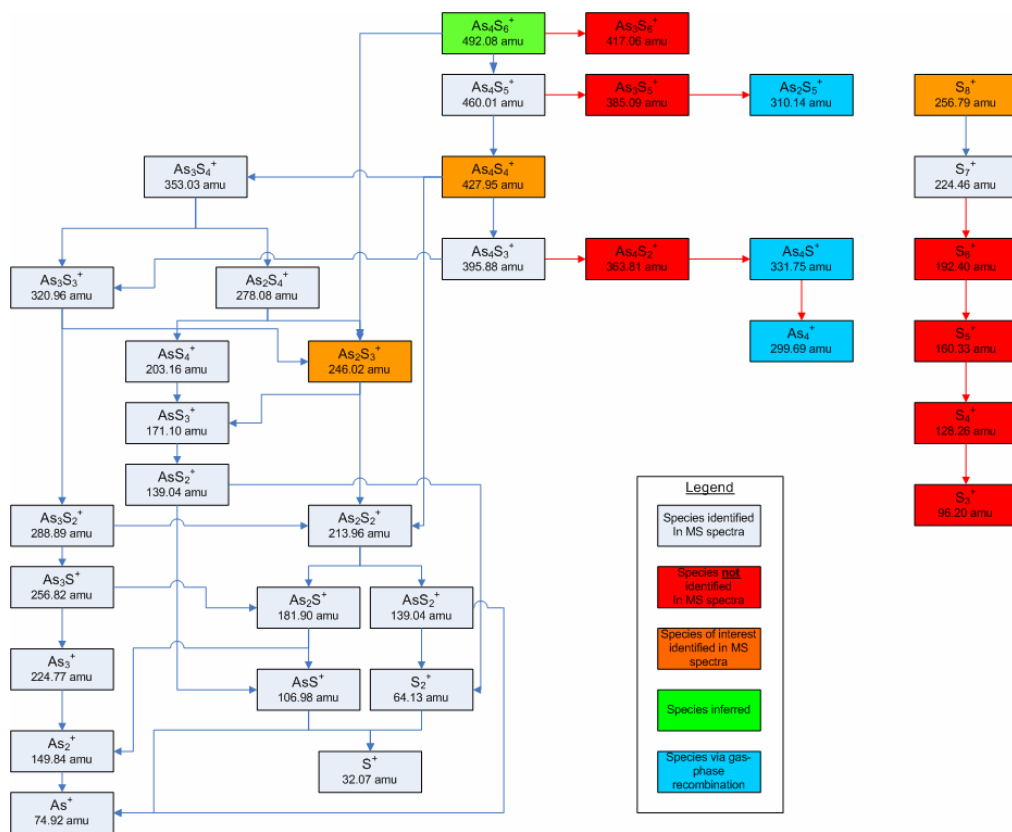
Figure 2.4 The fragmentation pathway of the species that have been identified from the mass spectrum of the As_2S_3 precursor glass using the MS2 mass spectrum. Using the species that have been identified and the ones that have not been observed, we can deduce the presence of the As_4S_6 molecular fragment. Blue arrows indicate a fragmentation pathway that leads to an observed species. Red arrows indicate that the fragmentation pathway does not lead to a species that is observed in the gas-phase.

behavior of, as well as the relative amount of vapor generation from, the sample can be correlated to the temperature of the source material. However, the draw-back with this setup was that the mass range of the mass spectrometer was limited to below 233 atomic mass units (amu). Therefore, the larger parent ions of the As_2S_3 precursor could not be directly detected. To overcome this problem, a second mass spectrometer (MASSPEC II system, MSS, Manchester, UK), which has a dynamic range of up to 1000 amu was used to further analyze the species generated in the gas phase; we will call this second system MS2.
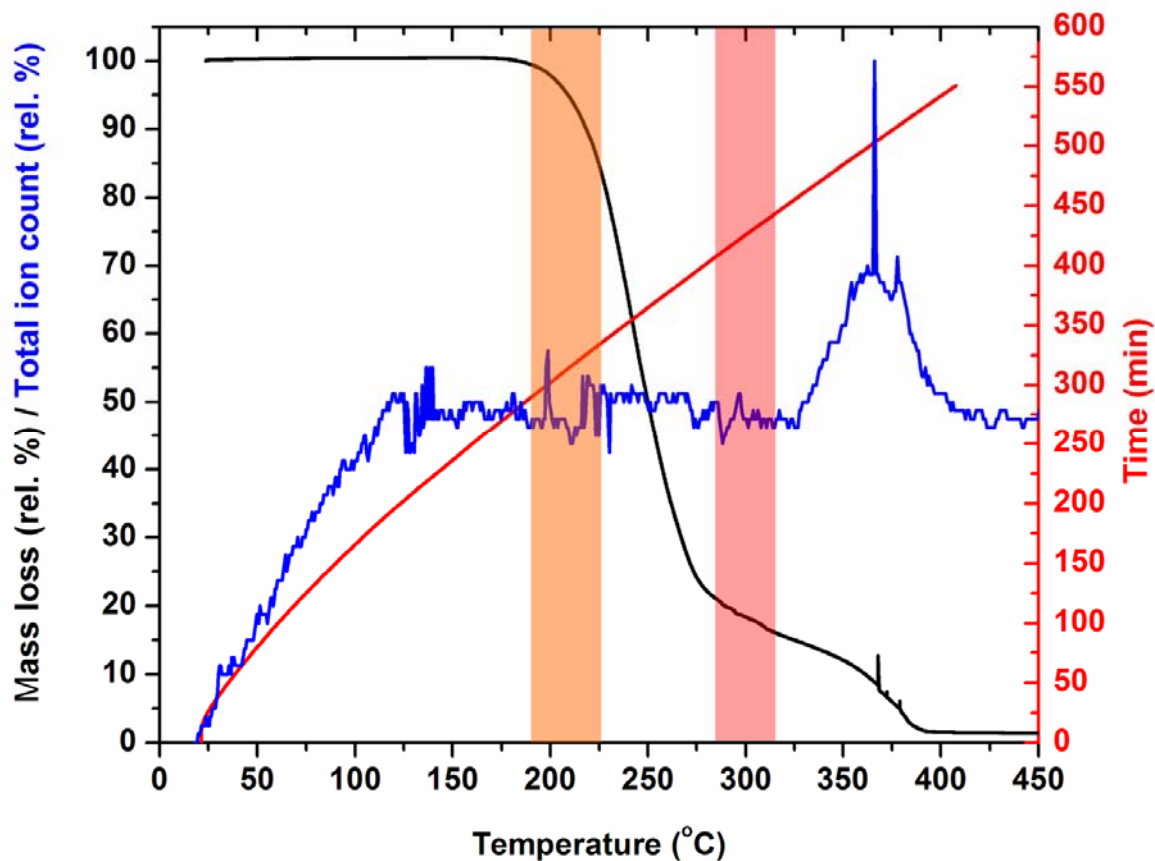
Figure 2.5 A TGA-MS spectrum of the thermal evaporation of the As_2S_3 glass precursor. The black curve is the percentage mass loss of the precursor sample and the blue curve is the total-ion count that is generated in from the sample. The behaviors of these two curves are dependant on the heating temperature of the source. The heating profile of the source is depicted by the red curve. The TGA-MS setup is configured so that it mimics the high-vacuum conditions that are experienced in the vacuum thermal deposition setup which is use to produce the photosensitive As_2S_3 thin films. The orange area marks the temperature range of the glass-transition (T_g) and the pink area marks the temperature range of the melting point of the glass (T_M).

The TGA-MS system (Netzsch TGA-MS system) consisted of a thermogravimeteric analysis (TGA) mass balance (Netzch 409 CD) that was coupled to a quadrapolar mass spectrometer via a heated transfer line (Netzsch QMS 403/5 "Skimmer" coupling system). The "Skimmer" coupling system contained a heated wall transfer system that prevented the condensation of gaseous species onto the walls of the transfer line during measurement. The heating of the transfer line is matched to the temperature of the source and therefore mimiced the source behavior. The

quadrapole MS used an electron impact ionization method, and the detector was set to detect positive ions. This system was operated in the mass range from 1 amu to 233 amu with a resolution of 0.01 amu. Using this setup, the percentage mass loss and the total ion count (a representation of the vapor flux) could be determined as a function of temperature. Samples were measured under a dynamic vacuum of 5×10^{-6} mbar to mimic the deposition conditions of the actual high-vacuum thermal evaporation chamber during the thin-film deposition process.

The MS2 system also consists of a quadrapolar mass spectrometer and used an electron impact ionization method, and the detector was also set to detect positive ions. This setup had a mass range from 1 amu to 1000 amu with a resolution of 0.01 amu. The thermal source of this setup was programmable and could provide temperature ramping and holding programs. The temperature profile that was obtained using the TGA-MS setup described above was fed into the temperature controller of this setup to simulate those conditions. The samples were measured under a dynamic vacuum of 1×10^{-8} mbar or lower. Using this method, fragments that were generated into the gas-phase which had a high-molecular mass could be analyzed.

Although the TGA-MS system suffered the problem that it could not detect fragments with a high molecular mass, the mass spectra that was collected did provided some valuable information regarding the masses of species were present in the gas phase, because the lower mass fragments from the characteristic fragmentation pattern of the As_2S_3 precursor could be analyzed using this system. In order to identify the parent ions and determine the characteristic fragmentation pattern of the precursor glass, the MS2 system, with its larger mass range, was used.

The mass spectrum, shown in Figure 2.3, is a representative spectrum of a MS2 scan. There the parent ion, the fragment with the highest molecular mass, of 459.2

amu can be observed, and it is identified as $As_4S_5^+$. In these scans, although fragments that contain even higher masses are observed, they are present in very low amounts relative to the main signals of interest. These larger fragments are a result of gas-phase rearrangements of the ions that have been generated by the electron impact ionization. In previous studies by other investigators, these large fragments are only observed at significant numbers at higher evaporation temperatures[43]. Therefore, their identification is omitted in this analysis.

From the analysis of the major species that have been identified in the gas-phase we reconstructed the fragmentation pathway of the parent ion. Using the reconstruction shown in Figure 2.4, we could determine which species present in the gas-phase were the parent ions, and which species were present due to the fragmentation of those parent ions[57,58]. Using the fragmentation pathway that we constructed, we identified two other major parent ions of interest, and those were S_8^+ and $As_4S_4^+$ ions. The presence of those two ions in the gas-phase was not surprising as their presence had been reported in many previous studies into the photoresist films that were produced using the high-vacuum thermal evaporation process, and also in laser-assisted desorption studies[53,57,58]. Furthermore, although the As_4S_6 molecule could not be directly observed as a fragment in the mass-spectra, the fragmentation pathway provided good evidence for the presence of the As_4S_6 molecule. If one examines the pathway closer, every fragment of the As_4S_6 molecule could be accounted for. In past studies, it had been established that the identification of the As_4S_6 molecule in the gas-phase using mass spectroscopy could be difficult. This is because most mass spectrometers employ an electron impact method to generate ions in the gas-phase. It had been argued that the As_4S_6 is prone to the fragmentation from the impact of these electrons[43,59]. The fragmentation pathway that is presented here provides very good

support to previous observations, and strongly suggests the presence of the As_4S_6 molecule. The overall analysis of the fragmentation pathway also suggests that As_4S_6 is not the exclusive molecule present in the gas-phase, as the other parent ions such as S_8 and As_4S_4 are also observed in the mass spectrum analysis. Since the presence of all three molecular compounds were well documented in the literature, the presence of all of three fragments; S_8, As_4S_4, and As_4S_6 will be considered together in this thesis work.

After having established the fragmentation pathway of the As_2S_3 precursor, we proceeded to analyze the TGA-MS spectrum. A representative TGA-MS spectrum of the As_2S_3 precursor is shown in Figure 2.5. Three curves are plotted in the spectrum. The two temperature dependant curves are: the black curve, which is the mass loss curve obtained from the thermogravimetric analysis, and the blue curve, which is the total ion count (TIC) as collected by the mass spectrometer. The red curve is the temperature profile of the heating program used to generate the behaviors that are observed in both the blue and black curves.

By examining this TGA-MS spectrum, we can observe some key features in the collected spectrum during the thermal evaporation process. First, in the TIC spectrum (blue curve), we observe that there is a steadily increasing vapor pressure starting from room temperature, which reaches a steady state of 50% of the relative maximum between 105ºC to 320 ºC, before exhibiting a Gaussian profile between 320 ºC to 400 ºC. Second, in the TGA spectrum (black curve), we observe that the mass loss occurs in two pronounced steps at 195 ºC and at 270 ºC. Noting these key transition points, we will structure the analysis of the TGA spectrum by separating the temperature range into four intervals and discuss them separately. These four individual segments are: room temperature to 105ºC, 105ºC to 195ºC, 195ºC to 270ºC and 270ºC to 400ºC.

In the first segment, room temperature to 105ºC, we observe that there is a steady increase in the relative total-ion count despite observing relatively no change in the mass loss of the source. When the mass spectra obtained at these temperatures were analyzed, it was observed that the species present in the gas phase were very light ions such as oxygen, water, carbon monoxide, nitrogen, and argon. Although they contribute to the total ion count, since these residual gas species are very light atoms and molecules they have a negligible effect on the change of the sample mass. In the mass spectra collected in these temperature ranges, there were no indications that any As-S clusters were present in the gas-phase. Since we know, from the MS2 mass-spectrum collected earlier, that if an arsenic-sulfide containing ion was present in the gas-phase, the mass of 106 amu, which is indicative of the AsS^+ ion, must be present. Therefore, from this analysis, the material that was emitted into the vapor was the surface contaminants of the crushed glass precursor, and no As-S fragments were being emitted at this temperature range.

In the second interval, from 105ºC to 195ºC, we observe a steady relative total-ion count. When we examine the ions that were present in the gas-phase during this range, we observed the same set of mass peaks as was recorded in the first interval. Furthermore, there continued to be no significant mass-loss during this interval. These results indicate that at this temperature range the sample continues to out-gas or desorb the species that were present on its surfaces.

In the third interval, from 195ºC to 270ºC, we begin to observe a dramatic loss in the mass of the sample. The beginning of this mass-loss step at 210 ºC corresponded to the beginning of the glass transition temperature (Tg) of the As_2S_3 precursor[28,33]. The Tg is the temperature at which the solid glass begins to soften. Over 80% of the relative mass of the sample was lost during this temperature range. When one

analyzed the mass spectrum of the gas phase species that were generated at this temperature range, the mass of 106 amu, which is indicative of the AsS^+ ion, began to appear. This was a good indication that fragments with As-S bonds were beginning to appear. When the vapor that was produced at this temperature range was cross-checked with the MS2 system, we were able to observe the presence of significant amounts of $As_4S_5^+$ ion. This measurement indicated that as soon as the Tg was reached the solid glass began to melt, and at those temperatures it was sufficient to allow for the generation of the desired molecular species into the gas phase. The generation of the gas-phase species was very controlled and no spikes or increases in the total ion count were observed during the mass-loss of the sample.

In the fourth and final interval, from 270ºC to 400ºC, once again we observe a dramatic loss in the mass of the sample. In this instance, near the beginning of the mass loss step at 310 ºC, the melting point (Mp) of the As_2S_3 precursor began to set in[28,33]. At this temperature, the soft glass transformed into a liquid, and between the temperatures of 330 ºC to 390 ºC, there was a substantial increase in the TIC, which exhibited a Gaussian-shaped intensity profile, within this temperature range. This indicated that within this range, there was a point where a maximum amount of vapor species were being generated in the gas-phase at a very rapid rate. The mass spectrum of the vapor species generated at this temperature showed fragments which belonged to the $As_4S_5^+$ ion. At 365 ºC there was even a large spike in the total-ion count curve as well as a spiking behavior in the TGA curve. The temperature at which this maximum evaporation occurred was unexpected, as one would expect the onset of high rates of evaporation to occur near the Mp of the glass, which is at 310 ºC. Furthermore, the spiking behavior recorded in both the TIC and TGA-MS curves is common in samples that have melted during the temperature scan, and is caused by

the ejection of large fragments during the bubbling of a molten liquid. This effect is also known as "source spitting".

Through the above investigation we established that, under conditions that were similar to our experimental setup, high rates of evaporation were obtained 50 °C beyond the Mp of the glass. Furthermore, the results of this TGA-MS analysis provided information regarding the temperature characteristics of the high vacuum thermal evaporation process. The elucidation of the most suitable temperature profile provided us with important information regarding the evaporation characteristic of As_2S_3. This knowledge enabled us to develop a suitable heating program for our thermal evaporation setup, enabling the correct phase of As_2S_3 to be obtained in the gas-phase, while achieving both an appreciable and steady rate of film deposition over the course of the entire thermal evaporation process. The information that was obtained here was valuable since one could not obtain this detailed information from the literature.

The heating program that we have developed had a source heating rate which mimics the temperature profile as used in the TGA-MS analysis, and the main deposition temperature was set between 365°C to 390°C. The rate of evaporation at these temperatures could be held constant at a value between 1 nm/s to 6 nm/s. We chose to use the higher temperature range of segment 4 rather than the lower temperature range of segment 3, because in the actual thin-film evaporation deposition setup, the source crucible was much larger than the source used in the TGA-MS simulation. The crucible used in the actual thin film deposition held approximately 300 times more precursor material (by mass) and had 9 times higher surface area at the source opening than the source that was used in the TGA-MS simulation. The larger surface area of the deposition source caused it to cool very
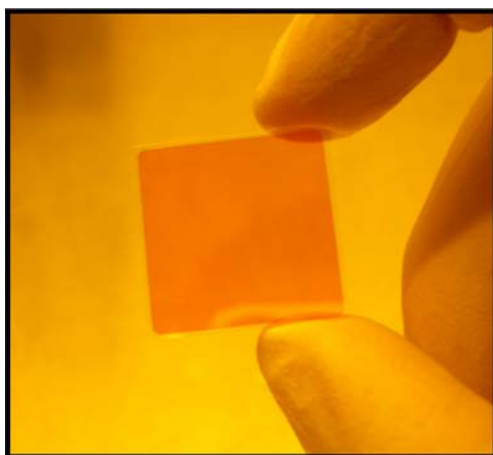
Figure 2.6 A typical as-deposited As_2S_3 photoresist thin film on a silica glass substrate. The film is orange in color and optically, clear and transparent.

quickly during the evaporation process, and because the evaporation temperature in segment 3 was so close to the Tg, any rapid cooling during evaporation caused a rapid solidification of the melt, which resulted in the formation of a plug at the exit of the thermal source. The presence of this solid plug of material stopped the deposition process by effectively sealing the opening of the thermal source. The re-heating of the plugged source was very difficult since the large mass of precursor that must now be heated through the glass-transition point was no longer centralized inside the hot-zone of the crucible oven, but is solidified at the exit point of the oven. If this plugged source was simply heated with progressively higher temperatures, a pressure would build up inside the source and the plug would eventually shoot out of the oven. This unpredictable behavior prevented any type of control over the deposition process. Therefore, we decided to use the upper end of the heating range, so as to operate the thermal evaporation source away from the Tg and completely prevent the re-solidification of the precursor from occurring.

By programming the optimized heating ramps and rates that we had determined here, into the computer controller of the high-vacuum thermal evaporation system, we

can reproducibly obtain as-deposited photoresist films that are orange in color, and optically clear and transparent. A picture of a typical photoresist film that is produced is shown in Figure 2.6.

2.4 Materials Characterization

2.4.1 Chemical Properties

Once we determined the set of evaporation conditions required for generating the desired gas-phase molecules, and we collected them on a substrate to form a thin-film, the stochiometry, as well as the phase of the material, that is present must also be determined.

Since a high degree of thermal fragmentation was observed in the thermal evaporation method, a deviation from the ideal stochiometry from that of As_2S_3 precursor was highly likely. A deviation from the ideal stochiometry (As:S ratio of 2:3) was undesired since this would change the materials properties of the system. For example, if there was an increase in the As concentration away from the ideal stochiometry, the photosensitivity will be reduced and the material becomes less sensitive to base etchants. Furthermore, an increase in the sulfur content had the effect of reducing the refractive index and also made the material more susceptible to room temperature oxidation[60,61,62]. Therefore, in order to determine if our high vacuum thermal evaporation technique could produce a thin film near the ideal stochiometry, we analyzed its chemical composition using energy dispersive X-ray analysis and also with Rutherford backscattering spectroscopy.

In these analysis methods, the EDX method was useful for characterizing the relative amounts of the atoms present on surface of the samples, while the RBS

Method	As	S	Stoichiometry
EDX	39.97 (rel. at %)	59.17 (rel. at %)	$As_{2.02}S_3$
RBS	40.2 (abs. at. conc.)	59.8 (abs. at conc.)	$As_{2.01}S_3$
XPS	40 (rel. at %)	60 (rel. at %)	As_2S_3

Figure 2.7 Tabulated data of the stochiometry of the as deposited thin films that are obtained from the high-vacuum thermal evaporation thin-film deposition. All three analysis methods indicate that the as-deposited films that are produced exhibit a stochiometry that is close to that of the As_2S_3 precursor.

method was able to provide the absolute concentration of each atomic species that were present in the entire volume of the sample. (cf. Chapter 5.2.2. and Chapter 6) Furthermore, the stochiometry was also extracted from an XPS analysis which was performed as part of another investigation. (see page 49) The result of these analyses is tabulated in Figure 2.7. The results of these measurements showed that the thin films produced here possessed an As to S stochiometry very close to the ideal ratio of 2 to 3, which was the stochiometry of the original glass precursor.

Having analyzed the stochiometry of the as-evaporated film, we also examined the surface of the thin film to determine what types of molecular species were collected from the gas-phase. The usual technique for the analysis of the morphology of molecules that are present on the surface of film is through the use of the powder X-ray diffraction method. However, in this case, since molecular clusters, or chalcogenide glasses in general, do not possess any long range order in their atomic structure, these films do not provide any clear diffraction peaks using PXRD and this poses a problem for a clear elucidation of their atomic structure[63]. Therefore, a method that is routinely used to analyze chalcogenide glasses is Raman spectroscopy[53,64,65].
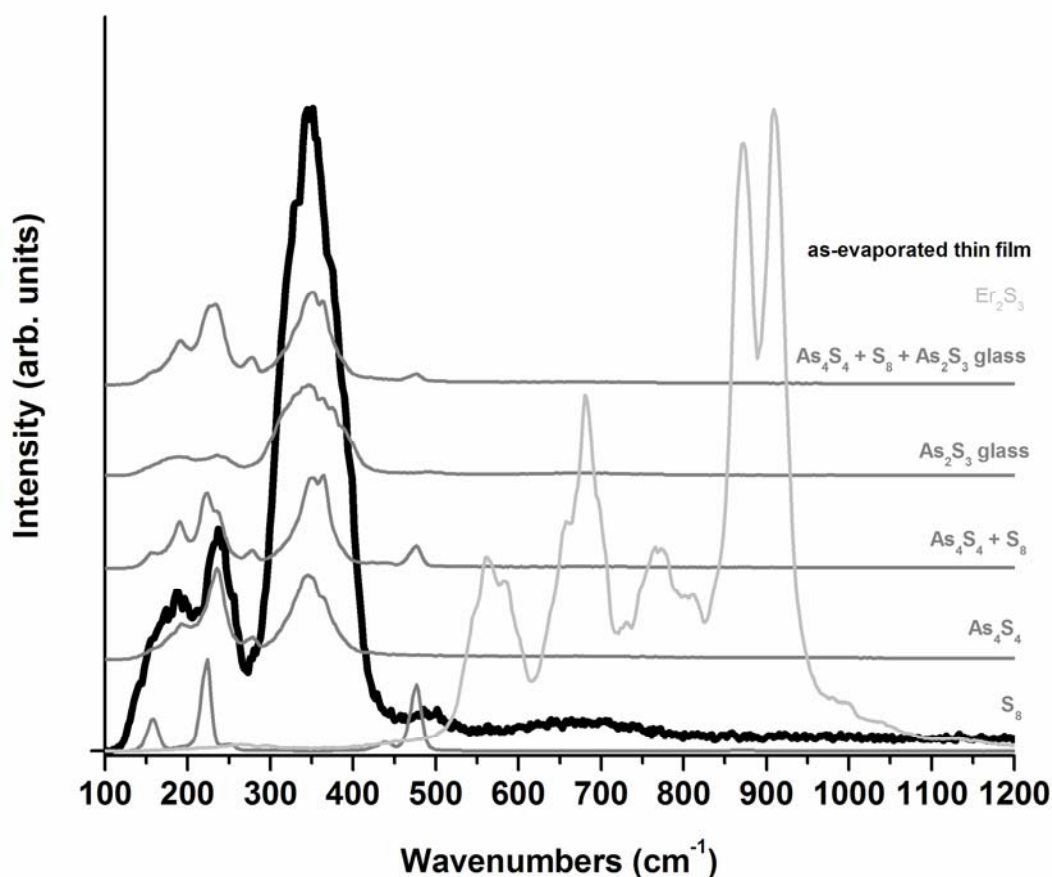
Figure 2.8 A comparison of the Raman spectrum of the as-deposited film and the pure compounds and their mixtures. Once can easily distinguish the contributions of each compound in the as-deposited thin film. The numerical assignments of the bands are provided in the text and in Figure 2.8.

Raman spectroscopy is a useful method to analyze the vibration spectra of the molecular species that are present in amorphous arsenic trisulfide glasses. This method is often used it is effective in the absence of a crystalline lattice. The assignment of the vibrational bands that are present in the as-deposited film is well documented in the literature[66,67,68,69]. However, because of the varying film fabrication conditions are used in the literature, we must also perform a detailed analysis of the species that were present in our samples and compare our result to those found in the literature. The analysis methodology that we chose to employ was to reconstruct the Raman spectrum of the thin film through a combination of the pure compounds. By breaking down the film into its constituent species, we could obtain

46

Sample	Wavenumber (cm^{-1})												
as-evaporated	156	190	226	238		275	346	356		375			493
As$_4$S$_4$ + S$_8$ + As$_2$S$_3$		190	223	238		275	347	352	364	375	385		476
As$_2$S$_3$ glass	137	190		232			346		361	375	390		
As$_2$S$_3$ glass	140	189		230			340						
As$_2$S$_3$ crystal	136	199	202			291	310	355		383			
As$_4$S$_4$ + S$_8$	157	190	223	237		275	350		364				475
As$_4$S$_4$		192		235			346	363					
As$_4$S$_4$	143	194	221				345	355	370	376			
S$_8$	157		226		249							439	476
S$_8$	151	187	218		248	273					416	437	474

Figure 2.9 A tabulation of the peaks of the Raman spectrum that are displayed in Figure 2.7 (black text) and a comparison to the data that is recorded in the literature (grey text). The results here show that the Raman spectrum of the pure compounds obtained in this investigation corresponds to the known band-assignments that are present in the literature. Furthermore, the as-deposited films that are obtained in the high-temperature thermal evaporation process can be approximated using a stoichiometric combination of the pure compounds.

some insight into the presence of the major species that were present in the as-evaporated thin films.

For this analysis, we used the pure compounds of each of the parent molecules that were identified in the gas phase. The compounds of S$_8$ and As$_4$S$_4$ could be easily obtained or synthesized and purified (cf. Chapter 7.). However, the compound As$_4$S$_6$ could not be synthesized using the same melt synthesis method that was employed for the synthesis of As$_4$S$_4$. One explanation for this difficulty in the melt-synthesis of As$_4$S$_6$ was that this molecule was easily polymerized and that it could only be collected during the gas-phase dissociation of the As$_2$S$_3$ precursor glass [33]. Furthermore, the As$_2$S$_3$ composition itself is a very good glass former and crystallization at this stochiometry had been shown to be very difficult [65]. Therefore, measurements of the crystalline forms of As$_2$S$_3$ were usually performed on naturally occurring geological samples. However, the characteristic As-S vibrations of the

AsS_3 pyramid present in the As_4S_6 molecular cluster could also be found in the structure of the fully polymerized precursor glass itself[69]. Therefore, we decided to substitute the As_4S_6 molecule with the amorphous As_2S_3 precursor glass. Although this substitution is far from perfect, the inclusion of a substance containing the AsS_3 pyramid was essential, because it was necessary to provide an accurate accounting of the possible species that could be present in the as-deposited thin film.

The Raman spectra of each individual pure compound, and their mixtures, were collected and then compared to the Raman spectra of an as-deposited thin film. It is important to point out here that in order to provide a more accurate analysis, the Raman spectra of the compound mixtures, were collected from a sample that was prepared by physically mixing and homogenizing together the pure compounds, and not simply reconstructed via the superposition of individual Raman spectrum collected from separate pure samples. Furthermore, in the sample that contained all of the molecular species which are representative of the as-deposited thin film, the individual compounds were mixed together with a stochiometry that is consistent with the collection of S_8, As_4S_4 and As_4S_6 molecules generated from the As_2S_3 precursor in the gas phase, as represented in the equation found in Figure 2.1. The collected Raman spectra are presented in Figure 2.8.

By comparing the spectra plotted in Figure 2.8, one an easily recognize that the features present in the Raman spectrum of the as-deposited thin film (black curve) can be accurately approximated by combining together individual pure compounds that were present on the thin film (top grey curve). Furthermore, the contributions of the individual molecules of S_8, As_4S_4 and As_2S_3 to the overall Raman spectrum of the as-deposited films can also be clearly observed. Tabulated data of the main vibration features found on the Raman spectra are provided in Figure 2.9.

48

The Raman spectra of the as-deposited film can be analyzed by taking into account of all of the structural subunits of the molecular species that are present. The As_4S_6 molecule (as represented by As_2S_3) contains only hetero-polar As-S bonds in the framework. This structure can be broken down into AsS_3 pyramidal sub-units and bridging As-S-As fragments. The dominant feature in the As_4S_6 Raman spectrum is the AsS_3 pyramidal unit that exhibits a strong band at 346 cm^{-1}. This central peak is broadened due to the overlapping of several vibrational overtones of the three species that are present in the as-deposited thin film. Furthermore, the interaction between neighboring AsS_3 subunits via the As-S-As bridges are responsible for the appearance of the wide shoulder at 380-400 cm^{-1}, causing the central peak to become unsymmetrical about its peak[64]. There are also other detectable bands that are present in this Raman spectrum, the appearance of the band at 363 cm^{-1} is due to the presence of the As_4S_4 molecule, and the spectral features at the positions of 192 and 225 cm^{-1} are attributed to the presence of As-As bonds in this molecule. The presence of the S_8 molecules in the as-deposited film were confirmed by the presence of the characteristic vibrations of the S-S bonds which appear as spectral features positioned at 218 and 493 cm^{-1} [69].

The spectral features obtained from the Raman vibration analysis conducted here correspond well to the Raman vibrations of the pure compounds that were documented in the literature. One important observation that should be made here is that the Raman vibration bands of a natural sample of crystalline As_4S_6 crystal [69], matches the major Raman vibration frequencies of the As_2S_3 glass sample used here. The similarities of their Raman spectra indicated that a glassy sample of As_2S_3 can be substituted, with good approximation, for a single crystalline sample of As_4S_6, in the set of Raman analysis that was performed in this work. Overall, the ability to
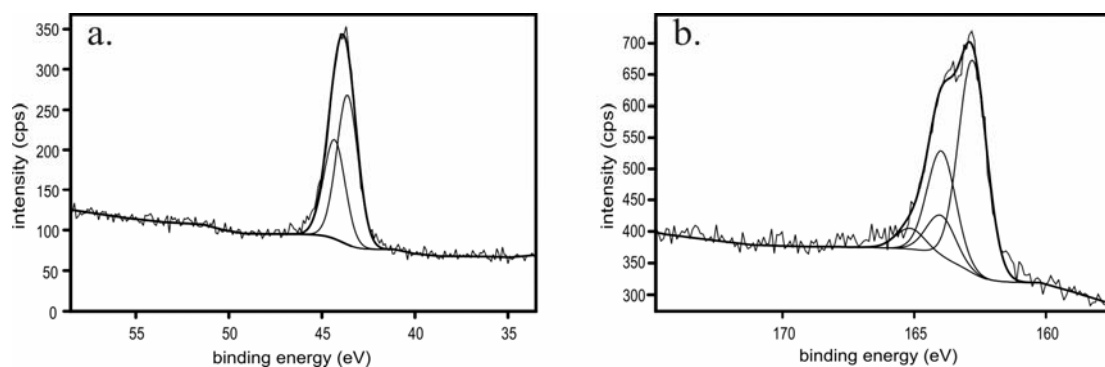
Figure 2.10 XPS spectra of the surface of an as-deposited film. a) The positions of the binding energies of the As_{3d} spectrum is consistent with the presence of molecular species containing As-S bonds such as As_4S_4 and As_4S_6. b.) The positions of the binding energies of the S_{2p} spectra implies that sulphur is present in both an oxidation state of zero (163.9 eV) and -2 (162.7 eV), and suggests that S_8 is present alongside the As-S containing species. The result of this analysis confirms that S_8, As_4S_4 and As_4S_6 species are present on the surface of the film.

reconstruct the as-deposited film was important because it provided a verification of the presence of S_8, As_4S_4 and As_4S_6 species inside the as-deposited thin film sample.

A further examination of the thin film surface was conducted using the X-ray photoemission spectroscopy (XPS) analysis technique. The results are presented in Figure 2.10. Using this method we had identified the binding energy (BE) of the species that were present on the surface of the film. In the As_{3d} spectrum, the position of the BE was consistent with the presence of molecular species containing As-S bonds such as As_4S_4 and As_4S_6. Second, the peaks identified in the S_{2p} spectra implied that sulphur was present in both an oxidation state of zero (163.9 eV) and -2 (162.7 eV), and suggested that S_8 was present alongside the As-S containing species[70,71,72]. Furthermore, the analysis of the peak areas revealed that the atomic ratio of arsenic to sulphur was 2 to 3, this provided a further indication that the stochiometry of the precursor was preserved in the as-deposited film. The XPS results obtained here were in good agreement with the results recorded in the literature. Furthermore, the identification of S_8, As_4S_4 and As_4S_6 species, via XPS

analysis, on the surface of the film, via XPS, confirmed our mass spectrometry and Raman spectroscopy analyses.

Overall, the analyses that we have conducted here provided further evidence to the presence of the proposed species that were obtained during the high vacuum thermal evaporation process as depicted in Figure 2.1.

2.4.2 Optical Properties

Another crucial materials property of the as-deposited As_2S_3 film was its optical properties. Ideally, this material should be transparent to the wavelength of operation of the femtosecond laser that was used in the 3D DLW process. Furthermore, the photo-resist film should also possess an index of refraction (n) at a value near 2.45 after the photo-polymerization process.

Ultra-violet-Visible (UV-VIS) spectroscopy was used to investigate the transmission characteristics of both an as-deposited and a photo-polymerized thin film. These transmittance spectra are shown in Figure 2.11. The oscillations that are observed in the spectra are the Fabry-Perot fringes that arise due to the thin-film interference of the photoresist sample. The transmittance of such a thin-film sample was only 64% because the high-refractive index of the photoresist caused a partial reflection of the incident beam. The calculated reflectance for a thin-film with such a high index of refraction was about 18%, and is responsible for the lowered transmittance of these photoresist thin films.

The UV-VIS transmittance spectrum showed three important properties of these photoresist thin-films. The first, and also the most pronounced effect, occurred at the absorption edge of the transmittance spectra. The absorption edge of the photo-polymerized sample was red-shifted relative to the as-deposited film. The difference
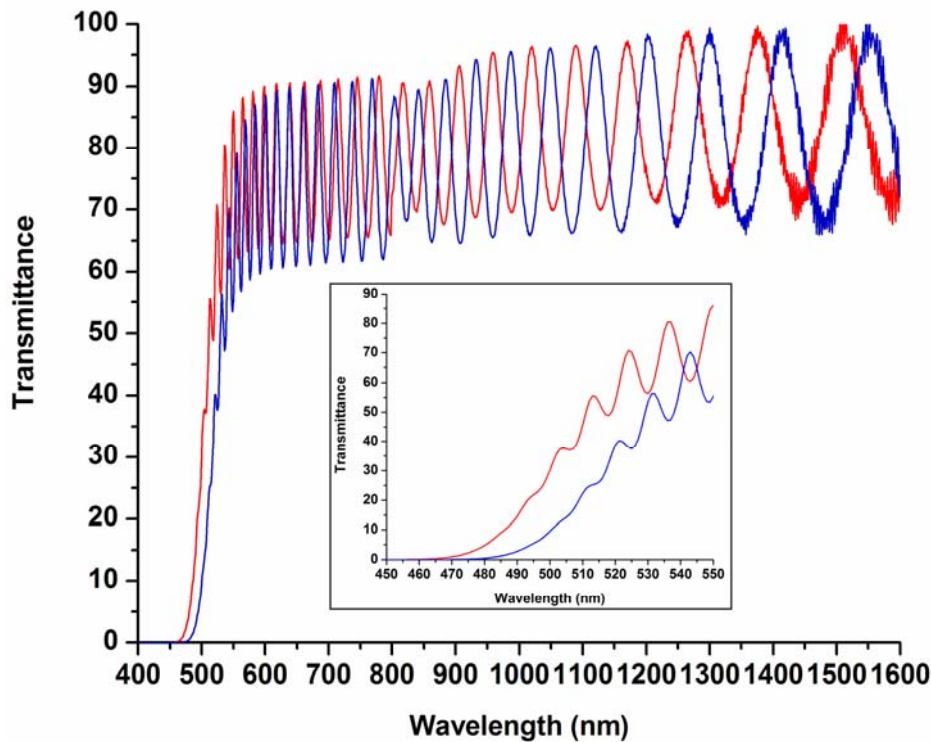
Figure 2.11 UV-VIS spectra of the As_2S_3 photoresist as an as-deposited film (red curve) and after photo-exposed (blue curve). The 18% transmittance loss is due to the reflection of the incident beam at the air-chalgenide glass interface. The as-deposited film show good transmittance at the wavelength of 800 nm. High transmittance at this wavelength is important because the laser used in the 3D DLW setup operates at this wavelength. The absorption edge also displays a red-shift upon photo-polymerization (inset). This is an characteristic property of the photo-polymerization of an as-deposited film of As_2S_3 photoresist.

in the position of the absorption edge was due to a shift in the optical band-gap and was related to the difference in the atomic bonding present in the two different morphologies of the material. The presence of this shift was important as this gave us the first verification that photo-polymerization occurred in the as-deposited material after photo-exposure[52,56].

The second important property was that the as-deposited film exhibited good transmittance at 800 nm. Once again we must stress here that the reduction in the transmittance at 800 nm was not due to absorption by the photoresist, but was due to the reflection of the incident beam as it encounters the interface of the photoresist,
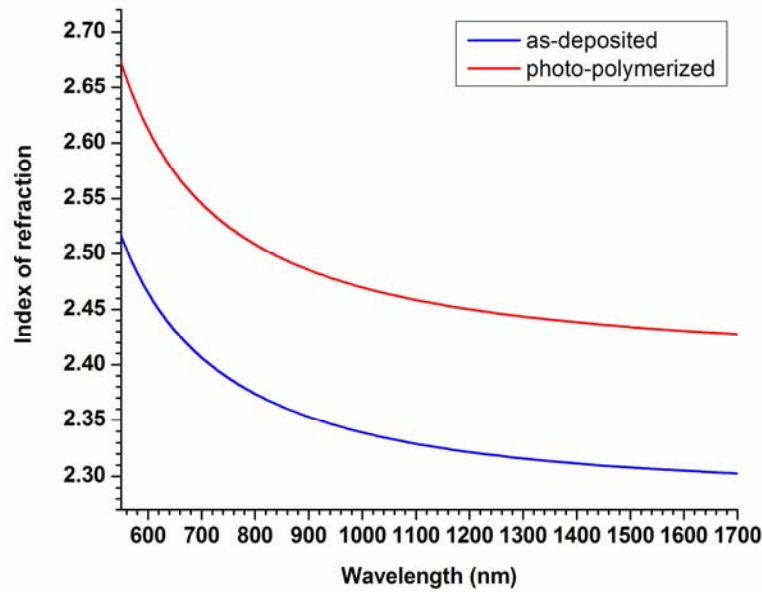
Figure 2.12 The refractive index dispersion curve of the As_2S_3 photoresist in the as-deposited form (blue curve) and the photo-polymerized form (red-curve). The refractive index exhibits an increase upon photo-polymerization from 2.31 to a value of 2.45 at the wavelength of 1550 nm. This represents a 5.5% increase in the refractive index.

which has a higher index of refraction than air. This point was crucial because the laser used in the 3D DLW setup operated at a wavelength of 800 nm, and therefore, there must be negligible 1-photon absorption at this wavelength for the 3D DLW process to function as desired.

Third, the photoresist film did not exhibit any intrinsic absorption up to and beyond the important optical telecommunication window which is centered at 1550 nm. The absence of any intrinsic absorption was important because this would allow any 3D structure made from this material to access the entire telecommunications window between the wavelengths of 1300 nm to 1600 nm.[1] The uninterrupted access to the entire telecommunications window is a property that is currently not possible with silica glass based photonic devices. (cf. Chapter 5)

---

[1] A far infra-red spectrum, showing that this material is transparent up to 4 micrometers wavelength, is provided in section F of the Appendix.

The index of refraction of an as-deposited film and a photo-polymerized film was determined using a thin-film ellipsometery technique.   The ellipsometery data is presented in Figure 2.12.   At the wavelength of 1550 nm the index of refraction of the as-deposited film was 2.31, and after photo-polymerization it increased to a value of 2.45.   Overall, there was a 5.5 % increase in the refractive index after photo-polymerization.   Furthermore, information about the optical band-gap E_g of the film was also obtained from this measurement.   The E_g decreases upon photo-exposure, from 2.36 eV in the as-deposited film, to 2.34 eV in the photo-polymerized film.   This decrease of the optical band-gap upon photo-exposure of an as-deposited film (corresponding to the red-shifting of the absorption edge as mentioned previously) is another verification of the presence of the photo-polymerization effect[33,52,56].   The observed changes in the refractive index and the optical band-edge after the photo-exposure of an as-deposited thin film of As_2S_3 agreed very well with the documented effects of photo-polymerization of these photoresist films[73,74,75].

2.5 Photo-polymerization Process

In order to rationalize the data that was presented here in the preceding sections, we begin with a discussion of the molecular bonding that is found in arsenic-sulfide based glasses[33].   In the glassy amorphous state, or the photo-polymerized state, the arsenic in the arsenic-sulfide system has 5 valence electrons, 3 electrons are used for valence bonds with 3 neighboring sulfur atoms and the other 2 remaining electrons reside in non-bonding-orbitals.   The sulfur atom has 6 valence electrons of which 2 are used for bonding with arsenic and the other 4 electrons reside in the 2s and 2p orbitals.   The electronegativity difference between the arsenic and sulfur corresponds to a maximum bond ionicity of about 6% and therefore the intramolecular As-S bonds

are predominately covalent in character. The intermolecular bonding forces between the As-S sheets are majority Van der Waals in nature and present are due to the interaction between the lone pair of electrons on the p-orbitals of the sulfur atom. In this fully polymerized glassy material, the As-S bonds are linked together to form an amorphous network solid and the elementary subunits are AsS_3 pyramidal subunits. This amorphous network is characterized by its lack of long-range order that is found in crystalline solids.

In the As_2S_3 glass described above, the large arsenic atoms posses a formal charge of +3. Such a highly charged atom interacts strongly with the incident electromagnetic field that travels through this material. Furthermore, the sulfur is also a large and highly-polarizable atom which also interacts with the incident electromagnetic radiation. The presence of these interactions acts to reduce the group velocity of the electromagnetic wave as it progresses through the material and this is manifested as an increase in the index of refraction[28]. Besides the amorphous As_2S_3 compound, several different arsenic-sulfide compounds with various stochiometries exist[76]. Some of the most important room-temperature stable species that are pertinent to this investigation are As_4S_4 and As_4S_6 as shown in Figure 2.1. The As-S bonding in these compounds are similar to those described for the case of the glassy amorphous solid.

Another important component of the as-evaporated photoresist is the sulfur compound α-S_8. Sulfur compounds also exist in many crystalline and non-crystalline polymorphs. The molecular units can vary from 2 to 32 sulfur atoms. However, the only room temperature stable form of sulfur is the octahedral α-S_8 form that has been detected in our MS study. All other forms that have been synthesized tend to revert back to this form upon standing at room temperatures[76]. The ability of sulfur to display a wide variety of geometries stems from the bonding of the sulfur atom. The

atoms possess 6 valence electrons, 2p electrons are used to form covalent σ-bonds between the atoms and the remaining 2 unpaired p electrons are oriented perpendicularly to the sigma bond. The combination of low co-ordination and a large rotational freedom between adjacent atoms accounts for the enhanced mobility of the sulfur atoms and their ability to form a wide variety of polymorphs[74,75,77].

With the above analysis in mind, if we examined the structure of all the molecules that are collected from the thermal evaporation, and focused on the sulfur atom, we notice that whether it is in the form that is complexed to the arsenic atom or in the molecular S_8 form, it will contain unpaired electrons in its 2p orbitals. Many experiments and theoretical considerations into the photo-induced behaviors of arsenic-sulfide based glasses, have led to the consensus that photo-structural changes are only possible due to the presence of these lone pairs of electrons on the p orbital of the sulfur atom[74,75,78]. A model which focused on the reaction of these lone pair of electrons in the p orbital of the sulfur atom and their interaction with surrounding arsenic and sulfur atoms had been proposed to explain the photo-polymerization process. This model is called the valence-alteration pair (VAP) model[79].

The VAP model states that the mechanism of photo-structural changes, induced by electromagnetic radiation, in the chalcogenide glass system is due to the presence of a non-bonding lone pair of 2p electrons that are present in 2-fold coordinated sulfur atom. In this theory, when band-gap energy light is absorbed by the material, an exciton is generated. One of the non-radiative decay pathways of this exciton is via coupling to the lattice phonons which are then trapped by the non-bonding lone pairs of electrons on the chalcogenide atom which result in the formation of a low-energy, meta-stable defect called an intimate valence alteration pair or a self-trapped exciton[28,75,80]. (see Figure 2.13) During the creation of this meta-stable state, a bond

rearrangement occurs which shifts and rearranges the atoms towards its neighbors. Furthermore, it is proposed in this theory, that the ease of the bond rearrangement is further facilitated by the high flexibility of the As-S and S-S sigma bonds. The subsequent recombination of the self-trapped exciton allows the system to revert back to the ground state and locks-in the new positions of these atoms. This entire process manifests itself macroscopically as photo-polymerization[78]. Therefore, the presence of the lone pair of electrons on the sulfur atom is viewed as being very important for the observation of photo-induced effects such as photo-polymerization. In fact, in an experimental investigation where the lone pair of electrons on the p orbital of the sulfur is removed via complexation with another metal cation (eg. copper), the photo-polymerization becomes completely inhibited[81]. It is worth mentioning that the same effect that is observed in the sulfur atom is not observed on the lone pairs of the arsenic atom. This is because the lone pair of electron on the arsenic atom resides in the 4s orbital which is more stable than the 3p orbital of the sulfur atom. Overall, it is this bond rearrangement and formation of the lone pair of 2p electrons on the sulfur atom, during the photo-polymerization process, that S-S of the S_8 molecule and As-As of the As_4S_4 molecules is rearranged and becomes homogenized into As-S bonds. Furthermore, the As-S bonds in the As_4S_6 molecules also become cross-link with each other during this process to reform the As_2S_3 glass.

Another aspect that is also important for photo-polymerization is the lower density of the as-deposited films versus the photo-polymerized films. The lowered density of the as-deposited films affords more mobility to the sulfur atoms during the process of creating a self trapped exciton, which facilitates atomic movement over large inter-atomic distances [78].
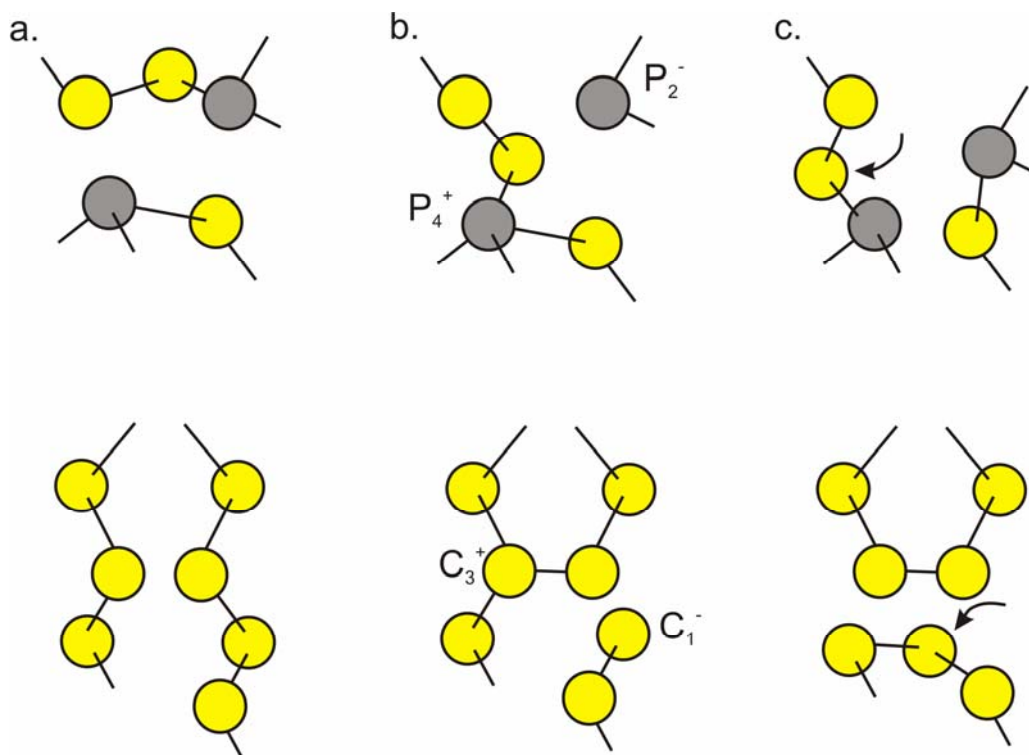
Figure 2.13 The bond rearrangement process that is proposed in the valence-alteration pair (VAP) theory. Top series represents the motion of atoms in arsenic (Pnitide)-sulfur (Chalcogenide) containing molecules, and the bottom series depicts the motion of atoms in homoatomic sulfur molecules. **a.** the initial state of the arsenic and sulfur atoms. **b.** upon absorption of light with sufficient photon energy an exciton is created which can be trapped by the one-pair of electrons resulting in the creation of an intimate valence alteration pair, which is a meta-stable charged defect. During the creation of this charged defect, sulfur atoms migrate to another position amongst its nearest neighbors. **c.** Further atomic movement results in the recombination of this charged defect and the new atomic positions are locked-in. This photo-induced bond rearrangement process results in the photo-polymerization that is observed in as-deposited As_2S_3.

Overall, the photo-polymerization process causes the film to undergo densification and an increase in the average co-ordination number of the arsenic atoms. These effects act to contribute to the increase the refractive index that we observe when the as-deposited material has been photo-polymerized[28,35].

The VAP theory can also be illustrated using a band picture[78]. The lone-pairs of unshared electrons of the sulfur atoms create the valence band, and the anti-bonding states form the conduction band. When photo-polymerization occurs, the reaction

between the lone pairs of electrons of the sulfur atoms which reside near the valence band is removed via the reaction with arsenic atoms and results in the formation of As-S bonds. These new As-S bonds have energies that place them deeper into the optical band-gap and the result is a reduction in the energy of the band-gap. This reduction in the energy of the optical band-gap upon photo-polymerization was also observed in our investigation[78,82].

One must point out that although the VAP theory is used to describe many of the photo-induced bond rearrangement phenomena in chalcogenide glasses, the bond rearrangement phenomena is only called photo-polymerization if the illuminated substrate is an as-deposited film. This is obvious since further photo-polymerization of a polymerized glass will not result in further polymerization.

From the results of the various analyses that were performed in this chapter, we have determined that the high-vacuum thermal evaporation technique used in this work was able to produce thin films that contained arsenic-sulfide and sulfur molecules, which enabled these films to exhibit photo-polymerization behavior. Therefore, the As_2S_3 films produced here indicate they are suitable for use as a photoresist with the three-dimensional direct laser writing process. In the next chapter, we will demonstrate the use of these photosensitive thin films for 3D DLW of 3D nanostructures.

Chapter 3 - Three-Dimensional Direct Laser Writing

In chapter 2, we developed a set of parameters which allowed the high-vacuum thermal evaporation method to produce a form of arsenic trisulfide that exhibited the photo-polymerization effect. In this chapter, we will take these photosensitive films and use them as photoresist for 3D DLW. This chapter contains the results of 2 separate investigations. The first investigation involved determining if As_2S_3 is a suitable photoresist material for use with the 3D DLW method. From this initial investigation, we encountered and identified focus aberration issues during the 3D DLW process that lead to strongly distorted 3D structures. Therefore, in the second investigation, we provided the results of some counter-measures that had to be devised to overcome most of these focus aberration problems. Furthermore, we will provide the working principle of these counter-measures and examples of structures that were fabricated with these corrective measures in place.

3.1 The 3D DLW Concept

The three-dimensional direct laser writing technique (3D DLW) is a photolithographic tool that is capable of producing 3D structures directly inside the volume of the material. With the 3D DLW technique, a photoresist exhibiting an intensity threshold for exposure is illuminated by laser light whose photon energy is insufficient to expose the photoresist by a one-photon absorption process. If this laser light is tightly focused into the photoresist, however, the light intensity inside a small volume element ("voxel") enclosing the focus may become sufficiently high to exceed the exposure threshold by multi-photon processes[17]. By scanning the focus relative to the photoresist, in principle, any three-dimensional connected structure

60
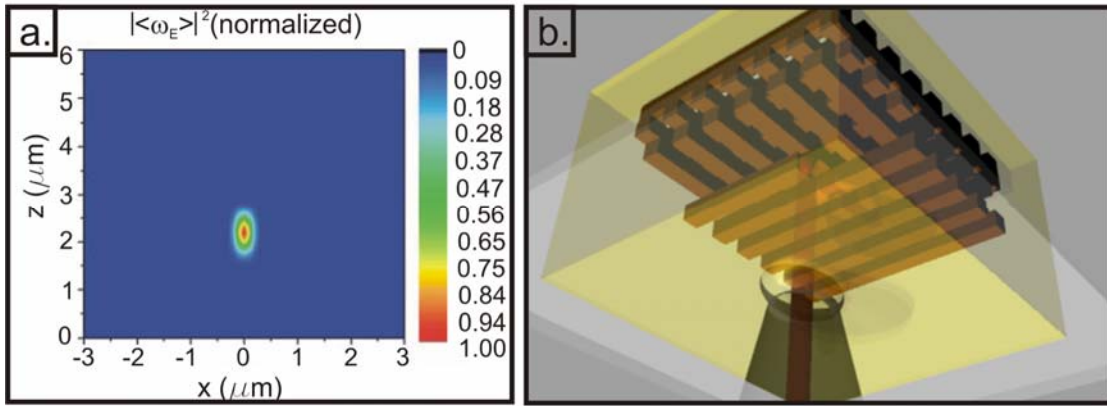
Figure 3.1 a. A simulation of the voxel that is generated in the conventional organic photoresist SU-8. The normalized square of the time averaged electric energy density $|\omega_E|^2$ exhibits iso-intensity surfaces of different intensities inside the volume of the focal spot. **b.** A graphical depiction of the 3D DLW process. Here the focus of the laser is scanned inside the photoresist material to trace out the design of the 3D structure.

consisting of these voxels maybe written directly into the photoresist[83]. Since the phenomenon of 2-photon absorption is a non-linear process, it is dependant on the square of the intensity of the incident laser. Therefore, photo-polymerization can only be generated if high laser intensities are used.

One method to generate high intensities for 2-photon absorption is by tightly focusing a femtosecond laser beam into a small focal volume. Using the vectorial Debye theory[84], the normalized square of the time averaged electric energy density, $|\omega_E|^2$, distribution inside the focal volume is calculated in a conventional organic photopolymer SU-8, and is presented in Figure 3.1 a. From this figure it is evident that there are different iso-intensity profiles in the focal volume. The presence of these iso-intensity profiles inside the focal volume is important because only the intensity that can overcome polymerization threshold of the photoresist material will cause photo-polymerization. The combined contribution of the focal volume and the polymerization threshold thus allows sub-diffraction limited resolution to be obtained
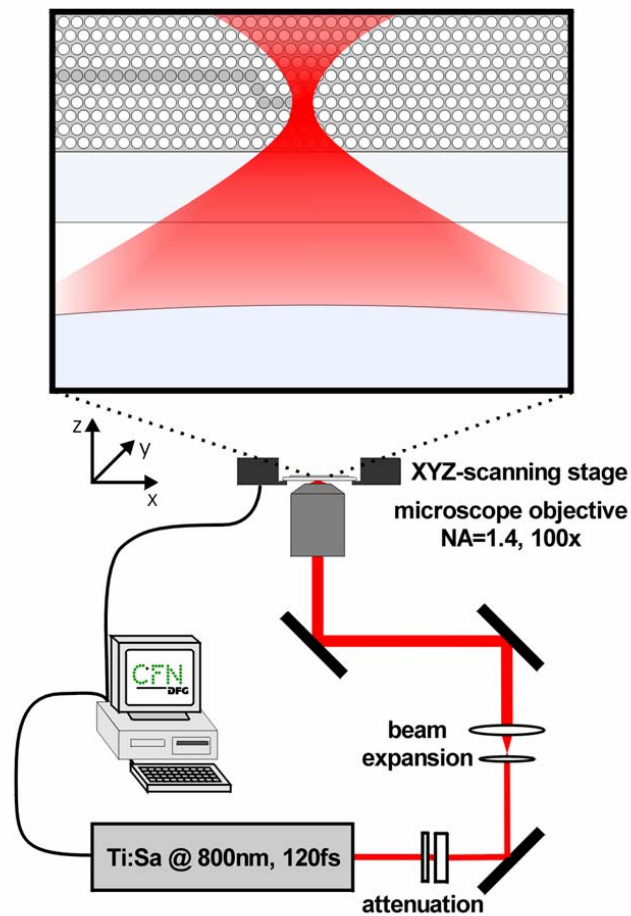
Figure 3.2 In the 3D DLW setup used in this thesis, a femtosecond laser with a wavelength of 800 nm, a wavelength that is insufficient to cause 1 photon photo-polymerization in the photopolymer, is used. In order to get the intensities of this laser beam to the high intensities that are required to cause 2-photon polymerization, a high-numerical aperture microscope objective is used to tightly focus the beam down to a small volume inside the material. Inside this focal volume, and only inside this volume, is the intensity of the laser high enough to cause 2-photon absorption. Since the 2-photon absorption is confined inside this focal volume, the photo-polymerization process is also confined there, thus generating a voxel. The combination of the 2-photon polymerization process and its interaction with the threshold polymerization intensity of the photoresist, enables sub-diffraction limited resolution to be realized.

in the 3D DLW setup[17]. To trace out the 3D structure, this voxel is simply moved around inside the material to polymerize the desired volumes. An illustrative figure of this process is provided in Figure 3.1 b.

3.1.1 3D DLW Setup

A schematic of the setup is provided in Figure 3.2. The laser source is a regeneratively amplified Ti:sapphire laser system (SpectraPhysics Hurricane) with a pulse duration of 120 fs and the repetition rate could be computer controlled from 1 kHz to single shots. The wavelength was tuned to 800 nm, where one-photon absorption of the chalcogenide glass was negligible. The output beam was attenuated by a half-wave plate/polarizer combination and passed through a quarter-wave plate; after beam expansion, typically 9.5 nJ of single pulse energy is coupled into an inverted microscope (Leica). The femtosecond pulses were focused into the chalcogenide film by a 100× oil-immersion objective with a high numerical aperture (NA= 1.4, Leica). The sample was placed on a capacitively controlled, three-axis piezo scanning stage, which was operated in a closed loop providing a resolution of better than 5 nm at the full scanning range of 200 μm× 200 μm×20 μm (Physik Instrumente). The scanning operation of the piezo was computer controlled and its movements were synchronized with the output of the laser system.

3.2 Experimental Results and Discussion

The 3D photonic crystal structure that we had investigated intensively in this thesis was the woodpile structure. This design became the focus of our investigation because it was one of the most studied and understood 3D photonic crystal structure[85]. Furthermore, since the 3D DLW method was already used for producing this structure, and its expected optical behavior was well known, any flaws in the fabrication process can be easily diagnosed[22]. This simplifies the development process to allow research efforts to be focused on developing the new photoresist system.
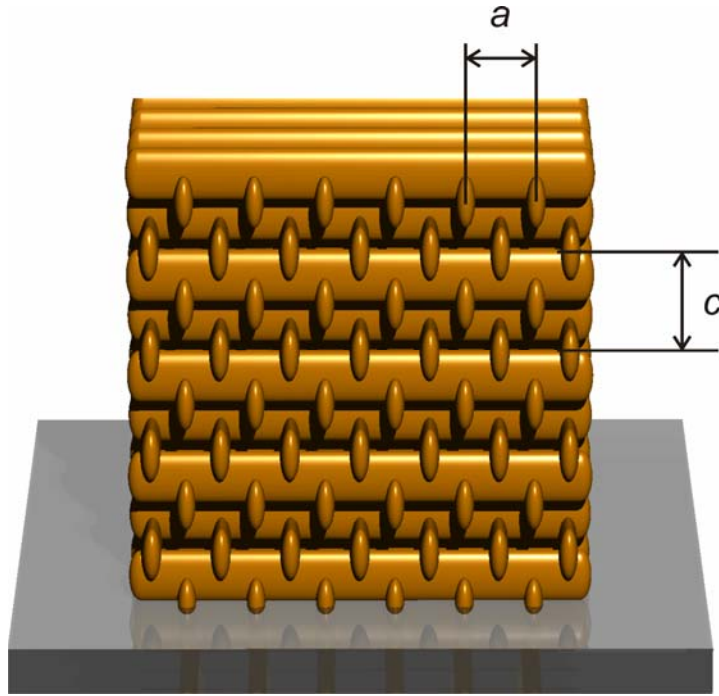
Figure 3.3 A schematic representation of the 3D woodpile structure that is investigated in this work. This lattice of this woodpile structure consists of 4 layers and is described by the lattice constant *c*. The first layer of this four layer lattice consists of straight rods with a rod centre-to-centre distance *a*. The second layer is then rotated by 90º with respect to the first layer and placed on top of the first layer, the third layer is parallel to the first layer but displaced laterally by *a*/2, the fourth layer is parallel to the second layer, but also displaced laterally by *a*/2.

A model of this woodpile structure is shown in Figure 3.3. The structures that were fabricated here had a rod spacing of $a = 1$ μm and unit cell dimension of $c = \sqrt{2}/a$ for face-centered-cubic translational symmetry. The structures fabricated had a footprint of 22 μm x 22 μm, and a thickness of eight to twelve rod layers, which corresponded to 2 and 3 unit-cells of the photonic crystal structure. Walls and posts were used to surround the structure in order to provide anchoring of the photonic crystal to the surface of the substrate.

The etchant used here in this current investigation contained the diisopentlyamine molecule dissolved in dimethylsulfoxide[54]. It provided suitable etch selectivity for the proof of concept experiments that were carried out in the first part of this investigation.
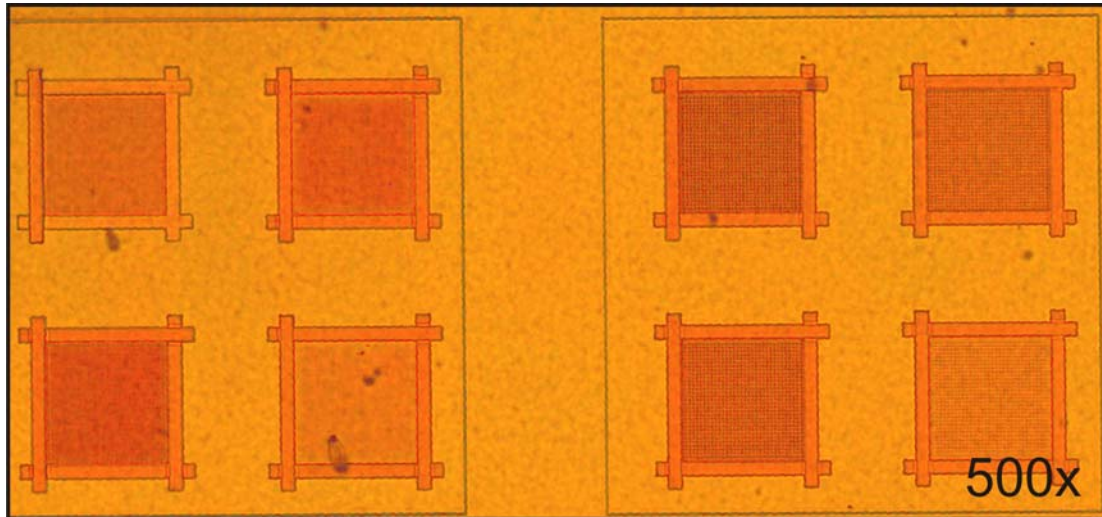
Figure 3.4 An optical microscope image of the structures that have been photo-patterned into the photoresist material using the 3D DLW process. The structures are directly visible after the 3D DLW process due to the increase in the refractive index that is experienced upon photo-polymerization.

Although a more advanced etchant molecule, *N*-(4-methoxybenzyl)-(pyren-1-yl)amine, was developed to provide highly-selective etching for 3D structures[70], we restrict its discussion to chapter 4 where we will provide a full treatise of its synthesis and characterization.

Using the structural parameters described above, we photo-patterned the photoresist using the 3D DLW setup. Optical microscope images of the structures that were written into the sample, and before etching, are shown in Figure 3.4. The photo-exposed areas are the dark orange-red areas, and the light orange areas are the un-exposed areas. The structures of the 3D photonic crystal could be observed immediately after photo-polymerization because of the increase in the refractive index that accompanied the polymerization of As_2S_3. (cf. Chapter 2) Although the 3D photonic crystal structure could already be clearly observed, this embedded structure did not possess a full-PBG. The reason was because the contrast in the index of refraction (Δn) between the polymerized ($n = 2.45$) and the as-deposited areas ($n = 2.30$) was only 0.10, which was too small to support a full 3D PBG. Therefore, the
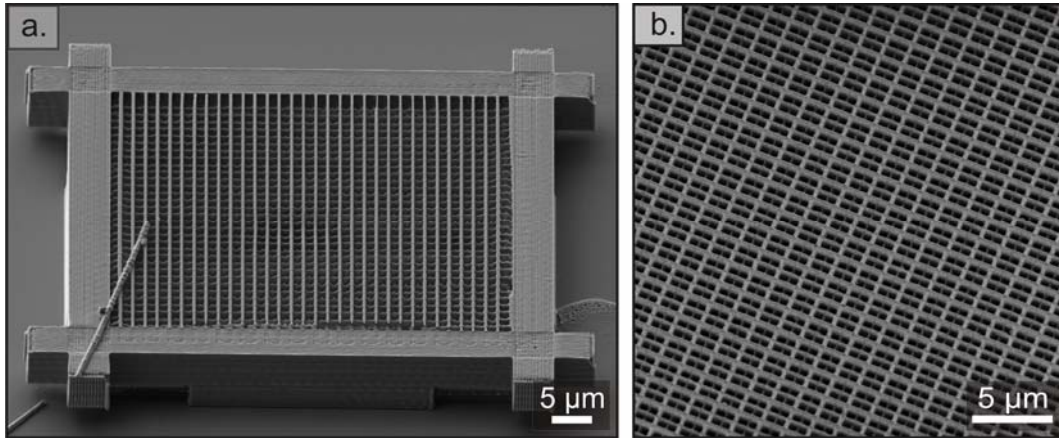
Figure 3.5 SEM images of As_2S_3 woodpile structures that have been etched out using a wet-etchant containing the diisopentylamine molecule. **a.** The structures are perfectly straight and there are no shrinkage effects that are commonly experienced with structures that are produced using organic photoresist such as SU-8. **b.** A close-up image of the surface of the structure reveals that the rods are smooth and exhibit excellent in-plane periodicity.

polymerized structure must be etched out in order to provide sufficient contrast in the refractive index.

After the polymerization process, the photoresist films was etched using the etchant which contained the diisopentylamine molecule. The result of the etching process was that the photo-polymerized structure was freed from the surrounding as-evaporated material. SEM images of the freed structure are shown in Figure 3.5. These images shows that the structure produced have well defined edges and are free of shrinkage effects that were experienced in organic photopolymers such as SU-8[86]. Furthermore, a close-up image of this structure shows that the rods of the woodpile are perfectly straight and defect free. To further investigate the internal components of this structure, we used a focus-ion beam method to obtain a cross-section SEM image of this structure. The cross-section image is shown in Figure 3.6 c. It revealed that the sample contained some significant deviations from the ideal structure that is shown in Figure 3.3.
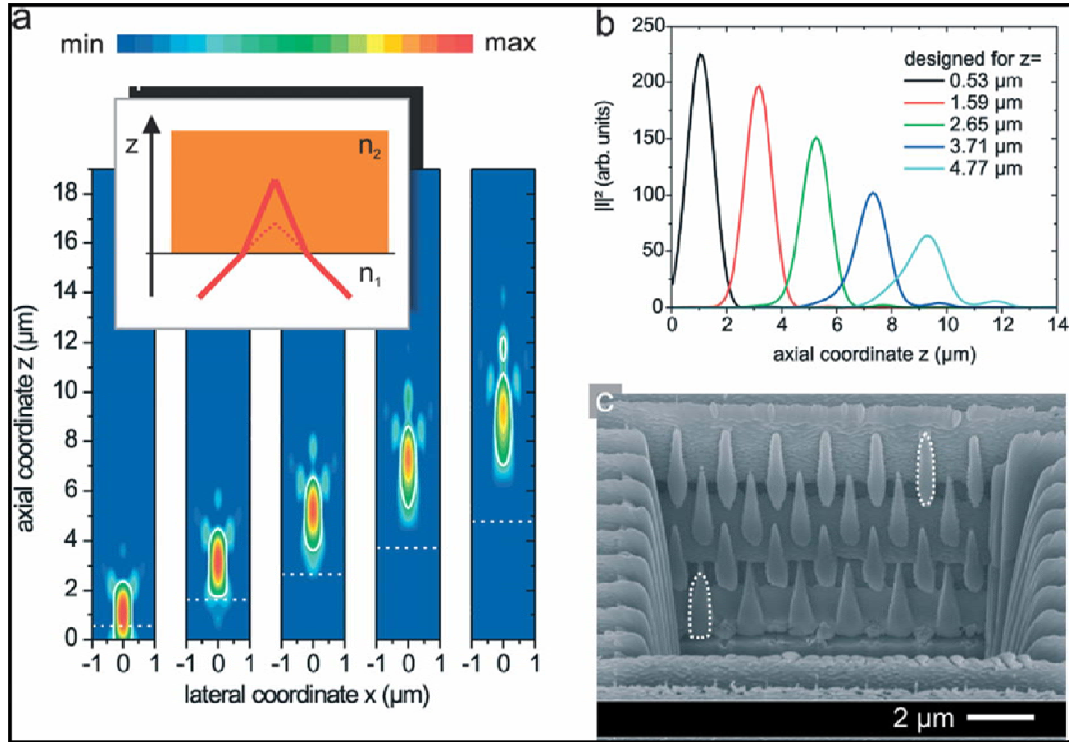
Figure 3.6 Influence of the index mismatch on the voxel shape. **a.** Two-photon intensity $|I|^2$ distribution near the focus calculated for different writing depths d. The interface is located at $z = 0$. With increasing writing depth the intended writing position (indicated by the dashed white line) significantly deviates from the position of the intensity maximum as a result of defocusing (color coding on a logarithmic scale). The inset illustrates the origin of the defocus in a simplified geometrical picture for the transition from a medium with index n_1 to a medium with $n_2 > n_1$. Additionally, voxels become more distorted owing to higher-order spherical aberrations (solid white lines are guides to the eyes). **b.** Cross sections of the intensity distributions in **a.** along the $x = 0$ μm axis. In addition to the distortions visible in a. the maximum intensity in the focus significantly decreases with increased writing depth d. **c.** Focused-ion-beam cross section of an eight-layer woodpile written in a single pass per rod without any corrections. The asymmetric shape qualitatively resembles the calculated intensity distribution in a. (dotted white lines are guides to the eye). Note that the horizontal and the vertical scales in a. and c. are directly comparable.

First, the cross-section of the rods exhibited a tear-drop shape, and not the designed shape of an ellipsoid. Secondly, the vertical spacing of the rods was progressively increased as the focus moved deeper into the photoresist and therefore, the three-dimensional translational symmetry of the structure was destroyed. Due to these strong distortions from the ideal geometry, this structure was no longer periodic in all

67

three-dimensions, and this severely inhibited the ability for such a structure to exhibit a full-PBG. Solutions to correct these distortions had to be found if As_2S_3 was to be used successfully as a photoresist for 3D DLW. Therefore, in the next section we will first discuss and identify the origins of these optical aberrations and then provide some solutions to correct these optical aberrations.

3.2.1 Effects of Optical Aberrations on Structure Quality

As we demonstrated in section 3.1, when an incident laser beam is focused with an oil immersion objective into an index-matched medium, the exposed volume pixels (so-called voxels) are of near ellipsoidal shape which had an aspect ratio between the axial diameter and the lateral diameter of about 2.7 (e.g., measured in SU-8)[21] for the experimental conditions used. However, in the case where we used the same optical components to focus into As_2S_3, which was a medium with significantly higher refractive index than the optical components, a number of negative issues which caused significant deviation from the ideal case where the medium is index-matched arose. First, and the most striking aspect, was the defocus of the focal spot. The defocusing of the focal spot meant that an axial movement of the chalcogenide film, by means of the piezoelectric translation stage, of, e.g., 2 μm, lead to a much larger axial shift of the position of the exposed voxel. Under the experimental conditions used here, the discrepancy between the actual and intended writing position was roughly a factor of two.

Intuitively, in a ray-optics picture, the rays are refracted towards the surface normal inside the chalcogenide as the focus is positioned deeper into the material (see inset in Fig. 3.6a). This simplistic reasoning is confirmed by state-of-the-art numerical calculations of the intensity distribution, based on the vectorial Debye theory (Fig. 3.6
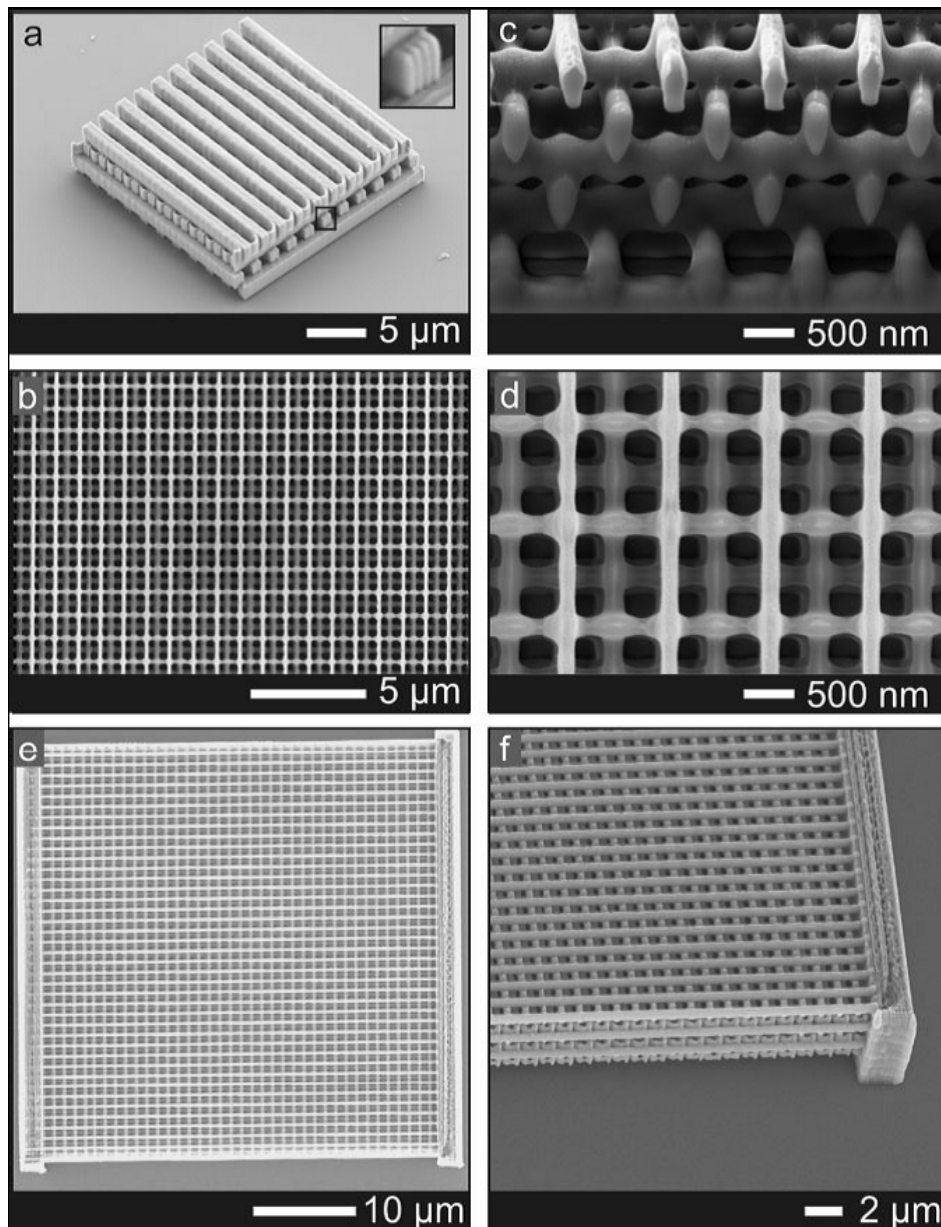
Figure 3.7 Scanning electron microscopy images of As$_2$S$_3$ woodpiles. **a.** Woodpile with rod distance a = 2 μm to illustrate the construction principle of the rods. Each rod is made from eight parallel sub-rods to yield a rod aspect ratio of almost 1.0 (see inset). **b.** Top view of a woodpile with rod distance a= 1 μm. Note the perfectly straight rods. **c.** Focused-ion beam cross section of the woodpile in b.. **d.** Close up of b.. Note the smoothness of the rod surfaces. **e.** Top view of a woodpile similar to the one shown in b. but with a 40 μm × 40 μm footprint and twelve layers. **f.** Side view of the woodpile shown in **e.** The walls merely serve as a support for the woodpile, which is intentionally raised off the substrate.

a). The incident polarization was chosen along the x direction. Here, we defined the intensity, I, as the square modulus of the electric field vector and plotted the square of this intensity, which mimicked the two-photon absorption process. The defocus

became apparent from comparing the naively expected focus position (white dashed lines) with the actual focus position.

Second, the refraction of rays towards the surface normal reduced the opening angle (see inset), and hence the effective numerical aperture of the focusing optics. This effect lead to a drastic elongation of the voxels from the above-mentioned factor of 2.7 to about 8 for a focus close to the interface (see Fig. 3.6 a).

Third, due to higher-order spherical aberrations, this elongation factor also depended on the axial focus position, as can be seen from Figure 3.6 a. Furthermore, the shape of the voxel changed with increasing focus depth. In particular, side lobes emerged and eventually merged with the main maximum. As a direct consequence, the peak intensity and hence the two-photon absorption decreased. For example, the peak intensity (I^2) decreased by as much as a factor of two for a focusing depth of 6 µm (see Fig. 3.6 b). The three aspects mentioned above all contributed to producing the distorted structures that was observed in Figure 3.6 c. Consequently, to implement DLW into chalcogenide glasses, counter measures had to be taken to overcome all three of these undesired aspects that were encountered when working with materials with a high index of refraction.

3.2.2 Corrective Measures for the Optical Aberrations

Generally, the following countermeasures could be taken. First, the apparent defocus could be corrected by choosing the proper writing depth according to the theoretically expected position of the maximum intensity. For moderate focusing depths, this corresponded to a constant factor. Therefore, the defocusing of the beam could be counter-acted by pre-compressing the initial design of the 3D structure. By pre-compressing the design of the structure in the z-direction and allowing the
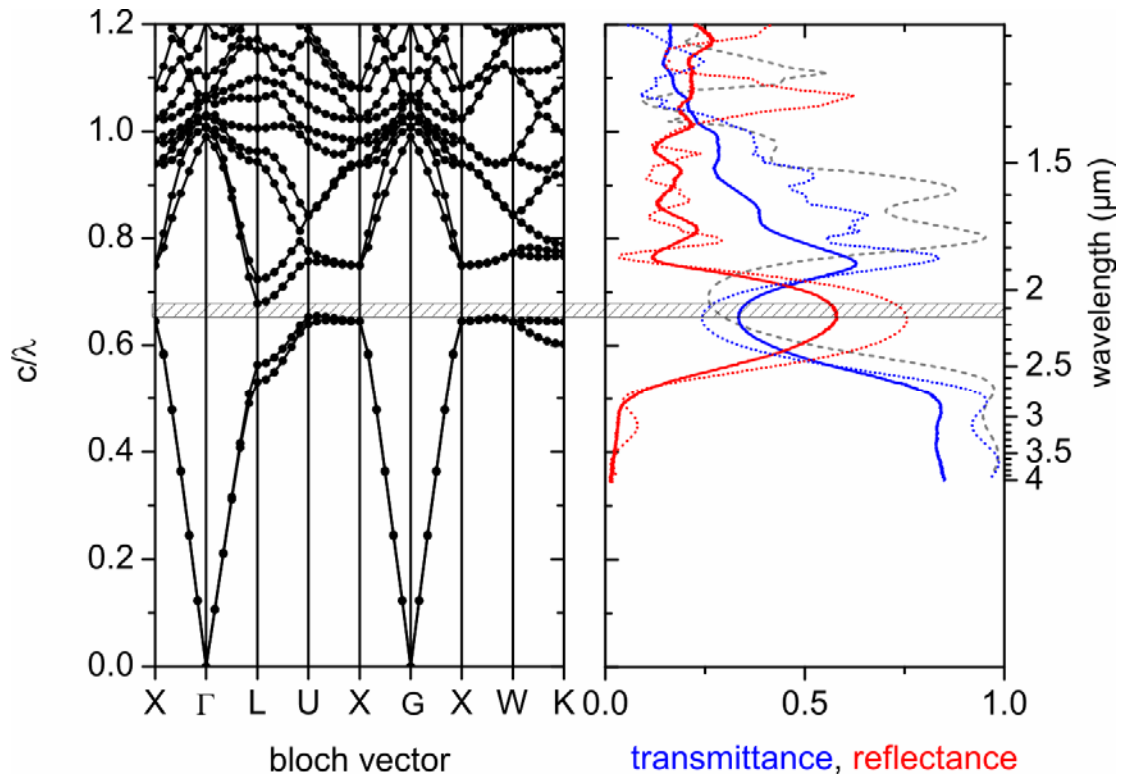
Figure 3.8 Optical characterization: a comparison between band-structure calculation (left-hand side) and transmittance (right-hand side, blue solid curve) and reflectance spectra (right-hand side, red solid curve). The hashed area marks the complete gap, which is in good correspondence with the optical spectra. The dotted curves are scattering matrix calculations, averaged over the experimental angles. The grey curve represents a calculation for perpendicular incidence without any angle averaging

defocusing to expand the structure to the correct position, we could obtain the desired geometries in the final structure.

Second, the voxel elongation could be corrected by placing several "meta" voxels side by side to correct for the oblong cross section of the single rods. By placing several "meta" voxel side by side, the aspect ratio of the rod cross section could be effectively reduced from eight to at least three. (According to our simulations, an elongation factor of 3 was the maximum value allowable for producing a woodpile structure with a complete PBG.) This "meta" voxel approach is exemplified in Figure 3.7 a, for a four-layer woodpile with a rod distance of $a = 2$ μm. The inset clearly
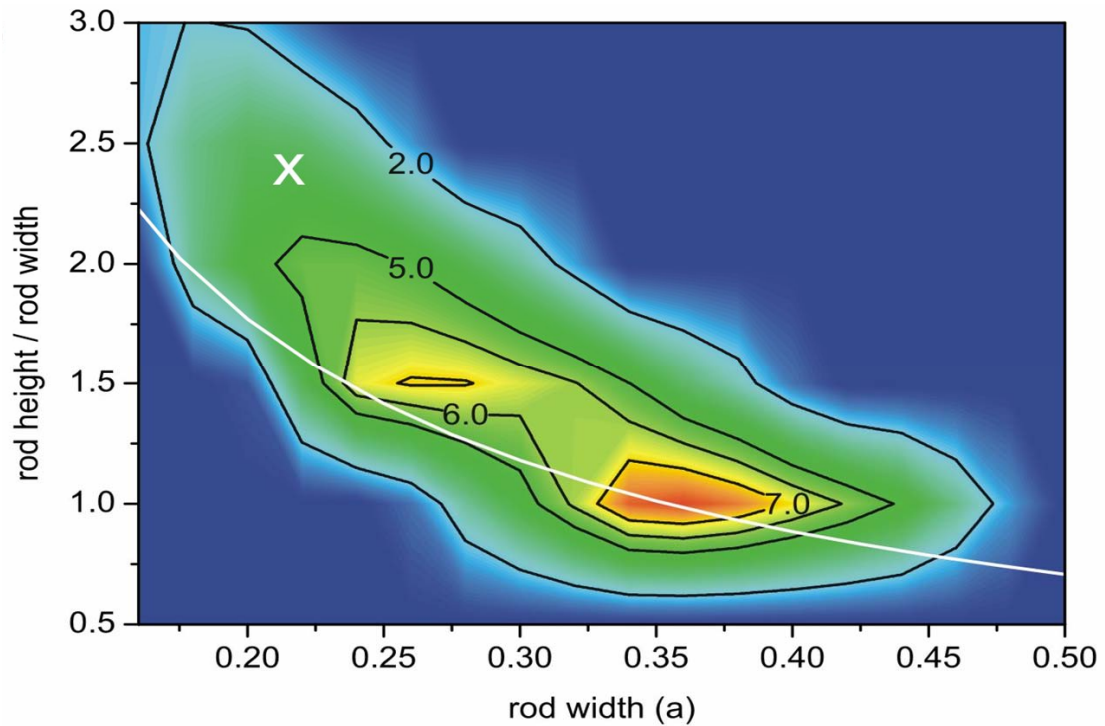
Figure 3.9 Gap-width map in percent of the mid-gap frequency for the independently adjustable parameters. The white cross marks the position corresponding to the sample measured in (a). Refining the parameters can yield a gap width of up to 8.8%, for a rod aspect ratio of almost 1.0. Structures below the solid white line are not mechanically stable.

shows four pairs of single-pass rods, which resulted in an overall rod cross-section that is almost rectangular.

Third, an even more elaborate correction technique [87,88] would be the introduction of additional optics into the system to pre-compensate for the higher-order spherical aberrations that were introduced by the index mismatch. This would counter-act the decrease in intensity and the distortion of the voxel shape at increased writing depths. However, the implementation of this approach was beyond the scope of this thesis because it would have involved a severe modification of the 3D DLW setup. Therefore, this correction technique was not investigated here.

3.2.3 Woodpile Photonic Crystals Produced Using Corrective Measures

Using both the pre-compression and multi-voxel approaches, we once again wrote woodpiles with a rod spacing of $a = 1$ μm. Here, in this case the defocus was corrected to yield the proper unit cell dimension of $c = \sqrt{2}/a$ for face-centered-cubic translational symmetry. To correct the rod cross section, each rod was constructed of six single voxel lines, written 40 nm apart from each other, which resulted in a rod width after etching of approximately 220 nm and an average aspect ratio of about 2.4. However, as was mentioned in the previous section, these two corrective steps could not overcome the decrease in intensity due to spherical aberrations; therefore only structures with a limited number of layers were possible in this case. The writing time for an eight-layer structure with a 22 μm×22 μm footprint was below 10 minutes. The subsequent wet-etching step was performed with an etchant containing diisopentylamine that was dissolved in dimethylsulfoxide. Figure 3.7 b, shows a top view of the structure. Note the perfectly straight bars due to the negligible shrinkage. A focused-ion-beam cross section reveals the rod dimensions (Fig. 3.7 c).

As a further refinement to the first test of these two corrective steps, we again fabricate a woodpile with the same parameters as discussed above, but different in three aspects. First, it was raised from the substrate so that the walls merely acted as a mechanical support. Second, it was larger with four times the footprint. Third, it was thicker with twelve instead of eight layers. This structure is shown in Figure 3.7 e and f. In sharp contrast to corresponding structures fabricated in organic photopolymers such as SU-8[21], none of the images shown in Figure 3.7 exhibits any significant distortion of the rods due to sample shrinkage.

Figure 3.8 shows measured transmittance and reflectance spectra for the sample shown in Figures 3 b to d. The transmittance spectrum (Fig. 3.8 right hand side, blue
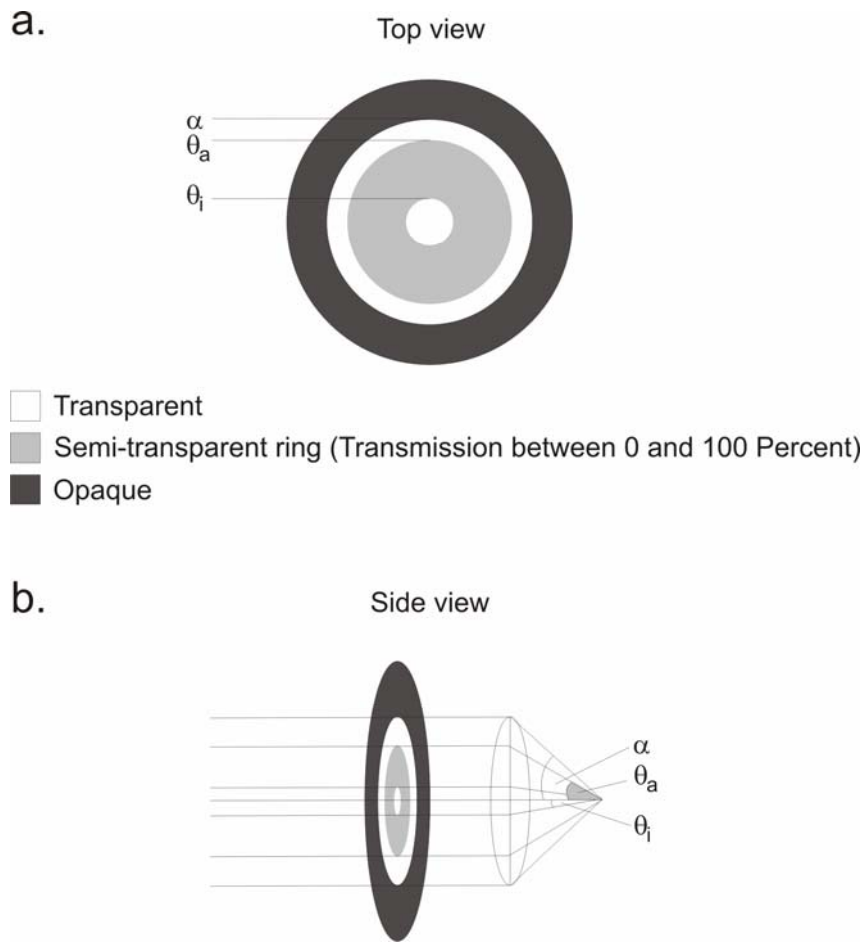
Figure 3.10 A schematic diagram of the "Shaded-Ring Filter" that is used to reduce the elongation of the voxel in the axial direction. **a.** A top view of the filter. The filter consists of a transparent centre circle, a semi-transparent middle ring, and a transparent outer ring. The inner and outer diameters or each ring are defined by the parameters α, θ_a and θ_i. **b.** A side view of the filter. The parameters of α, θ_a and θ_i are determined by a ray-tracing diagram to the focal volume.

curve) shows high transmittance on the long-wavelength side with suppression down to 30% at a wavelength of 2.16 μm. The transmittance recovers on the short-wavelength side to almost 65 %, before higher bands and diffraction lead to a further reduction in transmittance. The reflectance spectrum (red curve) shows corresponding features. Band-structure calculations,[33] with parameters taken from the electron microscopy images, and especially taking into account the measured ellipsoidal rod
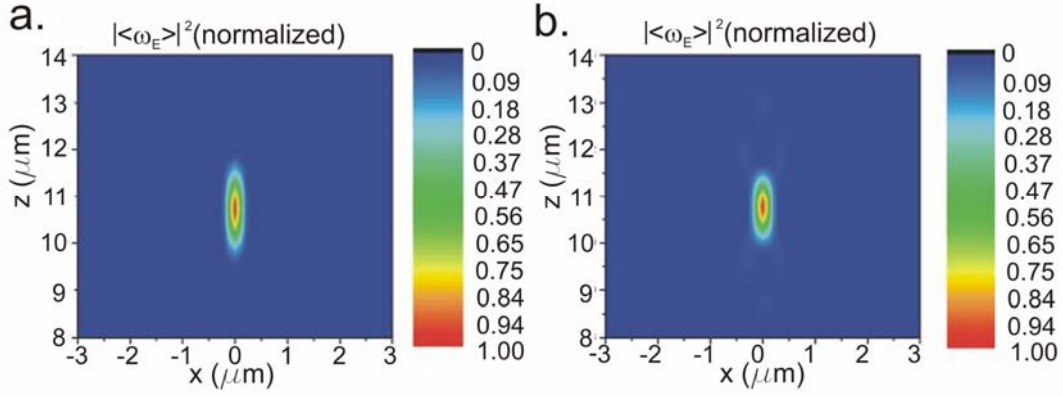
Figure 3.11 A comparison of the normalized square of the time averaged electric energy density $|\omega_E|^2$ that is 10.8 μm into the depth (z) of an As_2S_3 photoresist. **a.** the $|\omega_E|^2$ without shaded- ring filter and **b.** the $|\omega_E|^2$ with the shaded ring filter. Once can see that elongation of the voxel can be improved from 6:1 to 4:1 via the introduction of the shaded ring filter.

cross-section, revealed a PBG of 3.5 % and is marked by the hashed bar on the left hand side of Figure 3.8.

At first sight, one might expect larger effects in the optical spectra. To allow for a direct comparison with the theoretical ideal, we have calculated the corresponding spectra using a scattering-matrix approach[89] with the similar parameters used for the band-structure calculations, but taking into account the finite size of the sample. The overall agreement between the calculations (dotted curves) and experimental results (solid curves) is very good. (Figure 3.8)

To mimic the experimental measurement apparatus (c.f. chapter 6), in particular the finite-opening angle due to the Cassegrain optics, we averaged the calculated transmittance spectra over an angle of incidence between 15 and 30° with respect to the surface normal. Remaining discrepancies could be explained by structural imperfections of the sample. However, the effect of angle averaging is rather small. To show this, we also calculated the transmittance spectrum for normal incidence *without* any angle averaging (dashed grey curve). Recall that we have used similar
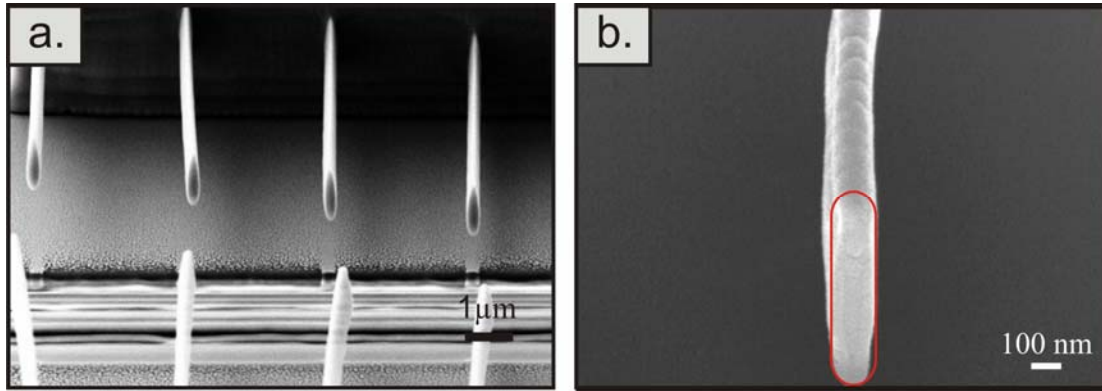
Figure 3.12 a. FIB cross-section of the step-ladder test structures that are routinely produced using the 3D DLW with the shaded-ring filter in-place. **b.** the individual bars have a lateral resolution of 180 nm and has an aspect ratio as expected from the simulation of the normalized square of the time averaged electric energy density $|\omega_E|^2$ inside As_2S_3.(see Figure 3.11)

structural parameters in both the scattering-matrix calculations (for the finite structure) and the band-structure calculations (for a fictitious infinite structure) and that the latter revealed a complete PBG with 3.5% gap/midgap ratio.

Thus, our experimental results were compatible with this PBG calculation. To demonstrate the potential of our approach, we present a gap-width map in Figure 3.9 which denotes the maximum achievable PBG for the parameters accessible by means of a modified rod design. The white cross marks the position for the sample presented. Further modification of the writing parameters might lead to a complete gap approaching a gap/mid-gap ratio of 9%.

The effectiveness of these 2 corrective measures resulted in an astounding improvement to the structural quality of the final 3D structures. However, a further correction step could be taken to account for the voxel elongation that was caused by the reduction of the opening angle of the microscope objective. For this correction, an amplitude mask which we call a "shaded-ring filter" had been developed to address the problem of the elongation of the voxel in the axial direction[90]. This shaded-ring filter was shown in Figure 3.11. The shaded-ring filter provided an amplitude

modulation of the illumination beam. A simple ray tracing diagram showed that the amplitude filter provides a reduction in the opening angle of the incident beam to create a modified focal volume. (Figure 3.10)

The shaded-ring filter borrows from a family of leaky filters whose function is to provide pupil spatial filtering[91]. The shaded ring filter has a semi-transparent centre because simple dark-ring filters (opaque region only, no semi-transparent region) which can also provide axial compression, generated large amplitude side lobes. The emergence of side lobes is undesired since the energy contained in these lobes may also cause the photo-polymerization, which leads to the generation of undesired side structures. Here, by incorporating the semi-transparent region into the filter design, it simultaneously allowed for axial compression of an elongated voxel, and the suppression of unwanted side lobes.

The simulated results, using the vector-Debye theory, for an un-corrected, and a shaded-ring filter corrected, voxel in As_2S_3 is shown in Figure 3.11. Here, the corrected single voxel is more isotropic in all of its axes, and improved the overall aspect ratio of the voxel. Figure 3.12 shows an SEM image of a single, free-standing rod that was written in the As_2S_3 photoresist with the shaded-ring filter in place[ii]. The lateral resolution of this free-standing rod was 180 nm and it exhibited a voxel shape that has an aspect ratio as expected from the simulations that were carried out for chalcogenide photoresist.

With these advanced optical corrective measures in place, we significantly improved one of the key components which enabled the fabrication of 3D PBG structures with fine feature resolutions. However, the diisopentylamie based etchant that we used here for the majority of these optical correction investigations did not

---

[ii] N.B. The etchant used here is the highly-selective etchant containing the molecule N-4-methoxybenzyl-pyren-1-ylamien (cf. chapter 4).

have the etch selectivity to produce thicker structures that contain even finer feature resolutions. In order to fabricate a 3D woodpile photonic crystal structure with a full-PBG centered at the important telecommunication wavelengths of 1.55 μm, a thicker structure composed of individual rods with widths well below 200 nm was required. Therefore, before we could proceed to fabricate even finer 3D structures, via 3D DLW, the next component in this photoresist system that must be investigated and optimized is the wet-etchant. The results of this investigation into a new highly-selective etchant are provided in the following chapter.

Chapter 4 – Development of a Highly-Selective Wet Etchant

4.1 Introduction

In the previous two chapters, we have demonstrated that with the correct thermal evaporation parameters, it was possible to transform glassy As_2S_3 into a photoresist that was compatible with the 3D DLW process. Using this photoresist, we have shown that it was possible to create high quality, free-standing, 3D PBG structures. However, as we have hinted near the end of chapter 3, any further improvement of the feature resolutions would require the use of a new and novel wet-etchant that possessed high etch selectivity. Such a wet-etchant does not currently exist and must be developed in order to continue to improve the resolution of the As_2S_3 photoresist system, so as to allow it to record the sub-micron feature sizes that are routinely achievable with the 3D DLW method. In this chapter, we will provide the development details of a molecule that enables highly-selective wet-etching in this photoresist system.

We begin by making the important point that a wet-etchant was chosen for the etching step because a wet-etchant allows the etching process to simultaneously occur on all sides of the 3D structure. Furthermore, the etchant could diffuse into the pores of the structure to remove volumes of material around intricate features inside the 3D structure. These properties provide distinct advantages over line-of-sight etching techniques such as reactive-ion etching, where omni-directional etching around three-dimensional features is impossible. Although other omni-directional etching techniques, such as isotropic oxygen plasma, is available, we must stress that the as-deposited and photopolymerized form of As_2S_3 both have the same etch rates in this
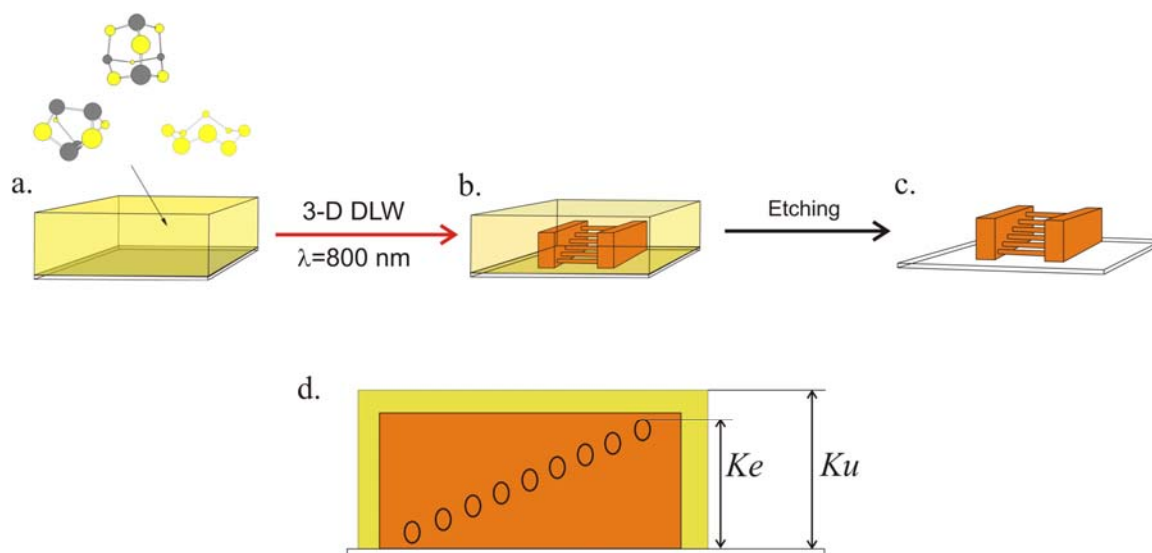
Figure 4.1. Illustration showing the fabrication process of a free-standing 3D "step-ladder" test structures in arsenic-sulphide based photoresist, using the 3D DLW method and subsequent wet-etching. **a.** The unexposed photoresist contains As_4S_6, As_4S_4 and S_8 molecules (yellow area). **b.** The 3D latent image is already visible inside the photoresist after 3D DLW due to the refractive index increase after writing. **c.** The final free-standing 3D structure obtained after removal of the As_4S_6, As_4S_4 and S_8 molecules using an etchant solution containing the amine *N*-(4-methoxybenzyl)-(pyren-1-yl)amine **16**. **d.** The convention used to define the selectivity is the ratio between the rate of removal of the unexposed area, **K*u***, and the rate of removal of the exposed area, **K*e***. (ie. γ = **K*u***/**K*e***)

process. Therefore, using such a technique will result in isotropic etching on all areas of the photoresist, which results in the complete removal of the structure, and no selectivity can be obtained,.

For the wet-etchants that are under consideration here, it is important that it enabled a photoresist to generate large structures with a large aspect ratio thus allowing it to contain elements with sub-micron resolution. In order to achieve this feat, the selectivity of the wet-etchant must be very high. The selectivity of an etchant (γ) is defined as the ratio between the rate of removal of the unexposed (**K*u***) and exposed areas (**K*e***) of the photoresist. Therefore, when developing As_2S_3 as a negative-tone photoresist, the unexposed areas should be removed as quickly as possible (large **K*u***)

Equation 1. $\qquad$ $2(m+n)\ As_2S_3 \xrightarrow{\text{high vacuum, 390 }^\circ\text{C}} n\ (As_4S_4 + 1/4\ S_8) + m\ As_4S_6$

Equation 2. $\qquad$ $R_2NH + S_8 \longrightarrow R_2N{-}S_8{-}H \longrightarrow R_2N{-}S_x{}^\bullet + \bullet S_{8\text{-}x}{-}H$

Equation 3. a.

$$R_2NH$$

$$-\overset{|}{\underset{|}{As}}{-}S \longrightarrow -\overset{R_2NH^+}{\underset{|}{As}} + \overset{-}{\underset{|}{S}}$$

b.

$$-\overset{R_2NH^+}{\underset{|}{As}} + \overset{-}{\underset{|}{S}} + R_2NH \longrightarrow -\overset{R_2N}{\underset{|}{As}} + \overset{R_2NH_2{}^+}{\underset{|}{S}}$$
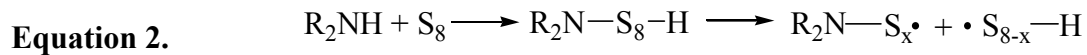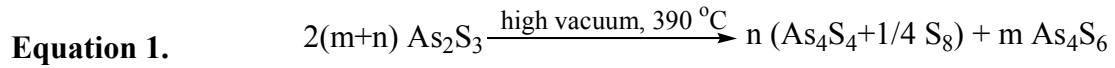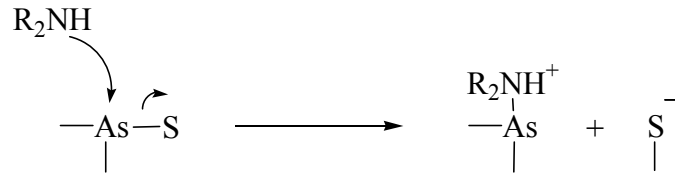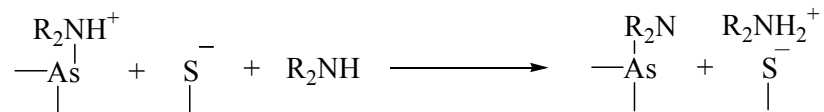
Figure 4.2. The chemical reactions that have been proposed to occur during the different stages of the etching process. Equation 1 shows the species that are generated during the thermal evaporation of the precursor material. Equation 2 shows the initial steps of a multi-step reaction where an amine catalyzes the ring-opening scission of S-S bonds in the S_8 molecules. Equations 3a and b show the two reaction steps that take place on the surface of the exposed areas.

relative to the exposed areas (small **Ke**), so as to afford a large γ, which will allow high resolution features in thick structures to be produced. (see Figure 4.1 d.)

One additional challenge that is encountered when etching intricate 3D PBG structures is that they must be immersed for long periods of time in the wet-etchant. The increased etch times over a solid 3D structure was a result of the slower diffusion of the liquid etchant though the more tortuous architectures of the porous sub-nanoscale voids of a 3D PBG structure. A further challenge relates to the higher reaction rate on areas that had already been developed by the etchant in 3D microstructures. This was due to the surface area per unit volume of a 3D nanoporous material being much larger than that of a solid 3D structure. Currently available wet-etchant compositions present in the literature that dealt with As_2S_3 as a photoresist have only been applied to 2D structures less than 500 nm in height[30,31]. Under these

circumstances, etch-selectivity requirements are much more relaxed. With these considerations in mind, we began our investigation by reviewing some early investigations concerning the solution phase chemistry of the arsenic sulphide/sulphur system[38,39]. It was proposed that the reactions between the chemical species on the surface of the film and an amine, occurring in polar aprotic organic solvents[92,93], proceeded *via* a series of S_N2 nucleophillic displacement reactions. This series of reactions, occurring in polar aprotic organic solvents, were exemplified in Figure 4.2 by Equations 2 and 3. Equation 2 shows that during etching of the unexposed areas, the amine first catalyzed the ring opening of the S_8 molecules that were present in the film[92]. It was well known that this type of reaction leads to the formation of a complex mixture of charged sulphur species, some of which included anion radicals of sulphur of various chain lengths which are highly oxidizing[94,95,96,97,98,99,100]. It had been proposed that these highly oxidizing species then served to oxidize any As-As and As-S bonds, which resulted in the dissolution of both the molecular species and exposed As_2S_3[92]. Since both the exposed and un-exposed areas were eventually removed, it resulted in a γ that was too small to be useful for directly etching 3D microstructures.

However, in alternative investigations on the dissolution of the As_2S_3 bulk glass, it was observed that when a reaction was performed using short-chain primary amines as neat solvents, under atmospheric conditions, the Lewis basicity of the lone electron pair on the nitrogen of the amine caused a nucleophillic displacement reaction to occur. The products that were identified in this reaction solution were micellar-like amine and quaternary ammonium cation capped-clusters of As_2S_3 which contained As-N bonds as well as the ammonium cation of the amine[101,102,103]. These nucleophillic reactions as shown in Equation 3 of Figure 4.2 were proposed to start at

the surface and progressed into the bulk material which resulted in the subsequent removal of clusters of the glassy network by these small amine molecules. When the liberated clusters became sufficiently small, its surfaces became completely capped by amine and quaternary ammonium cation molecules. These capping species acts to protect the surface from further bond cleavage and oxidation and thus served to protect the remaining volume of the cluster from complete dissolution.

Taken together, these reactions indicated that it may be possible to limit, or to inhibit, oxidizing reactions from occurring at the surface of the exposed areas *via* the coordination of large amine molecules onto the surface, so as to utilize the amine molecule as a surface passivation layer. Moreover, such an amine must also simultaneously carry out the reactions shown in Equation 2 and 3 of Figure 4.2, so as to also remove the unexposed areas. In order to investigate this hypothesis, the secondary aryl amine molecule, dibenzylamine, was chosen as the synthetic substrate because it was sterically larger relative to most primary and short chain secondary amines. Therefore, theoretically, this molecule should serve to provide an adequate surface passivation layer and act as a starting point for our investigation.

There are two main investigations performed in this chapter. In the first investigation, we conducted a series of systematic synthetic modifications of the dibenzylamine molecule, and investigated their etching behavior in an organic solvent based As_2S_3 etching system. By synthesizing this amine library, and conducting a systematic study, the association between the molecular structure and etch selectivity was identified. At the end of this investigation, we described the synthesis of a novel etchant molecule, *N*-(4-methoxybenzyl)-(pyren-1-yl)amine. This molecule allowed 3D structures that were created by photo-patterning of as-deposited As_2S_3 with 3D DLW to be etched out with high selectivity in one simple etching process.

In the second investigation, we studied the mode of reaction of the *N*-(4-methoxybenzyl)-(pyren-1-yl)amine molecule as it was used to etch the As_2S_3 photoresist. Here, the surfaces of the photoresist films were first analyzed using X-ray photoemission spectroscopy (XPS) in order to determine the species that were present on the film surface after etching. Using this method, the products of the reactions that were previously described in solution was identified on a solid surface. Furthermore, a ^{1}H-NMR analysis of the etching process in the solution phase was also carried out. Using ^{1}H-NMR, a serial investigation into the reactivity between the species found in the As_2S_3 photo-resist film, the *N*-(4-methoxybenzyl)-(pyren-1-yl)amine molecule and the organic solvents used was conducted. From this analysis we were able to identify and determine which species were responsible for generating the signals observed in the XPS analysis. This investigation provided a further understanding of the etching mechanism that was previously proposed for this system.

4.2. Experimental Results and Discussions

The As_2S_3 photoresist preparation, as well as the 3D DLW method that was used, followed the exact same procedures as those outlined in chapter 2 and 3. The details of the synthesis are provided in chapter 7 and a summary of the spectroscopic characterization of the individual amines are provided in the Appendix section.

4.2.1 Systematic Molecular Modification of the Dibenzylamine Backbone

Before we could test the library of amines and determine the relationships between the molecular structure of the dibenzylamine molecule and its macroscopic effect on the etch selectivity, we required a standard 3D test structure. Such a structure was necessary because we had identified early on that the surface area per unit volume of
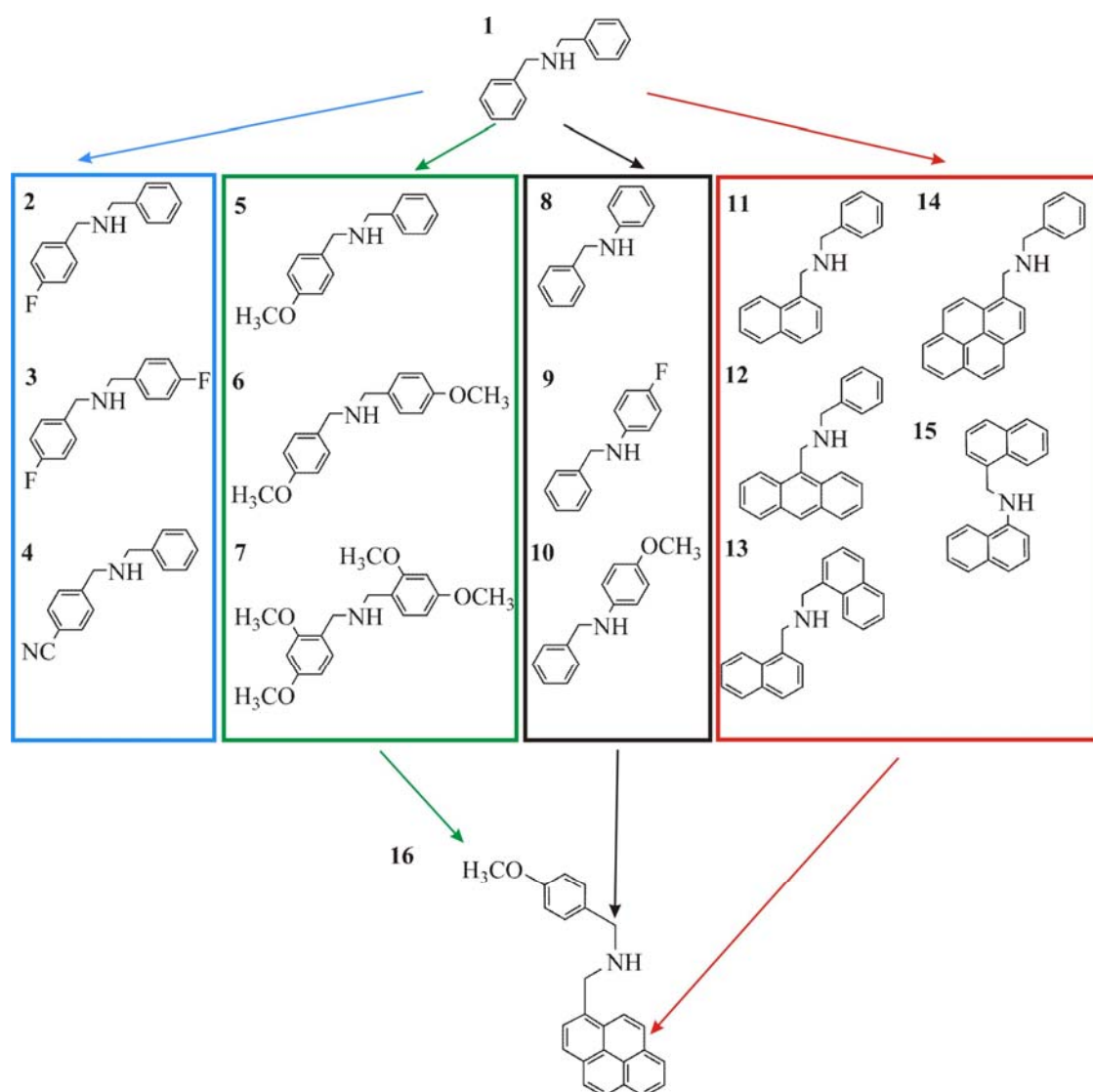
Figure 4.3. Examples of dibenzylamine derivatives that have been synthesized for this study: the colour codes blue, green, black and red outline the modifications that have been made to amine molecule **1**, namely electron-withdrawing, electron-donating, bridging methylene removed, and steric size increase respectively. *N*-(4-methoxybenzyl)-(pyren-1-yl)amine **16** is the resulting amine molecule that embodies all of the desired attributes of each of the modifications.

a 3D nano-porous structure played a large role in the etch selectivity of an etchant, therefore we needed to devise a standard 3D structure that could serve as a testing benchmark to provide a figure of merit that could be compared amongst all of the different amine molecules that were synthesized and tested. Therefore, for this purpose, we have devised a unique step-ladder testing structure which allowed for the testing of the 3D etch selectivity. A schematic of this step-ladder structure is shown
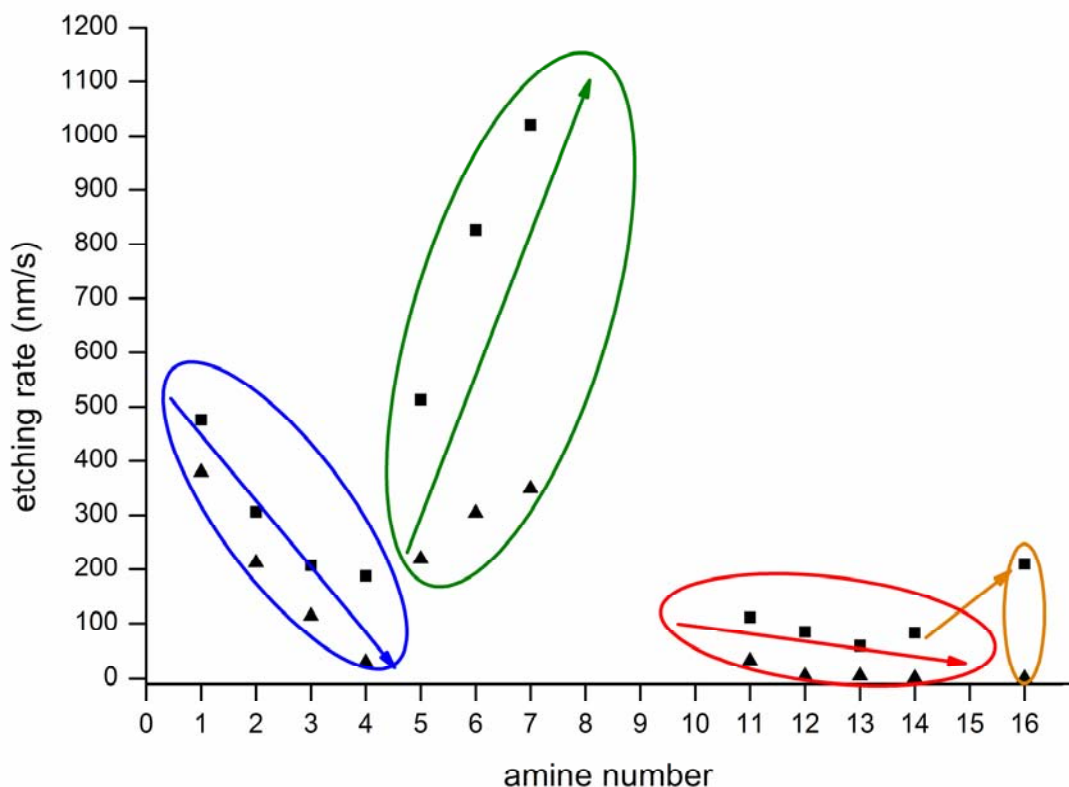
Figure 4.4 A plot of the *Ku* (■) and the *Ke* (▲) of the different amines. The distinct molecular modifications to the dibenzylamine backbone: electron-withdrawing, electron-donating, and steric size effects are marked by the colored circles blue, green, and red respectively. Arrows indicate the direction of the trends in the etch rates that develop for each modification of the amine. A downward arrow indicates a decrease in the etch rate and vice versa. The orange circle contains optimized amine **16** which possesses both a sterically large pyrenyl arm and an electron donating group on the benzyl ring thus enabling it to realize a larger *Ku* than its analogue **14**. Amines **8** to **10** and **15** are not plotted on this graph as these amines showed no reaction when used as the active species in the etchants.

in Figure 4.1 d.

Such a step-ladder structure consists of 20 microns long rungs which were staggered with 250 nm vertical and 2 micron lateral distance between the rung. Their ends were attached to two supporting walls. This "step-ladder" geometry contains sub-200 nm features, and allowed for convenient observation and evaluation of the selectivity via optical microscopy. The removal of the unexposed areas could be visually determined when the color of the unexposed photoresist disappears. The removal of the rungs of the ladder could also be followed with an optical microscope and was

periodically inspected until the structure is etched to destruction, or if the structure continues to remain, the time is stopped after 72 hours (3 days) have elapsed. The overall etch selectivity γ (which is the figure of merit that will be compared amongst the different amines) was then calculated as the ratio between the rate of removal of the unexposed (***Ku***) and exposed areas (***Ke***) respectively. Since this step-ladder test structure consisted of the one of the most basic connected 3D elements, which is a line, it can accurately represent the high surface areas and the slow diffusion of etchant solutions that were encountered when etching complex 3D structures.[iii]

4.2.2 Testing of the Small Molecule Library

For the first investigation, 2 systematic series of synthetic modifications were performed on the dibenzylamine molecule. The first series of modifications focused on controlling the basicity of the amine nitrogen *via* the addition of electron donating or withdrawing groups on the benzyl ring. The second series of modifications focused on increasing the steric demands of the amine molecule *via* the substitution of the benzyl groups with progressively larger aryl ring moieties. All sixteen dibenzylamine derivatives synthesized in this study are shown in Figure 4.3. The etch rates of the unexposed and exposed areas are graphically summarized in Figure 4.4. Furthermore, a plot of the etch selectivity based on these etch rate values are summarized graphically in Figure 4.5.

On surveying Figure 4.4, distinct trends in the etch rates could be identified as the dibenzylamine backbone was systematically modified. Amines 2 to 7 had different electron donating and withdrawing groups attached to the benzyl ring. The

---

[iii] Note: Although the most basic 3D element is a point. It is impossible to investigate a single free-standing point in 3D space after the etching process. This is because the single point has no support structure around it and it will be washed away during the etching process. However, the cross-section of a line is a point. Such a cross-sectioning can be achieved using a focused ion-beam cutting method. This result will be shown later in the thesis.
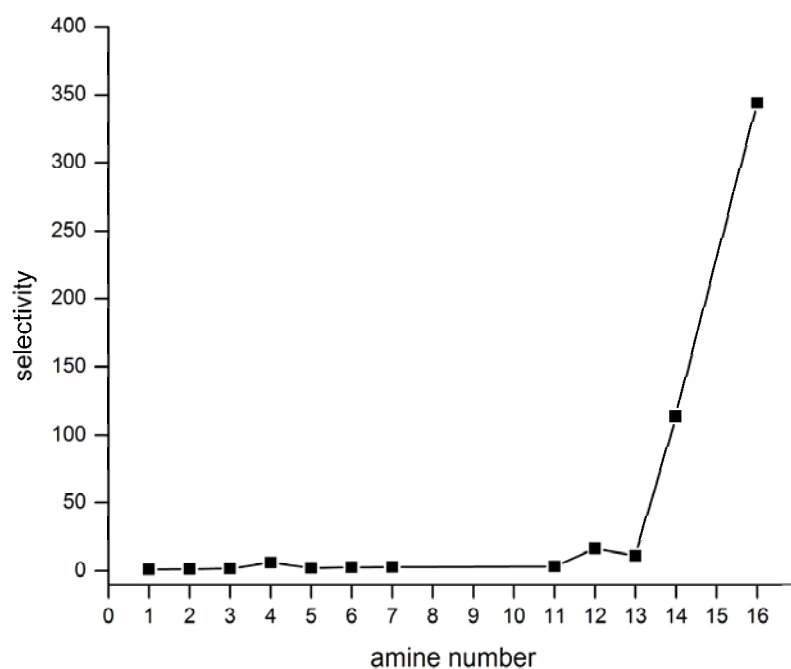
Figure 4.5   A plot showing the selectivity γ of the different amine molecules synthesized in this study. It can be clearly seen in this graph, that there is a dramatic increase in the selectivity as the steric size of the amine increases.   Amines **8** to **10** and **15** are not plotted on this graph as these amines did not show any showed no reaction when used as the active species in the etchant.

dibenzylamine derivatives 2 to 4 contained electron withdrawing groups and are marked within the blue outline.   The overall trend, as denoted by the blue arrow, shows a continuous decrease in the etch rate as the strength and the number of electron withdrawing groups increased on the benzyl ring.   Amines 5 to 7 are contained within the green outline and these were modified with electron donating groups. Here the etch rates increased as the amount of electron-donating groups that were substituted on the benzyl ring increased. The reason for this behavior could be explained by examining Equation 2. Since the generation of the oxidizing sulphur species by an amine was a S_N2 type reaction[96,100], the effects of the addition of electron-withdrawing groups served to slow the etch rates, and the addition of electron donating groups had the opposite effect. However, despite providing control of the reaction rates, the graph in Figure 4.5 shows that these modifications alone did

not provide any dramatic increase in the overall etch-selectivity from that of **1**, the original dibenzylamine molecule.

Another approach to further increase the etch selectivity (γ) was to increase the etch rates of the unexposed area so as to increase the (**Ku**). One modification that may provide this type of control was the removal of the -CH_2- bridge between the nitrogen and the phenyl ring. Due to the direct linkage between the nitrogen and the phenyl group this should serve to decrease the steric hindrance of the amine molecule, while at the same time increase the electronic effectiveness of the substituent groups on the phenyl ring. These types of modifications were made in molecules **8** to **10**. Such modifications should have the effect of increasing the etch rate of the unexposed areas (**Ku**), and thus provide an increase in the overall selectivity. However, despite the advantages listed above, these modified amines exhibited no reaction towards the unexposed areas - the entire film was not etched at all. One plausible explanation could be that this modification increased the steric crowding directly adjacent to the nitrogen atom, thus shielding the nitrogen lone-pair from gaining access to electrophillic sites[95]. Therefore, the inability to catalyze the formation of the oxidizing sulfur species, as shown in Equation 2 of Figure 4.2, prevented the etching of the unexposed areas. As a result this molecular modification overrode any benefits to the electronic effects that could be gained by using a shorter connection between the nitrogen and the phenyl ring.

We can conclude from these observations that electronic modifications alone do not serve to increase the etch selectivity. This could be due to an insufficient steric coverage by the dibenzylamine backbone which maybe necessary so as to provide effective passivation to the surface of the exposed areas, as suggested by etching Equation 3 in Figure 4.2.

To alleviate the deficiency in the surface passivation ability due to a lack of steric bulk of the dibenzylamine backbone, the second set of molecular modifications focused on a progressive increase to the steric size of the rings on the benzyl substituent group. In compounds **11** to **14**, one arm of the dibenzylamine had been modified by an increasingly larger aromatic moiety. These molecules are highlighted with a red outline in Figure 4.3 and 4.4. In Figure 4.4, we observe that the values of *Ku* and the *Ke* are much lower compared to **1**. This is due to the restricted exposure of the electron lone pair on the nitrogen as a result of the increased steric hindrance of the larger aryl group. However, despite a much lower rate of reaction, upon inspection of Figure 4.5, the etch selectivity did tend to increase dramatically as the aromatic group was increased in size. In fact, there was almost a 100 fold increase in the etch selectivity on moving from the benzyl- arm of **1** to a pyrenyl- arm of **15**.

Therefore, to further increase the steric bulk of the amine, we synthesized amine **13** where we replaced both of the benzyl groups with napthyl- groups. As expected, the *Ku* decreased due to the increase in the steric bulk, but the overall selectivity did not improve. A possible explanation is that although the reaction depicted in Equation 2 of Figure 4.2 was slowed down due to the steric hindrance of the larger aryl groups, these were not large enough to fully passivate the surface from further reaction. The inability to provide full passivation allowed the oxidizing species to continue to attack the exposed areas which resulted in the eventual total dissolution of the structure.

To further prove that the -CH$_2$- linkage is required in the structure of the amine molecule, irrespective of the steric size of the amine itself, we synthesized amine **15**, an analogue of **13**, but without the -CH$_2$- linkage between the nitrogen and the aryl ring. Here, no reaction was observed with amine **15**, although etching was observed with **13**. The result obtained here for the sterically large amines was similar to the
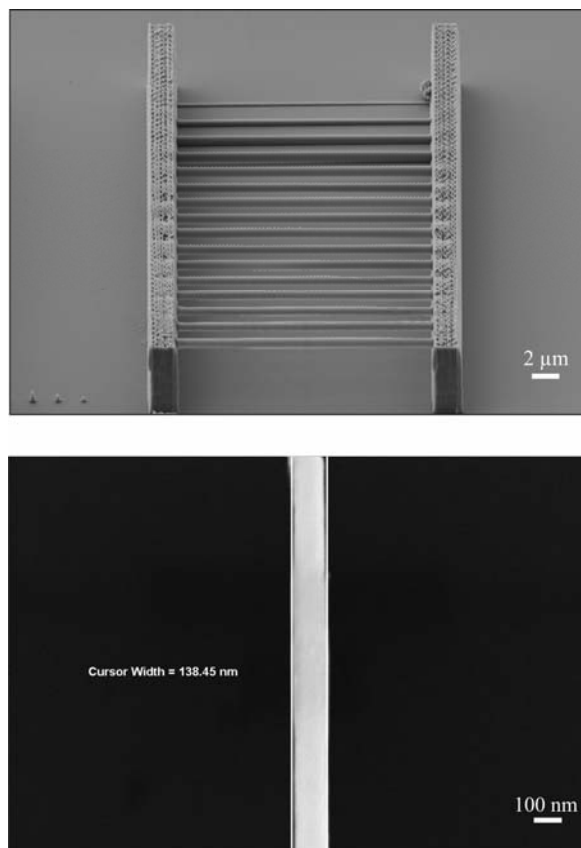
Figure 4.6 (Top) SEM image of a test-ladder structure that has been etched with an etchant solution containing the highly-selective amine *N*-(4-methoxybenzyl)-(pyren-1-yl)amine. Such a test-ladder demonstrates the ability to simulate 3D structures because it contains freely suspended nano-rods which can serve to represent a true 3D feature. (Bottom) An SEM image of the highest lateral line-resolution that can be achieved using the step-ladder test structure.

less sterically hindered amines, **8** to **10**. This reinforced the observation that the presence of a -CH$_2$- linkage was necessary for the occurrence of the reactions in Equation 2 of Figure 4.2.

Our series of modifications revealed two main amine design criteria for the amine molecule: First, to form an effective passivation layer it was sufficient to increase thesteric size of only one arm of the amine. Second, the extra degree of freedom provided by the methylene linkage was essential for enabling the reaction in Equation 2 to occur. Fulfilling both design criteria allowed the amine molecule to provide high
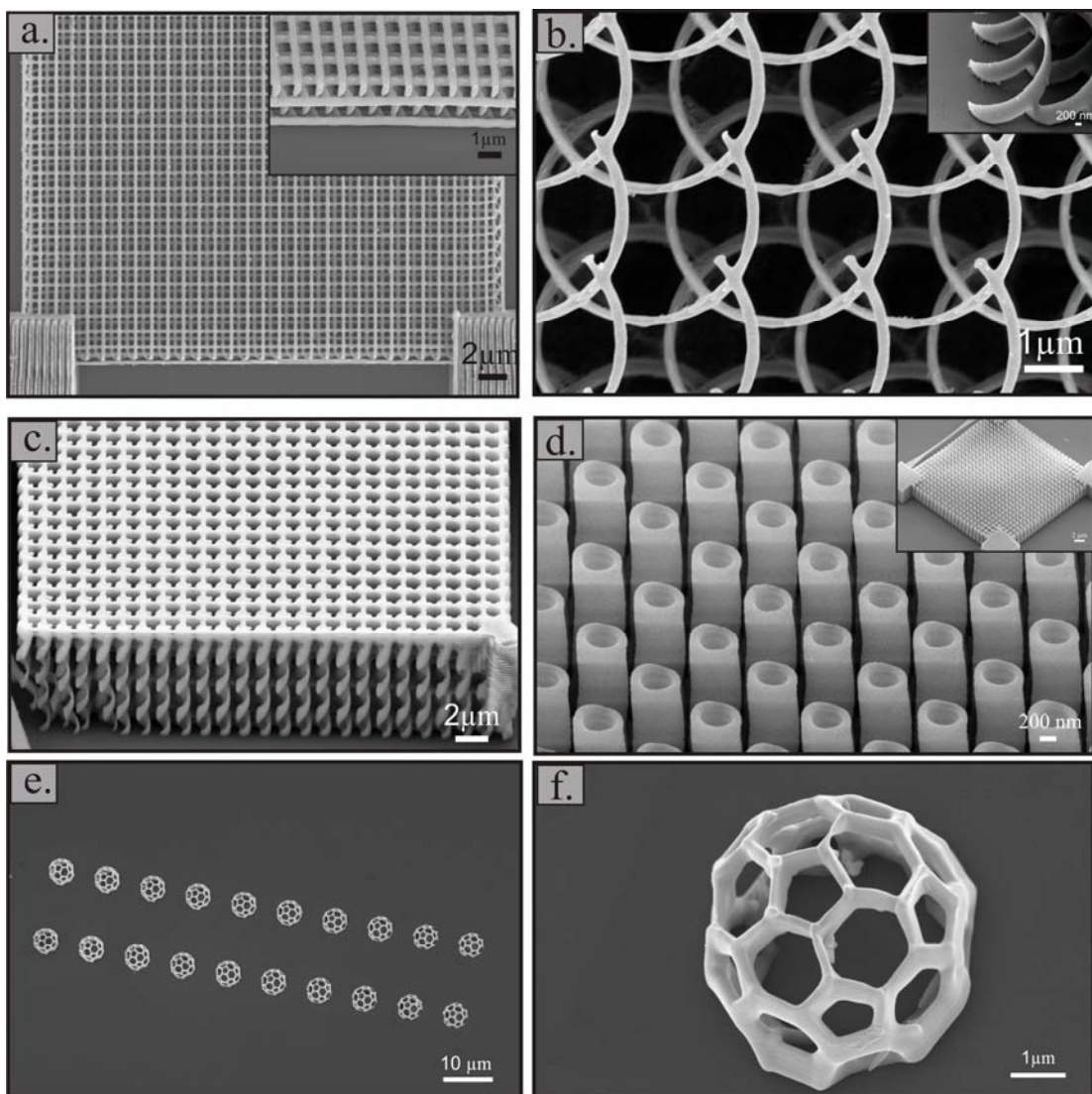
Figure 4.7 These images show that various 3D As_2S_3 microstructures can be easily fabricated using an etchant containing molecule **16**. It is important to note that these structures possess exceptionally smooth close-to-perfect surfaces. Such aspects are critical for highly demanding applications of nanostructures, such as those intended for optical applications. **a.** A 3D woodpile photonic crystal with a lattice constant of 700 nm, and a side-view of this structure (inset). **b.** The top view of a 3D array of fine spirals with individual feature sizes on the order of 180 nm (inset). **c.** A 3D array of spirals. **d.** A high magnification image of an array of nanotubes, and an overview of the perfect square array of these nanotubes. **e.** A perfectly aligned array of micro-bucky balls. **f.** A close-up of e. showing a single micro-bucky ball.

etch selectivity which could be rationalized along the lines of the etching reactions that are presented in Equation 2 and 3 in Figure 4.2.

Although these results even suggested the use of a tertiary amine for the etching process, this approach failed. The reason was because a tertiary amine lacked a proton on the nitrogen atom. Therefore, the initial proton transfer as required by Equation 2 of Figure 4.2 could not occur[95,96]. Indeed, when the simple tertiary amine, triethylamine, was used in this investigation, the entire photoresist film was not etched at all. This observation also explained the results of amine **4**: Since the nitrogen on the cyano-side group of **4** did not contain a proton, it could not serve as a reactive centre in a manner as depicted in Equation 2 of Figure 4.2, and therefore, it could not enhance the *Ku*. Indeed this is what we observe. In fact, the *Ku* observed for amine **4** was even lower than for the unmodified amine **1**. Furthermore, the lower etch rates obtained by **4** are comparable to that of amine **3**. Thus, the cyano-group merely had an electron-withdrawing function and was not an active participant in the etching reaction.

Based on these results we designed and synthesized a novel molecule, *N*-(4-methoxybenzyl)-(pyren-1-yl)amine (**16)**, which possessed all the attributes that were required to etch 3D DLW films with high selectivity. In **16**, the bulky pyrenyl-arm, together with an electronic donating methoxy-group on the benzyl ring, acted together to provide our best recorded etch selectivity of 344:1. SEM images of optimized test-ladder structures developed with an etchant solution containing **16** are presented in Figure 4.6. Here we show that the best lateral resolution of a free-standing line that was achieved with this photoresist system had a width of 138 nm. Furthermore, to show the resolution and capabilities of this photoresist system, various 3D nanostructures were also fabricated. These include woodpile photonic crystals, spiral photonic crystals, an array of nano-tubes, and a free-standing bucky-ball structure. SEM images of these nanostructures are presented in Figure 4.7.

4.2.3 XPS Characterization of the Photoresist Surfaces

We began the investigation into the etching mechanism by first establishing the species that were present on the thin film surface after the wet-etching reaction using the XPS analysis method. In order to provide a direct comparison, the results of the XPS analysis of an as-deposited film is presented in Figure 4.8 a. and b.

These results for this as-deposited film suggested the presence of molecular species on it surface. In the As_{3d} spectrum (Figure 4.8 a) the position of the binding energy (BE) was consistent with the presence of molecular species containing As-S bonds such as As_4S_4 and As_4S_6. Second, the peaks identified on the S_{2p} spectra (Figure 4.8 b) implied that sulphur was present in both an oxidation state of zero (163.9 eV) and -2 (162.7 eV), and suggested that S_8 was present alongside the As-S containing species. Furthermore, the analysis of the peak areas reveaed that the atomic ratio of arsenic to sulphur was 2 to 3, (c.f. chapter 2) this indicated that the stochiometry of the precursor was preserved in the as-deposited film. The results obtained here were in good agreement with those found in the literature[71,72].

Analysis of the film treated with an etchant that contained amine **16** revealed interesting changes on the surface of the film after immersion. In the As_{3d} spectra (Figure 4.8 c) there was an emergence of a new spectral feature at 45.6 eV. Similarly, in the S_{2p} spectra an additional spectral feature emerged at the BE of 168.3 eV (Figure 4.8 d). It is important to point out that the appearance of these species were not observed on films that had not been treated with the etchant, and no reactions occurred when they were treated only with the pure solvents. Therefore, this indicated that their presence was a direct result of chemical reactions that occurred during etching.

The BE of the new feature on the S_{2p} spectra was consistent with sulphate and/or
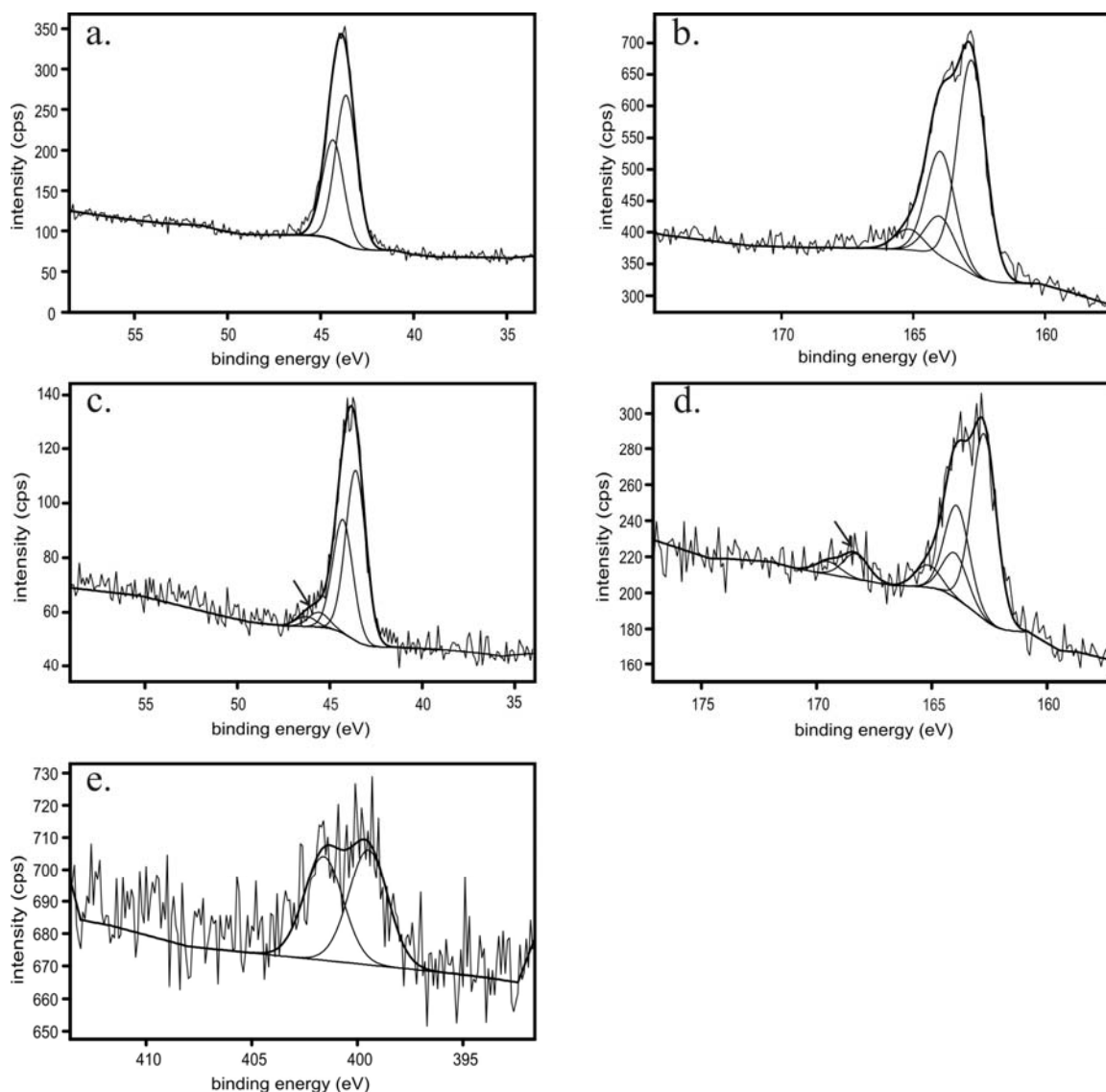
Figure 4.8 XPS spectra of the surface of thin films of arsenic-sulphide based photoresist. Spectra of the as-deposited film are shown in graphs **a.** As$_{3d}$ and **b.** S$_{2p}$, and a UV-exposed film that has been immersed in an etchant containing molecule **16**, are shown in graphs **c.** As$_{3d}$, **d.** S$_{2p}$ and **e.** N$_{1s}$. Black arrows in spectra c. and d. indicate new features that arose in the spectra after immersion in the etchant containing **16**. (See main text for discussion).

thiosulphate species being present on the surface of the film[104,105,106]. To account for the presence of sulphate or thiosulphate species on the surface, we begin by mentioning that polysulfide anions, similar to those generated from the amine catalyzed reactions shown in Equations 2 and 3 in Figure 4.2, were known to undergo rapid auto-oxidation into sulphate and thiosulphate in many industrial processes

where wet-oxidization was employed[107]. Furthermore, the new spectra feature in the As$_{3d}$ spectra (Figure 4.8 c) was also consistent with the presence of arsenic oxides[108].

Since the highly selective etchant used here was prepared and used under atmospheric conditions without the need for any special apparatus or dry solvents, traces of water and oxygen will undoubtedly be present. It is likely that this was the reason for the presence of oxidation products to be observed on the surface of the films treated with the etchant. Despite these products of oxidation being present, SEM images of the 3D microstructures produced here (Figure 4.6 and 4.7) show that their influence is limited as the final surfaces remain smooth and defect free.

We obtained further information upon an inspection of the N$_{1s}$ spectra (Figure 4.8 e). There, two distinct signals suggested the presence of different nitrogen atomic environments which are both in the -3 oxidation state. The first signal at 401.6 eV was consistent with nitrogen present as the ammonium cation[106], and the second signal at 399.5 eV with the presence of an As (+3)-N(-3) direct bond[104,109]. The identification of these species were in-line with the expected reaction products of Equation 3, in Figure 4.2. Furthermore, the second result here implied that another arsenic species besides the oxide existed on the surface. Namely, the new feature in the As$_{3d}$ spectra (Figure 4.8 c) at the BE of 45.6 eV was also consistent with a +3 oxidation state of an organo-arsenic species. This observation was not immediately obvious in the As$_{3d}$ spectra since both arsenic oxides and the organo-arsenic species possessed similar binding energies[71].

Previous literature investigating etching mechanisms of As-S based photoresist did not take into account of the effects of atmospheric water and oxygen in their analyses[92,93,101,102] From the XPS results presented here, it seemed that their presence, along with amine **16**, produced reaction products that were previously unexpected.

Furthermore since the generation of the species observed here could be accomplished via different reaction pathways, the etching mechanism maybe much more complex than previously indicated. The analysis performed here suggested the presence of a mixed surface passivation layer and various oxidation products, providing possible new insights into the etching mechanism. In order to provide a further investigation into the etching mechanism, where the contributions of atmospheric water and oxygen were essentially eliminated, we have decided to carry out the etching experiments under an inert atmosphere. The result of this investigation is provided in the next section.

4.2.4 ^{1}H-NMR Analysis into the Etching Mechanism

Although the reaction products that are postulated in the chemical reactions found in Equations 1 to 3 in Figure 4.2, were observed using the XPS method, and served to aid in the development of the highly selective amine molecules, some questions regarding the mutual interaction between each of the constituent molecules found on the surface of the films still remain. Most importantly, their individual and combined effects on the reaction mechanism still remained unclear. Some of these interesting and important questions are:

- Which species reacted with the amine reagent N-4-methoxybenyl-pyren-1-yl-amine?

- Which molecules were responsible for generating the species that are observed in the XPS study?

- What were the roles of the different solvents?

- Did the solvents themselves participate in the etching reaction?

Group A

1. dmso + S_8 $\longrightarrow$ NR

2. dmso + As_4S_4 $\longrightarrow$ NR

3. dmso + As_2S_3 $\longrightarrow$ NR

4. dmso + N4MBPA $\longrightarrow$ Shows spectra of N4MBPA

5. dmso + cp + S_8 $\longrightarrow$ NR

6. dmso + cp + As_4S_4 $\longrightarrow$ NR

7. dmso + cp + As_2S_3 $\longrightarrow$ NR

8. dmso + cp + N4MBPA $\longrightarrow$ Shows spectra of N4MBPA

Group B

9. dmso + cp + S_8 + As_4S_4 $\longrightarrow$ NR

10. dmso + cp + S_8 + As_2S_3 $\longrightarrow$ NR

11. dmso + cp + S_8 + N4MBPA $\longrightarrow$ Shows presence of N4MBPAH$^+$Cl$^-$

12. dmso + cp + As_4S_4 + As_2S_3 $\longrightarrow$ NR

13. dmso + cp + As_4S_4 + N4MBPA $\longrightarrow$ Shows splitting of N4MBPA

14. dmso + cp + As_2S_3 + N4MBPA $\longrightarrow$ Shows splitting of N4MBPA

15. dmso + cp + as-evaporated film + N4MBPA $\longrightarrow$ Shows splitting of N4MBPA

Figure 4.9 The etching reactions that were investigated with the ^{1}H-NMR method. Here, the amine N-4-methoxybenzyl-pyren-1-ylamine is abbreviated as N4MBPA. All the reactions were performed under an inert atmosphere of nitrogen and can be divided into 2 groups. Group A examined the reaction of the pure compounds, and served to determine if there are any background reactions between the pure compounds and the solvents that are used in this study. Group B examined the simultaneous reaction of 2 pure compounds. These reactions served to determine which combination of compounds resulted in a shift in the ^{1}H-NMR spectrum of the signal of either the solvent or the amine molecule.

Here, an analysis of the etching reaction as a whole is inherently difficult because of the presence of a mixture of different species on the surface of the as-evaporated thin film.

Therefore, a simple analysis of the etching reaction of the photoresist film itself, in hopes of assigning the roles of the individual species in the etching reaction, becomes impossible. Furthermore, in order to characterize the etching reaction in its native state, a sensitive and simple spectroscopic probe that can analyze and track a common effect of the individual molecules in the reaction, in-situ, should be employed.

With these above requirements, we decided to breakdown the etching reaction to its individual molecules so as to allow for the analysis of their individual interactions in the solution phase. In order to further aid in the data interpretation of the etching reactions, we carried out the reactions under an inert atmosphere in order to reduce the effects of atmospheric water and oxygen and suppress the effects of any side reactions that could complicate the interpretation of the results obtained in this analysis.

The common effect that we decided to track and compare was the proton shifts that occurred in the solutions as different species were combined together using ^{1}H-NMR analysis. The choice to track the proton shift using this analysis method was two-fold. First, ^{1}H-NMR is a very sensitive probe for solution phase reactions, concentrations on the order of parts-per million are easily identifiable using this technique. Secondly, due to electronic effects, the hydrogen nuclei show a strong sensitivity to the hybridization of the atom to which the proton is attached to. This enables sensitive identification of the changes to the surrounding chemical environment. This sensitivity is especially useful for the identification and discernment of the *N*-(4-methoxybenzyl)-(pyren-1-yl)amine between the bound form (As-N) and the ammonium form, as was identified by XPS spectroscopy. Furthermore, the solvents used in the etching reactions all contain protons which can also be recorded and examined to determine their participation in the etching reaction.
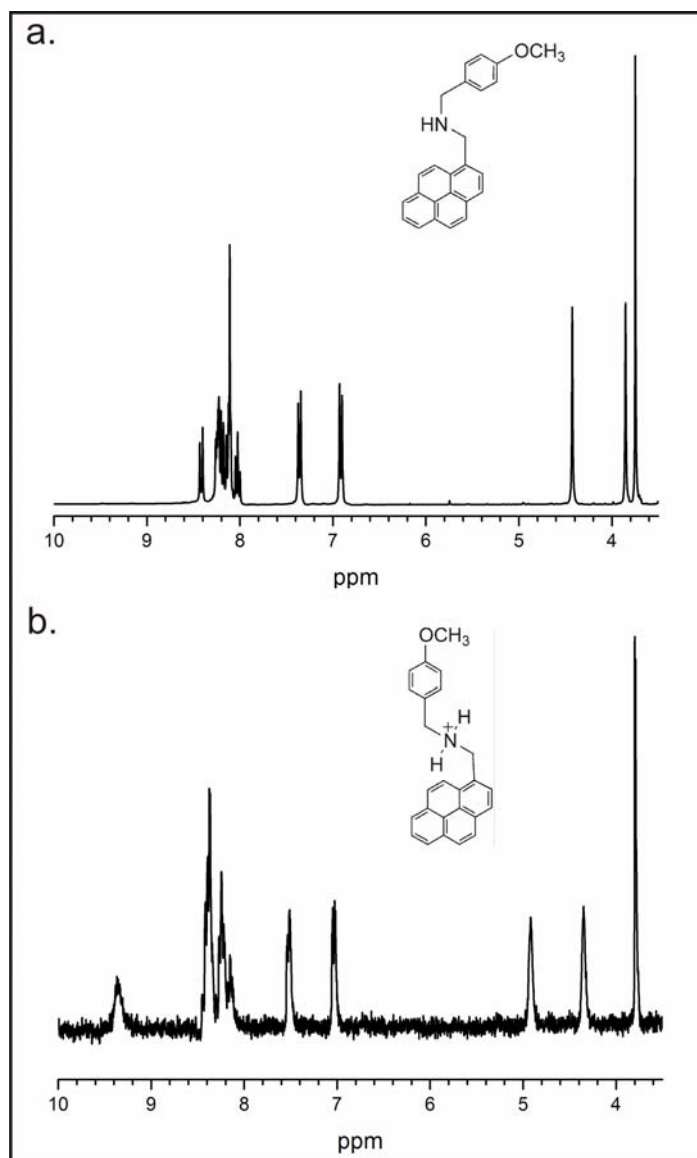
Figure 4.10 a. ^{1}H-NMR spectra of N-4-methoxybenzyl-pyren-1-ylamine in the cp-dmso system **b.** N-4-methoxybenzyl-pyren-1-ylammonium chloride in the same cp-dmso solvent system. Notice the appearance of the new proton signal at δ = 9.355 ppm. The appearance of this signal is due to the second proton that is on the nitrogen atom of the ammonium cation.

In contrast, the use of the sulfur nucleus as the NMR probe is not a good choice because the NMR sensitive isotope [33]S has a very low-abundance, which results in very low-sensitivities. Furthermore, the sulfur atom contains a significant quadrapolar moment in its nucleus, leading to quadrapolar relaxation, which results in the generation of very broad signal that are difficult to detect. The arsenic atom is also not a suitable choice as an NMR probe. Although the [75]As nucleus has 100%

natural abundance, and hence good NMR sensitivities, it also possesses a large quadrapolar moment, and as a result it suffers from the same drawbacks as the sulfur atoms during NMR analysis[110].

The reactions that were analyzed by the ^{1}H-NMR method are tabulated in Figure 4.9. The analysis were split into two main groups; Group A, contains the results from the reactions between pure compounds, and group B are the results of the simultaneous reactions between 2 pure compounds. All analyses were conducted using dry d^6-dmso as the solvent.

To begin, we have analyzed the contribution of the co-solvent, cyclopentanone. The result of the addition of the co-solvent to dmso did not cause any shifting or splitting of the dmso signal. Furthermore, the cp retained the same signal splitting behavior as if it was dissolved in other solvents such as $CDCl_3$. Therefore, from this analysis it was evident that the co-solvent did not react with the dmso solvent. It was important to establish that there was no reaction between the solvents themselves because if they exhibit mutual interactions, then this would have to be accounted for in the overall analysis and it will significantly complicate any further analysis steps.

Now we turned to the actual analysis of the interaction between different molecular species. First, we will present and discuss the results that were obtained in reaction group A, the reaction between pure compounds. We performed this set of reactions in order to determine if the individual pure compounds reacted with the organic solvents that were used in the etching reaction.

When the amine *N*-(4-methoxybenzyl)-(pyren-1-yl)amine was dissolved in the cp-d^6-dmso mixture, a ^{1}H-NMR spectra of this molecule could be clearly recorded. (Figure 4.10, top) In contrast the amine could not be totally dissolved in pure d^6-dmso alone. In fact, after two hours of stirring, the amine remains un-dissolved in

pure d^6-dmso versus a total dissolution in the cp-d^6-dmso solvent system in less than two minutes. This is confirmed visually, as well as in the NMR spectra (very low signal strength). This established that the cyclopentanone was required to be present as the co-solvent in order for complete dissolution of the amine.

This co-solvent behavior can be explained by examining the Hildenbrand constants of the individual solvents. The Hildenbrand constant of dmso is 24.5, and for cyclopentanone it is 19.5. We have experimentally determined that if these two solvents were combined in a volume ratio which yield an effective Hildenbrand constant of 20.5, it would facilitate the complete dissolution of the amine. In fact, different solvents combinations could be substituted for the dmso/cyclopentanone systems, these included, but are not limited to, a pairing of acetone/toluene, and dmso/1,2-dicholorethane. We have found that a variety of solvents could be used, as long as one of the solvents is a polar, aprotic solvent and that the overall effective Hildenbrand constant of the mixture was 20.5. The fact that one of the solvents that were chosen must be polar and aprotic was because the overall etching reaction exhibits a S_N2 type reaction behavior, and the use of polar, aprotic solvents, such as dmso, is know to facilitate these types of reactions[111,112,113]. Despite the wide variety of possible solvent combinations, the dmso/cyclopentanone combination was chosen as the working solvent system because it exhibited a very low vapor pressure. This technical advantage enabled the overall solvent system to remain more stable over longer periods of time. This long-term stability was required as complex 3D structures with nano-porosity may take up to 36 hours to etch due to the restricted rate of diffusion through the nano-porous architecture of these complex 3D structures.

As for the molecules that are found on the thin film, such as S_8, A_4S_4 and As_2S_3 (substitution for As_4S_6, cf. Chapter 2) they also did not dissolve in pure in d^6-dmso or

in the cp-d^6-dmso mixture after three days of stirring at room temperature. These mixtures remained heterogeneous and did not cause any shifting of the proton peaks of the d^6-dmso solvent peaks nor the peaks associated with the cp-d^6-dmso mixture. Furthermore, since these compounds themselves did not contain any protons, no additional peaks other than those belonging to the solvent could be observed here. In fact, a clear colorless solution was observed when the precipitates were allowed to settle back to the bottom of the flask. Therefore, from this analysis, it was established that the individual molecules of S_8, A_4S_4 and As_2S_3 did not react with the pure solvents that were used for the reaction. Furthermore, these molecules did not contribute any signals to the ^{1}H-NMR spectrum.

Overall, from the analysis of the reactions in group A, it was concluded that that the co-solvent did not react with the main solvent, and furthermore, the pure compounds did not react with either of the solvents used. These results were important because this indicated that the solvents themselves did not participate actively in the reaction, and that the etching could be solely attributed to the design of the amine molecule itself.

In reaction group B, the reactions between 2 pure compounds, the 4 solid compounds, S_8, A_4S_4 and As_2S_3 and *N*-4-methoxybenzyl-pyren-1-ylamine were combined together, two at a time. Here, we wanted to learn if any proton shifting could be observed when different molecules were combined. What we have observed here was that no shifting of the solvent proton peaks could be observed if the two reagents that were combined together were both the pure inorganic compounds. (e.g. Figure 4.9 reactions 9, 10 and 12) However, when *N*-4-methoxybenzyl-pyren-1-ylamine was added as a reagent along with one of the inorganic compounds, a shifting of the proton signals of the amine could be observed.
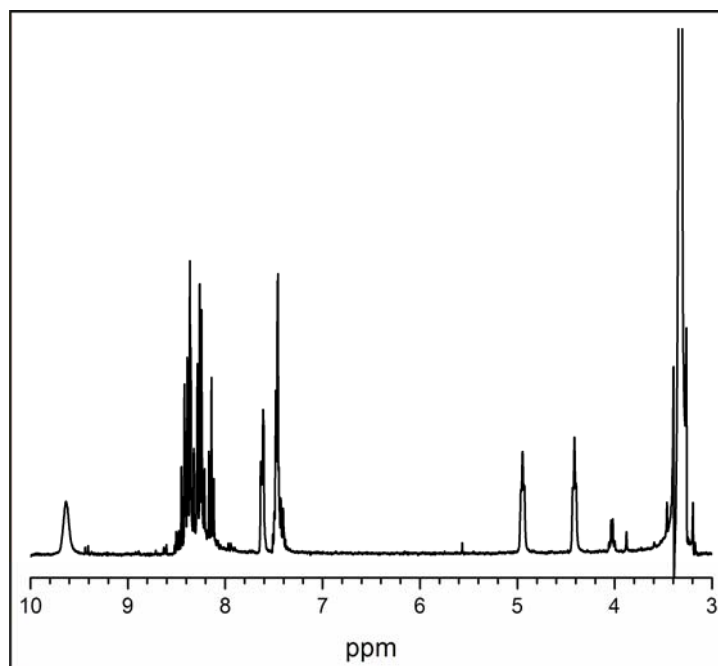
Figure 4.11 ^{1}H-NMR of the reaction between S_8 + N4MBPA in dmso and cyclopentanone. (Reaction 11 in Figure 4.9) The spectra clearly shows the presence of a new peak at δ = 9.639 ppm which is attributed to the presence of the N-4-methoxybenzyl-pyren-1-ylammonium ion.

For the reaction of the amine with S_8 (Figure 4.9, reaction 11), it was observed that an initially clear, colorless solution of the solvent containing S_8 immediately turned blue upon the addition of the amine. It was well documented the reaction of sulfur with primary and secondary amines produces a blue color in solution due to the formation of sulfur radicals[98,99,100]. The appearance of the blue color here was a good indication that the sulfur radical has formed in the solution. Furthermore, all of the S_8 powder dissolved after 1 hour of stirring. The NMR of this reaction (Figure 4.11) showed that there was a clear appearance of a new peak at a chemical shift of 9.639 ppm. The removal of this signal could be achieved through the addition of small amounts of D$_2$O. From this observation, it was suggested that this new signal stemmed from the appearance of the ammonium form of the *N*-4-methoxybenzyl-pyren-1-ylamine molecule. Since the proton on the ammonium cation could exchange

with the deuterium of the D_2O, the signal due to the second proton of the ammonium cation could be removed from the ^{1}H-NMR spectrum upon the addition of D_2O.

In order to provide further evidence that the ammonium ion was indeed being generated in this reaction, a standard ammonium salt of the amine, *N*-4-methoxybenzyl-pyren-1-ylammonium chloride was first synthesized, purified and then analyzed with mass-spectrometry and single-crystal x-ray diffraction. Then, a ^{1}H-NMR of this molecule was obtained, (Figure 4.10 bottom) and compared with the previous reaction. The ^{1}H-NMR of the ammonium ion standard clearly showed the presence of a peak signal at δ=9.35 ppm, and this signal could also be removed via the addition of small amount of D_2O. Therefore, the identity of this peak could be assigned to the proton on the nitrogen of the ammonium ion.

A comparison of the ^{1}H-NMR of the pure ammonium molecule (Figure 4.10 bottom) and the etching reaction to which the ammonium cation is speculated to have been generated (Figure 4.11) shows a close, overall match in both the position of the signal near $\delta = 9.3$ ppm to $\delta = 9.6$ ppm as well as the splitting patterns of the other proton signals of the ammonium ion. Therefore, this comparison strongly suggested that the reaction of *N*-4-methoxybenzyl-pyren-1-ylamine with S_8 resulted in the generation of the ammonium ion from the amine molecule.

In the reaction of the amine with As_4S_4 (Figure 4.9 reaction 13), a homogenous solution that was, clear and orange in color was obtained upon mixing. However, in the reaction of the amine with As_2S_3 (Figure 4.9 reaction 14), a heterogeneous solution that was orange in color was obtained. The particles that were present in this second solution could not be dissolved after 1 week of stirring at room temperature, nor with additional stirring for another 7 days at 80º C. Despite this difference in the observed reactivity, the ^{1}H-NMR spectra analyses of both solutions (Figure 4.12)
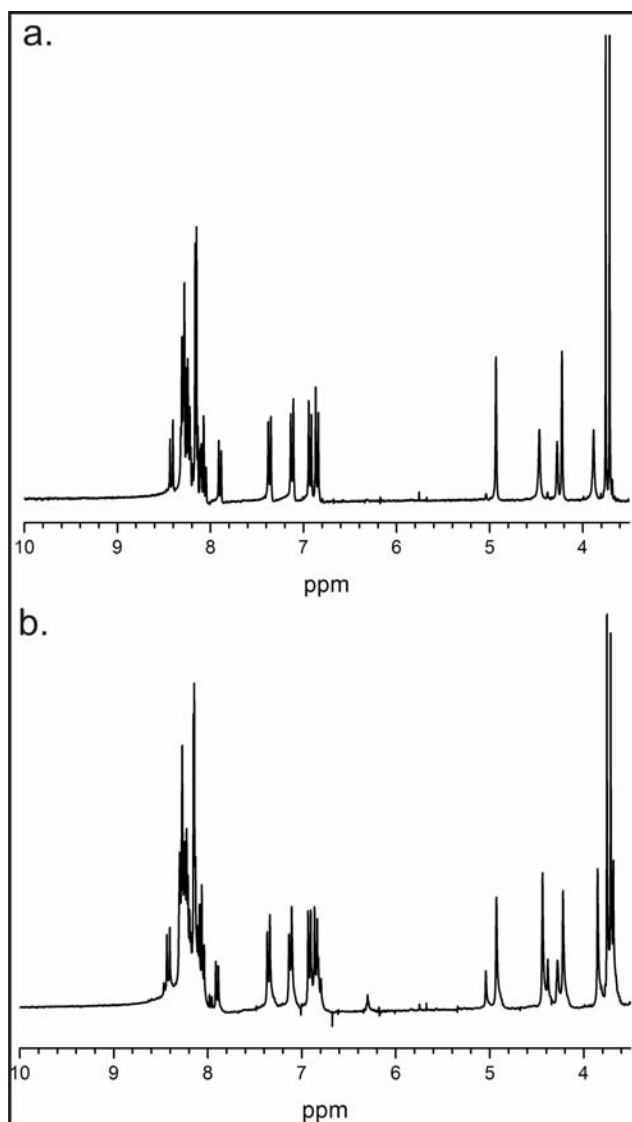
Figure 4.12 a. The ^{1}H-NMR spectra of the reaction, As_2S_3 + N4BPMA in the cp-dmso solvent system. **b.** The ^{1}H-NMR spectra of the reaction, As_4S_4+N4BPMA in the cp-dmso solvent system. The two spectrum shows very similar splitting of their benzyl and methylene protons. The signal due to the ammonium cation ($\delta = 9.3 – 9.6$) is not observed here. This strongly suggests that the splitting is due to the formation of an As-N bond.

exhibited a similar splitting pattern of the proton signals of the amine. The ^{1}H-NMR spectra of these two reactions are shown in Figure 4.12. Here, the splitting of the signals that occurred at a chemical shift from $\delta = 7.6$ to $\delta = 7.0$ belonged to the protons on the benzyl rings, and the signals at a chemical shift from $\delta = 5.2$ to $\delta = 3.8$, belonged to the protons of the methylene bridging groups of the amine molecule. The

most striking aspect of the splitting pattern of these peaks was that they exhibited a mirrored splitting of the pure amine molecule. (e.g. A double-set of peaks belonging to the amine molecule but slightly shifted by a few ppm.) This mirrored splitting suggested that some of the amine molecules are located at a different chemical environment than the free-amine, which strongly indicates the presence of another form of the amine molecule. However, in both of these cases, there was an absence of the ammonium signal around the $\delta = 9.4$ to $\delta = 9.6$ ppm region. This suggested that the new species present was not the ammonium cation of the amine.

One interpretation of these observations was that the reaction of the amine with As_4S_4 and As_2S_3 both resulted in the formation of an As-N bond. The formation of this bond is plausible since it provided a different chemical environment that would account for the splitting of the proton signals on the methylene and benzyl protons, and at the same time not generating any ammonium signal because the attachment is on an arsenic atom and not a hydrogen atom. The formation of an As-N bond supported the identification of this type of bond as was observed in the XPS analysis of the film surface that has been treated with the etchant.

However, there was a noticeable difference between these 2 reactions. This was that the As_2S_3 did not totally dissolve, despite longer reaction times and higher reaction temperatures. From these observations it became apparent that we could not assume that As_4S_6 could be chemically represented by As_2S_3. This is because As_4S_6 should become completely dissolved, as it is a molecular. Therefore, although the As_2S_3 glass maybe used as an aid for the spectroscopic representation of As_4S_6, (cf. chapter 2), it could not serve to represent As_4S_6 in chemical reactions.

Despite the observation that the As_2S_3 glass could not be used to represent As_4S_6 in chemical reactions, the As_2S_3 glass did serve to represent the photo-polymerized
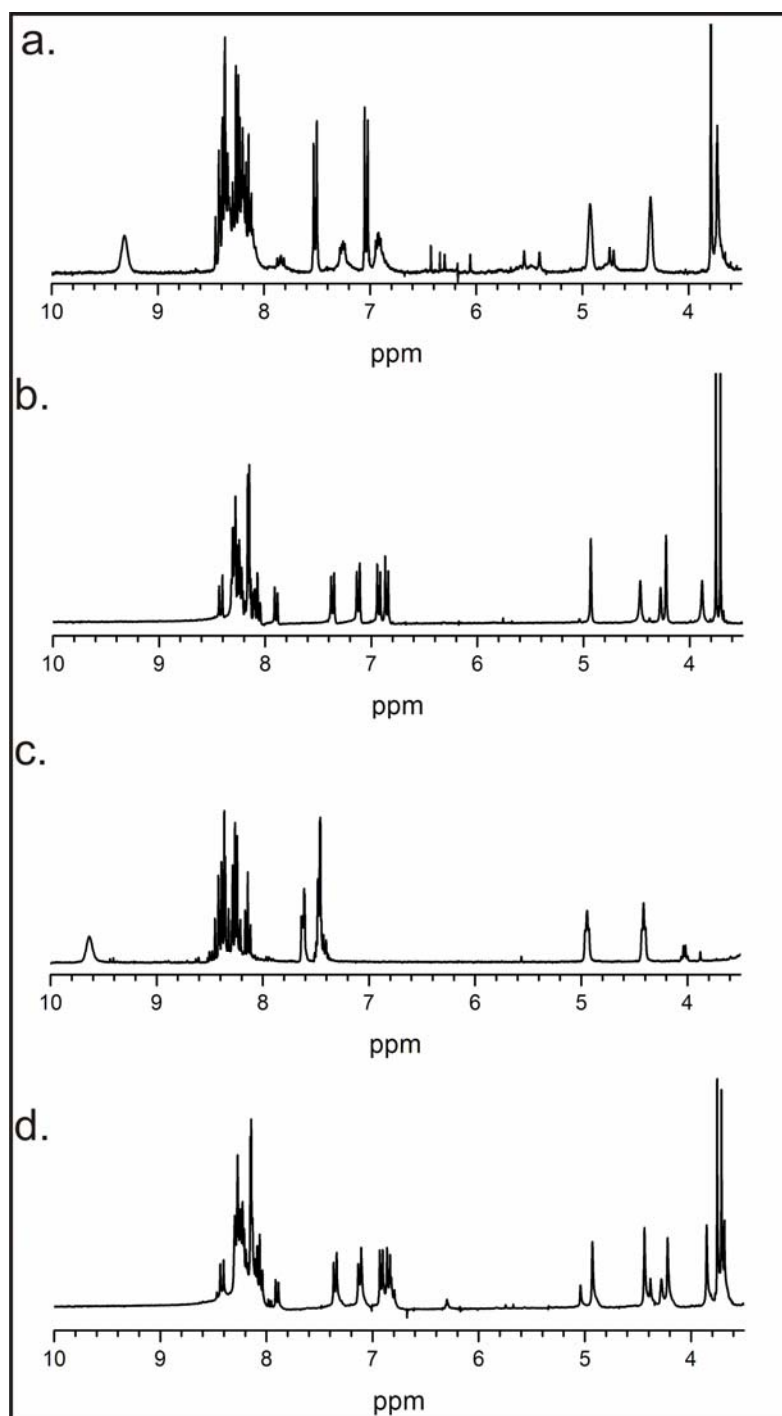
Figure 4.13 A comparison of the ^{1}H-NMR spectra of the etching reactions using *N*-4-methoxybenzyl-pyren-1-ylamine (N4MPBA) in a cp-dmso solvent mixture on **a.** an as-deposited film, **b.** As_4S_4, **c.** S_8 and **d.** As_2S_3. Spectrum **a.** clearly shows the presence of the ammonium ion due to the presence of S_8 on the surface of the film, and the complex splitting pattern of the protons of the N4MPBA molecule were due to the presence of both the bound amine, which contributed the As-N bond, the original amine molecule and the ammonium ion.

photoresist material. The result that the fully polymerized As_2S_3 glass does not dissolve in the etchant, even after long reaction times at elevated temperature, was the property which was desired for the highly selective etchant on the photo-polymerized areas. To provide a comparison of the significance of this observation, in studies where sterically small, short chain amines such as ethylamine, propylamine and butylamine were used in the etching reaction, the highly cross-linked As_2S_3 glass was completely solvated into a homogenous yellow liquid at room temperature within 4 hours[101,102]. Comparing those results with the results obtained here provided further evidence that the steric properties of the amine molecule played a key role on the surface passivation theory that was proposed in Figure 4.2, Equations 3 a and 3 b. Furthermore, the results here indicated that the *N*-4-methoxybenzyl-pyren-1-yl-amine served as an excellent surface passivation layer on the surface of photo-polymerized As_2S_3.

However, one question still remained, and that was the origin of the ammonium ion that had been identified in the XPS spectra of a polymerized film. Since the reaction between As_2S_3 and the amine did not produce any ammonium ions, its presence should not be observed on the film surface after the etching process. To provide a possible explanation to this observation, we examined an etching solution that was used to etch an as-deposited thin film, which contains S_8, As_4S_4, and As_2S_3, and compared it to the ^{1}H-NMR spectra of reactions of pairs of reactants as discussed above. A side-by-side comparison of these spectra is provided in Figure 4.13.

In Figure 4.13, we can clearly observe that in the ^{1}H-NMR spectra of the as-deposited film (top spectrum), the splitting of the methylene and benzyl protons of the amine are present, and the signal from the presence of the ammonium ion is also present. This indicates that the ammonium ion observed in the XPS investigation

could in fact be the remnants of the reaction between the amine with the S_8 species of the thin film which have not been thoroughly rinsed off after the etching process. Or, the ammonium ion could be attached to the surface via partially polymerized S_8 molecules, which remained due to the incomplete polymerization of the as-deposited thin film during the photo-polymerization of the photoresist film with the broadband UV light source used to illuminate the large samples areas that were required for the XPS experiments. In this case, the fragments of the S_8 molecule may continue to persist and generate the ammonium ions that were observed in the XPS analysis.

The results obtained by carrying out the reaction under inert environmental conditions, so as to reduce the contributions of atmospheric water and oxygen, provided some insights to the 4 important questions about this etchant system which were posed at the beginning of this chapter. The key observations in this current study were that the molecular components of the as-evaporated film did not react with the pure solvents used in the reaction, and the reaction would only proceed if the amine molecule was present. Furthermore, the reaction products that were identified here provided some insights to the origins of the observations that were made with the XPS analysis, and these were: the *N*-4-methoxybenzyl-yren-1-amine directly generated the As-N bond, and the presence of the ammonium ion was due to the reaction of the S_8 ions. Through the separate analysis of the reactions of different constituents found on the as-evaporated thin-films via ^{1}H-NMR, we were able to provide further insight into the origins of the presence of the As-N bonds as well as the ammonium ion that was previously observed by Chen et al. via IR spectroscopy,[101.102] and also in our own XPS investigations.

Despite the useful insights that were obtained from the ^{1}H-NMR study, some issues remained unresolved. The most important issues that remains to be investigated is the

contribution of the As_4S_6 molecule on the etching reaction. Since this molecule is a component that was identified on the surface of the film, a ^{1}H-NMR characterization which includes this molecule as part of the analysis is necessary in order to provide a full accounting of the chemical reactions that are occurring in the etching reaction. Furthermore, despite rigorous drying of the dimethylsulfoxide solvent, small amounts of water continued to remain in the solvent which was detectable in trace amounts by the ^{1}H-NMR technique. The total removal of the presence of water was very difficult in a hygroscopic solvent such as dmso. A total removal of the presence of water may require the pre-silanization of all glassware that is used, or the use of all-fluorinated plastic apparatus, in order to achieve the total removal of the last traces of water that is present on the surface of the glass.

Another observation made in this investigation which was difficult to explain, was the pathway towards the formation of the ammonium ion in the reaction where S_8 was reacted with the *N*-4-methoxybenzylpyren-1-ylamine. (Reaction 4.9, reaction 11) In the original set of reaction equations that are proposed in Figure 4.2, the appearance of the ammonium ion was attributed to the reaction with the As-S bonds (Figure 4.2, reaction 3) and the reaction with the S_8 should only generate sulfur radicals. This observation could not be easily explained here, and future work using more stringent reaction conditions focusing on this particular reaction must be made in order to elucidate the pathway which leads to the appearance of the ammonium cation in this particular reaction.

Although limitations to the XPS and inert atmosphere investigations do exist, the information that was garnered from these analyses do serve to provide valuable insight into the contribution and participation of the individual molecular species and solvents used in the atmospheric etching reactions as proposed in Figure 4.2. Future

work to clearly elucidate the atmospheric etching mechanism would likely involve studying the individual contributions of water and oxygen through their controlled introduction to the reaction mixture. Furthermore, kinetic studies to each individual step of the reaction should be made to clearly define the steps in the etching mechanism.

Despite a lack of a definitive elucidation of the reaction mechanism, we must point out that the highly-selective etchant, consisting of the N-4-methoxybenzyl-pyren-1-ylamine molecule, was able to function under ambient conditions, in a predictable and reproducible manner, so as to allow the etching of various intricate 3D structures that are demonstrated here in this current work. This is a pre-requisite for any practical future manufacturing process of As_2S_3 based devices using 3D DLW.

Chapter 5 - Erbium Doped As$_2$S$_3$

5.1 Introduction

The results that were presented in chapter 3 demonstrated that the combination of 3D DLW and As$_2$S$_3$ is a very versatile and powerful method for producing complex and intricate 3D PBG structures. However, since As$_2$S$_3$ itself does not possess any intrinsic room temperature photoluminescence, the final 3D PBG structures remained optically passive. These meant that these structures only served as passive Bragg reflectors, but were not capable of performing any active functions such as light amplification. Some examples of conventional 2D photonic structures that are optically passive include waveguides and Y-couplers.

However, in practice, optically active structures are an essential part of a photonic circuit. This is because the signals of the photonic circuit must first be generated, and then boosted while in transmission. Some classical 2D photonic structures with optical activity are lasers[114,115] and fiber amplifiers[40,116]. In the case of 3D PBG structures, the ability to exhibit optical activity allows them to display far more interesting properties such as zero-threshold lasing[3]. However, in order to provide photoluminescence to these structures, optically active species must be incorporated into them.

Currently, the method that has received the most attention in the 3D DLW community is the post-fabrication infiltration of quantum dot solutions into a 3D PC structure. Since the quantum dots are photoluminescent, their inclusion provides optical activity to the 3D PC structures fabricated by 3D DLW[8,9,10]. However, there are 3 main drawbacks to this infiltration method:

1. **The quantum dots are on the outside of the dielectric material**. Infiltration of large qualities of quantum dots causes surface roughness and a reduction of the photonic stop-gap due to the decrease in the refractive index contrast.

2. **The host material exhibits a low refractive index.** Despite attempts to mix the quantum dots directly into the organic photoresist, the refractive index of the material still remains too low to support a full-photonic band-gap.

3. **The infiltration processes is isotropic.** This means that every surface of each structure that is on the substrate will receive, or contain, quantum dots. This limitation renders it impossible to provide selective doping (e.g. individual layers of a 3D PC structure).

Therefore, in order to develop a material that can simultaneously address all of the 3 key drawbacks that are mentioned above, we have developed a gas-phase direct doping (GPDD) technique that is able to dope As_2S_3 photoresist with photoluminescent Er atoms. Using this doping technique, films of Er doped As_2S_3 (Er:As_2S_3), which can act as a photoresist for the 3D DLW can be produced. This chapter provides a description of this technique, and a detailed analysis of the resulting photoluminescence photoresist. The fabrication of optically active 3D PC structures, as well as other photonic structures with interesting optical properties is demonstrated using this photoluminescent photoresist.

5.1.1 Rare-Earth Elements

The term "rare-earth" is usually used to describe the elements that are found in the lanthanide series of the periodic table. However, the term "rare-earth" is a misnomer since most of the elements in this group are present in significant amounts in the

Earths' crust. The term is a relic from its early discovery, when the elements were truly rare due to the difficulty in separating them from each other. A more accurate term for these series of elements should be the "lanthanides", which take its name from the element that begins this group in the periodic table, lanthanum[76].

This lanthanide series begins with the element lanthanum ($Z = 57$) and ends with the elements lutetium ($Z = 71$), there are 15 elements in this series. The electronic configuration of the free atoms in this group generally displays the arrangement of [Xe] $4f^n 5d^0 6s^2$ (where $n = 0$ to 14). The elements of this series are generally found in the +3 oxidation state. The 4f shell can accommodate a total of 14 electrons in total. The occupation begins with cerium ($n = 1$) and continues to fill with 1 electron at a time, until it reaches lutetium which contains 14 electrons.

The lanthanides display a very interesting property in its electronic configuration due to the shielding of the partially filled 4f shell by the electrons on the outer shells. This shielding has the effect that the energy levels of this 4f shell are largely insensitive to the environment that they reside in. Therefore, the crystal-field splitting plays a smaller role on the 4f shell as it is effectively shielded from the effects of the surrounding ligand field. Instead, due to the orbital characteristics of the 4f shell, the dominant interactions causing the splitting of the energy of the shells are mainly due to the spin-orbital coupling interactions. The strong spin-orbital interaction has the most significant effect (energies on the order of 2000 cm^{-1}) compared to crystal-field splitting (energies of 100 cm^{-1}) on the electronic transitions inside the 4f shell.

Since the electronic transitions that occur in the 4f shell only involve a redistribution of the electrons in the f-orbitals, these f-f transitions are parity forbidden. However, these ions still continue to exhibit atomic-like spectra because of a relaxation of the selection rules due to a disruption of the symmetry of the

molecular orbitals. However, the disruption of the symmetry is not due to the usual crystal-field splitting that is prevalent in d-d transition, this is because the ligand effects are shielded from the 4f shells by the electrons from the outer shells as previously mentioned. Instead, it is the spin-orbital coupling that relaxes these selection conditions and allows for the f-f transitions to occur. The consequences of the parity forbidden transition are that the emission colors are less intense and the rare-earth ions possess meta-stable states with long luminescent lifetimes typically in the millisecond range. Furthermore, the line-widths of the emission are very narrow because the electronic states are less perturbed by thermal vibrations and the chelated ligands that surround the rare-earth ions. However, the chelated ligands surrounding the rare-earth ion do contribute a small-degree of crystal-field splitting of the coupled terms into hyperfine states. This splitting is manifested in the appearance of hypersensitive bands in the atomic spectra. This splitting of the atomic levels due to a static electric field is also known as Stark splitting[116,117,118].

A full range of emission wavelengths from the visible region and into the near-infrared can be observed in different rare-earth elements, as one moves across the lanthanide series. The atomic-like energy levels, and hence the spectral position of the emission, of the rare-earth element do not drastically change as they are inserted into a crystalline or amorphous host material. This is once again due to the shielding of the inner f-shell electrons by the outer 6s shells. The oxidation state of the inserted ions continues to be dominated by the +3 state, and these are the most interesting for optical applications because they retain their ability to provide narrow-band luminescence that is comparable to that of the free ion. Due to these unique optical properties, the elements in the lanthanide series are often employed in a wide variety
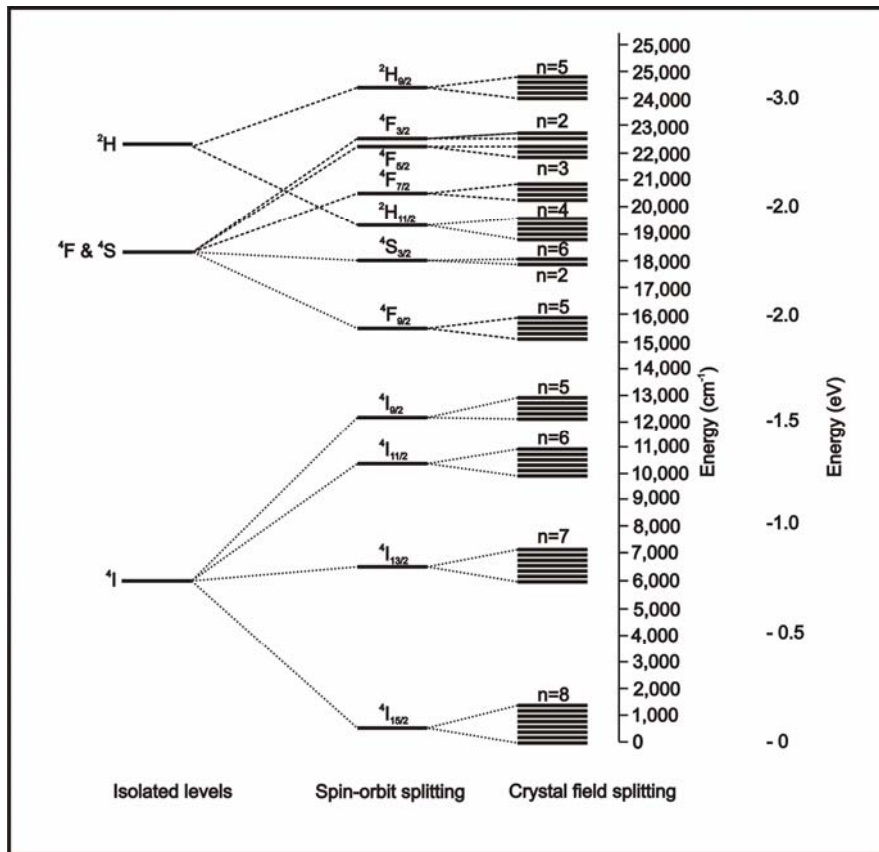
Figure 5.1 The splitting of the erbium atomic levels. The isolated levels of the erbium atom are first split into different manifolds due to the large spin-orbital coupling that is experienced in this atom. The crystal field splitting also plays a small role in the splitting of the coupled terms into hyperfine states due to a static electromagnetic field. This effect is also known as Stark splitting.

of host matrices to provide luminescence materials for the field of opto-electronics. These materials are used in traditional CRT screens as red,green and blue phosphors, as gain media in lasers such as Nd:YAG (**N**eodymium doped **Y**ttrium **Al**uminum **G**arnet), and more recently, in optical fibers for optical telecommunications[118].

From the lanthanides series, the element erbium has emerged as one of the most important rare-earth element for telecommunications. Figure 5.1 shows the electronic energy levels of the trivalent Er ion. Despite the large spin-orbital coupling that is observed in the lanthanides, the term symbols derived using the Russell-Saunders coupling scheme can still be used to as labels because the coupling conditions for

nuclear sub-shells are closer to the Russell-Sanders coupling scheme rather than the j-j coupling scheme, which are used for the analysis of very heavy atoms[117,118].

The Er^{3+} ion contains 11 electrons in its 4f shell. The ground state has the term $^4I_{15/2}$. The electrons from this ground state can be promoted to any one of the higher energy states through the absorption a photon of sufficient energy. The trivalent erbium ion, Er^{3+}, exhibits a strong emission band that is situated around 1535 nm wavelength from the emission of a photon due to the transition of an electron from the $^4I_{13/2}$ meta-stable state to the $^4I_{15/2}$ ground state. The $^4I_{13/2}$ is the meta-stable state that exhibits long luminescent lifetimes enabling this atom to sustain population inversion. Since the Er^{3+} ion can sustain population inversion at telecommunication frequencies, it has been heavily employed for use in devices that operate in the popular "C"-band (1530 nm to 1565 nm wavelength) and "L"-band (1565 to 1625 nm wavelength) of the optical telecommunications spectrum.

One of the most important uses of Er^{3+} is its inclusion into silica to form the erbium doped fiber amplifier (EDFA). The EDFA has become a very important component in optical telecommunications as they are routinely used for signal boosting during long-distance signal transmission to maintain signal quality. The EDFA is particularly attractive because it allows the amplification of an optical signal without the need to first take the optical signal out of the fiber and converting it into an electrical signal before the amplification step, thus enabling a dramatic simplification in the equipment that is used. Secondly, because Er^{3+} ions display photoluminescence covering both the C- and L- bands, it is particularly suitable for high-capacity wavelength-division-multiplexed systems. With reduced deployment complexity and versatility, EDFA's have become an integral part of any existing long-haul optical data carrier network.

Due to its prominence in the telecommunications field, great research effort has been placed on Er doped materials. The host materials for the Er can be crystalline, such as Si, SiC, GaAs, and GaP, or amorphous, such as silica, alumina and in chalcogenide glasses. All of these systems have its advantages as hosts for the Er^{+3} ions. However, we will pay particular attention to the advances of erbium doping in chalcogenide glass hosts because of the interest in these materials in our current work. Chalcogenide hosts such as As_2S_3 are particularly suited as a host for erbium because this material exhibits the properties of possessing very low phonon energies, photosensitivity, and the added benefit that it does not inherently contain any hydroxyl or silicon oxide groups[118,119,120].

Hosts with low-phonon energy hosts are desired for rare-earth ions because multi-phonon relaxation pathways can result in a rapid depopulation of the upper excited state and cause quenching of the photoluminescence. As a rule-of-thumb, the rare-earth photoluminescence will be completely quenched by multi-phonon relaxations if the phonon cut-off energy of the matrix is greater than 25 % of the energy gap between the upper excited state and the lower electronic state of the rare earth ion. When the phonon cut-off energy is 10% to 25 % of the energy gap, the luminescence lifetime will exhibit a temperature dependency. The energy gap of erbium, between the meta-stable $^4I_{13/2}$ level and $^4I_{15/2}$ ground-state level, is approximately 6500 cm^{-1}. The phonon cut-off energy for As_2S_3 is about 400 to 450 cm^{-1}. The phonon energy of As_2S_3 translates to 6.9 % of the energy gap of erbium. Therefore, quenching due to multi-phonon relaxation in As_2S_3 is negligible[118,121].

The inherent photosensitivity and photoresist properties of As_2S_3 are well documented in the literature and throughout this thesis. The advantage of photoresist properties in this material enables simple fabrication of conventional 2D optical
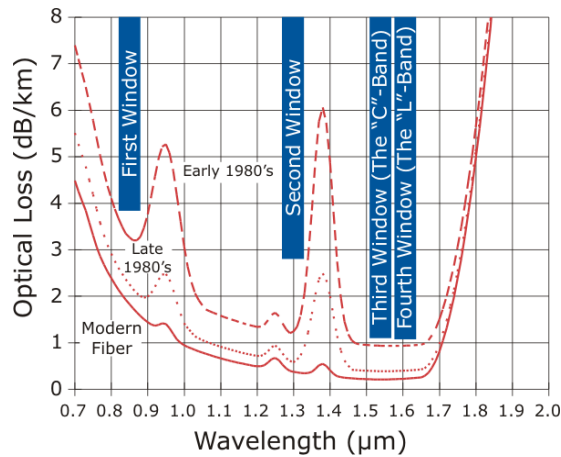
Figure 5.2 A graph of the coverage of the telecommunication wavelength by silica based optical fibers. The entire wavelength region is bound at the lower wavelength limit by the Rayleigh scattering of metal impurities in the fiber, and at the long-wavelength limit by the intrinsic IR absorption of the Si-O bonds. Absorption of the vibration overtones of the hydroxyl species situated at 950 nm, 1240 nm and 1400 nm further sub-divide this wavelength range. In order to circumvent the losses that are introduced by these materials limits, 4 windows where the absorption losses are minimal are introduced. The most common of which are the "C"-band at wavelengths between 1530 nm to 1565 nm, and the "L"-band at wavelengths between 1565 to 1625 nm. Although technological improvements to fiber processing have been able to reduce these intrinsic absorption losses, and slightly widen the windows of operations, these separate windows of operations continue to exist today. (Figure from reference 119.)

devices, such as Bragg gratings and wave-guides, and 3D photonic crystals. This important property provides yet another reason for using chalcogenide glass as the host material for rare-earth ions.

One may have noticed that the telecommunications spectrum is not a continuous spectrum, but it is separated into 2 low-loss windows. The first window is situated between the wavelengths of 1200 nm to 1350 nm, which contains the "O"- band (1260 nm to 1360 nm). The second and third "ultra-low loss" window occurs between the wavelengths of 1450 to 1600 nm, and these are known as the "C"-band (1530 nm to 1565 nm) and "L"-band (1565 to 1625 nm). The reason for this division is because silica, used in the manufacturing of optical glass fibers, intrinsically contains hydroxyl- and Si-O groups, and these functional groups exhibit optical absorption

inside this spectral region. The free-radical and vibration overtones of the hydroxyl-species are situated at 950 nm, 1240 nm, and 1400 nm and the presence of these absorption bands is the reason why the telecommunications spectrum is divided into 2 low-loss windows. The presence of the IR absorption of Si-O species also introduces a band-tail which marks the long-wavelength limit of the second telecommunications window. Furthermore, the presence of impurities also causes Rayleigh scattering which adds to the loss of the fiber and is the limiting factor at the short wavelength transmission limit of the fiber[119]. These consequences on the signal attenuation due to the absorption and loss mechanisms are presented in Figure 5.2.

Although, a decrease in Rayleigh scattering through the reduction of impurities is technically achievable by using highly pure quartz as the precursor material, the presence of hydroxyl- and Si-O groups are intrinsic to silica and cannot be eliminated. Therefore, the added benefit of using chalcogenide based glasses such as As_2S_3 is its absence of the hydroxyl- and Si-O groups. In fact, As_2S_3 is free of absorbers that may cause absorption losses between the wavelengths of 700 nm to 3 μm and is therefore highly transparent at these wavelengths[32]. This suggests that devices fabricated with this material can access the entire telecommunications spectrum from 1200 nm wavelength to 1600 nm wavelength thus enabling access to an extra 100 nm or 25 % more wavelength channels over silica based devices.

5.1.2 Erbium Doped As_2S_3

Having discussed the individual and mutual benefits and advantages of the element Er and As_2S_3 glass, the next step was to find a method to combine the 2 materials together to form a new system with a synergy of both materials. Doping Er into various host materials including As_2S_3 is a well-studied and established

field[122,123,124,125]. However, in most of those works, the interest was to fabricate large pieces of doped glass, usually involving a melt-synthesis technique to incorporate Er into the matrix material. However, like As_2S_3 glasses, Er doped As_2S_3 glasses that were synthesized using the melt-synthesis technique were not suitable for use as a photoresist because they did not possess the correct structure which allowed them to exhibit photo-polymerization.(cf chapter 2). In order to transform $Er:As_2S_3$ into a material that was suitable for use with 3D DLW, one must thermally evaporate this material to generate the species that were needed for photo-polymerization.[iv]

In the simplest case, one would be tempted to simply thermally evaporate $Er:As_2S_3$ itself, since it already contained the necessary elements. However, upon closer examination, one noticed that Er has a drastically different melting point than As_2S_3. This also translates to widely different vapor pressures for the 2 materials. This means that when a piece of $Er:As_2S_3$ glass is thermally evaporated under high-vacuum conditions, most of the Er would remain behind in the source and a majority of As_2S_3 would be collected on the substrate[126].

In order to alleviate the problem associated with the varying temperatures of vaporization, Er must be introduced separately using a co-evaporation technique. In these co-evaporation techniques, the Er used is usually in the form of a binary inorganic compound, such as Er_2S_3[126], or as an organometallic precursor such as a tris-dipivalozylmethanato erbium (III), Er(*thd*)$_3$, complex[127]. Although, doping of As_2S_3 via the use of these erbium derivatives had been successful, each precursor possessed some disadvantages. For Er_2S_3, since it was a very air sensitive compound, special handling precautions must be taken to avoid oxidation. Air sensitivity of the

---

[iv] To maintain stochiometry during deposition, other physical vapor deposition techniques such as ion-sputtering can be used. However, they do not generate the small molecules obtained from the thermal evaporation technique, which were established as being essential for photo-polymerization. (cf. chapter 2). Furthermore, Er can be been introduced via ion implantation in to bulk glass samples[125]. However, photo-polymerization behavior in these samples has not been documented in the literature.

precursor is undesirable from a technological perspective since the equipment must be enclosed in an inert atmosphere to handle this material.   Furthermore, since the oxide and the sulfide have very similar vaporization temperatures, elimination of any oxides before doping using an in-situ vacuum distillation step is not possible. (i.e. to use a heating step to first evaporate away the oxide layer before depositing.)   Another inconvenience for using this material was that a precise control of the stochiometry could not be easily obtained because the incorporation of 2 erbium atoms will also lead to the incorporation of 3 sulfur atoms. This causes an increase in the sulfur fraction in the As_2S_3 thin film and would result in the decrease in the refractive index of the host material[51].

For the organometallic complex Er(*thd*)$_3$, the organic moieties in the complex themselves contained a large amount of carbon and oxygen. Their concentration rose dramatically as the concentration of erbium was increased. The inclusion of oxygen and carbon inside the final material was undesirable as these impurities may contribute to non-radiative defect states and unwanted absorption inside the final material, thus degrading its photoluminescence behavior and optical properties. Since the negative aspects associated with precursor based sources mentioned above were fundamental problems, stringent control of impurities in the final photoresist film was very difficult.   Therefore, a different doping strategy was needed to produce contamination free Er doped As_2S_3 photoresist thin films.

In this work, we demonstrate a gas-phase direct doping technique to enable the doping of elemental erbium directly into As_2S_3. We chose to use pure elemental erbium because of these following advantages:

1.   **Elemental erbium could be separated from its oxide (Er_2O_3) in-situ.**

2.   **The stochiometry could be easily controlled.**

3.   Elemental erbium does not intrinsically contain any carbon.

   Although erbium was also susceptible to oxidation, elemental erbium already had an appreciable vapor pressure of 1x 10^{-6} mbar at 775 ºC, while Er_2O_3 did not begin to exhibit any vapor pressure until 1600 ºC[76,128].   Therefore, the Er was automatically separated from the oxide during the doping process.   Furthermore, since the source only emitted Er atoms, it provided simple control of the stochiometry and did not contribute any carbon contamination to the film.   The use of elemental erbium as the direct source of erbium ion is the reason this doping process described here is called the "gas-phase direct doping" (GPDD) technique.   Each of these factors was critical for producing photoresist films that were essentially free from contamination and contributed towards the fabrication of high-quality 3D structures.   The details of this GPDD technique will be given in the proceeding section.

5.2 Experimental Results and Discussion

5.2.1 Gas-Phase Direct Doping (GPDD) Technique

   As we have mentioned before, the gas-phase direct doping (GPDD) technique presented here used high purity Er metal (99.99%, Alfa Aesar.) as the dopant source. The picture of the evaporation chamber is shown in Figure 2.2.   The doping was carried out using a co-evaporation geometry.   The solid As_2S_3 glass was crushed, placed into an alumina crucible and then inserted into the vertical ovens.   Pure erbium metal was placed directly in the tungsten boat, located in the rear of the evaporation chamber.   The two sources were arranged in co-evaporation geometry, where the 2 vapor cones emanating from their respective thermal sources provided an area of overlap at the substrate.   The substrates were mounted onto a water-cooled, rotating substrate holder situated directly opposite to the sources.   The evaporation of the 2
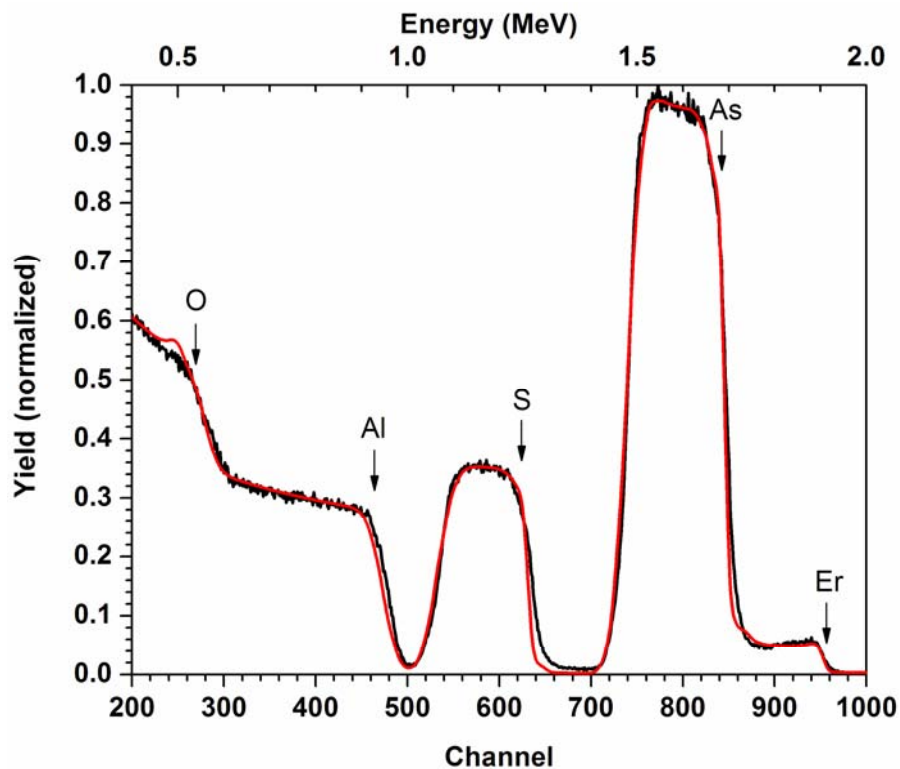
Figure 5.3 RBS experimental spectrum (black curve) and the simulation (red curve) of an Er doped As_2S_3 thin film on a sapphire substrate. The simulation agrees well with the experimental data. The stochiometry of this film is $Er_{0.4}As_{39.4}S_{60.2}$ and represents an erbium concentration of 1.35 wt %.

materials was carried out simultaneously and their rates were monitored by 2 quartz micro-balances mounted in a staggered formation to avoid cross-contamination. The evaporation process took place under high vacuum conditions ($P < 2$ x 10^{-6} mbar). The entire deposition process was fully-automated to ensure reproducibility.

The control in the Er doping concentration was realized by holding the evaporation rate of the As_2S_3 constant while the evaporation rates of the Er source was varied. Depending on the concentration of Er, the color of the as-deposited films ranged from an optically clear and transparent light orange, to a slightly transparent to almost opaque dark red color. All films produced, regardless of concentration, were optically smooth and homogenous. Films with thicknesses from 500 nm to 10 microns were routinely obtained using this process.

5.2.2 Materials Characterization

In this section we provide the chemical and optical characterization of Er: As_2S_3 thin films produced using the GPDD technique. We began with a study of the stochiometry and homogeneity of the thin films using Rutherford back-scattering spectroscopy. Then the molecular species that are present in the thin films were examined using Raman spectroscopy. An investigation of the refractive index of these Er:As_2S_3 thin-films were conducted using thin-film ellipsometery. Finally, the photoluminescent behavior of the material was examined using spatially resolved photoluminescence excitation spectroscopy.

Rutherford Backscattering Spectroscopy

We employed the Rutherford backscattering (RBS) technique to characterize the purity as well as the homogeneity of the Er doped arsenic trisulfide (Er: As_2S_3) thin films that were produced. (The details of the experiment are provided in the experimental section in chapter 7.) The RBS technique provided a non-destructive and quantitative depth-profile analysis which enabled the concentration of different elements contained within the thin film to be studied as a function of depth. The data collected using this method allowed the assessment of the homogeneity of the Er doping as well as the stochiometry of the overall film, with atomic precision.

The samples used for RBS analysis were typically thinner (200 nm) than the samples used for the 3D DLW process (10 to 20 micrometer). The reason for using thinner films was to avoid the increased energy loss associated with the need for a back-scattered helium atom to travel large distances inside a dense sample, containing heavy erbium atoms, before exiting. If the helium ion lost too much energy via secondary collisions its final energy was no longer a true representation of the initial

collision event. This effect is known as straggling. A typical RBS spectrum of a 200 nm thick Er: As_2S_3 film, with a concentration that is typically used for the 3D DLW process, is presented in Figure 5.3.

In the RBS experimental spectrum (black curve), the signal of each element can be clearly resolved in its own channel. The signal beginning at each channel is marked with a black arrow. The channel beginning at 950 is assigned to erbium, 850 assigned to arsenic and 650 assigned to sulfur. The signals beginning at channel 475 and 275 belong to aluminum and oxygen respectively and their presence is solely attributed to the presence of the sapphire substrate. To analyze the data, the erbium, arsenic and sulfur channels in the experimental spectrum were simulated with a box shaped profile (red curve). In the simulation, the overall width of the peak was proportional to the physical thickness of the film, and its area beginning at the high energy edge and ending at the low energy edge, represented the concentration of each element in the film. In order to extract the compositional information from the experimental data, each peak is simulated (red curve) by a summation of thin slices. Physically, the thickness of each thin slice in the simulation represented a planar layer inside the film that was parallel to the substrate. The height of each slice represented the concentration of that element at a particular planar layer. This re-construction of the experimental spectrum using this method allowed cross-sections of the sample to be analyzed, allowing the absolute ratios of the elements to be obtained by comparing the areas under each curve. Figure 5.3 shows that the simulation agrees well with the experimental data. The stochiometry of this film is $Er_{0.4}As_{39.4}S_{60.2}$ and represents an erbium concentration of 1.35 wt %.

From the overall RBS analysis, the width of the boxes representing each of the elements is equal, and the tops of the boxes are flat. This indicated that the film was
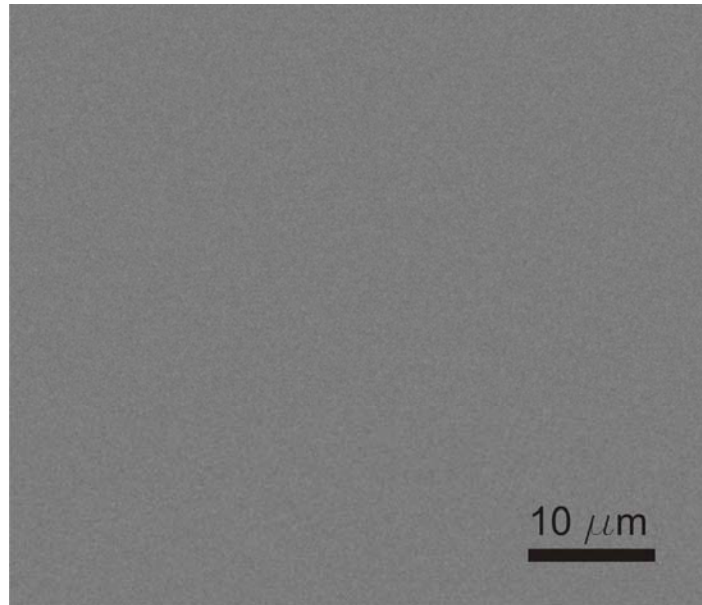
Figure 5.4 The surface of an As_2S_3 photoresist film that has been doped with Er. The SEM image shows that the surface is perfectly smooth and defect free.

homogenously doped as each element present had a constant concentration throughout the thickness of the film. However, the front and trailing edges of the boxes were not sharp, but contained a slight slope. This slight slope was accounted for in the simulation of the experimental spectra as surface roughness. The surfaces were not atomically abrupt at the thin outer layers belonging to the substrate/Er: As_2S_3 and Er: As_2S_3/air interfaces. Since the surface roughness was accounted for in the RBS analysis, the depth of the roughened surfaces could be obtained. The depth of the surface roughness at each interface was about 0.2 $x10^{18}$ atoms/cm^2 thick, or roughly 12.5 % of the thickness of this sample. This percentage seemed quite high, but one should bear in mind that the physical thickness of the RBS sample was only 200 nm thin. When this percentage was translated to a physical thickness value of the sample, the depth of the rough interface layer was only 37.5 nm thin. Since the surface roughness was only confined to the surface, irrespective of the thickness of the sample, in thicker samples such as the 20 micron film routinely used for 3D DLW, the fraction
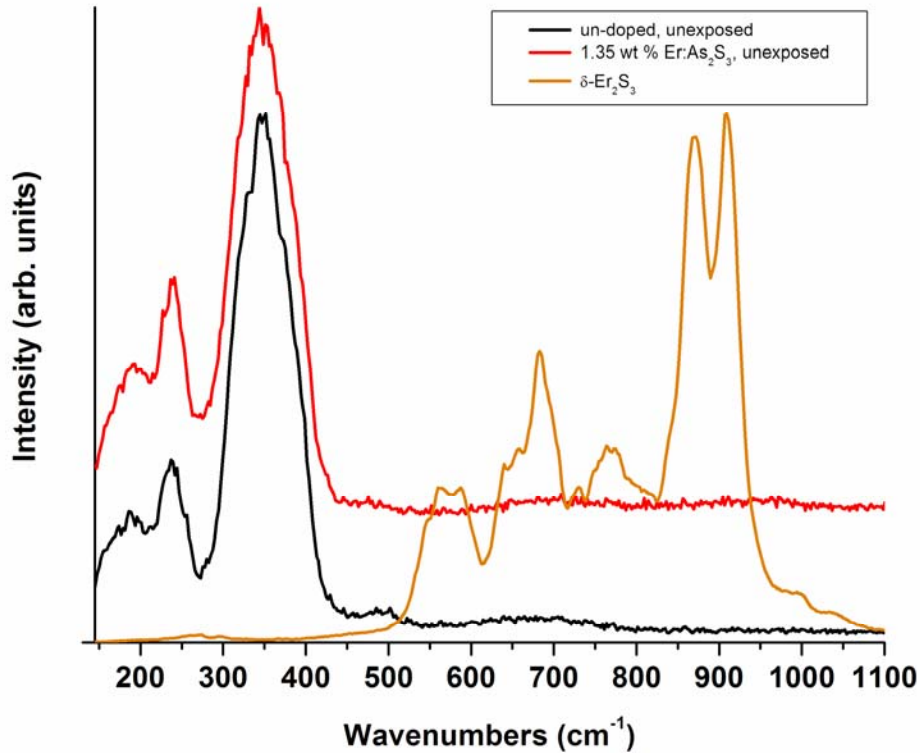
Figure 5.5 Raman spectrums of as-evaporated As_2S_3 that are un-doped (black curve) and doped with 1.35 wt % Er (red curve). The individual spectra are vertically staggered for clear representation of the data. The comparison of these two films show that the Er doped As_2S_3 film retains all the characteristics of the un-doped sample. Here, a Raman spectrum of polycrystalline δ-Er_2S_3 (orange curve) is also provided for comparison. Here we can see that the As_2S_3 film doped with 1.35 wt % does not exhibit any of the characteristic Raman signatures of the polycrystalline sample. This is a good indication that the Er dopant is not agglomerated into Er_2S_3 clusters inside the As_2S_3 host matrix during the evaporation process.

of the surface roughness falls to a negligible value of 0.188 % of the total film thickness.

One explanation for the presence of surface roughness at the substrate/Er:As_2S_3 interface, was the de-wetting that is caused by the mismatch of surface energies between the substrate and the photoresist films. Since the sapphire substrate has a hydrophilic surface whereas the Er: As_2S_3 is hydrophobic, a de-wetting of the Er: As_2S_3 during film growth could occur. The de-wetting caused the formation of droplets resulting in a roughened interface of pits and pores. The roughness did not

propagate into the film because as the film growth continues, the pores became closed and the pits were smoothed out and the overlying film becomes smoother during growth. Furthermore, we examined the Er: As_2S_3/air interface using a SEM. The SEM image showed that the surface was perfectly flat and smooth. (Figure 5.4) Furthermore, when a 43 nm metal layer is deposited on top of this surface (cf. Chapter 5.5.3) this metal layer also did not exhibit any surface roughness. Therefore, the roughness values for the Er:As_2S_3/air interface that were obtained from the simulations should be interpreted with caution considering these further experimental observations.

The most important data from the RBS analysis was the composition and quality of the middle layer, or the core working layer of the photoresist. This 200 nm thick Er: As_2S_3, produced with the same thermal evaporation parameters as films that were suitable for 3D DLW, had a stochiometry of $Er_{0.4}As_{39.4}S_{60.2}$. Notice such an Er: As_2S_3 film fabricated with the GPDD technique did not disturb the stochiometry of As to S but allowed it to be maintained near the optimum ratio of 2 to 3. Furthermore, this analysis also showed that there was no oxygen or carbon inside the as-deposited film. The layer thickness of this film is 1.2×10^{18} atoms/cm^2, with a density of 6.00×10^{22} atoms/cm^3. These RBS results clearly showed that the GPDD technique was able to fabricate contamination free films of controlled stochiometry.

Raman Spectroscopy

Raman spectroscopy was used to investigate the molecular species present in Er:As_2S_3 photoresist films produced using the GPDD technique. Using the same experimental methodology presented in Chapter 2.3, an as-deposited Er:As_2S_3 thin

film with 1.35 wt% Er concentration and an as-deposited As_2S_3 thin film that was un-doped was examined. However, for this experiment a sample of pure polycrystalline δ-Er_2S_3 was also analyzed. The results of these three Raman investigations are shown in Figure 5.5.

The Raman spectra of these two photoresist films are very similar. All the key features that were previously identified in an un-doped, as-deposited As_2S_3 thin film can be found in the sample containing Er doping. (cf. chapter 2) This indicates that the Er doping process did not cause any significant changes to the as-evaporated film during the incorporation of Er. Therefore, it is expected that the Er:As_2S_3 sample would exhibit the required photo-polymerization and etching behaviors of the host material.

Furthermore, the Raman spectrum of the films did not exhibit any diagnostic peaks such as those present in the pure, polycrystalline δ-Er_2S_3 sample. Therefore, this result provides the first suggestion that the GPDD technique did not cause the Er dopant to become agglomerated into small clusters inside the as-deposited photoresist film. This result was important because agglomeration of the Er-S clusters would degrade the resolution of the photoresist, and also create rough surfaces which will cause scattering in the final etched structures.

5.2.3 Optical Characterization

Thin Film Ellipsometery

Thin film ellipsometery was performed on an Er:As_2S_3 sample containing 1.35 wt% Er in both the as-deposited and photo-exposed states. The results of this investigation are presented in Figure 5.6 and compared with results presented in Chapter 2..
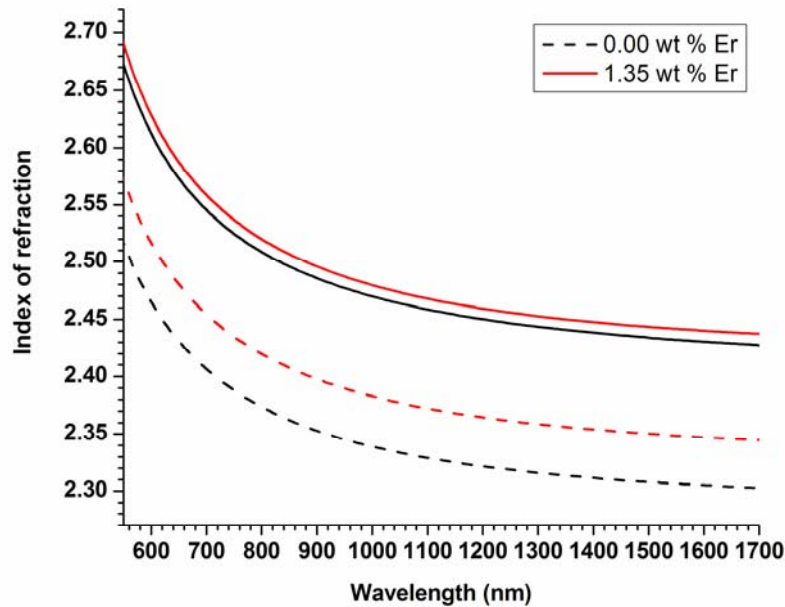
Figure 5.6 The refractive index dispersion curve that is obtained from the thin film ellipsometry of an un-doped sample (black curve) and a 1.35 wt % Er doped sample (red curve), in both the as-deposited and photo-polymerized states.

In figure 5.6, the dispersion curves of the refractive index (n) are displayed. Two important behaviors are worth nothing. First, in the as-deposited films, the doping of Er into the As_2S_3 host caused a 1.97 % increase in the refractive index over that of the un-doped sample. A possible explanation to this result was that since erbium is a heavy element, it caused the As_2S_3 host material to become denser. The increase in the density of the glass caused the phase velocity of light to travel slower inside the glass, and this resulted in an increase in the refractive index. A comparison of the densities of as-deposited films in both the doped and un-doped case, as obtained from the RBS experiments, provided support to this argument. The density of a film of Er: As_2S_3 containing 1.35 wt % Er was 6.00×10^{22} atoms/cm^3 while an un-doped As_2S_3 film had a density of 3.00×10^{22} atoms/cm^3.

The second observation was, after photo-exposure the refractive index of both samples reached a common value near 2.45. An explanation to this observation was

132

not a simple one and could not be explained using only the results of 2 samples. Instead a systematic study of a series of samples was required to provide an explanation for this observation. Such a systematic study is provided in section 5.4 of this thesis. At this point, the only observation is that the photo-darkening effect has taken place and this was a good indication that photo-polymerization has occurred, as these two effects are associated with each other.

The results of the ellipsometery study indicated that an As_2S_3 film that had been doped with 1.35 wt % Er exhibited photo-polymerization behavior and the refractive index at a wavelength of 1550 nm, after polymerization, was 2.45.

Photoluminescence Properties

The Er doped As_2S_3 film was also examined for its photoluminescence (PL) properties. To determine the PL characteristics, the Er:As_2S_3 sample was excited with a 632.8 nm CW He-Ne laser and the photoluminescence collected using a spectrometer that operated between 500 nm to 2.3 micrometers wavelength. The results are displayed in Figure 5.7. The spectra show that there was a single broad photoluminescent feature that is produced. The maximum intensity of this feature was centered at 1536 nm wavelength and exhibited a FWHM of 43 nm. The spectral position of the PL was characteristic of a transition between the $^4I_{13/2}$ and $^4I_{15/2}$ manifolds of the Er^{3+} ion[118]. However, the emission peak was not a sharp line, such as the spectra that is obtained when Er^{3+} is in a crystalline matrix, but was broadened. The broadening of the PL spectrum was due to inhomogeneous line broadening brought about by the low site symmetries of the Er^{3+} ions inside the amorphous As_2S_3 matrix, and from Stark splitting[118,129]. The broadened spectra
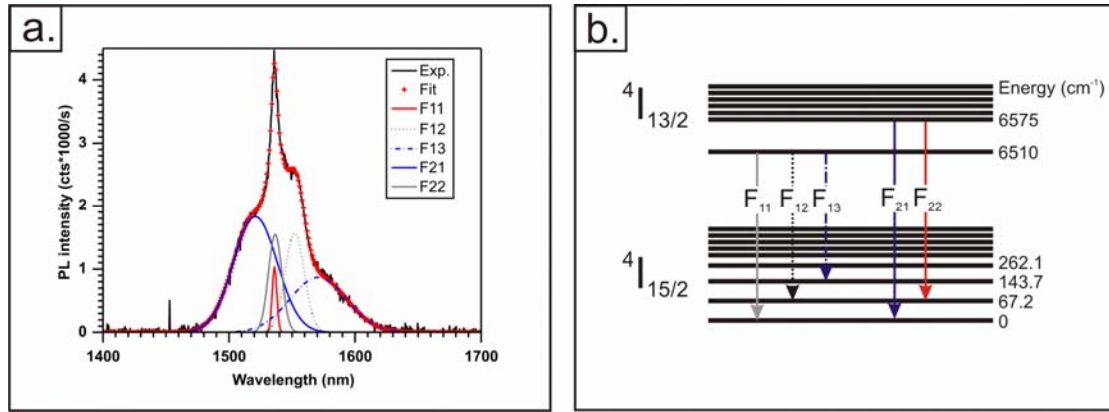
Figure 5.7 a. The PL spectra that is collected from an experiment where an Er: As_2S_3 sample was excited with a He-Ne laser. (Black curve) The fit of the experimental spectra (dotted red curve) using the Stark splitting of the $^4I_{15/2}$ and $^4I_{13/2}$ manifolds (curves under the main spectra) of an Er^{3+} ion in an amorphous matrix, to account for the in-homogenous line broadening. **b.** The Stark levels that are used to account for the in-homogenous line broadening of the spectra in **a**..

(Figure 5.7, left) could be fitted with a model which accounted for the Stark splitting of the $^4I_{15/2}$ and $^4I_{13/2}$ manifolds of an Er^{3+} ion in an amorphous matrix[124,130]. (Figure 5.7, right). Here three levels were taken to account for the $^4I_{15/2}$ level, and two levels were taken to account for the $^4I_{13/2}$ level. It was assumed that the population of the $^4I_{13/2}$ level was thermalized and that the inhomogeneous line broadening was dominant. These assumptions were made to in order to limit the free parameters that were required for the fitting algorithm. (cf. Chapter 7) Furthermore, the PL spectrum that was displayed here does not exhibit any sharp transition peaks, such as those samples where polycrystalline δ-Er_2S_3 had been directly embedded in an As_2S_3 matrix[131]. Therefore, this was another indication that the GPDD technique did not cause Er dopants to become agglomerated into micrometer sized crystals inside the as-deposited photoresist film. Instead the PL spectra indicated that the Er is well dispersed inside the As_2S_3 matrix. This result was important because clustering of the Er^{3+} ions would cause non-radiative relaxations which would cause decreased photoluminescent efficiency and excited state lifetimes.

134

Once the PL behavior of the Er:As$_2$S$_3$ was established, it was necessary to determine the excitation wavelength that excited the Er^{3+} ion most efficiently or to find the excitation resonance. It was important to determine the excitation resonances because if this material is to be used as a laser gain medium, the optimum wavelength that is required to optically excite this material to achieve population inversion must be known. Photoluminescence excitation spectroscopy (PLE) was the analysis technique used to determine these parameters.

The PLE technique enabled the monitoring of the PL intensity generated from the sample, as a function of the pump wavelength. In other words, the technique collects the PL intensity that is generated in a set wavelength range while a laser source excited the sample with different frequencies. These excitation wavelength dependant PL intensity spectra were then plotted in a 2D graph and compared to determine which excitation wavelength caused the maximum PL intensity to be generated.

In the PLE experiment, a 1.35 wt % Er:As$_2$S$_3$ sample was excited using 3 tunable lasers that covered a range from 638 nm to 1000 nm, with resolution of 1 nm. The PL detector was set to monitor the photoluminescent intensity generated between the wavelengths of 1400 nm to 1600 nm, as the PL signal was previously determined to occur within this range. (Experimental details are provided in chapter 7) Using this setup, the excitation resonances of the material was mapped out as a function of the pump wavelength, and the data is displayed in a 2D map in Figure 5.8 a.

The PLE map indicated that there were 3 wavelength regions that exhibited moderate to high PL intensity in the desired PL wavelength range. These 3 wavelength regions corresponded to the 3 excitation resonances of the Er^{3+} ion inside the As$_2$S$_3$ matrix. These excitation resonances occurred at a pump wavelength of 650 nm, 810 nm and 980 nm and corresponded to a transition between the manifolds of
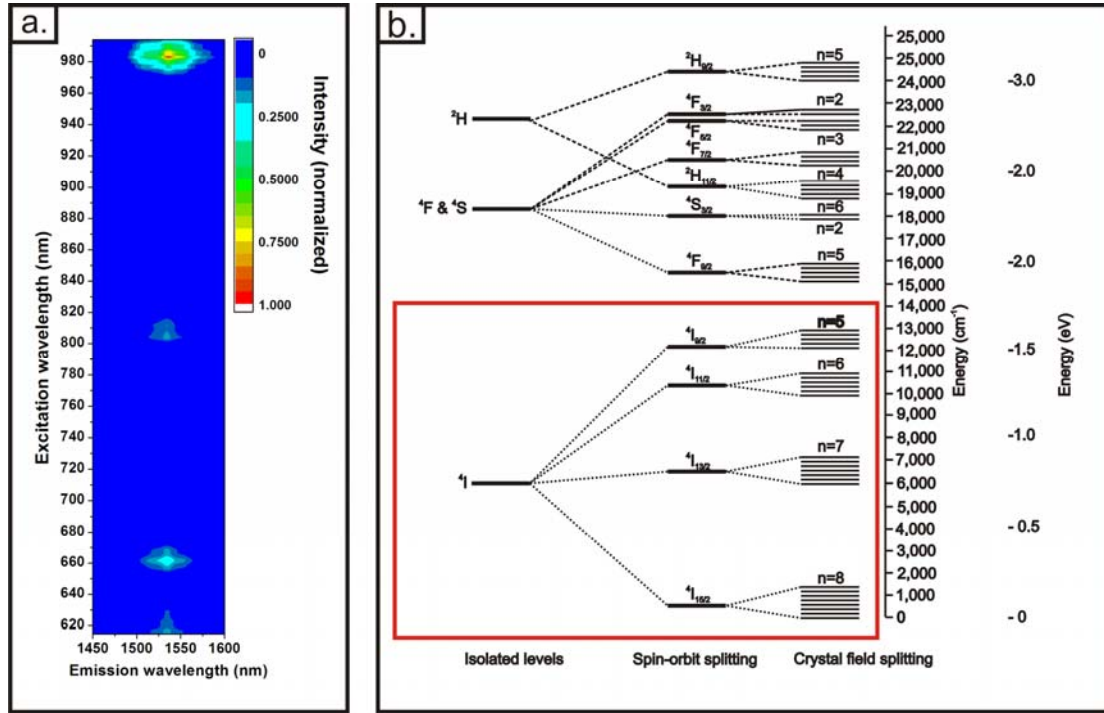
Figure 5.8 a. The PLE spectra of a 1.35 wt % Er doped As_2S_3 film. When the sample was excited using a laser with a wavelength of 980 nm, corresponding to the $^4I_{11/2} \rightarrow {}^4I_{15/2}$ transition, it generated the highest photoluminescent intensity. Other excitation wavelengths that generated PL were 650 nm and 810 nm and correspond to a transition between the manifolds of $^4F_{9/2} \rightarrow {}^4I_{15/2}$, $^4I_{9/2} \rightarrow {}^4I_{15/2}$, and respectively. PL was also collected near the 610 to 615 nm region and this PL was a result of the excitation of the tail states of the As_2S_3 matrix, and the transfer of the energy to the Er^{3+} ions. **b.** A diagram of the isolated energy levels of the Er^{3+} ions as a result of the spin-orbital coupling and Stark splitting (assuming a C_{3v} site symmetery[118]) that is experienced by the Er^{3+} ions in the As_2S_3 matrix. The PLE spectra was able to map out all of the resonances that are present in the ^4I level of the Er^{3+} ion (levels inside the red square).

$^4F_{9/2} \rightarrow {}^4I_{15/2}$, $^4I_{9/2} \rightarrow {}^4I_{15/2}$, and $^4I_{11/2} \rightarrow {}^4I_{15/2}$ respectively. A diagram of the isolated energy levels of the Er^{3+} ion as a result of the spin-orbital coupling and Stark splitting (assuming a C_{3v} site symmetery[118]) that is experienced by the Er^{3+} ions in the As_2S_3 matrix is provided in Figure 5.8 b.

The PLE map also indicated that the excitation wavelength which generated the highest photoluminescence intensity was situated at 980 nm. The maximum emission wavelength was found to be centered at 1536 nm irrespective of the pump wavelength used and was characteristic of an atomic transition from the $^4I_{13/2}$ meta-stable state to
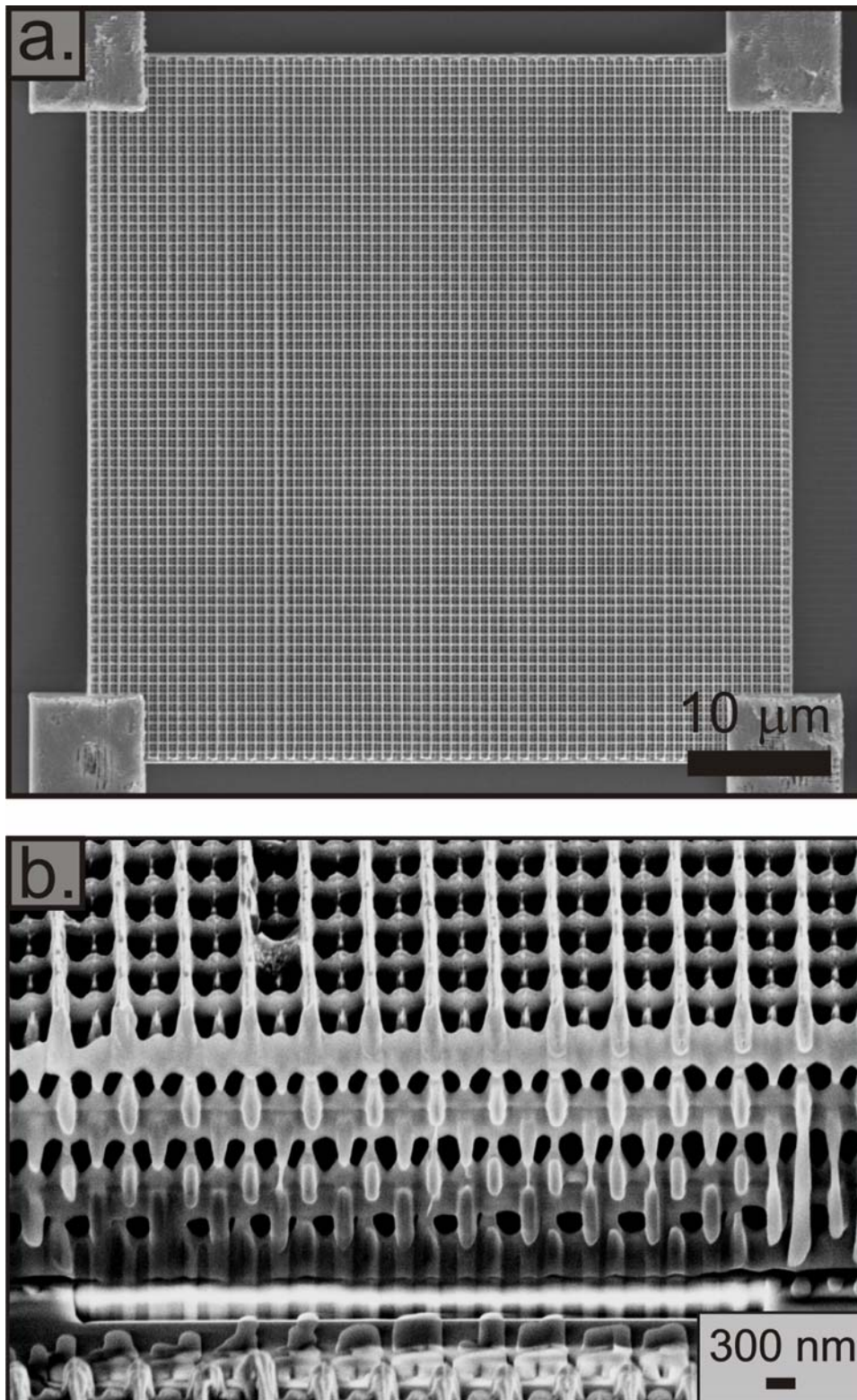
Figure 5.9 SEM images of the woodpile structures fabricated with an Er doped As_2S_3 photoresist film **a.** a low-magnification overview of the top of the woodpile structure. The in-plane rod distance, *a*, of this structure was 700 nm. **b.** Cross-section imaging of the woodpile structure showed that this structure exhibited periodicity in three-dimensions.

the $^4I_{15/2}$ ground state of the Er^{3+} ion[118]. Furthermore, PL was also collected near the wavelength range between 610 to 615 nm. The appearance of PL at this wavelength range was not due to the direct excitation of a transition to a state in the Er^{3+} ions, but was due to the excitation of the tail states of the As_2S_3 glass host[131]. The non-radiative transfer of this energy from the As_2S_3 glass host to the Er^{3+} ions, and the subsequent radiation of this energy by the Er^{3+} ions, caused the observed PL at these short excitation wavelengths.

The results of the PLE investigation indicated that if a 3D PBG structure was fabricated with this material, and excited with, but not exclusively, a 980 nm laser, it will exhibit PL properties at 1536 nm. These were interesting results because this suggested that by carefully designing 3D PBG structures, one maybe able to precisely tune the dispersion characteristics so as to enhance both the absorption of the excitation laser and the emission wavelength simultaneously. This material may provide a new avenue for creating very efficient 3D PBG based lasers[132].

5.3 Photoresist Behavior of Erbium Doped As_2S_3 Films

As a proof-of-concept demonstration that Er doped As_2S_3 films, produced using the GPDD technique, could be used as a photoresist for 3D DLW and be etched with the highly selective etchant *N*-4-methoxybnezyl-pyren-1-yl-amine, we fabricated a 3D woodpile PC structure by 3D DLW into this material. The woodpile PC structure fabricated here had an in-plane rod-distance, $a = 700$ nm, and a lattice constant $c = 989$ nm. SEM images of this structure are shown in Figure 5.9. The overall structure had a footprint of 50μm x 50μm and consisted of 12 layers. The 3D structures fabricated here exhibited the same high-quality features that were present in the un-doped As_2S_3 films. Most notably, the registry of the rods in the plane were perfectly
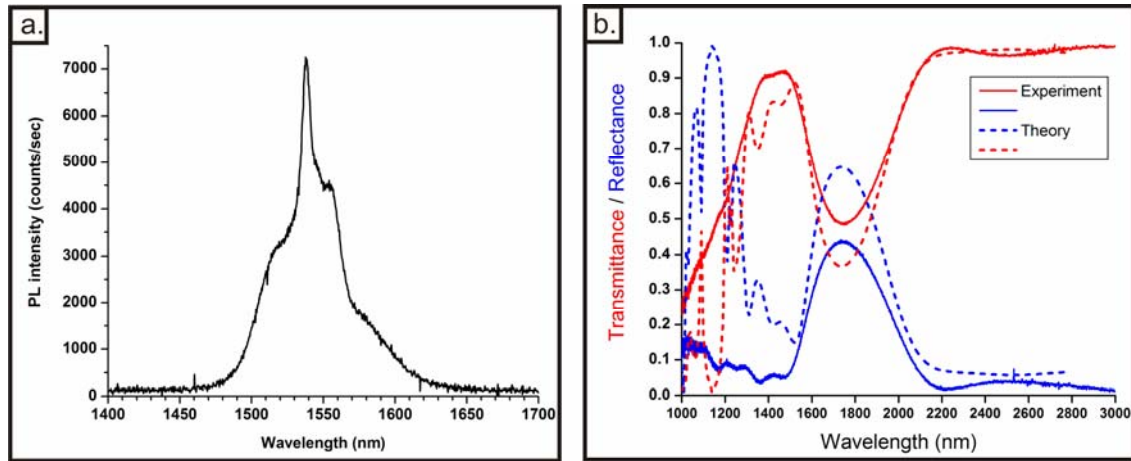
Figure 5.10 a. Photoluminescence that was collected from the woodpile PC structure shown in Figure 5.9. The photoluminescence collected here has a centre frequency of 1535 nm and a line-shape that is identical to photoluminescence of an unstructured Er:As_2S_3 film. (Figure 5.7) **b.** The transmittance and reflectance spectrum obtained from the woodpile structure that is shown in Figure 5.9. The solid lines were the spectrum collected from the experiment, and the dotted lines were the simulations of the structure calculated by scattering-matrix technique using the structural parameters obtained from the SEM image.

aligned and evenly spaced. A cross-section of the structure revealed that it exhibited periodicity in all spatial three-dimensions.

Furthermore, the photoluminescence behavior of this material was examined with the same photoluminescence setup used to measure the photoluminescence behavior of the Er doped As_2S_3 thin films. The photoluminescence that was collected from this sample is shown in Figure 5.9. When the photoluminescence spectrum generated from the 3D PC sample was compared with the photoluminescence of an unstructured Er doped As_2S_3 thin film, it was evident that the PL line-shapes of the 2 spectra were virtually identical. This observation provided experimental evidence that Er doped As_2S_3 could indeed be used as a photoresist for the fabrication of 3D PC structures.

However, during further optical characterization of the transmittance and reflectance properties of the 3D PC structure, it was discovered that the position of the photonic gap deviated greatly from the designed specification. The intended design

139

called for the placement of the full-photonic band-gap at a wavelength of 1550 nm, near the centre frequency of the erbium photoluminescence emission. The spectrum that was collected from the physical sample showed that a spectral feature from the 3D PC structure was located at the wavelength of 1.73 μm. A closer inspection of the cross-section of this 3D PC structure using a FIB and SEM indicated that the aspect ratios of the rods were closer to 3 to 1 instead of the designed aspect ratio of 2.25 to 1. (Fig 5.9, bottom) The elongation of the individual rod destroyed the symmetry of the structure and had the effect of closing the full-photonic band-gap of the structure. (See gap map in Figure 3.9) Furthermore, the increase in the filling fraction of the 3D structure resulted in the red-shifting of the spectral feature.

Scattering-matrix calculations were performed using the lattice parameters and the elongated aspect ratios, as was obtained from the SEM images, confirmed this observation. (Fig 5.10, b) Therefore, the 3D PC produced here only exhibited a stop-band and not a full-photonic band-gap. Further work on the 3D DLW setup to find a viable method for correcting the spherical aberrations is necessary before the 3D PC structures that are produced can attain the desired aspect ratio that is necessary to provide a full-PBG in these woodpile PC structures. (cf. chapter 3) Despite a lack of full functionality for this structure, the ability to use 3D DLW to fabricate a 3D PC using Er doped As_2S_3, served to demonstrate the viability to use this doped material as a photoluminescent photoresist.

Another desirable property of the GPDD technique is it ability to aid in the fabrication of 3D structures that contained spatially selective photoluminescence. In order to fabricate a 3D structure where spatially localized photoluminescence could be easily demonstrated, a tri-layer photoresist stack was first prepared using the GPDD technique by sequentially evaporating a 140 nm thin, 1.35 wt % Er doped
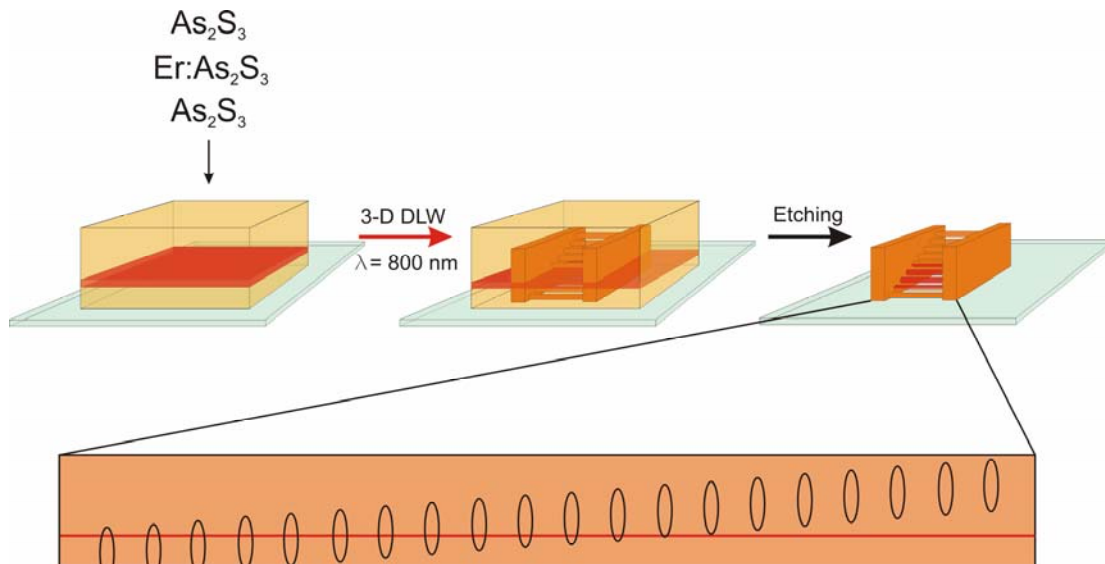
Figure 5.11 A schematic of the steps leading to the fabrication of a step-ladder structure which is used to demonstrate spatially selective photoluminescence.

layer between two un-doped As_2S_3 layers.

Then, 3D DLW was used to photo-pattern a 3D step-ladder structure consisting of bars that were vertically staggered by 200 nm and laterally separated by 5 micrometers into this tri-layer photoresist stack. The design of this 3D structure allows open visual access to the interior of the structure. This provides an unobstructed view of the Er doping layer, enabling a clear systematic analysis of its progression and spatially selective inclusion. After the photo-patterning process, the photoresist was developed using the highly-selective wet-etchant containing the molecule *N*-4-methoxybenzyl-pyren-1-yl-amine. (c.f. chapter 4) A schematic of this process is shown in Figure 5.11.

SEM images of this 3D structure are shown in Figure 5.12. One of the supporting walls of the step ladder structure has been removed via focused ion beam milling (FIB) to allow for a more detailed view of the progression of the Er doped layer through the individual bars inside the structure. The thin Er doped layer can be seen
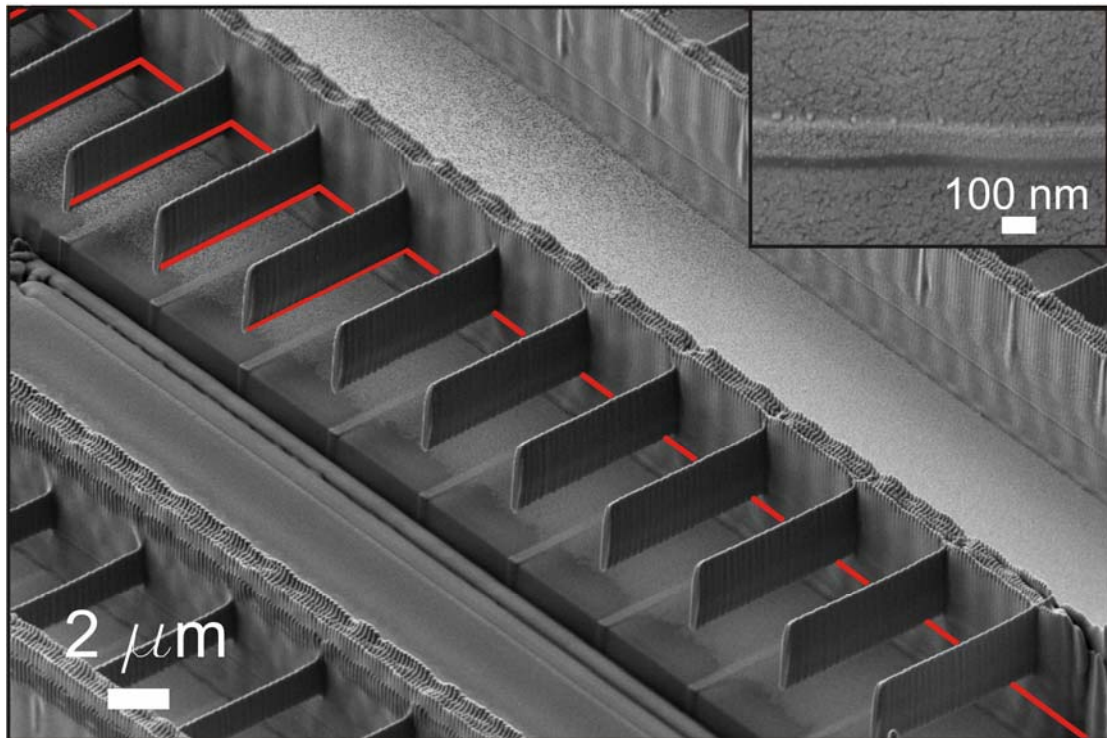
Figure 5.12 SEM image of the step-ladder structure with one of the supporting walls removed via FIB milling. The position of the Er doped layer is highlighted with a red line as a guide to the eye. The bars are systematically shifted vertically in 200 nm steps relative to the doping layer, starting from the substrate (top left side of the SEM image). High magnification SEM imaging of the Er:AS_2S_3 layer (inset) shows that it has a thickness of 139 nm (this value takes into account a sample stage tilt of 54º).

in the image as the thin straight line (highlighted in red) which conforms to the walls of the structure and traverses through the individual bars. As each bar is moved vertically, some of the bars intersect the Er doped layer and Er is incorporated into its structure, while bars that lie above the doped layer contain no Er doping. Careful examination of the SEM images in Figure 5.12 provides direct visual evidence that the Er doped layer is only incorporated into the individual bars intersecting this doping layer but not in the bars above. The inset image in Figure 5.12 shows a high magnification SEM image of the Er doped As_2S_3 layer which runs parallel to the substrate and is measured to be 139 nm thick.

To examine the photoluminescence behavior of this 3D structure, we have employed a spatially resolved confocal photoluminescence scanning technique to

image each bar of the step-ladder structure individually. An excitation laser tuned to the wavelength of 980 nm is focused using a microscope objective into a focal spot on the order of 500 nm. The photoluminescence between the wavelengths of 1475 nm to 1600 nm that was generated from the structure was collected thought the same objective, detected using an InGaAs detector array, and the intensity integrated. The spatially resolved imaging was performed in both a line-scanning mode and 2D imaging mode. A schematic of the spatially resolved confocal PL imaging technique is shown in Figure 5.13.

In the line scanning mode, the focal spot of the microscope objective is scanned through the entire structure at 200 nm steps, in a single straight line bisecting the centre of the bars. The lower image in Figure 5.13 a, is a plot of the line-scan recorded as the integrated photoluminescence intensity collected at each position of the structure. To interpret the collected line-scan, a simple geometric model of the bar, based on the SEM observations from each individual bar in the structure, is presented in Figure 5.13 b to aid in the analysis.

The geometric model of the progression of the Er doped layer inside bars positioned at different heights predicts that strong photoluminescence signals should only be collected from bars that contain the Er doped layer, starting from the first bar positioned at 5 μm to the bar at 65 μm. All subsequent bars should not exhibit any photoluminescence signals as they lie above the doped layer. Furthermore, since the volume of the Er doped layer changes as it moves through the profile of the bar, the intensity should also vary between them. These predictions are clearly observed in the measured line scan Figure 5.13a. In the line scan, strong photoluminescence is only collected in the first 13 bars, positioned at 5 μm to 65 μm. Beyond these positions of the bars which do not contain the Er doping layer, dips in the collected

143
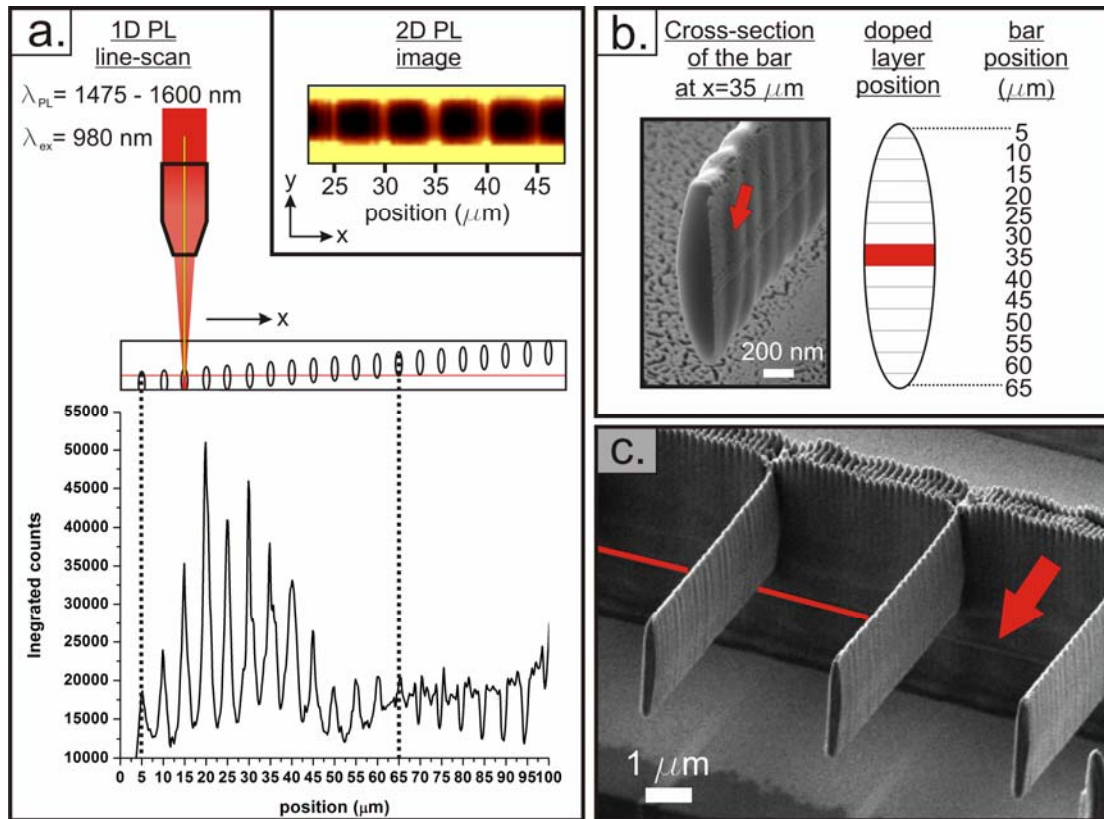
Figure 5.13 a. A schematic of the spatially resolved confocal PL imaging technique and the results of the 1-D line-scan mode (bottom) and 2D imaging mode (inset). **b.** A representative cross-section SEM image of the bars (left) that were examined to construct a model (centre) used to show the progression of the Er doping layer in the bars situated between at the positions between 5 μm and 65 μm of the step-ladder structure (right). **c.** SEM images of bars positioned above the erbium doping layer (highlighted in red). Part of the highlighting is removed to show actual Er:As$_2$S$_3$ layer (indicated with a red-arrow).

background photoluminescence indicate blocking of the collection through the microscope objective by these bars positioned between 70 to 100 μm,. In Figure 5.13 c, SEM images of the bars at positions from 90 μm to 100 μm clearly confirm that they do not interest the Er doping layer and therefore no Er is incorporated in its structure.

In the imaging mode, the focal spot of the detection apparatus is scanned through part of the 3D structure to excite and collect any photoluminescence that is emitted from the features situated between 22.5 μm to 47.5 μm. The photoluminescence

intensity collected from this spatially resolved scan is used to construct a two-dimensional image of the 3D structure, which is presented in the upper right corner of Figure 5.13 a. This image indicates that photoluminescence is confined to the individual bars as well as in the bracing wall of the structure, since both of these parts of the structure contain the erbium doping layer. This photoluminescence image conforms to the analysis of the SEM image in Figure 5.12, and demonstrates that photoluminescence is observed wherever the Er doped layer is present.

These results demonstrate that spatially selective photoluminescence at the important telecommunication wavelength of 1.5 μm can be achieved directly in a 3D nanostructure using Er: As_2S_3 photoresist prepared by GPDD and 3D DLW. Furthermore, these results provide three important structural aspects of this photoresist that is worth highlighting. First, the surfaces of the individual bars remain very smooth after etching, therefore and light-scattering due to surface roughness in a fabricated photonic structure is prevented[133]. Second, since the photoluminescent species are embedded inside the bars, the doping process does not alter the dielectric volume filling fraction of the final structure from its intended design. Third, the lateral resolution of the bar produced here is on the order of 180 nm, which is the same resolution that is obtained when un-doped As_2S_3 is used as the photoresist material, therefore the resolution of As_2S_3 is not altered due to the Er doping process[18].

These material properties of Er:As_2S_3 present obvious advantages over current schemes used to provide photoluminescence in 3D PC fabricated with organic photopolymers. In fact, since the GPDD technique allows for the position and thickness of the doped layer to be precisely tuned, complex 3D PC structures with multi-level designs schemes can also be implemented.[41]

145

5.4 Maximum Doping Limit

Throughout this chapter, an Er: As_2S_3 film, with an Er concentration 1.35 wt %, was demonstrated to possess suitable chemical and optical properties for the fabrication of various 3D structures. However, an investigation as to whether the concentration of Er could be increased to a higher level was interesting, since at a first approximation, a higher Er concentration would translate to stronger photoluminescence due to an increase in the amount of emitting centres.

However, as the Er concentration was increased beyond 1.35 wt %, while the film continued to exhibit photo-polymerization, it could no longer be etched by the standard etchant N-4-methoxybenzyl-pyren-1-ylamine. In fact, none of the other less selective amines were able to induce any reaction with a film that was doped beyond 1.35 wt % Er. Therefore, there was an apparent Er doping limit present in this photoresist system.

In order to understand the reason behind this apparent doping limit, a systematic study was conducted on a series of Er doped As_2S_3 films which contained different concentrations of Er. The Er concentration chosen for this study contained an Er concentration of 0.00 wt % (un-doped), 0.41 wt%, 1.35 wt %, 4.12 wt %, and 11.58 wt %. The concentrations of each sample were checked using EDX spectroscopy, except for the 1.35 wt % sample which was previously examined using the RBS technique.

Thin-Film Ellipsometery

The technique of thin-film ellipsometery was used to investigate this series of Er: As_2S_3 film to characterize their optical behavior. The data for this discussion is presented in Figure 5.14 and 5.15.

In Figure 5.14 the optical band-gaps of these films were compared. The overall trend of the optical band-gap energies of the as-deposited sample began to decrease with increasing Er doping concentration. The band-gap energy began at 2.36 eV for the un-doped sample and reduced linearly to a value of 2.23 eV for the sample doped with 11.85 wt % Er.

In order to attempt to understand the band-gap behavior and its relation to the Er doping, the bonding arrangement of the species inside Er: As_2S_3 should be examined. More specifically, it is the bonding arrangement of the doped metal atoms, as well as the role of the lone pair of p-orbital electrons present on the sulfur atom as they reside inside the As_2S_3 matrix, which should be closely examined. The band-gap results observed here can be rationalized through the use of the valence-alteration pair model (VAP) that was established in chapter 1. Just as a reminder, the VAP theory established that the lone pairs of p-orbital electrons present on the sulfur atom are located near the top of the valence band[77,79]. The presence of the lone pair of electrons on the sulfur atom was very important for the creation of the VAP, which are responsible for the observed photo-induced effects such as photo-polymerization[75,81]. These lone-pairs of electrons on the sulfur were observed to be scavenged when metals atoms such as copper, zinc or gallium were introduced into the matrix to form metal-sulfur bonds[81,134,135,136]. These newly formed metal-sulfur bonds in turn generated new states deeper into the optical band-gap and as a result caused its reduction. In general, it was documented that the magnitude of the reduction of the optical band-gap of the material was proportional to an increase in the metal doping concentration[135,137].

Through the ellipsometery method that was performed in the current study of Er:As_2S_3, a general reduction in the width of the optical band-gap of the as-deposited

material, as the Er concentration increased, was also observed. (Figure 5.14) In the as-deposited state, as soon as Er was introduced into the As_2S_3 an immediate reduction of the optical band-gap was observed, and it continued to narrow as the concentration of Er was increased. This analysis showed that new states were being created inside the optical band-gap upon Er doping, thus causing the observed reduction in the energy of the optical band-gap. A key point in this analysis was that these shifts in the optical band-gap already occurred in the as-deposited film as they were doped with Er. This strongly indicates that during the gas-phase direct doping process, a chemical reaction had already taken place between Er and S during the thin film formation process. This reaction was likely due to the thermal reaction between the hot vapors of Er atoms (> 960 ºC) as they came into contact with the arsenic-sulfide clusters in the gas-phase, or upon their condensation on the substrate[138]. Therefore, according to the VAP theory, since this process removed states near the valence band edge (lone pairs of electrons on the p-orbital of the sulfur), and created states that were deeper into the optical band-gap, the energy of the optical band-gap was expected to be reduced[77,79].

Experimentally, a reduction or loss, in photosensitivity to various photo-induced effects was observed in the As_2S_3 glass systems when elements such as Ag, Zn or Cu were introduced to the glass system. The reduction, or cessation of the photo-induced refractive index change was attributed to the removal of the lone pairs of p electrons in the sulfur atom though their bonding with the metals that were introduced[134,135,136]. Therefore, since the magnitude of the change in the index of refraction is related to the removal of the lone pairs of electrons on the sulfur atom, we can compare the magnitude of refractive index change upon doping of As_2S_3 films with different Er concentration. This comparison would provide further evidence that chemical
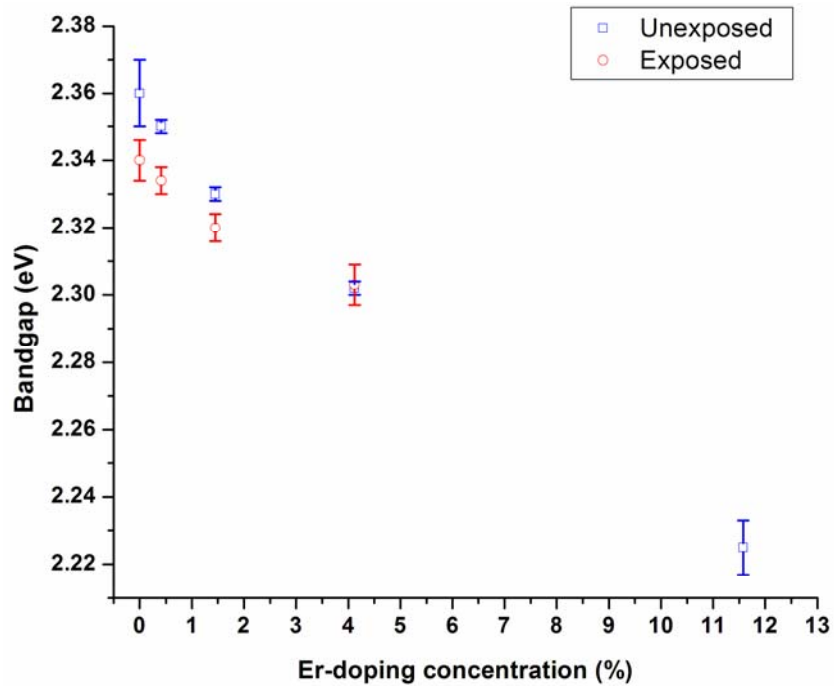
Figure 5.14 Optical band-gap of Er doped As_2S_3 films with increasing concentration of Er.

reactions between the Er and the sulfur lone pair have already taken place upon Er doping in the GPDD technique. The results of such a comparison are provided in Figure 5.15. On the left side of this figure is a plot of the percent change in the refractive index as a function of Er concentration. The un-doped films exhibited the largest magnitude of refractive index change upon photo-exposure ($\Delta n = 5.46\%$), and the addition of Er as the dopant had the effect of lowering the magnitude of this change. As the amount of Er was increased, the magnitude of the refractive index change, at 1550 nm wavelength, decreased to 3.96 % in the case for a 1.35 wt % Er doped film, to a value of 2.14 % in the film that was doped with 11.58 wt % Er. The magnitude of the decrease seems to reach a level of saturation at 11.58 wt % Er doping. The observed suppression of the photosensitivity upon Er doping was another indication that a reaction between the Er and the sulfur lone pairs already occurred during the Er doping process.

Another photo-induced effect that became affected as the Er concentration was increased, was the decrease in the magnitude of the band-gap change upon photo-exposure. (Figure 5.14) This decrease in the magnitude of the change in the energy gap was likely due to the reduction of the amount of sulfur lone pairs near the valence band edge that were available for As-S bond formation, as they have already reacted with the Er atoms during the deposition process[138].

In the various studies of metal doping in As_2S_3, the onset of a reduction in photosensitivity was observed to begin at a metal concentration limit near 1 at. % $Cu^{[81,135, 136]}$. Below this limit, metals dopants such as copper, was found to be in a low enough concentration that it did not disturb the overall photo-induced behavior of the bulk material. Although the experimentally observed doping limit of 0.4 at. % Er (1.35 wt % Er) in this As_2S_3 doping system was below the general limit observed using other metal dopants, one should point out that the doping limitation that is imposed here was not the onset of the reduction of the photo-induced processes. Instead, the doping limit here was the point when the highly selective etchant no longer causes etching. This is a key point, because for the purpose of using Er: As_2S_3 for 3D DLW, this material must function as a photoresist. The highly-selective etchant, containing *N*-4-methoxybenzyl-pyren-1-ylamine, is very sensitive to the presence of polymerized areas, and acts to preserve these areas, while removing the un-polymerized molecular species[70]. The analysis, based on the inspection of the relation between the Er concentration and its effect on the optical bandgap and index of refraction behavior, suggest that the addition of more than 1.35 wt % of Er metal, via the GPDD process, caused the formation of a large number of Er-S bonds, which has the same effect as photo-polymerization. Therefore, since the etchant will also act to preserve these
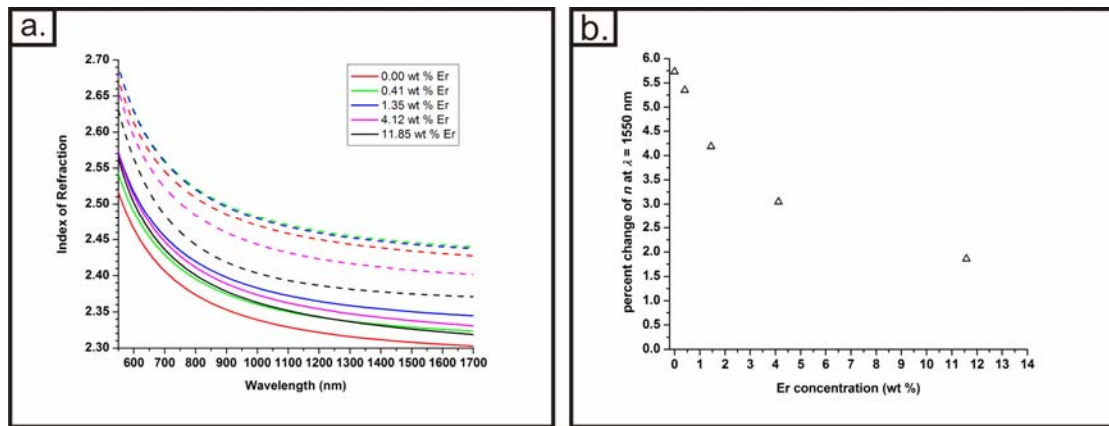
Figure 5.15 a. The refractive index dispersion curves for films doped with increasing concentrations of Er. **b.** The percentage change in the refractive index between an as-deposited films and a photo-exposed film, at 1550 nm wavelength, as a function of Er concentration.

areas, the overall effect was that no etching was observed where the Er concentration was increased above 0.4 at. % .

It is worthwhile to make two very important comments regarding the above analysis. The first comment is that the maximum doping limit that was determined here only applies to the photoresist system where the etchant containing *N*-4-methoxybenzyl-pyren-1-ylamine was used to etch the unexposed areas. In the case where a stronger, but less selective, etchant is used[93], (e.g aqueous-based etchant that are described in the literature) this doping limit may no longer apply. The second comment is that despite films doped with Er at concentrations higher than 1.35 wt % were unsuitable for use as a photoresist where the highly selective amine was use as the etchant, they did never-the-less continue to display photo-polymerization behavior and exhibit photoluminescence. It is important to make these two points clear because we do not want to mislead the reader by presenting the maximum doping limit that was determined here as an absolute limit which is applicable to all other etching systems currently documented in the literature.

At this point the two observations that were posed in chapter 5.2.3 should be revisited. The first observation was that in the as-deposited state, the refractive index of the film doped with 1.35 wt % Er was higher than the un-doped material. From the investigations presented above, it became evident that the Er enters the host as Er^{3+} ions. The Er^{3+} ions are large and polarizable ions that interacted strongly with the oscillating fields of the incident electromagnetic radiation. As a result, they slowed the phase velocity of light, and caused an increase in the refractive index. (This is very much like adding Pb^{2+} ions into regular silica glass to make lead-glass, which has a higher refractive index than silica[139].) The increase in the refractive index, due to an increase in the density, was the only factor that was previously considered because it was assumed there that the Er was present as the element only and not oxidized. In our system, the reaction of Er to form the Er^{+3} ions as it is being deposited from the gas-phase was not clear until the detailed ellipsometry investigation were conducted.

The second observation was that after photo-exposure, the film doped with 1.35 wt % Er had the same refractive index as an un-doped film after photo-polymerization, despite having a dissimilar refractive index in the as-deposited state. Again, from the above analysis, one possible explanation was that although the film doped with 1.35 wt % Er exhibited some different behaviors compared to an un-doped film, its properties had not deviated very far from the As_2S_3 host. The concentration of As-As, S-S and As-S bonds were still in majority over Er-S bonds. Therefore, when this film was polymerized, the majority of the bonds that were formed were As-S bonds. Similar observations from Cu doping experiments supported this argument[136]. Since an increase in the refractive index was also attributed to the increase in the coordination number of As and S (c.f. chapter 2), photo-polymerization behavior

retained the character of the host material and exhibited nearly the same refractive index of 2.44. The difference in the refractive index between the 2 films after photo-polymerization was very small and was only about 0.37 %, which was within the experimental error of the experiment itself.

Raman Spectroscopy

In order to further investigate the types of bonds that were formed upon Er inclusion using the GPDD technique, we used the Raman spectroscopy to examine the same series of unexposed Er:As_2S_3 films that were used in the ellipsometery investigation. The results of the serial Raman investigation are shown in Figure 5.16.

A careful inspection of the spectral features of the spectra indicated that upon increasing the Er concentration, the S-S vibration at 493 cm^{-1}, which belonged to the S_8 molecule, began to decrease, until this signal completely disappeared at the doping concentration of 11.58 wt %. Furthermore, the vibrations of S-S species at 187 cm^{-1} also began to disappear and merge with the peak at 226 cm^{-1} attributed to the As-S bonds of As_4S_4 molecules. At this high doping concentration, the Raman spectra were comparable to a photo-exposed film (Figure 5.14, top), where the individual molecules of the thin films were cross-linked together[67]. This type of behavior was previously observed in studies where As_2S_3 and its cogener As_2Se_3 were doped with different metals such as Ag, Dy, Sm, and Mn[140,141,142]. Furthermore, in the etching studies that were conducted here in this work (c.f. chapter 4), it was shown that for the etching with an amine to proceed, it was necessary for free molecular species, such as S_8, As_4S_4 and As_4S_6, to be present[54,70,92,93]. Therefore, the Raman spectroscopic investigation provided strong evidence that high Er doping had the same effect as photo-polymerization of the as-deposited thin films. This observation served to
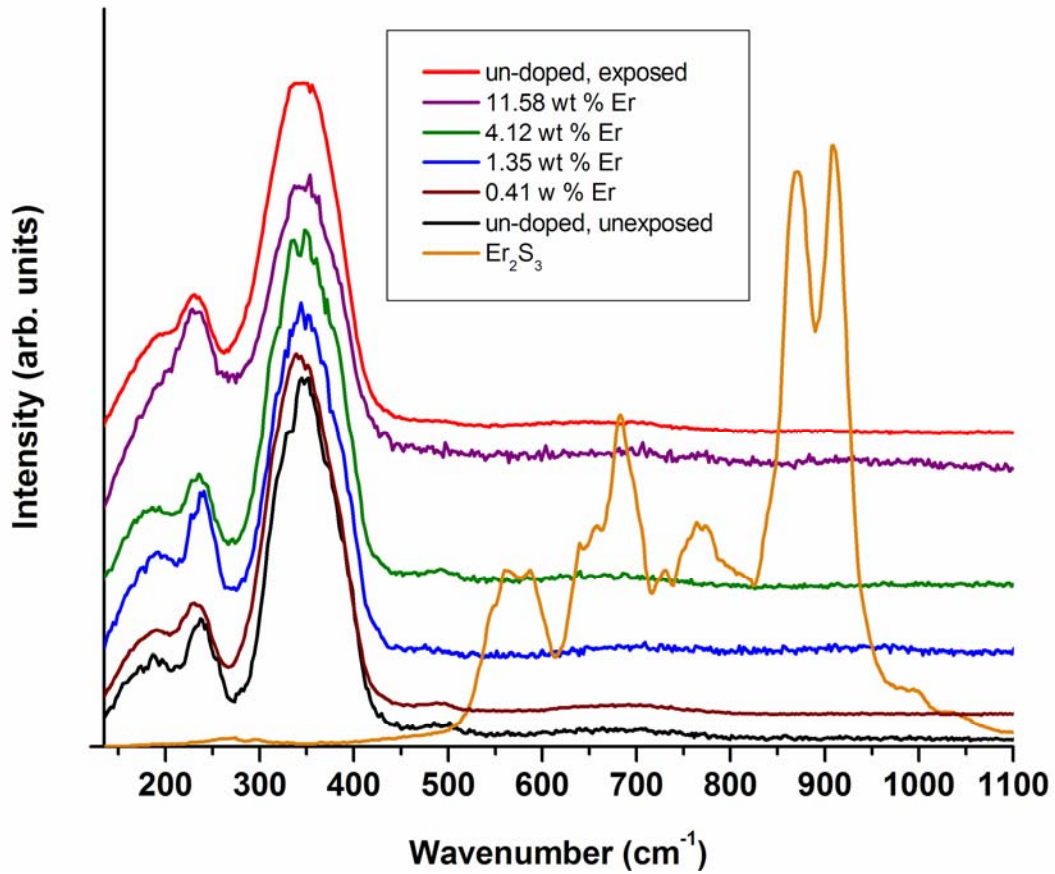
Figure 5.16 Raman spectrum of Er doped As_2S_3 films that contain different Er concentrations. The individual spectra are vertically staggered for clear representation of the data. A Raman spectrum of polycrystalline δ-Er_2S_3 is also overlaid here to show that the Er has not agglomerated into small clusters.

explain the loss in the ability for etching in both photo-polymerized films and heavily Er doped films.

Furthermore, Er doped thin films and a pure, polycrystalline δ-Er_2S_3 sample were also compared in this Raman analysis. This comparison showed that even at high Er concentrations, the doped thin films did not exhibit any characteristically sharp Raman peaks of the pure, polycrystalline δ-Er_2S_3 sample. Therefore, this strongly indicated that small crystals did not appear inside the as-deposited photoresist film at higher Er concentrations. This result suggested that for applications where etching

154

was not necessary, higher Er concentrations could be employed without any significant clustering effects being observed.

Extended X-ray Absorption Fine-Structure

Although the loss of the free sulfur species could be attributed to the addition of the Er dopant, the actual bonding to the Er atoms in the matrix remained unclear. In previous works regarding Er doping, it was speculated that the Er atom, when it is situated inside the As_2S_3, was in the 3+ oxidation state and is coordinated by 6 sulfur atoms in an octahedral geometry[124]. However from single crystal studies of various Er(III) organometallic complexes, the Er(III) atoms were usually found to be coordinated by 7 nearest neighbors, arranged in a trigonal prismatic geometry[143]. Furthermore, in a δ-Er_2S_3 single crystal, the Er(III) ions were found to be coordinated by both 6 and 7 sulfur atoms[144]. An understanding of the bonding of the Er atoms in the current photoresist system would serve as an aid to gain some insight into possible ways to improve its chemical properties, as well as to aid in understanding of the macroscopic optical properties that were observed in this study.

To establish the co-ordination of Er and the arrangement of the Er-S bonds found inside the As_2S_3 matrix, we analyzed a 1.35 wt % Er: As_2S_3 film that was photo-exposed using the extended X-ray absorption fine structure (EXAFS) technique. Furthermore, to establish the oxidation state of the Er atoms inside the As_2S_3 matrix, the same 1.35 wt % Er: As_2S_3 film, as well as pure Er metal and Er_2O_3 powder were measured using the X-ray absorption near edge spectroscopy (XANES) technique. The experimental details can be found in chapter 7. The results of these investigations are shown here in Figure 5.17.
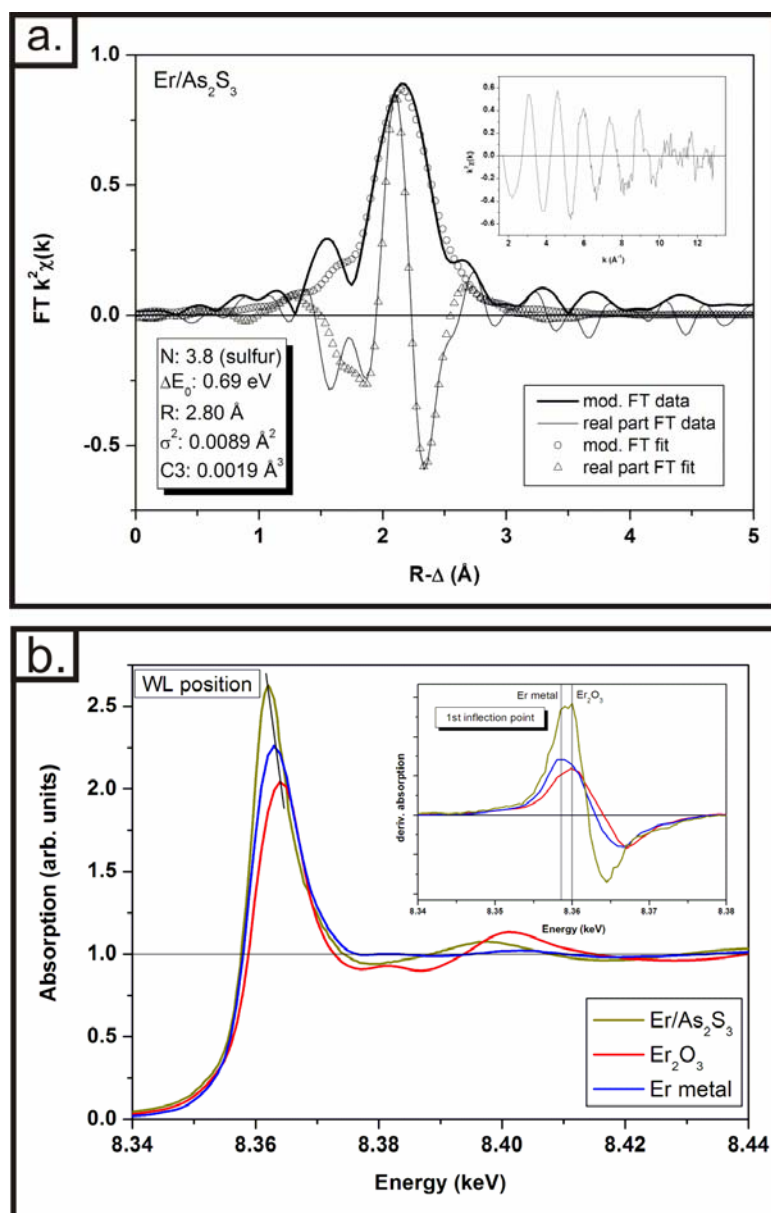
Figure 5.17 Synchrotron data collected from a 1.35 wt % Er doped As_2S_3 thin film and 2 reference samples of pure Er metal and Er_2O_3 powder. **a.** The spectrum of the EXAFS measurement on the 1.35 wt % Er doped As_2S_3 thin film. **b.** The spectrum of the XANES measurement of all 3 samples.

The XANES measurements indicated that in the photo-exposed $Er:As_2S_3$, the Er was in an oxidation state between (0) of the metal and (+3) of the fully oxidized Er^{3+} ion in Er_2O_3. The EXAFS results indicated that the Er was surrounded by 4 sulfur atoms in the first coordination sphere and it was arranged in a distorted tetrahedral geometry. Furthermore, the average bond lengths that were measured here is 260 pm,

which is much shorter than that the average Er-S bond length in a δ-Er_2S_3 single crystal, with average bond lengths between 269.7 pm to 273.8 pm at the ErS_6 sites, 278.0 pm to 279.8 pm at the ErS_7 sites[144]. These results was quite surprising since these intermediate oxidation states, low coordination numbers, and shortened bond lengths persisted even though the photoresist had been subjected to repeated doses of highly energetic beams of synchrotron radiation, which should have acted to thoroughly polymerized the photoresist.

The EXAFS results obtained in this work was rather surprising, because it suggested that the Er atoms were not in the most-energetically favorable geometry like those found in single crystals, but rather being stably locked in a non-equilibrium state inside this glassy amorphous As_2S_3 matrix. This results suggest that the previous work on the single crystal analogues of this material cannot be extrapolated directly to describe the glassy Er:As_2S_3 photoresist. Furthermore, despite the photoresist being subjected to high energy synchrotron radiation, the Er ions did not revert or relax into other geometries, and remained in this meta-stable arrangement. Therefore, the Er ions inside the final 3D structure, that were produced using the 3D DLW technique, should remain quite stable over long-periods of time because bonding rearrangement is unlikely to occur during room-temperature laser excitation/stimulation of the final device/structure.

The XANES result which suggested that the Er ion inside As_2S_3 was not in the fully oxidized +3 state was also surprising since Er is usually found to be oxidized ro the 3+ oxidation state in a number of organometallic compounds of Er, and also in its basic oxide [145,146]. The only lanthanides that were observed in the +2 oxidation state were Sm, Eu and Yb, and those were formed via the electrochemical reduction of their +3 solutions which succumb to rapid oxidizing in air and were therefore

unstable[76]. Since the Er ion in the As_2S_3 host matrix was not fully oxidized, this suggested that these species in the final structure may also be susceptible to further oxidation if they were removed from the protective As_2S_3 matrix.

A review of the EXAFS/XANES measurements that are documented in the literature for copper or zinc doping of As_2S_3 served to aid in the interpretation of the surprising results obtained here in the Er system. For the case of copper doping, the copper ions was found to be coordinated to 4 sulfur atoms inside the matrix[81,136,137,147]. For the zinc doping case, the oxidation state of zinc inside the As_2S_3 matrix was between that of the metal, with an oxidation state of zero, and that of crystalline zinc sulfide, where zinc is in the +2 oxidation state[135]. Furthermore, for the case of copper doping, the oxidataion state of copper ions are found to be between the +1 and the +2 state. In both doping cases, the photo-sensitivity of the metal doped films, and their susceptibility towards wet-etchants, was substantially decreased compared to the un-doped films. Those observations were attributed to the cross-linking of the matrix and the removal of the lone pair of p-electrons on the sulfur atom[81,137,148]. The results from these other studies closely resemble those observed for the current Er doping case.

Furthermore, this current analysis also shows that the Er reacts with sulfur upon photo-polymerization to scavenge photo-polarizable electron lone pairs on the sulfur atom and not the arsenic atoms. The results of this analysis provide another piece of evidence to support the argument that the inclusion of Er serves to cross-link the photoresist material, thus reducing its ability to be chemically etched by our standard etchant solution containing the amine molecule *N*-4-mehoxybenzyl-pyren-1-ylamine.

5.5 Non-Photoresist Applications of Erbium doped As$_2$S$_3$ Films

From the above analyses it had become clear that for Er doped As$_2$S$_3$ to retain its properties as a photoresist, the Er concentration inside an As$_2$S$_3$ matrix should ideally be kept below 1.35 wt % Er. However, for applications where photoresist behavior was not necessary, a logical question would then be, "Could the Er concentration be increased beyond 1.35 wt %?" For example, in applications where this material would only serve as a high refractive index coating that exhibited photoluminescence. For the case where Er:As$_2$S$_3$ was to be used only as a photoluminescent coating, the critical property for it should be its photoluminescent behavior, especially its PL intensity. To examine the PL intensity at various Er doping concentrations, we have once again employed the PLE analysis technique to examine the same series of films that were measured previously. 2D intensity maps were generated for the films which contained 1.35 wt % Er, 4.12 wt % Er and 11.58 wt % Er doping. The 0.41 wt % Er film was omitted in this analysis because it did not contain a high Er doping concentration. The results of this investigation are presented in Figure 5.18.

In the PLE spectrum, the wavelength which generated the highest PL intensity began to shift from 980 nm to 810 nm as the Er concentration was increased. For the case of 11.58 wt % Er doping, excitation with a laser source at a wavelength of 810 nm provided higher PL intensity than excitation with a laser source tuned to a wavelength of 980 nm. The change in the wavelength that caused the most efficient pumping intensity could be explained by the appearance of ion-ion interactions at increasingly higher Er concentrations[118]. The shift in the wavelength to shorter wavelengths was due to the cross-relaxation of one excited Er^{3+} ion with a neighboring Er^{3+} ion. In this cross-relaxation process, the first Er^{3+} ion was excited to the highly energetic ^{4}I$_{9/2}$ manifold, and when it relaxed to the meta-stable ^{4}I$_{13/2}$

159
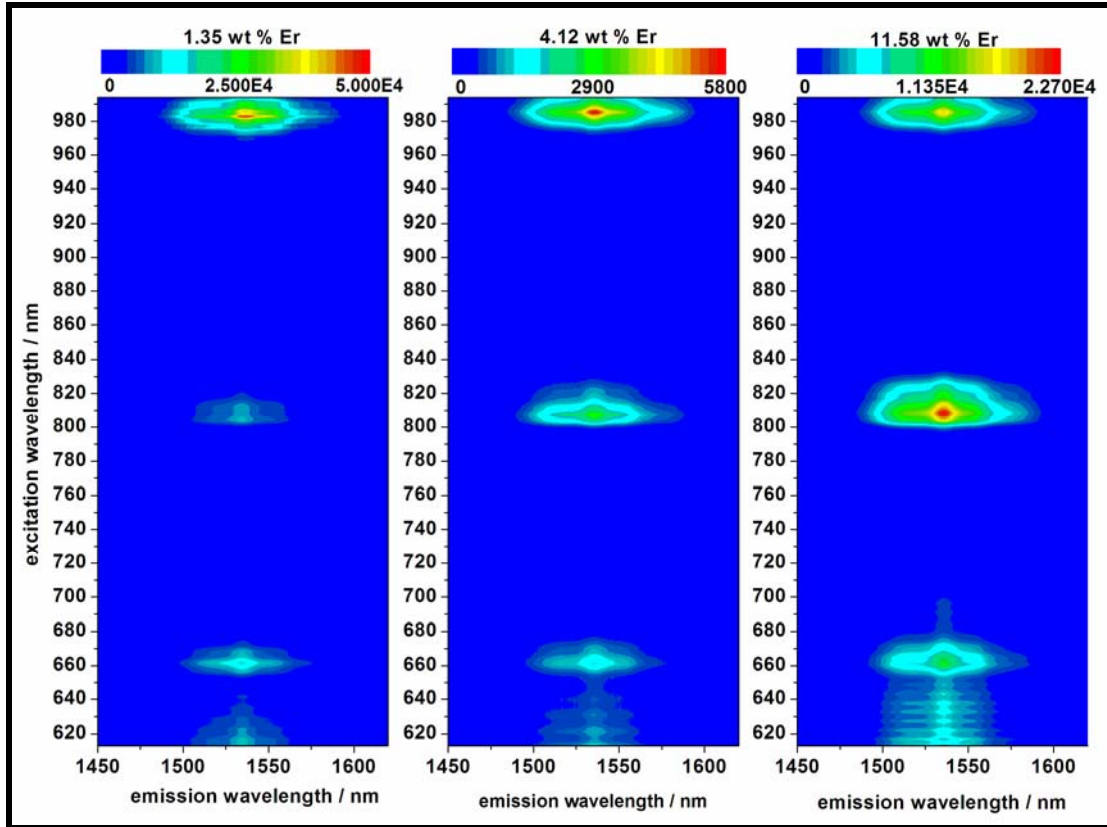
Figure 5.18 PLE spectra of 3 Er:As$_2$S$_3$ films doped with progressively higher Er concentrations.

manifold, the excess energy was transferred to a second neighboring Er^{3+} ion in the ground state, that is situated at close-proximity. The result of this cross-relaxation was that 2 atoms were now in the meta-stable ^{4}I$_{13/2}$ state[118]. Therefore, this excitation wavelength could generate a higher PL intensity over the other excitation wavelengths for that particular sample. Although it seems that excitation at 810 nm wavelength gives a higher PL intensity, if one carefully notes the absolute intensities between the 2D maps, one notices that the maximum PL intensity in the film doped with 11.58 wt % Er is actually half as intense as the films doped with 1.35 wt % Er, despite there being 8 times higher Er concentration in the former sample. The reason for this discrepancy was because other ion-ion interactions occurring along-side the cross-relaxation process, such as co-operative up-conversion and energy migration, are loss-mechanisms that increase non-radiative decay channels or luminescence from

unwanted transitions. Furthermore, the maximum intensity of the 4.15 wt% Er doped

film is actually the lowest of the 3 films measured. A plausible explanation to these

observations could be that the Er concentration for the 4.12 wt % Er doped film had

not reached a point where the cross-relaxation could dominate over the other ion-ion

interactions which caused non-radiative decay. Evidence for this suggestion stems

from the observation that the 810 nm excitation wavelength was only beginning to

become more significant when compared to the 1.35 wt % case, but not as significant

as the 11.58 wt % case.

Although the initial understanding of the PL behavior of heavily Er doped As_2S_3

film were provided here, we caution that this is only a small part of the overall PL

behavior that needed to be fully characterized. Although such a measurement was not

conducted as part of this thesis, the excited state lifetime is an important factor that

needs to be determined. This is because this property plays a significant role in the

ability for this material to sustain population inversion when used in laser applications.

If it is assumed that undesired ion-ion interactions begin to play a more significant

role as the Er concentration is increased, then one would predict that the lifetime of

the meta-stable excited state will become reduced as the increasing appearance of

non-radiative energy transfers processes begin to dominate[118].

One example of how Er doped As_2S_3 could be use only as a photoluminescent

coating is its use as a photoluminescent dielectric spacer in the fabrication of meta-

material samples. The inclusion of the Er doped As_2S_3 maybe beneficial to the

overall optical performance of meta-materials, as the inclusion of an emitter may have

the effect of compensating for the extrinsic losses observed in these types of

structure[149]. In Figure 5.19, a meta-material with cross-double wire geometry is
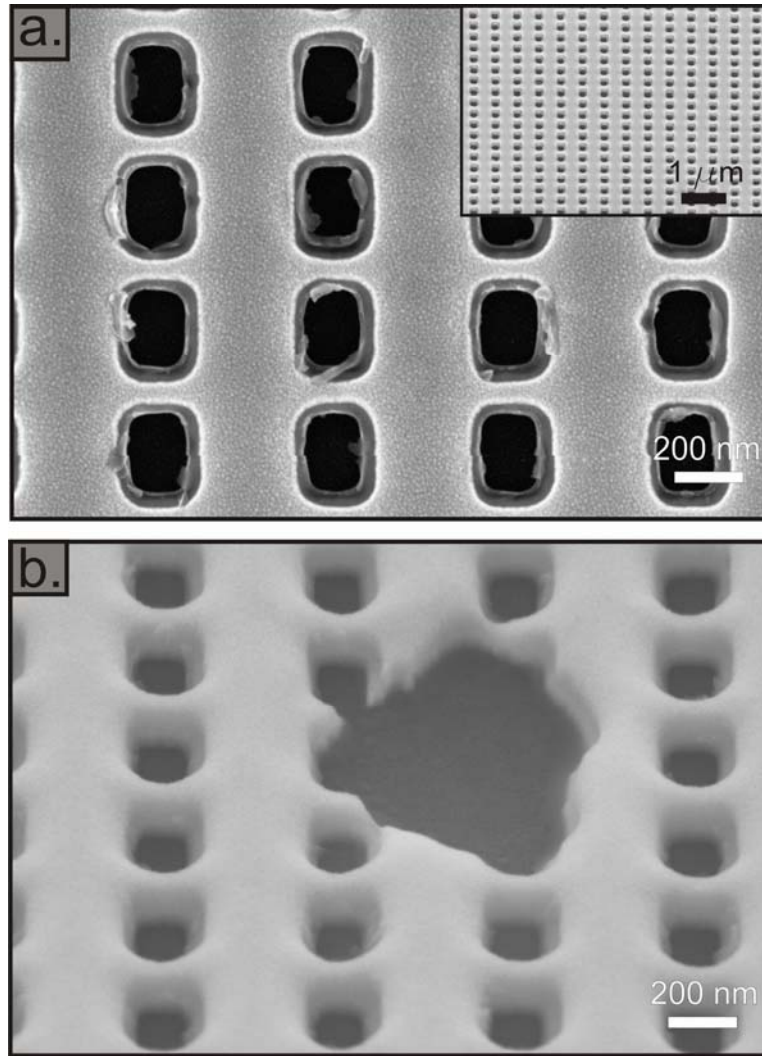
Figure 5.19 SEM images of a meta-material with cross-double wire geometry. **a.** A top view of the meta-material structure. (Top inset) A low-magnification overview of the surface this structure. **b.** A close-up view of a break in the meta-material film showing the brighter, top and bottom gold layers, and the semi-transparent middle layer which is the photoluminescent Er doped arsenic trisulfide dielectric spacer.

shown. This structure was fabricated using conventional 2D electron-beam lithography using a lift-off method. This lift-off technique is schematically depicted in Figure 5.20. Using this lift-off technique, the Er doped As_2S_3 was not required to possess any photo-resist behavior since the pattern has already been defined in the organic polymer (PMMA) by electron-beam lithography. In this structure, the top and bottom layers were made out of 40 nm of gold and the middle dielectric spacer layer
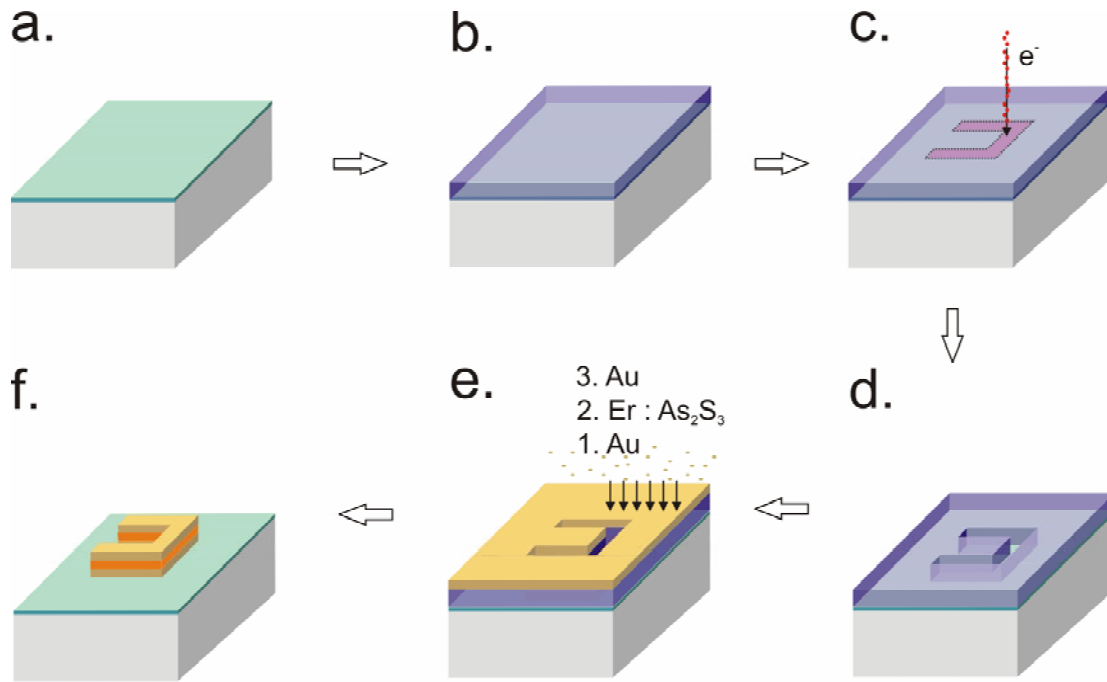
Figure 5.20 A schematic of the fabrication steps for 2D meta-materials using Er:As$_2$S$_3$ as the dielectric spacer layer. **a.** A layer of ITO was first placed onto the substrate. **b.** PMMA was spin-coated on the ITO layer and served as an electron-beam resist. **c.** The desire pattern was written into the PMMA layer. Here the split-ring geometry is shown but in practice, any 2D pattern can be written into the resist material. **d.** The exposed area was removed using a suitable developer. **e.** A sandwich layer of gold, Er:As$_2$S$_3$, and another gold layer was sequentially evaporated onto the pattern. **f.** The photoresist was then removed in a lift-off process to reveal the final structure.

was composed of As$_2$S$_3$ which has been doped with 4.15 wt % Er. Although the optical behavior of these structures still required optimization to exhibit the theoretically expected performance, the ability to fabricate the actual physical sample shown here provided the proof-of-concept experiment which demonstrated that Er doped As$_2$S$_3$ could be effectively integrated for used as a photoluminescent dielectric coating.

Conclusion

In this chapter we showed a gas-phase direct doping (GPDD) technique that was able to produce Er doped As$_2$S$_3$ photoresist films that were homogenous, possessed a

high-refractive index, and exhibited excellent room temperature photoluminescent properties at the telecommunication region of 1.5 μm. Most importantly, such a photoresist material could be patterned via the 3D DLW technique to produce 3D PC structures that were able to exhibit photoluminescence. Furthermore, we demonstrated that this doping method also allowed for the vertical control of Er doping, and enabled the 3D DLW method to selectively place a 2D photoluminescent doped layer inside a 3D structure. Using the Er doped As_2S_3 photoresist material we answered the 3 questions that were posed at the beginning of this chapter by demonstrating that a structure fabricated with 3D DLW could simultaneously possess a high refractive index, intrinsic photoluminescence, and allowed for spatial selective placement of the emitters. This new photoluminescent photoresist system could enable the realization of 3D PBG devices of the future, where active and passive components of a photonic circuit are envisioned to be integrated onto a single photonic chip.

Chapter 6 - Summary and Outlook

The idea of using 3D photonic crystals to "mold the flow of light" has generated great interest this field of research. The result is a global effort to improve different fabrication techniques which allow for the fabrication of intricate 3D photonic crystal designs. One fabrication method that is both flexible and versatile is the three-dimensional direct laser writing (3D DLW) method. This method is shown to be the only available one which allows for the fabrication of arbitrary 3D photonic crystals structures with feature resolutions on the nanometer length-scale. This method allows 3D photonic crystal structures to operate at telecommunications frequencies. The drawback to the 3D DLW method is that the organic photoresist materials used have a low index of refraction, making it impossible for the as-fabricated structures to exhibit a full-photonic band-gap directly after fabrication. Realizing this materials related problem, we addressed it in this thesis work by developing a suite of techniques to allow for the inorganic glass arsenic trisulfide (As_2S_3) to be used as a photoresist material for the 3D DLW process.

We began this thesis work by outlining the steps that were necessary to transform the material As_2S_3 into a photoresist system suitable for use with the 3D DLW technique. We first decided that this photoresist system should be formulated as a two-step, negative-tone photoresist system because this would be the most suitable method to implement this material for use with the 3D DLW process. The first step towards this photoresist system required the thermal evaporation of the As_2S_3 precursor in a high-vacuum environment to form a photosensitive thin film which can then be photo-patterned using the 3D DLW process. The second step consisted of

wet-etching the photo-patterned thin film using a highly-selective etching molecule to allow for etching of a free-standing 3D structure in a single etching step.

In order to achieve the goals that were set out above, we first analyzed the high-vacuum thermal evaporation technique to determine the correct conditions for generating the molecular species S_8, As_4S_4 and As_4S_6 from the As_2S_3 precursor glass. After the conditions of deposition have been established, the chemical and optical properties of the as-deposited thin film were established using a wide variety of characterization techniques. From this set of analyses we established that the as-deposited films possessed high transmission at the wavelength of 800 nm, which was the operating wavelength of the femtosecond laser source in the 3D DLW setup. Furthermore, these photoresist films exhibited photo-polymerization behavior upon photo-exposure.

In the next stage of the investigation we established that the as-deposited thin films could be photo-patterned using the 3D DLW technique. We also encountered four optical aberrations during the 3D DLW photo-patterning process. These optical aberrations were identified as defocusing, voxel elongation, the attenuation in the writing intensity as a function of depth and spherical aberrations of the writing beam. All these optical aberrations acted together to introduce undesirable artifacts which caused severe distortions to the designed structures. The origin of these optical aberrations was attributed to the refractive index mismatch between the high refractive index photoresist and the low index of refraction optical components that were used in the 3D DLW setup. To overcome these issues, we devised several counter-measures to overcome most of these optical aberrations. By implementing these corrective counter-measures we showed that a 3D woodpile photonic crystal structure with a full-photonic band-gap could be produced.

In the course of etching the 3D structures, we identified that the etching of a 3D structure containing nano-porosity, due to their large surface areas to volume ratio, required etchant molecules to provide higher etch selectivity than those currently being used to etch out solid structures. Furthermore, for the purpose of the development of such a highly selective etchant we implemented a standard testing method using a novel step-ladder test structure. Using this testing benchmark we conducted investigations into the dibenzylamine etching molecule through a systematic synthesis of a library of its derivatives and studying their individual etching behaviors. The result of this investigation allowed the relationship between the molecular structure of the molecule and its macroscopic manifestation on the etching behavior to be established. Using the body of knowledge that was obtained from this systematic study, we then synthesized the molecule N-4-methoxybenzyl-pyren1-1-ylamine to provide highly selective etching for this photoresist system. Through the use of this highly selective etchant, we were able to fabricate various intricate and free-standing 3D nanostructures. The minimum resolution obtained in a single suspended line was 138 nm.

Furthermore, we carried out a systematic investigation into the mechanism of the etching process. In this process we first analyzed and identified the species that were present on the surface of a thin film before and after the etching process using the XPS technique. The solution phase reactions that could occur on the surface of the thin films were then reproduce under inert atmospheric conditions and analyzed using ^{1}H-NMR spectroscopy. The results of this investigation provided important insights to the origins of the species observed on the surface of the thin film after the etching process.

In the final chapter of this thesis, a doping technique which provided intrinsic photoluminescence to the As_2S_3 photoresist material, via the introduction of photoluminescent Er atoms, was demonstrated. A gas-phase direct doping (GPDD) technique, which allowed for the controlled doping of Er into the As_2S_3 material during the thermal evaporation process, was elaborated. The thin films produced using the GPDD method exhibited photoluminescence at the wavelength of 1550 nm, and most importantly could be used as a photoresist for the 3D DLW method. Using this doped photoresist material, 3D woodpile photonic crystals that exhibited intrinsic photoluminescence were fabricated. However, the 3D woodpile structure that was produced did not exhibit the specifications which allowed them to exhibit a full-PBG at frequencies to enable it to take advantage of the photoluminescence of the material. This was due to stricter tolerances that were required to fabricate 3D PC structures with a smaller lattice constant so as to allow it to operate at a wavelength of 1.5 μm. The voxel elongation and spherical aberration had become too severe to be corrected by using the simple counter-measures that were introduced in this work. Nevertheless, the possibility for spatial selective doping was also demonstrated in this work and provided a working demonstration to the possibility for using this new and novel technique to impart spatially resolved photoluminescence to 3D structures.

Furthermore, we investigated the behavior of the photoresist films upon doping with Er atoms. We determined that if the as-deposited As_2S_3 is to continue to function as a photoresist, a maximum erbium doping limit of 1.35 wt % should not be exceeded. Despite the loss of its properties as a photoresist past this doping limit, the films continued to exhibit photoluminescence at the wavelength of 1550 nanometers. These results indicated that in cases where the photoresist properties are not required the highly erbium doped films could be used as a simple coating. We demonstrated

this form of use by introducing a highly Er doped As_2S_3 film as a photoluminescent dielectric spacer for the preparation of meta-materials.

In conclusion, we demonstrated in this thesis work that As_2S_3 can be made into a photoresist system that was suitable for the fabrication of 3D structures with the 3D DLW method. Furthermore, we demonstrated that photoluminescence can be introduced into this material through erbium doping, without any loss to its properties as a photoresist. The results obtained in this thesis work served as important proof-of-principal demonstrations to the feasibility of using As_2S_3 as a photoresist material for the direct fabrication of active and passive 3D photonic band-gap structures on a single substrate.

Future advances to this body of work would entail further research into new chalcogenide materials and an improvement to the 3D DLW method. Future research directions into chalcogenide-based photoresist materials should focus on the implementation of chalcogenide glasses with a higher index of refraction, such as As_2Se_3 ($n = 2.78$) or As–Se–Te composites (n up to 3.2), as photoresists[150,151,152]. The use of materials with higher indices of refraction should allow for even larger photonic band gaps to be realized. Furthermore, work aimed at correcting the higher-order spherical aberrations must be conducted in order to allow for the 3D DLW technique to reach its full potential when used with a chalcogenide based photoresist.

The future of chalcogenide based photoresist looks very promising[153,154,155]. This class of material possesses favorable optical and material properties which make them well suited for the production of 3D photonic crystal structures in the near-infrared and possibly even for the visible spectral region. Fundamental and applied research into the utilization of this material for photonics applications is beginning to gain greater attention[156,157]. This class of material may prove to be a powerful alternative

to common crystalline semiconductors used for photonic-crystal fabrication. The work that has been performed in this thesis will serve as a road-map to the investigative steps that are necessary for the development of new and exciting chalcogenide based photoresist materials.

Chapter 7 – Materials and Methods

7.1 Photonic Band-Structure Calculations

For the numerical calculations we used the freely available MIT photonic bands package to calculate the band structure[158], and our own scattering matrix code[89]. The required structural parameters for the band-structure calculations were obtained as follows: the rod aspect ratio was measured for all rods visible in Figure 2 c, and an average value of 2.4 was then used for the calculations. The same procedure was applied to determine the rod diameter (220 nm). We used a rod distance of 1 μm for calculation of the spectra, consistent with the rod distance found in the SEM images. A refractive index of 2.5 and a perfect ellipsoidal shape of the rods were used in the calculations unless otherwise stated.

7.2 Etching and Characterization Procedure

All etching and photoresist manipulation were performed under yellow light conditions. The etching was done in atmospheric conditions in a small Petri dish covered with a watch glass, and the film was simply placed in the etchant. The etch time is recorded with a stop watch. To ensure the comparability between different secondary amines, all etching solutions are prepared by dissolving the amine in an otherwise inert solvent system of dimethylsulfoxide (dmso) and 1,2-Dichloroethane (1,2-dce) or cyclopentanone (cp) at a concentration of 0.66 M. We chose dmso because it is a solvent that suitably facilitates S_N2 type reactions. The addition of small amounts of 1,2-dce or cp serves as an aid to dissolve larger, less-polar amine molecules.

For developing the exposed films, they are placed in the etchant and periodically removed. The overall etch selectivity γ is then calculated as the ratio between the rate of removal of the unexposed and exposed areas, **Ku** and **Ke**, respectively. To quantify the value of the etch selectivity for each modification step, we use the "step-ladder" test structure shown in Scheme 1: 20 microns long rungs are staggered with 250 nm vertical and 2 micron lateral distance. Their ends are attached to two supporting walls. This "step-ladder" geometry contains sub-200 nm features, while allowing convenient observation and evaluation of the selectivity *via* optical microscopy. The removal of the unexposed areas can be visually determined when the color of the photoresist disappears. The removal of the rungs of the ladder is followed with an optical microscope and periodically inspected until the structure is etched to destruction, or if the structure continues to remain, the time is stopped after reaching 72 hours (3 days). Inspection of fine surface details, as well as the cross-sections of individual bars was performed using a scanning electron microscope with a focused ion beam (Ga^+) attachment. All structures characterized using a SEM were first sputtered with 6-8 nm of gold to prevent charging.

7.3 ^{1}H-NMR Study

All chemicals were purchased from Merck KGaA (Darmstadt), Sigma-Aldrich (USA), Alfa Aesar (Karlsruhe) or Lancaster Synthesis (Cambridge, UK). The identity of the solvents and *N*-(4-methoxybenzyl)-(pyren-1-yl)amine was first verified with a 300 MHz ^{1}H-NMR (Varian Avance 300 MHz), using $CDCl_3$ or $(CD_3)_2CO$ as the solvent. The identity of the solid compounds was determined using a MALDI-TOF mass spectrometer (Perspective Biosystems, Voyager DE PRO) with ferrulic acid as the matrix. All solvents were dried prior to use in the experiments and stored under

nitrogen. The stock solvents were checked with ^{1}H-NMR for the presence of water prior to every experiment. All manipulations were carried out in a nitrogen filled glove-box or via Schlenk techniques.

Drying DMSO

d^6-DMSO and DMSO were first dried by stirring in activated 4Å molecular sieves, then decanted into a flask containing calcium hydride, stirred under nitrogen for 1 day, and then distilled under vacuum.

Drying Cyclopentanone

Cyclopentanone was dried by stirring twice in activated 4Å molecular sieves, then decanted and distilled under vacuum.

Drying Solid Reagents

Solid sulfur (99.999% electronic grade, Alfa Aesar), arsenic (99.999% electronic grade, Alfa Aesar) and *N*-(4-methoxybenzyl)-(pyren-1-yl)amine were evacuated under vacuum overnight and stored under nitrogen.

7.4 Optical Spectroscopy of 3D Structures

Transmittance and reflectance spectra were measured using a near-infrared Fourier-transform interferometer (Bruker Equinox 55, NIR halogen source) connected to an infrared microscope (Bruker Hyperion 1000, 36× Cassegrain lens, NA= 0.5, liquid N_2-cooled InSb detector). Due to the Cassegrain optics, the incident light spans an angle between 15 and 30 ° with respect to the surface normal for "normal incidence", spanning part of the LUX (see Fig. 4a) directions. The optical axis corresponds to the

ΓX direction for face-centered- cubic symmetry. The transmittance of the photonic crystal sample was normalized to the transmittance of the bare glass substrate. The reflectance was normalized to a silver mirror.

7.5 Photoluminescence / Photoluminescence Excitation Spectroscopy

PL spectra were collect using 2 separate setups. The PL only setup has the advantage that is can allow for angular dependant measurements, but has a limited choice of excitation laser wavelengths. The PLE setup has a large variety of laser excitation wavelengths that are available, but cannot perform angular resolved measurements.

In the PL only setup, the excitation source used is a CW He-Ne laser (Melles Griot He-NE 25LHP15) operating at 632.8 nm wavelength or a pulsed-laser source from a Ti:Sapphire laser (SpectraPhysics Hurricane) operating at a pulse duration of 150 fs and at a wavelength of 800 nm. Using silvered mirrors, the laser radiation is directed towards the sample, and the transmitted signal is then directed into an IR spectrometer (Horiba Jobin-Yves Horiba 6450 IR spectrometer) for analysis.

In the confocal PLE setup, the spectra were measured using a home-built near-infrared laser microscope equipped with wavelength-tuneable excitation sources. The latter could be automatically changed (in 1 nm steps) within the wavelength ranges 613–707 nm, 693–863 nm, and 832–994 nm as provided by a CW dye laser (spectra physics) and 2 Ti-sapphire lasers (spectra physics). A near-infrared microscope objective (15x, NA=0.4 for PLE mapping, and 100x, NA=0.95 using 980 nm excitation for PL imaging) was used to focus the excitation beam and to collect PL light. Excitation power in all measurements was ~0.8 mW. Emission spectra were acquired with a liquid nitrogen-cooled InGaAs photodiode array (sensitive in the

range of 800 nm – 1600 nm) attached to a 30 cm near-infrared spectrograph (Roper Scientific). The excitation lasers and spectrograph were coupled to the microscope via optical fibres, with the emission collection fibre also serving as a confocal pinhole.

The fitting of the PL spectra for the contribution of the Stark effects are performed using five transition levels, F_{11}, F_{12}, F_{13}, F_{21} and F_{22}. The photoluminescence spectrum consists of these five transition level and can therefore be represented by a weighted sum of these five Gaussian curves. The appropriate central wavelength curves are calculated from the energy level themselves. For example, the central wavelength of the transition F_{12} is:

$$\lambda = \frac{1}{6510 - 67.2}(\text{cm}^{-1}) = 1552\text{nm}$$

For the fitting of the PL spectra the following equation is used:

$$I_{PL} = A_{F_{11}} \cdot e^{-\left(\frac{\lambda - \lambda_{F_{11}}}{\sigma_{F_{11}}}\right)^2} + A_{F_{12}} \cdot e^{-\left(\frac{\lambda - \lambda_{F_{12}}}{\sigma_{F_{12}}}\right)^2} + A_{F_{13}} \cdot e^{-\left(\frac{\lambda - \lambda_{F_{13}}}{\sigma_{F_{13}}}\right)^2} + A_{F_{21}} \cdot e^{-\left(\frac{\lambda - \lambda_{F_{21}}}{\sigma_{F_{21}}}\right)^2} + A_{F_{22}} \cdot e^{-\left(\frac{\lambda - \lambda_{F_{22}}}{\sigma_{F_{22}}}\right)^2}$$

Here, A_{Fij} are the fitting parameters for the height of each transition, λ is the variable of the abscissa and the σ_{Fij} are the corresponding widths of each transition. While the central wavelengths of each transition λ_{Fij} are kept as fixed values, the other 10 parameters are optimized using a non-linear least squares algorithm to obtain the best fit to the experimental spectrum.

7.6 Powder X-ray Diffraction

Air sensitive powders are measured in a special diffractometer stage that can be enclosed with an air-tight Kapton cover. This special container allows for the manipulation of the powders inside a glove-box, and subsequent transport to, and

measurement in, the diffractometer (Phillips X'Pert MPD) without contact with the atmosphere. This stage was aligned to the correct diffraction height by placing a standard sample of Si powder (Alfa Aesar) on the stage, and positioning the stage until the position of the diffraction peaks matched those provided in the Joint Committee in Powder Diffraction Standards, International Centre for Diffraction Data (JCPDS-ICDD) database. The samples were typically measured between $2\theta = 10^{\circ}$ to 110°. The identity of the samples was verified by comparing the diffraction patterns obtained in the analysis, to those recorded in the JCPDS database.

7.7 Raman Spectroscopy

Raman spectra were measured using a Witec CRM 200 confocal Raman microscope. The laser with a wavelength of 633 nm was coupled through a microscope objective with 20x magnification and a NA=0.9. The Raman signal was collected in a backscattering geometry. In order to avoid the photo-exposure of the samples, lower laser powers were used. The typical excitation powers used in the measurements were 10 μW and a spot size of ~ 50 μm.

As$_2$S$_3$ and Er:As$_2$S$_3$ samples that had been deposited on a substrate were measured directly without further sample preparation. For investigation into powdered samples, the powders were first homogenized using a mortar and pestle inside a nitrogen-filled glove-box, and then pressed into a thin, smooth, flat disk using a die and a hydraulic press. Samples were kept inside the glove-box until they were measured.

7.8 Rutherford BackScattering Spectroscopy

Sapphire substrates (1 cm diameter, 2 mm thick) were used as substrates. Al$_2$O$_3$ was used as the substrate because it contains light elements which have their RBS signals positioned away from the spectra region of interest and therefore its presence

will not interfere with the RBS spectrum. A 300 – 500 nm thick film of either As_2S_3 or Er: As_2S_3 was deposited on this substrate for analysis.

The acceleration of the He^+ ions, to an energy of 2 MeV, was achieved using a tandem accelerator setup. All samples were measured in the Cornell geometry. The incident He^+ ion beam was arranged normal to the surface of the sample, and the backscattered ions were collected at a backscattering angle of 170°.

All spectra were fitted and analyzed using the RUMP code[159]. In the simulations for the un-doped As_2S_3 samples, it was sufficient to assume a constant layer composition and only the ratios between As, and S were varied. For the Er doped As_2S_3 samples the assumption of a constant layer composition did not result in a good fit of the spectra. This is because in these samples, the thin outer layers of the measured spectra show a rounder shape which is caused by the surface roughness of the sample. To accurately account for this surface roughness, the film was simulated using 2 iterations. In the first iteration, a rough fit was generated with the assumption of a constant layer composition, and only the ratios between As, S and Er was varied. Then the rough fitting was then further refined with a second iteration, where a three layer structure was used to simulate the film. In this 3-layer simulation; the composition of the thick central layer remains unchanged with respect to the first rough fit, but in the thin outer layers belonging to the substrate/ Er: As_2S_3 and Er: As_2S_3/air interfaces they are assumed to be slightly fuzzy (due to the surface roughness) instead of being atomically abrupt. The result of the 2 step-fitting processes yielded an improved fit to the measured spectra.

7.9 Scanning Electron Microscopy and Energy Dispersive X-ray Analysis

Scanning electron microscopes images were taken with either a LEO 1530 SEM with an EDX attachment (Oxford Instruments 6901), or a Carl Zeiss Cross-beam

microscope with focused ion beam (FIB) milling capabilities. For the FIB milling, gallium ions were used as the milling source. The ions were accelerated to 20 keV during milling. The milling is computer controlled and also monitored in-situ using the SEM function of the microscope.

For the EDX measurements, the spectrometer is calibrated to a cobalt standard prior to each measurement. Samples were mounted on an SEM stub and coated with a thin (3 nm) thick layer of platinum to avoid sample charging. The contributions of this Pt layer are removed in the software during the analysis of the sample. An acceleration voltage of 20 keV was used to excite the sample and x-ray electrons are collected at a 35 degree angle relative to the plane normal of the sample.

7.10 Shaded-Ring Filter Fabrication

The shaded-ring filter was fabricated by placing a thin gold layer (about 10 nm thick) on an appropriately shaped glass substrate using a lift-off technique. A positive tone photoresist (Microposit S1805, Allresist mbH) is first spun onto a glass substrate and then photo-patterned using a 2D direct laser writer (DWL66, Heidelberg Instruments GmbH). The photoresist is then developed, then gold is evaporated onto the pattern, and a final lift-off step is performed to obtain the final amplitude mask. The transmittance of the semi-transparent gold layer is about 10%.

7.11 Single-Crystal X-ray Diffraction

Single crystals of *N*-(4-methoxybenzyl)-(pyren-1-yl)amine were grown by first dissolving the pure compound in dmso and then layering acetone on top. The solvent was allowed to diffuse into each other and then was left open to air to allow the solvent to evaporate. The crystals were collected as thin, plates with a yellow tinge.

Single crystals of *N*-(4-methoxybenzyl)-(pyren-1-yl)ammonium chloride were prepared by first synthesizing the chloride salt of the amine. This was done by dissolving the amine in isopropanol, and then a 5 wt % HCl solution was slowly added to the mixture until a precipitate formed. The precipitate was collected via filtration and then dried to obtain a loose white powder. The identity of the white powder was verified using MALDI-TOF MS and IR spectroscopy. The powder was placed in a test tube and then dissolved in isopropanol, then hexane was slowly layered on top and was allowed to slowly diffuse into the underlying layer over a 1 week period. Long, thin, colorless needles approximately 5-10 mm in length were collected from this solution.

The diffraction data were collected with a STOE IPDS II diffractometer using Mo K-α (λ = 0.71073 Å) radiation. Structure solution and refinement against $F2$ were carried out using SHELXS and SHELXL software.[160] All carbon atoms could be located during the refinement process.

7.12 Synthesis and Purification of Dibenzylamine Derivatives

All chemicals were purchased from Merck KGaA (Darmstadt), Sigma-Aldrich (USA), Alfa Aesar (Karlsruhe) or Lancaster Synthesis (Cambridge, UK) and used as received. The identity of the compounds was verified with a 300 MHz ^{1}H NMR, using $CDCl_3$ or $(CD_3)_2CO$ as the solvent. Molecular mass of the compounds was determined using a MALDI-TOF mass spectrometer with ferrulic acid as the matrix.

Procedures for Amine Synthesis. Amine **1** and triethylamine were purchased from Sigma-Aldrich and Merck respectively and used without further purification. Unless otherwise indicated, all other secondary amines were synthesized in a general 2 step reaction. The first step consists of formation of imine *via* the condensation

coupling of the respective aldehyde (1 eq.), and the primary amine or aniline (1 eq.), in dry ethanol or benzene. Molecules **1** to **15** were synthesized as described previously in the literature [161, 162,163,164,165,166,167,168,169].

A typical reaction is as follows: *N*-**(4-methoxybenzyl)-(pyren-1-yl)amine 16**: The above reaction procedure was followed using 4-methoxybenzylamine (4.57 ml, 35 mmol) and 1-pyrenecaboxaldehyde (8.06 g, 35 mmol) dissolved in 250 ml dry benzene and refluxed overnight in a Dean-Stark trap to azeotropically remove water generated from the reaction. 1.6 equivalents of $NaBH_4$ (2.12 g, 56 mmol) was used to reduce the amine using methanol as the solvent. This mixture was allowed to stir at 40 °C for 2 hours and was then refluxed overnight. At the end of the reaction, the methanol was removed and the remaining solid was first acidified with 1M HCl and then quenched with 5 wt % $NaHCO_3$ until the solution was slightly basic. The aqueous phase was extracted 3 times with 75 ml CH_2Cl_2. The organic phase was then dried using Na_2SO_4, filtered, and the solvent was removed to afford the final amine. The crude products were purified *via* flash chromatography using silica gel (Kieselgel 60 (0.063-0.200 mm), Merck KGaA) with a mixture of hexane and ethyl acetate. The final product is a light yellow solid. ^{1}H-NMR (300 MHz, $CDCl_3$, 25 ºC): δ= 7.99 (m, 9H, $C_{16}H_9$), 7.3 (d, 2H, $C_6H_4OCH_3$), 6.9 (d, 2H, $C_6H_4OCH_3$), 4.5 (d, 2H, CH_2), 3.9 (d, 2H, CH_2), 3.8 (s, 3H, $C_6H_4OCH_3$). The molecular weight of the solid was determined via MALDI-TOF-MS using ferrulic acid as the matrix. Calculated $C_{25}H_{21}NO$: 351.4403 g/mol. Found [M+H]: 351.7667 g/mol.

7.13 Synthesis of As_4S_4

Electronic grade arsenic (99.999% metal basis, Alfa Aesar) and electronic grade sulfur (99.999% metal basis, Alfa Aesar) were mixed into a quartz tube in an argon filled glove-box in a 1 to 1.01 mole ratio. The tube was then evacuated to a pressure of 1×10^{-3} mbar and sealed using an oxy-acetylene torch. A quartz rod was also attached to the end of the tube to allow the tube and its contents to be mechanically rotated during the melt synthesis.

The tube is placed in a tube furnace and slowly heated to 100 ºC over a period of 3 hours and then to 400 ºC over 12 hours. The tube was held at this temperature for 72 hours and constantly rotated during the melt-synthesis to ensure the reaction was mixed homogenously. After the reaction was complete, the tube was slowly cooled to room temperature at a cooling rate of 10 ºC/ hour. The resulting material is a deep-red to blood-red colored solid. The material was then transferred, under an argon atmosphere, into a glass vessel of which a cold-finger apparatus is attached. The solid is heated while stirring at 80 º C to remove any excess sulfur. The final powder that is obtained is then crushed and a PXRD (spectra provided in the Appendix section) was obtained to verify its identity.

7.14 Thermal Evaporation

Solid As_2S_3 glass of >99.99% purity (Amorphous Materials, Garland, Texas) was used as the chalcogenide precursor material. Pure erbium metal of 99.99% purity (2 mm pieces, Alfa Aesar) was used as the erbium precursor material. The thin film preparation was performed using a high vacuum ($P < 2 \times 10^{-6}$ mbar), thermal evaporation deposition method. The chalcogenide glass is crushed and placed in an alumina crucible and the Er pieces are placed directly in a tungsten boat. The two sources were arranged in a co-evaporation setup, where the two vapor cones

emanating from their respective thermal sources were arranged so that they provide an area of overlap at the substrate. The substrates are mounted onto a water-cooled, rotating substrate holder directly opposite at the substrate position. The evaporation of the two materials is carried out simultaneously and their rates are monitored by two quartz micro-balances mounted in a staggered formation in order to avoid cross-contamination. The entire deposition process is fully-automated to ensure reproducibility. The as-deposited films are an optically clear and transparent light orange color. Films ranging from 500 nm to 10 microns are routinely obtained using this process.

The exact thickness of each individual photoresist film was measured using a fiber interferometer (Mikropak NanoCalc 2000). The optical constants of the interferometer were determined using data obtained from the ellipsometry measurements (see below) and the accuracy of the interferometer was cross checked from cross-section SEM images of the thin films.

7.15 Thermal Gravimetric Analysis / Mass Spectroscopy and Mass Spectroscopy

Mass spectroscopy was measured using two different setups, each providing its benefits. In the case of the TGA-MS (Netzsch TGA-MS system), the mass loss of the sample can be correlated to the vapor species that are generated in the gas-phase. However, the draw-back is that mass range of this setup is limited to below 233 amu. To overcome this problem a second mass spectrometer (MassSpec II), which can provide masses up to 1000 amu is used to analyze the species generated in the gas phase.

The TGA-MS system consists of a TGA mass balance (Netzch 409 CD) that is coupled to a quadrapolar mass spectrometer via a heated transfer line (Netzsch QMS

403/5 Skimmer coupling system). The Skimmer system contains a heated wall transfer system that prevents the condensation of gaseous species onto the walls of the transfer line during measurement. The heating of the transfer line is matched to the temperature of the source and therefore mimics the source behavior. The quadrapole MS uses an electron impact ionization method, and the detector is set to detect positive ions. This system is operated in the mass range from 1 amu to 233 amu with a resolution of 0.5 amu. Using this setup, the percentage mass loss and total ion flux, can be determined as a function of temperature. Samples are measured under a dynamic vacuum of 5×10^{-6} mbar to mimic the conditions of the thin-film evaporation process.

The thermal mass spectrometer is a quadrapolar mass spectrometer and uses an electron impact ionization method, and the detector is set to detect positive ions. This setup has a mass range from 1 amu to 1000 amu with a resolution of 0.1 amu. The thermal source of this setup is a programmable and can provide temperature ramping and holding programs. The temperature ramps that was obtained using the TGA-MS setup described above was fed into the temperature controller of this setup to simulate those conditions. The samples are measured under a dynamic vacuum of 1×10^{-8} mbar or lower.

7.16 Thin-Film Ellipsometery

2 microns of As_2S_3 or Er doped As_2S_3 photoresist in thickness were deposited on glass cover-slips using the thermal evaporation or GPD doping technique. As-deposited thin films were measured directly without further preparation. For the preparation of the photo-exposed samples, the as-depostied photoresist films were placed in a quartz tube and flood exposed with a broadband UV source while under

dynamic vacuum (1 x 10^{-3} mbar) for 45 min. The ellipsometery measurements were performed using a variable angle spectroscopic ellipsometer (JA Woollam). The spectral range of the measurements was 200 nm to 1800 nm. The sample was mounted in a vertical geometry and three angles of incidence (65º, 70º and 75º) were used in the measurements. The ellipsometery data were modeled using a four layer model consisting of the substrate (BK7 silica glass) and Er doped As_2S_3 layer, sandwiched between two rough surface layers (~1 nm) in order to simulate any surface roughness at the interfaces of the sample. The spectral data below the bandgap of the material were fitted using a Cauchy model while a single-oscillator model was used to fit the data above the bandgap region[170]. The fits were optimized using a fitting algorithm based on a non-linear least squares fitting method.

7.17 Three-Dimensional Direct Laser Writing

For 3D DLW a regeneratively amplified Ti:sapphire laser system (SpectraPhysics Hurricane) was used with a pulse duration of 120 fs. The repetition rate could be computer controlled from 1 kHz to single shots. The wavelength was tuned to 800 nm, where one-photon absorption of the chalcogenide glass was negligible. The output beam was attenuated by a half-wave plate/polarizer combination and passed through a quarter-wave plate; after beam expansion, typically 9.5 nJ of single pulse energy is coupled into an inverted microscope (Leica). The femtosecond pulses were focused into the chalcogenide film by a 100× oil-immersion objective with a high numerical aperture (NA= 1.4, Leica). The sample was placed on a capacitively controlled, three-axis piezo scanning stage, which was operated in a closed loop providing a resolution of better than 5 nm at the full scanning range of 200 μm × 200 μm × 20 μm (Physik

Instrumente). The scanning operation of the piezo was computer controlled and its movements were synchronized with the output of the laser system.

A commercially available 3D DLW system from Nanoscribe GmbH. was also used to fabricate more intricate 3D structures. This system essentially uses the same operating principals as the 3D DLW system described above.

7.18 Ultra-Violet / Visible and Near Infrared Spectroscopy

2 microns of As_2S_3 or Er doped As_2S_3 photoresist in thickness were deposited on glass cover-slips using the thermal evaporation or GPD doping technique. As-deposited thin films were measured directly without further preparation. For the preparation of the photo-exposed samples, the as-deposited photoresist films were placed in a quartz tube and flood exposed with a broadband UV source while under dynamic vacuum (1 x 10^{-3} mbar) for 45 min.

Transmittance and reflectance spectra were measured using a ultra-violet/visible and near-infrared Fourier-transform interferometer (Bruker Equinox 55, NIR halogen source) connected to an infrared microscope (Bruker Hyperion 1000, 36× Cassegrain lens, NA= 0.5) A silicon detector was used to detect the UV/VIS region (λ = 400 nm to 800 nm) and a liquid N_2-cooled InSb detector was used for detecting the NIR region (λ = 800 nm to 3500 nm).

7.19 Extended X-ray Absorption Fine Structure

Extended X-ray absorption fine structure (EXAFS) measurements were performed at the Er L_{III}-edge (8358 eV) at the ANKA INE-Beamline, located at the Forschungszentrum Karlsruhe, Germany[171]. The ANKA storage ring was operated at 2.5 GeV and a mean electron current of 150 mA. The fixed-exit X-ray

monochromator was equipped with a pair of Si{111} crystals ($2d$ = 6.271 Å). The Ni

K-edge (8.333 keV) X-ray absorption spectrum of a Ni metal foil was measured for

energy calibration in transmission mode. All sample holders were specially designed

to allow the samples to be prepared, transferred and measured without exposure to air.

All spectra were recorded at a step width of 5 eV in the pre-edge region 1 (8.200–

8.340 keV), of 2 eV in pre-edge region 2 (8.340 – 8.350 keV), of 0.5 eV at the rising

edge (8.350– 8.365 keV), and at equidistant k-steps (0.03 Å^{-1}) in the post-edge region

(8.365 – 8.450 keV).

Erbium (99.99% purity, Alfa Asear) and Erbium Oxide (99.99% purity (REO), Alfa

Aesar), were recorded as reference samples in transmission mode using N_2 filled

ionization chambers at ambient pressure. The Er metal was deposited as a 1.5 micron

thick film on KAPTON tape, and the Er_2O_3 was prepared in the form of a thin pressed

pellet consisting of a mixture of Er_2O_3 (30 mg) in a polyethylene matrix (90 mg).

Due to the low concentration of Er in the Er doped As_2S_3 sample, its spectrum was

taken in fluorescence mode, collecting Er Lα radiation (~6.940 keV) with a 5-pixel

Canberra LEGe solid state detector. All measurements were performed at room

temperature. Several scans were averaged to improve the signal to noise ratio.

EXAFS (Extended X-ray Absorption Fine Structure) analysis of the Er/As_2S_3 data

was based on standard least square fit techniques. The EXAFS χ(k) function was

extracted using the WinXAS[172] software; fitting the data in order to derive metric

parameters characterizing the first Er coordination sphere was performed by means of

the UWXAFS[173] program package.

XANES (X-ray Absorption Near-Edge Structure) spectra for all samples were

isolated from XAFS scans by subtraction of a linear pre-edge background and

normalization of the edge jump to unity, allowing quantitative comparison of the spectra.

7.20 X-ray Photoemission Spectroscopy

XPS analysis was performed with a Leybold MAX200 spectrometer, using Mg Kα radiation as the excitation source. The energy of the spectrometer was calibrated using the Cu $2p_{3/2}$ and Ag $3d_{5/2}$ lines. The peak fitting algorithm provided within the acquisition/analysis software (SPECS GmbH.) was used to fit the data to a series of Gaussian/Lorentzian (80/20%) peaks. Low resolution scans were made with the analyzer set at 192 eV constant pass energy, and high resolution scans at 48 eV constant pass energy. The average surface composition was calculated from the low-resolution spectra and was normalized to unit transmission of the spectrometer. All spectra were collected under a take-off angle (TOA) of 20º. The surface was analyzed for the elements of arsenic, sulphur, and nitrogen, using the binding energies (BE) of their 3d, 2p and 1s orbital respectively. Two different samples were examined: an as-deposited film and a film with a surface passivation layer on its surface. The surface passivation layer was prepared by first photo-polymerizing an as-deposited film using a broad-band UV source under vacuum, in order to avoid air oxidation upon illumination. Then it is immersed in an etchant containing amine **16** for 1 hour, and finally rinsed with copious amounts of acetone and dried under a stream of nitrogen.

Appendix

A. Key Material and Optical Data

	As$_2$S$_3$ (as-deposited)	As$_2$S$_3$ (exposed)	Er: As$_2$S$_3$ 1.35 wt % Er (as-deposited)	Er: As$_2$S$_3$, 1.35 wt % Er (exposed)
Index of refraction @ λ = 1550 nm	2.31	2.45	2.36	2.46
T$_g$	N/M[a]	190 º C[b]	N/M[a]	N/M[a]
M$_p$	N/M[a]	310 º C[b]	N/M[a]	N/M[a]
Absorption edge	λ = 500 nm	λ = 520 nm	λ =510 nm	λ =520 nm
Transmission range	N/M[a]	λ > 3000 nm	N/M[a]	λ >3000 nm
Optical bandgap	2.36 eV	2.34 eV	2.33 eV	2.32 eV
Photoluminescence	N/A	N/A	N/M[a]	λ range (FWHM): 1500 nm to 1580 nm Centre λ: 1535 nm
Excitation wavelengths for PL	N/A	N/A	N/M[a]	λ = 660 nm λ = 805 nm λ = 983 nm[c]
Etch selectivity with highly selective etchant.[d]	344 : 1		344 : 1	
Etch rate[d]	210 nm/min.	0.61 nm/min.	210 nm/min.	0.61 nm/min.

[a] N/M = Not measured.

[b] Values taken from measurements of bulk glass samples.

[c] This excitation wavelength generates the highest PL intensity.

[d] Values based on an etchant containing *N*-(4-methoxybenzyl)-(pyren-1-yl)amine.

B. Single Crystal X-ray Diffraction Data:

1. *N*-4-methoxybenzyl-pyren-1-ylamine.
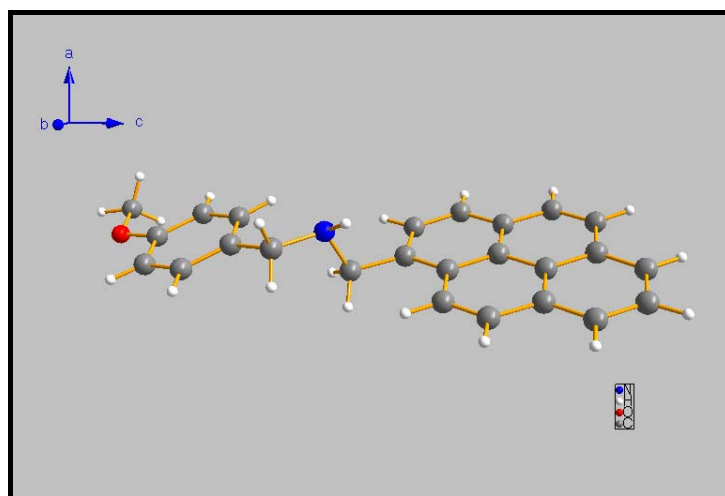
Table 1a. Crystal data and structure refinement for *N*-4-methoxybenzyl-pyren-1-ylamine.

Identification	*N*-4-methoxybenzyl-pyren-1-ylamine
Empirical formula	C25 H21 N O
Formula weight	351.43
Temperature	180(2) K
Wavelength	0.71073 A
Crystal system, space group	Orthorhombic, Pbca
Unit cell dimensions	a = 16.491(3) A alpha = 90 deg.
	b = 6.4590(13) A beta = 90 deg.
	c = 34.184(7) A gamma = 90 deg.
Volume	3641.1(13) A^3
Z, Calculated density	8, 1.282 Mg/m^3
Absorption coefficient	0.077 mm^-1
F(000)	1488
Crystal size	0.45 x 0.32 x 0.06 mm
Theta range for data collection	1.19 to 25.73 deg.
Limiting indices	-19<=h<=20, -7<=k<=7, -41<=l<=41
Reflections collected / unique	21955 / 3418 [R(int) = 0.1029]
Completeness to theta = 25.73	98.80%
Absorption correction	None
Refinement method	Full-matrix least-squares on F^2
Data / restraints / parameters	3418 / 0 / 329
Reflections with I>2sigma(I)	2649
Goodness-of-fit on F^2	1.101
Final R indices [I>2sigma(I)]	R1 = 0.0549, wR2 = 0.1158
R indices (all data)	R1 = 0.0737, wR2 = 0.1258
Extinction coefficient	0.0179(19)
Largest diff. peak and hole	0.167 and -0.150 e.A^-3

Table 1 b. Atomic coordinates (x 10^4) and equivalent isotropic displacement parameters (A^2 x 10^3) for N-4-methoxybenzyl-pyren-1-ylamine. U(eq) is defined as one third of the trace of the orthogonalized U_{ij} tensor.

	x	y	z	U(eq)
N(1)	0.65554(9)	0.3196(2)	0.23577(5)	.0467(4)
O(1)	0.64537(8)	0.1344(2)	0.05013(4)	.0510(4)
C(1)	0.63131(13)	0.4580(3)	0.20414(6)	.0494(5)
C(2)	0.63474(10)	0.3582(3)	0.16412(5)	.0417(4)
C(3)	0.59820(11)	0.4591(3)	0.13282(5)	.0445(4)
C(4)	0.60208(11)	0.3806(3)	0.09543(6)	.0446(4)
C(5)	0.64384(10)	0.1971(3)	0.08858(5)	.0420(4)
C(6)	0.68001(11)	0.0923(3)	0.11909(5)	.0440(4)
C(7)	0.67498(11)	0.1748(3)	0.15666(5)	.0439(4)
C(8)	0.68639(18)	-0.0530(4)	0.04136(7)	.0681(7)
C(9)	0.59188(12)	0.1722(3)	0.24695(6)	0.0509(5)
C(10)	0.61403(11)	0.0656(3)	0.28459(5)	.0450(4)
C(11)	0.59562(10)	0.1522(2)	0.32132(5)	.0391(4)
C(12)	0.55371(11)	0.3458(3)	0.32599(6)	.0434(4)
C(13)	0.53531(11)	0.4233(3)	0.36136(6)	.0431(4)
C(14)	0.55613(11)	0.3154(3)	0.39666(5)	.0418(4)
C(15)	0.53602(12)	0.3901(3)	0.43383(6)	.0513(5)
C(16)	0.55743(13)	0.2815(3)	0.46687(6)	.0588(5)
C(17)	0.60062(13)	0.0989(3)	0.46428(6)	.0558(5)
C(18)	0.62230(11)	0.0171(3)	0.42786(5)	.0459(4)
C(19)	0.66681(12)	-0.1718(3)	0.42386(6)	.0518(5)
C(20)	0.68573(11)	-0.2497(3)	0.38857(6)	.0490(5)
C(21)	0.66267(11)	-0.1452(3)	0.35325(5)	.0431(4)
C(22)	0.68163(11)	-0.2223(3)	0.31626(6)	0.0489(5)
C(23)	0.65738(11)	-0.1197(3)	0.28293(6)	.0500(5)
C(24)	0.61908(10)	0.0446(2)	0.35589(5)	.0388(4)
C(25)	0.59957(10)	0.1262(2)	0.39347(5)	.0390(4)

Table 1c. Bond lengths (pm) and angles (deg)

N(1)-C(1)	145.9(3)
N(1)-C(9)	146.8(2)
O(1)-C(5)	137.5(2)
O(1)-C(8)	141.9(3)
C(1)-C(2)	151.3(3)
C(2)-C(7)	138.2(2)
C(2)-C(3)	139.0(3)
C(3)-C(4)	137.6(3)
C(4)-C(5)	139.1(2)
C(5)-C(6)	137.9(3)
C(6)-C(7)	139.3(3)
C(9)-C(10)	150.4(3)
C(10)-C(23)	139.5(3)
C(10)-C(11)	140.8(2)
C(11)-C(24)	142.5(2)
C(11)-C(12)	143.7(2)
C(12)-C(13)	134.3(3)

```
C(13)-C(14)            143.5(2)
C(14)-C(15)            139.9(3)
C(14)-C(25)            142.1(2)
C(15)-C(16)            137.5(3)
C(16)-C(17)            138.1(3)
C(17)-C(18)            139.9(3)
C(18)-C(25)            142.1(2)
C(18)-C(19)            143.1(3)
C(19)-C(20)            134.3(3)
C(20)-C(21)            143.5(3)
C(21)-C(22)            139.4(3)
C(21)-C(24)            142.4(2)
C(22)-C(23)            137.8(3)
C(24)-C(25)            142.5(2)
C(1)-N(1)-C(9)         113.24(15)
C(5)-O(1)-C(8)         117.50(15)
N(1)-C(1)-C(2)         113.52(16)
C(7)-C(2)-C(3)         117.90(16)
C(7)-C(2)-C(1)         123.36(16)
C(3)-C(2)-C(1)         118.69(16)
C(4)-C(3)-C(2)         121.47(17)
C(3)-C(4)-C(5)         119.55(17)
O(1)-C(5)-C(6)         124.80(16)
O(1)-C(5)-C(4)         114.88(16)
C(6)-C(5)-C(4)         120.32(16)
C(5)-C(6)-C(7)         118.96(17)
C(2)-C(7)-C(6)         121.79(17)
N(1)-C(9)-C(10)        110.22(15)
C(23)-C(10)-C(11)      119.19(17)
C(23)-C(10)-C(9)       118.81(17)
C(11)-C(10)-C(9)       121.93(17)
C(10)-C(11)-C(24)      119.18(16)
C(10)-C(11)-C(12)      123.26(16)
C(24)-C(11)-C(12)      117.57(15)
C(13)-C(12)-C(11)      122.21(17)
C(12)-C(13)-C(14)      121.44(16)
C(15)-C(14)-C(25)      119.05(17)
C(15)-C(14)-C(13)      122.67(17)
C(25)-C(14)-C(13)      118.27(16)
C(16)-C(15)-C(14)      120.61(18)
C(15)-C(16)-C(17)      121.02(19)
C(16)-C(17)-C(18)      120.76(19)
C(17)-C(18)-C(25)      118.79(17)
C(17)-C(18)-C(19)      122.57(18)
C(25)-C(18)-C(19)      118.64(17)
C(20)-C(19)-C(18)      121.62(18)
C(19)-C(20)-C(21)      121.20(17)
C(22)-C(21)-C(24)      118.56(17)
C(22)-C(21)-C(20)      122.40(17)
C(24)-C(21)-C(20)      119.03(16)
C(23)-C(22)-C(21)      120.88(17)
C(22)-C(23)-C(10)      121.85(18)
C(21)-C(24)-C(11)      120.30(15)
C(21)-C(24)-C(25)      119.31(16)
C(11)-C(24)-C(25)      120.39(15)
C(18)-C(25)-C(14)      119.74(16)
C(18)-C(25)-C(24)      120.18(15)
C(14)-C(25)-C(24)      120.08(15)
```

Symmetry Transformations Used to Generate Equivalent Atoms:

Table 1d. Anisotropic displacement parameters (A^2 x 10^3). The anisotropic displacement factor exponent takes the form:

$$-2 \pi^2 [h^2 a^{*2} U_{11} + ... + 2 h k a^* b^* U_{12}]$$

	U_{12}	U_{11}	U_{22}	U_{33}	U_{23}	U_{13}
N(1)	47(1)	56(1)	38(1)	-3(1)	-2(1)	-(1)
O(1)	56(1)	57(1)	40(1)	-5(1)	-4(1)	(1)
C(1)	51(1)	52(1)	45(1)	-5(1)	4(1)	(1)
C(2)	38(1)	45(1)	43(1)	-1(1)	2(1)	(1)
C(3)	44(1)	41(1)	49(1)	1(1)	1(1)	(1)
C(4)	42(1)	48(1)	44(1)	5(1)	-4(1)	(1)
C(5)	41(1)	48(1)	38(1)	-2(1)	0(1)	-(1)
C(6)	43(1)	43(1)	46(1)	-1(1)	0(1)	(1)
C(7)	42(1)	48(1)	42(1)	3(1)	-1(1)	(1)
C(8)	82(2)	70(2)	52(1)	-16(1)	-6(1)	0(1)
C(9)	44(1)	69(1)	40(1)	-3(1)	0(1)	-2(1)
C(10)	38(1)	52(1)	46(1)	-5(1)	0(1)	-(1)
C(11)	36(1)	40(1)	42(1)	0(1)	1(1)	-(1)
C(12)	42(1)	41(1)	47(1)	3(1)	-2(1)	-(1)
C(13)	40(1)	35(1)	54(1)	-1(1)	-1(1)	2(1)
C(14)	40(1)	40(1)	46(1)	-4(1)	-1(1)	-(1)
C(15)	49(1)	54(1)	52(1)	-12(1)	0(1)	(1)
C(16)	61(1)	73(1)	43(1)	-10(1)	1(1)	(1)
C(17)	56(1)	69(1)	42(1)	4(1)	-4(1)	(1)
C(18)	42(1)	50(1)	46(1)	4(1)	-1(1)	-(1)
C(19)	50(1)	51(1)	55(1)	12(1)	-3(1)	(1)
C(20)	43(1)	38(1)	67(1)	7(1)	-2(1)	(1)
C(21)	38(1)	36(1)	55(1)	-2(1)	1(1)	-(1)
C(22)	45(1)	38(1)	64(1)	-10(1)	5(1)	-(1)
C(23)	46(1)	52(1)	53(1)	-12(1)	5(1)	-(1)
C(24)	35(1)	35(1)	46(1)	-1(1)	2(1)	-(1)
C(25)	36(1)	38(1)	43(1)	0(1)	-2(1)	-(1)

Table 1e. Hydrogen coordinates (x 10^4) and isotropic displacement parameters (A^2 x 10^3) for *N*-4-methoxybenzyl-pyren-1-ylamine.

	x	y	z	U(eq)
H(1)	0.6688(13)	0.402(3)	0.2569(7)	0.062(6)
H(1A)	0.5755(14)	0.519(3)	0.2084(6)	0.055(5)
H(1B)	0.6697(13)	0.582(3)	0.2044(6)	0.056(6)
H(3)	0.5683(12)	0.590(3)	0.1377(5)	0.048(5)
H(4)	0.5790(13)	0.449(3)	0.0734(6)	0.055(5)
H(6)	0.7078(13)	-0.039(3)	0.1137(5)	0.050(5)
H(7)	0.7014(13)	0.099(3)	0.1777(6)	0.055(6)
H(8A)	0.6807(14)	-0.066(3)	0.0114(8)	0.076(7)

H(8B)	0.7427(17)	−0.048(4)	0.0492(7)	0.074(7)
H(8C)	0.6639(16)	−0.171(4)	0.0563(8)	0.089(9)
H(9A)	0.5374(13)	0.242(3)	0.2489(6)	0.056(5)
H(9B)	0.5852(13)	0.066(3)	0.2257(6)	0.056(6)
H(12)	0.5381(11)	0.424(3)	0.3020(6)	0.047(5)
H(13)	0.5078(13)	0.557(3)	0.3632(5)	0.050(5)
H(15)	0.5057(14)	0.526(3)	0.4359(6)	0.062(6)
H(16)	0.5443(14)	0.332(3)	0.4941(7)	0.072(6)
H(17)	0.6169(14)	0.013(3)	0.4884(7)	0.073(7)
H(19)	0.6855(13)	−0.244(3)	0.4484(7)	0.069(6)
H(20)	0.7153(14)	−0.381(3)	0.3865(6)	0.062(6)
H(22)	0.7102(14)	−0.356(3)	0.3142(6)	0.061(6)
H(23)	0.6700(12)	−0.170(3)	0.2554(6)	0.059(6)

2. *N*-4-methoxybenzyl-pyren-1-ylammonium chloride
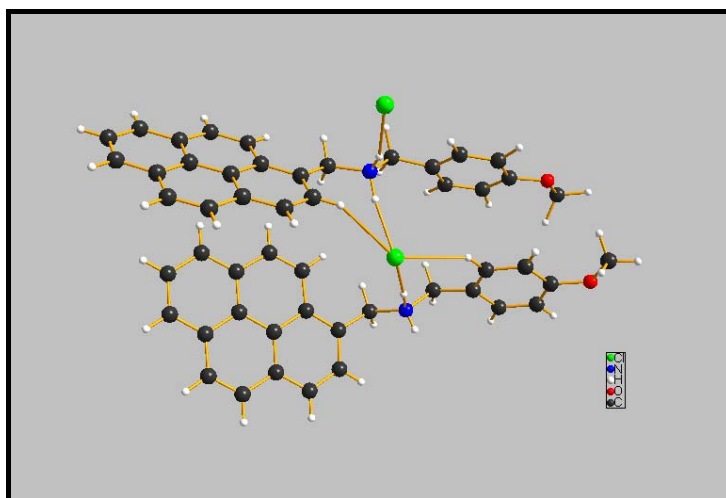
Table 2a. Crystal data and structure refinement for *N*-4-methoxybenzyl-pyren-1-ylammmonium chloride.

Identification	*N*-4-methoxybenzyl-pyren-1-yl-ammonium chloride
Empirical formula	C25 H22 Cl N O
Formula weight	387.89
Temperature	190(2) K
Wavelength	0.71073 A
Crystal system, space group	Orthorhombic, Pca2(1)
Unit cell dimensions	a = 34.630(7) A alpha = 90 deg.
	b = 7.5054(15) A beta = 90 deg.
	c = 14.779(3) A gamma = 90 deg.
Volume	3841.2(13) A^3
Z, Calculated density	8, 1.341 Mg/m^3
Absorption coefficient	0.215 mm^-1
F(000)	1632
Crystal size	0.34 x 0.31 x 0.03 mm
Theta range for data collection	1.81 to 25.69 deg.
Limiting indices	-36<=h<=42, -9<=k<=6, -17<=l<=14
Reflections collected / unique	9741 / 6112 [R(int) = 0.0702]
Completeness to theta = 25.69	97.40%
Absorption correction	None
Refinement method	Full-matrix least-squares on F^2
Data / restraints / parameters	6112 / 1 / 467
Reflections with I>2sigma(I)	3711
Goodness-of-fit on F^2	1.231
Final R indices [I>2sigma(I)]	R1 = 0.0540, wR2 = 0.1918
R indices (all data)	R1 = 0.1013, wR2 = 0.2042
Absolute structure parameter	0.19(15)
Extinction coefficient	0.0036(8)
Largest diff. peak and hole	0.234 and -0.265 e.A^-3

Table 2b. Atomic coordinates (A x $10^{4)}$ and equivalent isotropic displacement parameters (A^2 x 10^3). U(eq) is defined as one third of the trace of the orthogonalized U_{ij} tensor.

	x	y	z	U(eq)
Cl(1)	0.73364(5)	0.4509(3)	0.25383(15)	0.0430(5)
Cl(2)	0.74736(6)	-0.0322(3)	0.00388(15)	.0414(5)
N(1)	0.74008(17)	0.0373(11)	0.2119(5)	0.0358(16)
N(2)	0.75189(18)	0.5531(12)	0.4534(5)	0.0355(15)
O(1)	0.91971(13)	0.2907(8)	0.2483(4)	0.0462(14)
O(2)	0.92463(15)	0.7927(9)	0.3151(4)	0.0486(16)
C(1)	0.77474(19)	-0.0525(12)	0.2541(7)	0.0409(17)
C(2)	0.81112(18)	0.0549(10)	0.2524(6)	0.0349(15)
C(3)	0.8282(2)	0.1148(13)	0.1722(6)	0.040(2)
C(4)	0.8635(2)	0.1966(13)	0.1734(5)	0.039(2)
C(5)	0.88368(19)	0.2155(10)	0.2551(6)	0.0373(17)
C(6)	0.8672(2)	0.1582(12)	0.3341(6)	0.040(2)
C(7)	0.8309(2)	0.0803(12)	0.3335(6)	0.0359(19)
C(8)	0.9417(3)	0.301(2)	0.3293(7)	0.055(3)
C(9)	0.70495(4)	-0.0705(2)	0.23229(9)	0.041(2)
C(10)	0.66867(4)	-0.0038(2)	0.18697(9)	0.0351(18)
C(11)	0.66584(4)	0.1614(2)	0.14613(9)	0.042(2)
C(12)	0.63197(4)	0.2177(2)	0.10757(9)	0.046(2)
C(13)	0.59901(4)	0.1120(2)	0.10868(9)	0.0387(19)
C(14)	0.56273(4)	0.1683(2)	0.07059(9)	0.049(2)
C(15)	0.53136(4)	0.0649(2)	0.07288(9)	0.052(2)
C(16)	0.53256(4)	-0.1075(2)	0.11225(9)	0.049(2)
C(17)	0.50072(4)	-0.2227(2)	0.11395(9)	0.060(3)
C(18)	0.50302(4)	-0.3903(2)	0.15130(9)	0.063(3)
C(19)	0.53683(4)	-0.4501(2)	0.18886(9)	0.054(2)
C(20)	0.56970(4)	-0.3419(2)	0.19085(9)	0.046(2)
C(21)	0.60541(4)	-0.3972(2)	0.22997(9)	0.046(2)
C(22)	0.63708(4)	-0.2914(2)	0.23113(9)	0.038(2)
C(23)	0.63646(4)	-0.1179(2)	0.19006(9)	0.0346(17)
C(24)	0.60096(4)	-0.0587(2)	0.15027(9)	0.0380(19)
C(25)	0.56770(4)	-0.1689(2)	0.15152(9)	0.042(2)
C(26)	0.79197(4)	0.4806(2)	0.47319(9)	0.043(2)
C(27)	0.82449(4)	0.5766(2)	0.42580(9)	0.0345(18)
C(28)	0.82979(4)	0.5714(2)	0.33260(9)	0.0358(17)
C(29)	0.86223(4)	0.6446(2)	0.29208(9)	0.0385(19)
C(30)	0.89022(4)	0.7219(2)	0.34604(9)	0.0389(19)
C(31)	0.88510(4)	0.7327(2)	0.43872(9)	0.046(2)
C(32)	0.85222(4)	0.6617(2)	0.47784(9)	0.047(2)
C(33)	0.93064(4)	0.7914(2)	0.21943(9)	0.053(3)
C(34)	0.72328(4)	0.4581(2)	0.51340(9)	0.041(2)
C(35)	0.68207(4)	0.5159(2)	0.49785(9)	0.0393(19)
C(36)	0.67104(4)	0.6831(2)	0.52932(9)	0.043(2)
C(37)	0.63298(4)	0.7438(2)	0.52467(9)	0.045(2)
C(38)	0.60441(4)	0.6335(2)	0.49064(9)	0.0381(18)
C(39)	0.56495(4)	0.6882(2)	0.48727(9)	0.047(2)
C(40)	0.53711(4)	0.5797(2)	0.45546(9)	0.049(2)
C(41)	0.54588(4)	0.4044(2)	0.42373(9)	0.047(2)
C(42)	0.51723(4)	0.2910(2)	0.39083(9)	0.052(2)
C(43)	0.52657(4)	0.1220(2)	0.35975(9)	0.053(3)
C(44)	0.56500(4)	0.0640(2)	0.36055(9)	0.054(2)
C(45)	0.59417(4)	0.1724(2)	0.39264(9)	0.042(2)

```
C(46)     0.63353(4)     0.1211(2)      0.39642(9)      0.045(2)
C(47)     0.66187(4)     0.2282(2)      0.42712(9)      0.043(2)
C(48)     0.65380(4)     0.4035(2)      0.46114(9)    0.0340(18)
C(49)     0.61418(4)     0.4603(2)      0.45881(9)    0.0357(18)
C(50)     0.58514(4)     0.3463(2)      0.42514(9)      0.040(2)
```

Table 2c. Bond lengths (pm) and angles (deg).

```
N(1)-C(9)          149.2(7)
N(1)-C(1)          151.1(10)
N(2)-C(34)         150.8(7)
N(2)-C(26)         151.9(7)
O(1)-C(5)          137.3(8)
O(1)-C(8)          142.0(11)
O(2)-C(30)         138.2(6)
O(2)-C(33)         143.0(6)
C(1)-C(2)          149.6(10)
C(2)-C(7)          139.4(12)
C(2)-C(3)          139.8(12)
C(3)-C(4)          137.1(12)
C(4)-C(5)          140.2(12)
C(5)-C(6)          136.9(12)
C(6)-C(7)          138.4(12)
C(9)-C(10)         150.94
C(10)-C(11)        138.24
C(10)-C(23)        140.72
C(11)-C(12)        137.09
C(12)-C(13)        139.02
C(13)-C(24)        142.23
C(13)-C(14)        144.02
C(14)-C(15)        133.54
C(15)-C(16)        141.94
C(16)-C(17)        140.13
C(16)-C(25)        142.49
C(17)-C(18)        137.64
C(18)-C(19)        137.15
C(19)-C(20)        139.83
C(20)-C(25)        142.44
C(20)-C(21)        142.67
C(21)-C(22)        135.43
C(22)-C(23)        143.64
C(23)-C(24)        143.35
C(24)-C(25)        141.84
C(26)-C(27)        150.94
C(27)-C(32)        138.60
C(27)-C(28)        139.01
C(28)-C(29)        138.68
C(29)-C(30)        138.29
C(30)-C(31)        138.36
C(31)-C(32)        138.38
C(34)-C(35)        150.91
C(35)-C(36)        139.14
C(35)-C(48)        140.18
C(36)-C(37)        139.63
C(37)-C(38)        138.44
C(38)-C(49)        142.32
```

```
C(38)-C(39)                 142.76
C(39)-C(40)                 134.67
C(40)-C(41)                 142.98
C(41)-C(42)                 139.47
C(41)-C(50)                 142.79
C(42)-C(43)                 138.70
C(43)-C(44)                 140.05
C(44)-C(45)                 138.12
C(45)-C(46)                 141.75
C(45)-C(50)                 142.54
C(46)-C(47)                 134.70
C(47)-C(48)                 143.59
C(48)-C(49)                 143.75
C(49)-C(50)                 141.11
C(9)-N(1)-C(1)              108.8(6)
C(34)-N(2)-C(26)            108.5(5)
C(5)-O(1)-C(8)              116.6(8)
C(30)-O(2)-C(33)            116.7(4)
C(2)-C(1)-N(1)              114.9(7)
C(7)-C(2)-C(3)              118.5(6)
C(7)-C(2)-C(1)              118.3(8)
C(3)-C(2)-C(1)              122.9(9)
C(4)-C(3)-C(2)              120.7(8)
C(3)-C(4)-C(5)              120.0(8)
C(6)-C(5)-O(1)              124.8(8)
C(6)-C(5)-C(4)              119.7(6)
O(1)-C(5)-C(4)              115.5(7)
C(5)-C(6)-C(7)              120.4(8)
C(6)-C(7)-C(2)              120.6(8)
N(1)-C(9)-C(10)             114.2(3)
C(11)-C(10)-C(23)          120.3
C(11)-C(10)-C(9)           123.4
C(23)-C(10)-C(9)           116.3
C(12)-C(11)-C(10)          121.3
C(11)-C(12)-C(13)          121.4
C(12)-C(13)-C(24)          118.7
C(12)-C(13)-C(14)          123.0
C(24)-C(13)-C(14)          118.3
C(15)-C(14)-C(13)          121.9
C(14)-C(15)-C(16)          121.1
C(17)-C(16)-C(15)          123.1
C(17)-C(16)-C(25)          117.7
C(15)-C(16)-C(25)          119.1
C(18)-C(17)-C(16)          121.7
C(19)-C(18)-C(17)          120.7
C(18)-C(19)-C(20)          120.9
C(19)-C(20)-C(25)          118.8
C(19)-C(20)-C(21)          123.0
C(25)-C(20)-C(21)          118.2
C(22)-C(21)-C(20)          122.5
C(21)-C(22)-C(23)          120.9
C(10)-C(23)-C(24)          118.5
C(10)-C(23)-C(22)          123.6
C(24)-C(23)-C(22)          117.9
C(25)-C(24)-C(13)          119.5
C(25)-C(24)-C(23)          120.7
C(13)-C(24)-C(23)          119.8
C(24)-C(25)-C(20)          119.9
C(24)-C(25)-C(16)          120.0
C(20)-C(25)-C(16)          120.2
C(27)-C(26)-N(2)           114.9(3)
```

```
C(32)-C(27)-C(28)          118.1
C(32)-C(27)-C(26)          118.6
C(28)-C(27)-C(26)          123.0
C(29)-C(28)-C(27)          121.6
C(30)-C(29)-C(28)          119.0
O(2)-C(30)-C(29)           125.1(2)
O(2)-C(30)-C(31)           114.5(2)
C(29)-C(30)-C(31)          120.4
C(30)-C(31)-C(32)          119.8
C(31)-C(32)-C(27)          121.0
N(2)-C(34)-C(35)           113.3(3)
C(36)-C(35)-C(48)          118.7
C(36)-C(35)-C(34)          117.9
C(48)-C(35)-C(34)          123.1
C(35)-C(36)-C(37)          122.5
C(38)-C(37)-C(36)          119.8
C(37)-C(38)-C(49)          119.7
C(37)-C(38)-C(39)          121.7
C(49)-C(38)-C(39)          118.6
C(40)-C(39)-C(38)          121.6
C(39)-C(40)-C(41)          121.2
C(42)-C(41)-C(50)          119.7
C(42)-C(41)-C(40)          121.7
C(50)-C(41)-C(40)          118.6
C(43)-C(42)-C(41)          120.5
C(42)-C(43)-C(44)          120.2
C(45)-C(44)-C(43)          121.0
C(44)-C(45)-C(46)          123.8
C(44)-C(45)-C(50)          119.6
C(46)-C(45)-C(50)          116.5
C(47)-C(46)-C(45)          123.5
C(46)-C(47)-C(48)          121.5
C(35)-C(48)-C(47)          123.5
C(35)-C(48)-C(49)          119.8
C(47)-C(48)-C(49)          116.7
C(50)-C(49)-C(38)          120.1
C(50)-C(49)-C(48)          120.6
C(38)-C(49)-C(48)          119.4
C(49)-C(50)-C(45)          121.2
C(49)-C(50)-C(41)          119.9
C(45)-C(50)-C(41)          118.9
```

Symmetry Transformations Used to Generate Equivalent Atoms:

Table 2d. Anisotropic displacement parameters (A^2 x 10^3). The anisotropic displacement factor exponent takes the form:
$$-2 pi^2 [h^2 a*^2 U_{11} + ... + 2 h k a* b* U_{12}]$$

	U_{12}	U_{11}	U_{22}	U_{33}	U_{23}	U_{13}
Cl(1)	47(1)	38(1)	45(1)	−6(1)	−5(1)	0(1)
Cl(2)	44(1)	38(1)	42(1)	−3(1)	−6(1)	2(1)
N(1)	33(3)	41(5)	33(4)	−1(3)	−2(3)	1(3)
N(2)	35(3)	30(4)	41(4)	−1(3)	−1(3)	−1(3)
O(1)	33(3)	62(4)	44(3)	9(4)	−4(3)	−6(2)

|						
O(2)	40(3)	65(5)	41(3)	0(3)	2(2)	-3(3)
C(1)	41(4)	35(5)	46(4)	2(5)	-3(4)	1(3)
C(2)	36(3)	25(4)	43(4)	-2(4)	0(4)	(3)
C(3)	36(4)	41(6)	42(5)	0(4)	-2(4)	(4)
C(4)	43(4)	45(6)	30(5)	7(4)	2(3)	-2(4)
C(5)	37(4)	34(5)	41(4)	-2(5)	2(4)	1(3)
C(6)	40(4)	40(6)	39(5)	-2(4)	-9(4)	(4)
C(7)	38(4)	35(5)	35(4)	5(4)	0(3)	(4)
C(8)	44(5)	72(9)	48(6)	10(6)	-11(4)	-12(5)
C(9)	34(4)	44(6)	46(6)	4(4)	3(3)	-2(4)
C(10)	36(4)	34(5)	35(4)	1(3)	4(3)	3(3)
C(11)	41(4)	38(6)	47(5)	5(4)	-3(3)	-1(4)
C(12)	45(5)	37(6)	55(6)	2(5)	-11(4)	4(4)
C(13)	43(4)	39(5)	34(4)	0(4)	4(3)	-2(4)
C(14)	49(5)	56(7)	43(5)	-7(5)	-5(4)	8(5)
C(15)	46(5)	69(8)	41(5)	-4(5)	-9(4)	3(5)
C(16)	40(4)	70(8)	36(5)	-9(5)	0(3)	-7(5)
C(17)	40(5)	91(9)	49(5)	-18(6)	3(4)	-16(5)
C(18)	62(6)	73(9)	53(6)	-8(5)	11(5)	-29(6)
C(19)	62(6)	57(7)	44(5)	0(5)	5(4)	-16(5)
C(20)	56(5)	47(6)	33(4)	-10(4)	5(4)	-13(4)
C(21)	65(5)	37(5)	36(5)	0(3)	6(4)	-6(4)
C(22)	47(4)	35(5)	33(5)	-1(3)	1(3)	-2(4)
C(23)	40(4)	36(5)	29(4)	-2(3)	4(3)	2(4)
C(24)	42(4)	41(6)	31(4)	-3(4)	1(3)	(4)
C(25)	41(4)	48(6)	36(4)	-8(4)	7(3)	-9(4)
C(26)	32(4)	44(6)	53(5)	0(4)	-3(3)	9(4)
C(27)	27(3)	34(5)	43(4)	-2(4)	0(3)	7(3)
C(28)	33(4)	33(5)	41(4)	1(4)	-5(3)	5(4)
C(29)	38(4)	43(6)	35(4)	-2(4)	-1(3)	2(4)
C(30)	33(4)	39(5)	45(5)	2(4)	-2(3)	0(3)
C(31)	39(4)	61(7)	38(5)	-9(4)	-8(4)	-3(4)
C(32)	46(5)	55(7)	39(5)	-4(4)	-3(3)	7(4)
C(33)	46(5)	64(8)	48(5)	0(5)	9(4)	-2(5)
C(34)	39(4)	44(6)	41(5)	12(4)	7(4)	-3(4)
C(35)	35(4)	51(6)	32(4)	3(4)	3(3)	-2(4)
C(36)	44(5)	44(6)	39(5)	-4(4)	3(3)	-8(4)
C(37)	52(5)	37(6)	47(5)	-9(4)	6(4)	-2(4)
C(38)	46(4)	34(5)	34(4)	3(4)	2(3)	-1(4)
C(39)	52(5)	44(6)	46(5)	-2(4)	4(4)	12(4)
C(40)	38(4)	60(7)	50(5)	8(5)	2(4)	5(4)
C(41)	45(5)	51(7)	45(5)	8(4)	-6(4)	-7(4)
C(42)	46(5)	62(7)	48(5)	4(5)	-3(4)	-4(4)
C(43)	51(5)	66(8)	44(5)	5(5)	-3(4)	-18(5)
C(44)	77(6)	48(7)	38(5)	-1(4)	3(4)	-17(5)
C(45)	48(5)	37(5)	41(5)	1(4)	0(4)	-5(4)
C(46)	64(6)	36(5)	36(5)	-1(4)	4(4)	-6(4)
C(47)	43(5)	49(6)	38(5)	0(4)	5(3)	-1(4)
C(48)	39(4)	34(5)	29(4)	1(3)	1(3)	2(3)
C(49)	42(4)	40(5)	25(4)	3(4)	2(3)	-5(4)
C(50)	46(4)	46(6)	28(4)	4(4)	-2(3)	-6(4)

Table 2e. Hydrogen coordinates (x 10^4) and isotropic displacement parameters (A^2 x 10^3) for *N*-4-methoxybenzyl-pyren-1-yl-ammonium chloride.

	x	y	z	U(eq)
H(1A)	0.736(3)	0.162(17)	0.233(8)	0.09(4)
H(1B)	0.746(2)	0.039(12)	0.154(6)	0.04(2)
H(2A)	0.7530(19)	0.656(12)	0.461(5)	0.02(2)
H(2B)	0.746(2)	0.528(15)	0.383(7)	0.08(3)
H(1C)	0.766(2)	-0.062(12)	0.318(6)	0.04(2)
H(1D)	0.776(2)	-0.173(13)	0.216(5)	0.04(2)
H(3)	0.815(2)	0.096(10)	0.121(5)	0.026(19)
H(4)	0.877(3)	0.223(14)	0.113(7)	0.07(3)
H(6)	0.878(2)	0.192(14)	0.393(7)	0.06(3)
H(7)	0.819(2)	0.036(12)	0.392(6)	0.05(2)
H(8A)	0.971(2)	0.351(12)	0.310(6)	0.05(2)
H(8B)	0.943(3)	0.205(16)	0.350(7)	0.05(3)
H(8C)	0.926(3)	0.379(19)	0.382(10)	0.11(4)
H(9A)	0.7008	-0.0713	0.2986	0.08(3)
H(9B)	0.7096	-0.1950	0.2130	0.06(3)
H(11)	0.6878	0.2373	0.1447	0.06(3)
H(12)	0.6310	0.3315	0.0795	0.024(18)
H(14)	0.5611	0.2824	0.0430	0.05(3)
H(15)	0.5079	0.1074	0.0477	0.09(4)
H(17)	0.4769	-0.1840	0.0887	0.09(4)
H(18)	0.4809	-0.4655	0.1511	0.11(4)
H(19)	0.5379	-0.5666	0.2139	0.06(3)
H(21)	0.6070	-0.5125	0.2562	0.05(2)
H(22)	0.6600	-0.3324	0.2595	0.033(18)
H(26A)	0.7965	0.4862	0.5393	0.04(2)
H(26B)	0.7926	0.3536	0.4552	0.05(3)
H(28)	0.8107	0.5163	0.2958	0.07(3)
H(29)	0.8652	0.6416	0.2282	0.05(3)
H(31)	0.9041	0.7887	0.4754	0.028(19)
H(32)	0.8486	0.6713	0.5414	0.05(2)
H(33A)	0.9555	0.8470	0.2055	0.08(3)
H(33B)	0.9099	0.8580	0.1897	0.04(2)
H(33C)	0.9306	0.6681	0.1975	0.04(2)
H(34A)	0.7253	0.3284	0.5022	0.06(3)
H(34B)	0.7301	0.4799	0.5775	0.06(3)
H(36)	0.6901	0.7587	0.5549	0.06(3)
H(37)	0.6267	0.8604	0.5448	0.07(3)
H(39)	0.5582	0.8039	0.5080	0.04(2)
H(40)	0.5111	0.6205	0.4541	0.05(3)
H(42)	0.4911	0.3298	0.3897	0.029(19)
H(43)	0.5068	0.0454	0.3379	0.07(3)
H(44)	0.5711	-0.0517	0.3387	0.04(2)
H(46)	0.6403	0.0051	0.3762	0.07(3)
H(47)	0.6878	0.1867	0.4263	0.04(2)

C. Powder X-ray Diffraction Data

1. As$_4$S$_4$

a. Data Collected From the Experiment.
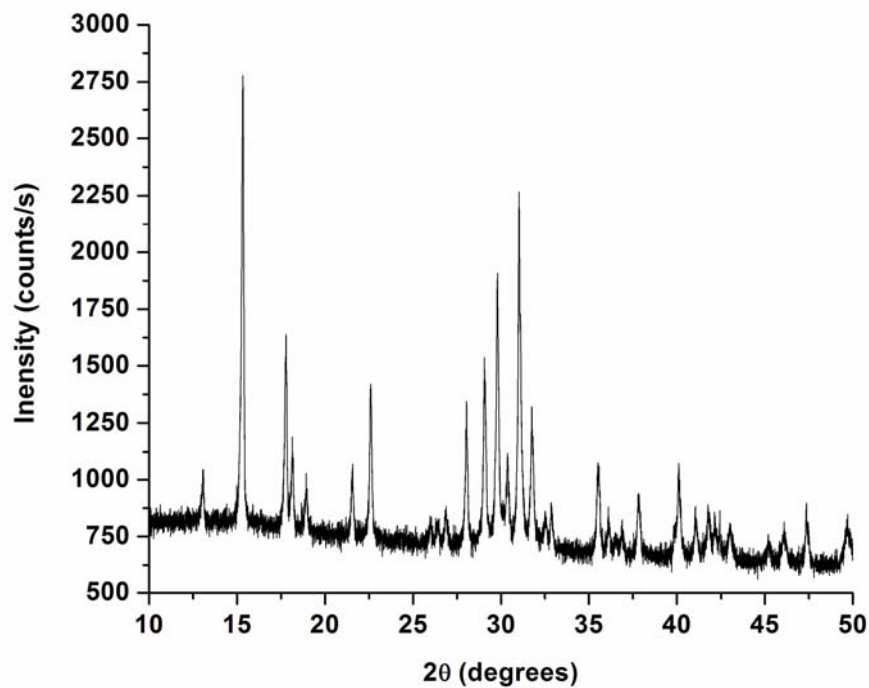
b. As$_4$S$_4$ Spectrum From the JCPDS-ICDD Database (PDF # 24-0078).
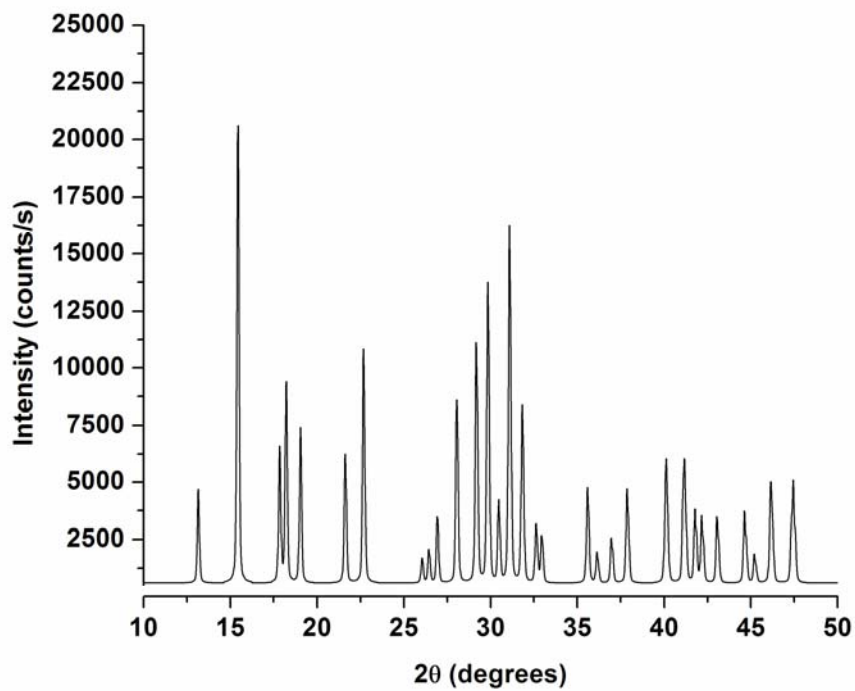
2. Er$_2$S$_3$

a. Data Collected From the Experiment.
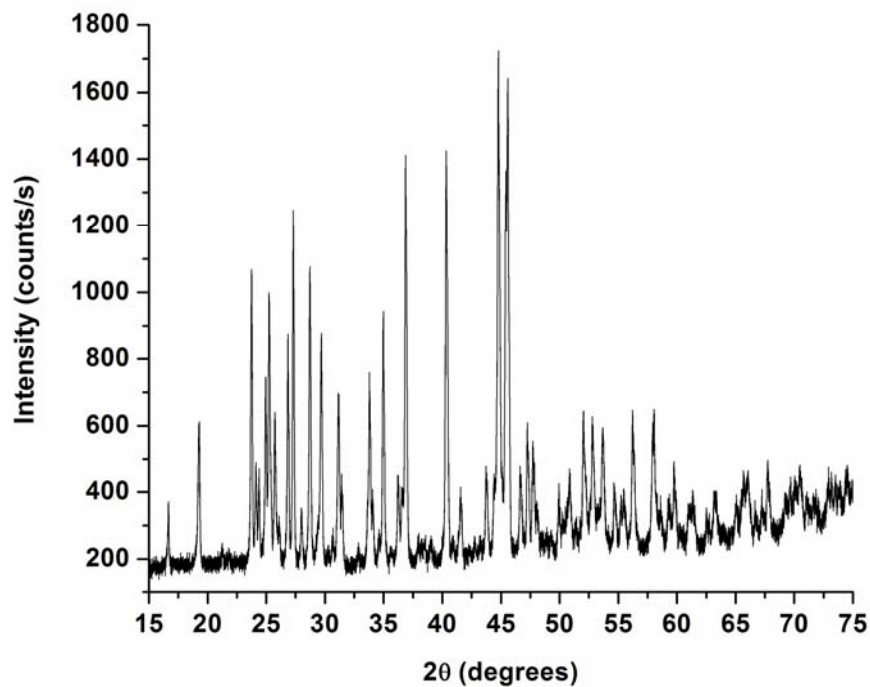
b. Er$_2$S$_3$ Spectrum From the JCPDS-ICDD Database (PDF # 44-1155).
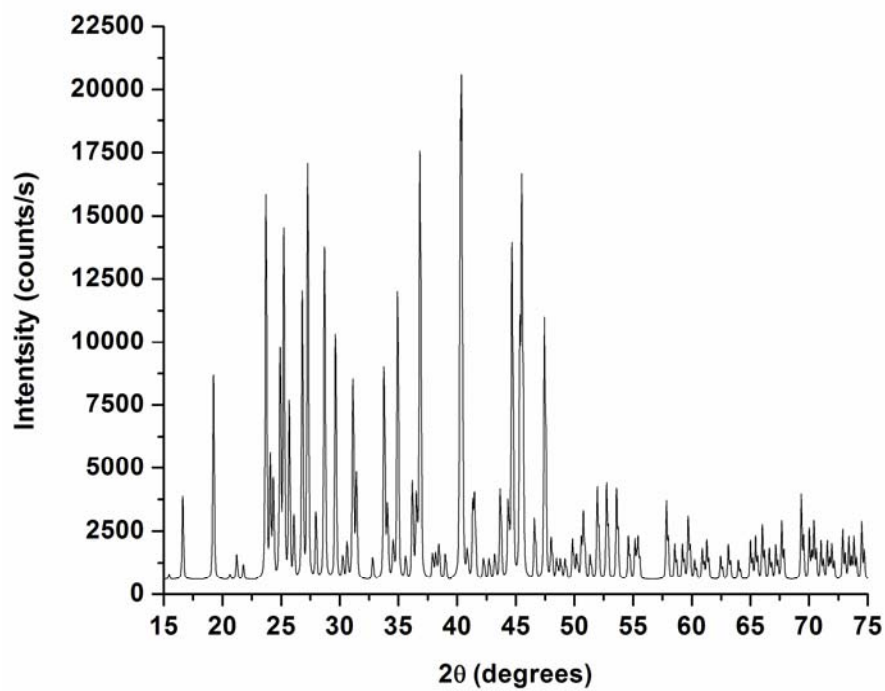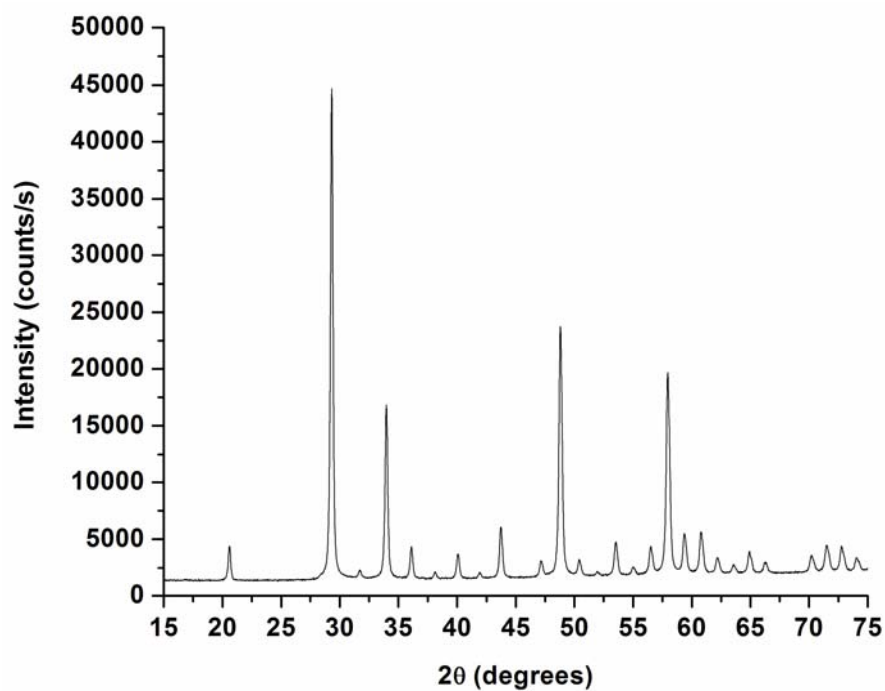
3. Er_2O_3

a. Data Collected From the Experiment.
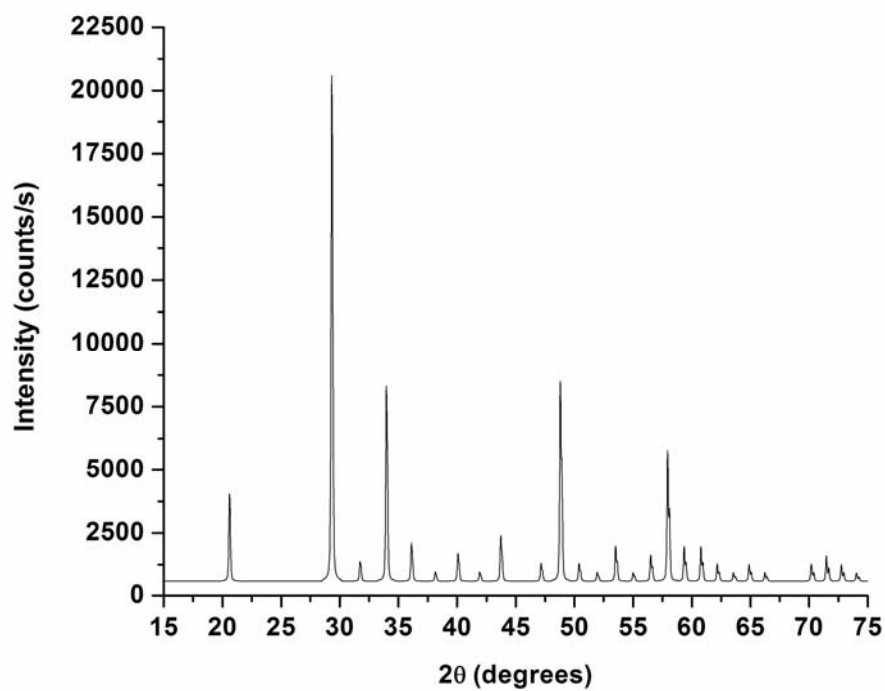
b. Er_2O_3 Spectrum From the JCPDS-ICDD Database (PDF # 08-0050).

D. ^{1}H-NMR and MALDI-TOF Data of All Synthesized Amines.

2. *N*-benzyl-*N*-4-fluorobenzylamine: Light yellow liquid. ^{1}H-NMR (300 MHz, CDCl$_3$, 25 ºC): δ= 7.4 (m, 5H, C$_6$H$_5$), 7.2 (d, 4H, C$_6$H$_4$), 3.8 (d, 4H, 2CH2).
M$_w$= [M+H] = 215.7419 g/mol

3. *Bis*-(4-fluorobenzyl)amine: Yellow liquid. ^{1}H-NMR (300 MHz, CDCl$_3$, 25 ºC): δ= 7.3 (m, 4H, C$_6$H$_4$), 6.9 (m, 4H, C$_6$H$_4$), 3.8 (d, 4H, 2CH2).
M$_w$= [M+H] = 233.5966 g/mol

4. *N*-4-cyanobenzyl-benzonitrile: *(For this reaction, the general reaction procedure was followed, except during the reduction step, the solution was not refluxed, but only allowed to stir at room temperature for 4 hours.)* Yellow-brown liquid. ^{1}H NMR (300 MHz, CDCl$_3$, 25 ºC): δ= 7.6 (d, 2H, C$_6$H$_4$), 7.5 (d, 2H, C$_6$H$_4$), 7.3 (m, 5H, C$_6$H$_5$), 4.1(s, 2H, CH_2), 3.9(s, 2H, CH_2).
M$_w$ = [M+H] = 223.0410 g/mol

5. *N*-benzyl-N-4-methoxybenzylamine: Light yellow liquid. ^{1}H-NMR (300 MHz, CDCl$_3$, 25 ºC): δ= 7.3 (m, 5H, C$_6$H$_5$), 7.2 (d, 2H, C$_6$H$_4$), 6.9 (d, 2H, C$_6$H$_4$), 3.8(d, 7H, 2CH_2, OCH_3).
M$_w$ = [M+H] = 227.7604 g/mol

6. *Bis*-(4-methoxybenzyl)amine: Yellow liquid. ^{1}H-NMR (300 MHz, CDCl$_3$, 25 ºC): δ= 7.6 (d, 4H, 2C$_6$H$_4$), 7.3 (d, 4H, 2C$_6$H$_4$), 4.1(s, 6H, OCH_3), 3.9(s, 4H, 2CH_2).
M$_w$ = [M+H] = 258.8854 g/mol

7. *Bis*-(2,4-dimethoxybenzyl)amine: (*Purchased from Merck KGaA, 99%)*. Almond coloured powder. ^{1}H-NMR (300 MHz, CDCl$_3$, 25 ºC): δ= 7.1 (d, 2H, C$_6$H$_3$), 3.8 (d, 12H, 2xOCH$_3$), 3.7 (s, 2H, CH_2).
M$_w$ = [M+H] = 317.5214 g/mol

8. *N*-benzylaniline: Brown liquid. ^{1}H-NMR (300 MHz, CDCl$_3$, 25 ºC): δ= 7.3 (m, 5H, C$_6$H$_5$), 7.2 (d, 2H, C$_6$H$_4$), 6.7 (m, 3H, C$_6$H$_5$), 4.3(s, 2H, CH_2).
M$_w$ = [M+H] = 183.8854 g/mol

9. *N*-benzyl-4-fluoroaniline: Light brown liquid. ^{1}H-NMR (300 MHz, CDCl$_3$, 25 ºC): δ= 7.3 (m, 5H, C$_6$H$_5$), 6.8 (t, 2H, C$_6$H$_4$), 6.6 (q, 2H, C$_6$H$_4$), 4.3 (s, 2H, CH_2).
M$_w$ = [M+H] = 201.8775 g/mol

10. *N*-benzyl-4-methoxyaniline: Dark, black brown liquid. ^{1}H-NMR (300 MHz, CDCl$_3$, 25 ºC): δ= 7.3 (m, 5H, C$_6$H$_5$), 6.8 (d, 2H, C$_6$H$_4$), 6.6 (d, 2H, C$_6$H$_4$), 4.3(s, 2H, CH_2), 3.7(s, 3H, OCH_2).
M$_w$ = [M+H] = 213.4167 g/mol

11. *N*-benzylnaphthalen-1-ylmethanamine: Brown liquid, ^{1}H NMR (300 MHz, CDCl$_3$, 25 ºC): δ= 8.1 (d, 1H, C$_{10}$H$_7$), 7.8 (dd, 2H, C$_{10}$H$_7$), 7.3 (m, 9H, C$_6$H$_5$, C$_{10}$H$_7$), 4.3 (s, 2H, CH_2), 3.9 (s, 2H, CH_2).
M$_w$ = [M+H] = 247.7438 g/mol

12. 1-(9-anthryl)-*N*-benzylmethanamine: Yellow solid. ^{1}H NMR (300 MHz, CDCl$_3$, 25 ºC): δ= 8.4 (s, 1H, C$_{14}$H$_9$), 8.2 (d, 2H, C$_{14}$H$_9$), 8.0 (d, 2H, C$_{14}$H$_9$), 7.3 (m, 11H, C$_6$H$_5$, C$_{10}$H$_7$), 4.7 (s, 2H, CH$_2$), 4.0 (s, 2H, CH$_2$).
M$_w$ = [M+H] = 297.0961 g/mol

13. *Bis*-(1-naphthylmethyl)amine: Brown liquid, ^{1}H NMR (300 MHz, CDCl$_3$, 25 ºC): δ= 8.1 (d, 2H, 2C$_{10}$H$_7$), 7.9 (d, 2H, 2C$_{10}$H$_7$), 7.8 (d, 2H, 2C$_{10}$H$_7$), 7.3 (m, 8H, 2C$_{10}$H$_7$), 4.4 (s, 4H, 2CH$_2$).
M$_w$ = [M+H] = 297.8560 g/mol

14. 1-(1-pyrenyl)-*N*-benzylmethanamine: Orange solid. ^{1}H NMR (300 MHz, CDCl$_3$, 25 ºC): δ= 8.3 (d, 1H, C$_{16}$H$_9$), 8.0 (m, 8H, C$_{16}$H$_9$), 7.3 (m, 5H, C$_6$H$_5$), 4.0 (s, 2H, CH$_2$). M$_w$ = [M+H] = 321.8269 g/mol

15. 1-(1-naphthyl)-*N*-(1-naphthylmethyl)methanamine: White flakes. ^{1}H NMR (300 MHz, (C$_6$D$_6$, 25 ºC): δ= 8.1 (d, 1H, C$_{10}$H$_7$), 7.8 (d, 2H, C$_{10}$H$_7$), 7.7 (d, 2H, C$_{10}$H$_7$), 7.3 (m, 7H, C$_{10}$H$_7$), 4.6 (d, 2H, CH$_2$).
M$_w$ = [M+H] = 282.5986 g/mol

E. Tabulated Data of the Etch Rates and Etch Selectivity of the Amine Molecules Used in This Study

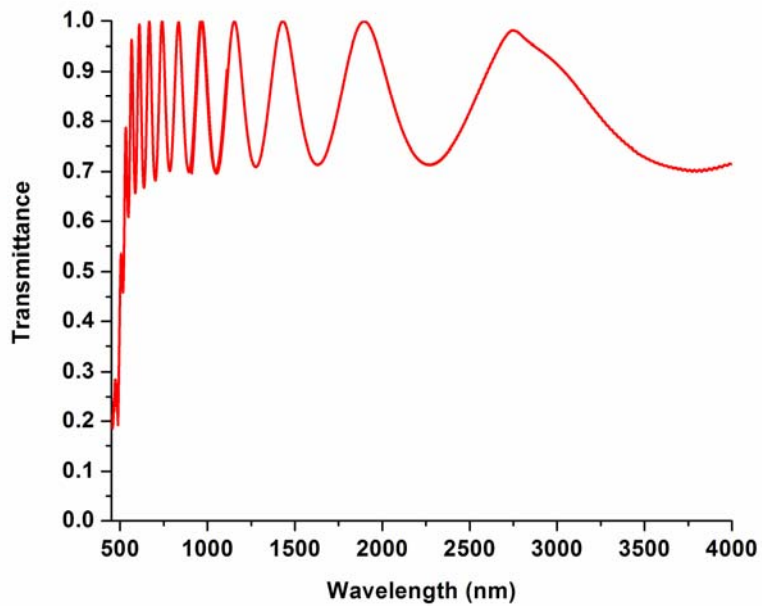| Amine identity	K_u (nm/min)	K_e (nm/min)	Selectivity (γ)
1	476	379	1.26
2	306	212	1.44
3	207	114	1.81
4	188	30	6.27
5	513	219	2.34
6	826	304	2.72
7	1020	349	2.92
8	NR	NR	-
9	NR	NR	-
10	NR	NR	-
11	111	33	3.36
12	84.7	5.02	16.87
13	59.7	5.31	11.24
14	98	0.87	113.79
15	NR	NR	-
16	210	0.61	344.26
triethylamine	NR	NR	-

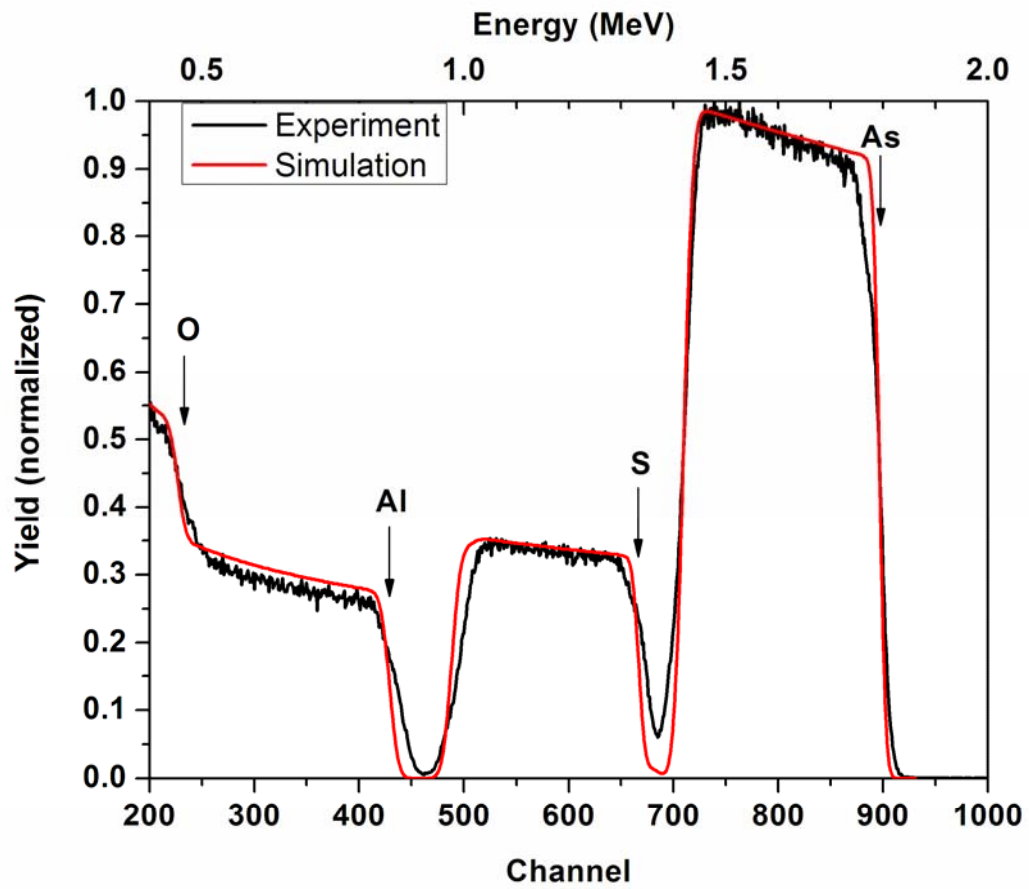## F. VIS/NIR Spectrum of Photo-Exposed As_2S_3 and $Er:As_2S_3$

1. As_2S_3
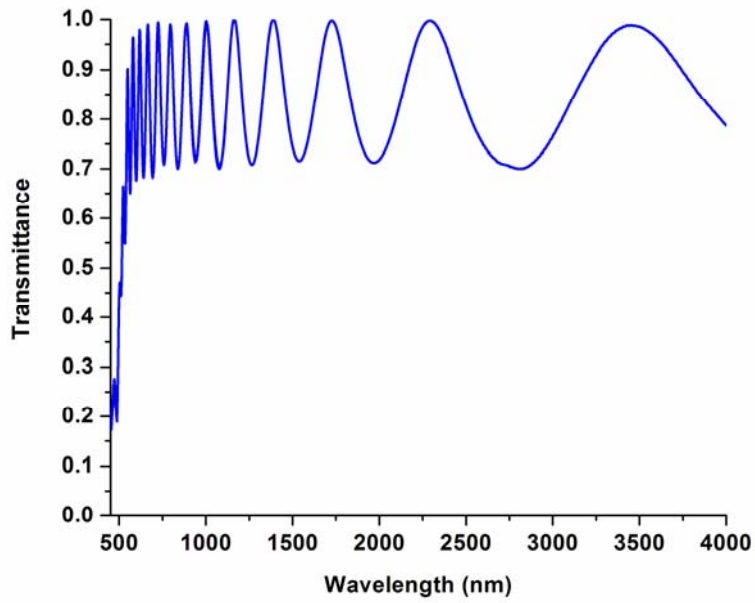
2. $Er:As_2S_3$ (1.35 wt %)

G. Rutherford Backscattering Data for As$_2$S$_3$

Acknowledgements

First and foremost, I would like to thank Prof. Dr. Martin Wegener and Prof. Dr. Dieter Fenske for inviting me to the Universität Karlruhe (TH) to conduct research towards obtaining my Doctoral thesis. It had been a wonderful opportunity to study abroad and to learn and do things from a different perspective. The almost unlimited financial support that was available for experimental work has enabled me to perform research that was only limited by my own ambitions and abilities.

I would also like to thank Dr. Georg von Freymann for providing me with support and help of all kinds during my Doctoral research work, and most importantly, for being a good friend and mentor at all times. It is nice to see that a friendship and scientific collaborations starting in Toronto can end successfully with publications, patents and a start-up in Karlsruhe. I would say that this 3 year journey had been unpredictable and had many surprising and rewarding outcomes. This is just how I like it.

I would like to thank Prof. Geoffrey A. Ozin for being there to consult me during my thesis work and provide much needed guidance to get me out of the low points and dead-ends. Thank you for being there for me throughout my scientific career, through the good and the bad, locally in Toronto and across the ocean in Germany. Your care and cultivation throughout the years has played a large role in my progress as a materials chemist.

I would also like to thank the people that I have had the pleasure to work with throughout these past few years in the workgroup of Prof. Wegener, especially:

Dr. Stefan Linden, Dr. Christian Enkrich, Dr. Markus Deubel, Dr. Torsten Trichler, Dr. Christiane Becker, Dr. Daniel Meisel, Martin Hermatschweiler, Wolfram Kwapil, Boris Reidel, Alexandra Ledermann, Isabelle Staude, Dominic Deichle, Nils Feth, Michael Rill, Matthias Ruther, Christian Röthig and Jörge Wissler.

Furthermore, I would like to thank the following co-investigators that have contributed their time and efforts towards the experimental results that are presented in this Doctoral thesis:

- Michael "Direct-Mike" Thiel (INT,FZK and AP, UniKa) for 3D structural design and implementation.
- Markus Braun (INT, FZK) for contributing towards the successful Er doping experiments.
- Peter Brodersen (University of Toronto, Canada) for the XPS spectroscopy experiments.
- Dr. Jorge K. Lindner (Universität Augsburg) for the RBS spectroscopy experiments.
- Dr. Frank Peiris and Nirajan Mandal (Kenyon College, USA) for the thin film ellipsometery experiments.
- Oliver Kiowski and Prof. Manfred Kappes (INT, FZK and IPC, UniKa) for PL and PLE experiments.
- Dr. Aline Leon (INT, FZK) and Dr. Jörge Röthe (INE,FZK) for EXAFS measurements and analysis.

Curriculum Vitae

Name: Sean Hang Edmond Wong

Date and place of birth: July 06, 1979 in Hong Kong, China

Current Citizenship status: Canadian

Education

1993 to 1998 Attended Brebeuf College Secondary School in Toronto, Canada.

1998 to 2003 Studied materials chemistry at the undergraduate level at the University of Toronto, Canada.
Degree obtained: Hon.B.Sc. Materials Chemistry.

2003 to 2004 Studied inorganic chemistry at the Master's level at the University of Toronto, Canada. (Thesis supervised by Prof. Dr. Geoffrey A. Ozin.)
Degree obtained: M.Sc. Inorganic Chemistry.

Thesis topic: Fabrication of three-dimensional photonic crystals via direct laser writing in an all-inorganic photoresist.

2005 to 2008 Joined the research group of Prof. Dr. Martin Wegener (Institut für Angewandte Physik) and Prof. Dr. Dieter Fenske (Institut für Anorganishe Chemie), at the Universität Karlsruhe (TH), in Karlsruhe, Germany.
Candidate for the degree of: Dr. rer. nat. Inorganic Chemistry.

Thesis topic: Arsenic Trisulfide Inorganic Photoresist for Three-Dimensional Photolithography.

2007 to pres. Accepted as a collegiate in the Karlsruhe School of Optics (KSOP).

Scientific work experience

2007 to pres. Leader of material research and development. **Nanoscribe GmbH,** Karlsruhe, Germany.

Scientific patents

1. WO 2006015989   February 2006   S. Wong, et al.

2. US 2008128391   June 2008   S. Wong, et al.

List of scientific publications (years 2006 – 2008)

Elastic photonic crystals: from color fingerprinting to control of photoluminescence, Andre Arsenault, Ludovico Cademartiri, Tim Clark, Nicolas Tetreault, Augustin Mihi, Evangellos Vekris, Xavier Sapienza, Dedrick Wiersma, Sean Wong, Sajeev John, Ian Manners, Geoffery A. Ozin, *Nature Materials* (2006), 5, 179-184.

Direct Laser Writing of Three-Dimensional Photonic Crystals with a Complete Photonic Bandgap in Chalcogenide Glasses, Sean Wong, Markus Deubel, Fabian Pérez-Willard, Sajeev John, Geoffrey A. Ozin, Martin Wegener, and Georg von Freymann, *Advanced Materials* (2006), 3, 265-269.

Phase-matched non-degenerate four-wave mixing in one-dimensional photonic crystals, Christiane Becker, Martin Wegener, Sean Wong, Georg von Freymann, Applied Physics Letters (2006), 89, 131122.

Highly Selective Wet Etch for High Resolution Three-Dimensional Nanostructures in Arsenic Sulphide All Inorganic Photoresist, Sean H. Wong, Michael Thiel, Peter Brodersen, Dieter Fenske, Geoffrey A. Ozin, Martin Wegener, Georg von Freymann, *Chemistry of Materials* (2007), 19(17), 4213.

Spatially localized photoluminescence at 1.5 micrometers wavelength in direct laser written 3D structures. Sean Wong, Oliver Kiowski, Manfred Kappes, Jörge K. Lindner, Nirajan Mandal, Frank C. Peiris, Geoffrey A. Ozin, Michael Thiel, Markus Braun, Martin Wegener, and Georg von Freymann. *Advanced Materials* (2008), *Accepted.*

Others literary contributions:

 "A new way to Control light" *Nature Nanozone* (Online research highlight written by the editor of the journal, Phillip Ball.) 12 January, 2006.

"**Here is a new direct laser-writing technique.**" *Heart Cut* (Online research highlight of the American Chemical Society (ACS), written by George Xiu Song Zhao.) March 20, 2006.

Scientific conference contributions

Oral presentation: Direct Laser Writing of Three-Dimensional Photonic Crystals in High Index of Refraction Chalcogenide Glasses. S.Wong, G. von Freymann, M. Deubel, G. A. Ozin, and M. Wegener.
Frühjahrstagung der DPG 2005 (2005 Spring conference of the German Physical Society), March 3-9, Berlin, Germany.

Oral presentation: *Fabrication of 3D nanostructures using an all-inorganic glass As_2S_3.*
S.Wong, M.Thiel, M. Braun, A. Lederman, G. A. Ozin, D. Fenske, M. Wegener, G. von Freymann.
2007 MRS Spring meeting, April 9 - 13, 2007, San Francisco, USA.

Oral presentation: *Er Doped As_2S_3 Photoresist for 3D Direct Laser Fabrication of 3D Nanosctructures.* S. Wong, G. von Freymann, D. Fenske, O. Kiowski, M. Kappes, F. Peiris, J. Lindner, G. A. Ozin, M. Thiel, M. Braun, A. Ledermann and M. Wegener.
2008 CLEO/QUELS, May 5 - 9, 2008, San Jose, USA.

Industrial conference contributions

Oral presentation: *As_2S_3-an inorganic photoresist system for 3D photolithography.*
S.Wong, M.Thiel, M. Braun, G. A. Ozin, D. Fenske, M. Wegener, G. von Freymann.
KSOP Autumn Colloquium 2007, September 20-21, 2007, Carl Zeiss AG, Oberkochen, Germany.

Poster presentation: *Fabrication of 3D structures in an all-inorganic glass As_2S_3.*
S. Wong, M. Thiel, G. Ozin, D. Fenske, M. Wegener, G. Freymann.
BASF Conference on Nanotechnology, October 21-23, 2007, Singapore, Singapore.

References:

[1] Yablonovitch, E. Inhibited spontaneous emission in solid state-physics and electronics. *Phys. Rev. Lett.* **58**, 2059–2062 (1987).

[2] John, S. Strong localization of photons in certain disordered dielectric superlattices. *Phys. Rev. Lett.* **58**, 2486–2489 (1987).

[3] Vukovic, J., Loncar, M., Mabuchi, H., Scherer, A. Design of photonic crystal microcavities for cavity QED. *Phys. Rev. E* **65**, 016608 (2002).

[4] Florescu, M., John, S. Resonance fluorescence in photonic band gap waveguide architectures: Engineering the vacuum for all-optical switching. *Phys. Rev. A* **69**, 053810 (2004).

[5] Ogawa, S. P. et al. Control of light emission by 3D photonic crystals. *Science* **305**, 227-229 (2004).

[6] Tétreault, N. et al. New route to three-dimensional photonic-bandgap materials: silicon double inversion of polymer templates. *Adv. Mater.* **18**, 457-460 (2006).

[7] Hermatschweiler, M., Ledermann, A., Ozin, G. A., Wegener, M., von Freymann, G. Fabrication of silicon inverse woodpile photonic crystals. *Adv. Func. Mater.* **17**, 14, 2273-2277 (2007).

[8] Ventura, M. J., Bullen, C., Min, G. Direct laser writing of three-dimensional photonic crystal lattices within a PbS quantum-dot-doped polymer material, *Optics Express* **15**, 1817-1822 (2007).

[9] Sun, Z.-B. et al. Multicolor polymer nanocomposites: *In situ* synthesis and fabrication of 3D microstructures. *Adv. Mater.* **20**, 5, 914-919 (2008).

[10] Lodal, P. et al. Controlling the dymanics of spontaneous emission from quantum dots by photonic crystals. *Nature* **430**, 654-657 (2004).

[11] Busch, K. et al. Periodic nanostructures for photonics. *Physics Reports* **444**, 101-202 (2007).

[12] Joannopoulous, J. D. *Photonic crystals: Molding the flow of light*. (Princepton University Press, New Jersey, 1995).

[13] Chutinan, A., John, S., Toader, O. Diffractionless flow of light in All-optical microchips. *Phys. Rev. Lett.* **90**, 233901 (2003).

[14] Chutinan, A., John, S. Diffractionless flow of light in two- and three-dimensinoal photonic bandgap hetereostructures: Theory, design rules, and simulations. *Phys. Rev. Lett.* **71**, 026605 (2005).

[15] Wong, S., Kitaev, V, Ozin, G. A. Colloidal crystal films: Advances in universality and perfection. *J. Am. Chem. Soc.* **125**, 50, 15589-15598 (2003).

[16] Meisel, D. C., Wegener, M., Busch, K. Three-dimensional phtonic crystals by holographic lithography using the umbrella configuration: symmetries and complete photonic band gaps. *Phys. Rev B* **70**, 165104 (2004).

[17] Kawata, S., Sun, H.-B., Tanaka, T. & Takada, K. Finer features for functional microdevices. *Nature* **412**, 697–698 (2001).

[18] Vekris, V. et al. Visualization of stacking faults and their formation in colloidal photonic crystal films. *Adv. Mater.* **20**, 6, in-press (2008).

[19] Rinnie, S. A., García-Santamaria, F., Braun, P. V. Embedded cavities and waveguides in three-dimensional photonic crystals. *Nat. Mater.* **2**, 52-56 (2008).

[20] Tétreault, N. et al. New route to three-dimensional photonic-bandgap materials: silicon double inversion of polymer templates. *Adv. Mater.* **18**, 457-460 (2006).

[21] Deubel, M., Wegener, M., Linden, S., von Freymann, G., John, S. 3D-2D-3D photonic crystal heterostructures by direct laser writing. *Opt. Lett.* **31**, 805-807 (2006).

[22] Deubel, M. et al. Direct laser writing of three-dimensional photonic-crystal templates for telecommunications. *Nature Mater.* **3**, 444-447 (2004).

[23] Deubel, M., Wegener, M., Kaso, A. & John, S. Direct laser writing and characterization of "Slanted Pore" photonic crystals. *Appl. Phys. Lett.* **85**, 1895-1897 (2004).

[24] Seet, K. K., Mizeikis, V., Matsuo, S., Juodkazis, S. & Misawa, H. Three-dimensional spiral-architecture photonic crystals obtained by direct laser writing. *Adv. Mater.* **17**, 541-545 (2005).

[25] Hermatschweiler, M., Ledermann, A., Ozin, G. A., Wegener, M., von Freymann, G. Fabrication of silicon inverse woodpile photonic crystals. *Adv. Func. Mater.* **17**, 14, 2273-2277 (2007).

[26] Ledermann, A. et al. Three-dimensional silicon inverse photonic quasicrystals for infrared wavelengths. *Nature Mater.* **5**, 942-945 (2006).

[27] Popescu, M. *Non-Crystalline Chalcogenides*. pp 109 (Kluwer Academic Publishers, Dordrecht, Netherlands, 2000).

[28] Kolobov, A. *Photo-induced metastability in amorphous semiconductors*. (Wiley-VCH GmbH & Co. KGaA, Weinheim, 2003).

[29] Kolobov, A. V. et al. Understanding the phase-change mechanism of rewritable optical media. *Nat. Mater.* **3**, 703-708 (2004).

[30] Feigel, A. et al. Three-dimensional simple cubic woodpile photonic crystals made from chalcogenide glasses. *Appl. Phys. Lett.* **83**, 4480-4482 (2003).

[31] Feigel, A. et al. Chalcogenide glass-based three-dimensional photonic crystals. *Appl. Phys. Lett.* **77**, 3221-3223 (2000).

[32] Hilton, A.R., Hayes, D.J., Rechtin, M.D. Infrared absorption of some high-purity chalcogenide glasses. *J. Non-Cryst. Sol.*, **17**, 319-338 (1975).

[33] Popescu, M. *Non-crystalline chalcogenides*. pg 4 - 44 (Kluwer Academic Publishers, Dordrecht, Netherlands, 2000).

[34] Stuke, J. Review of optical and electrical properties of amorphous semiconductors. *J. Non-Cryst. Solids.*, **4** 1-26 (1970).

[35] Polak, Z., Frumari, M., Frumarová, B. Photoinduced changes of the structure and index of refraction of amorphous As-S films. *Thin Solid Films* **343-344**, 484-487 (1999).

[36] Aleksandrov, A.P. et al. Formation of microstructures in As_2S_3 by a femtosecond laser pulse train. *Quant. Electron.* **31**, 5, 398-400 (2001).

[37] Frumar, M., Vleck, M., Polak, Z., Cernosek, Z. Photoinduced changes of the reactivity of amorphous chalcogenide layers. *J. Non-Cryst. Sol.* **221**, 27-33 (1997).

[38] Stoycheva, R., Simidchieva, P., Buroff, A. Temperature dependence of the photodissociation of a-As_2S_3. *J. Non-Cryst. Solids* **90**, 541-544 (1987).

[39] Vlček, M., Prokop, J., Frumar, M. Positive and negative etching of As-S thin layers. *Int. J. Electronics* **77**, 6, 969-973 (1994).

[40] Desurvire, E., Simpson, J. R., Becker, P. C. High-gain erbium-doped travelling-wave fiber amplifier. *Optics Lett.* **12**, 11, 888-980 (1987).

[41] Chutinan, A., John, S. 3+1 dimensional integrated optics with localized light in a photonic band gap. *Optics Express* **14**, 3, 1266-1279 (2006).

[42] Tanaka, K. Reversible photostructural change: Mechanisms, properties and applications. *J. Non-Cryst. Solids* **35&36**, 1023-1034 (1980).

[43] Martin T. P. Arsenic trisulfide clusters. *Solid State Comm.* **47**, 2 111-114 (1983).

[44] De Neufville, J. P., Moss, S. C., Ovshinsky, S. R. Photostructural transformations in amorphous As_2Se_3 and As_2S_3 films. *J. Non-Cryst. Solids* **13**, 191-223 (1973/74).

[45] Sarsembinov, Sh. Sh. et al. Differences in local structure between amorphous As-Se films prepared by different methods. *Semicond. Sci. Technol.* **17**, 1072-1074 (2002).

[46] Wright, A. C., Sinclair, R. N., Leadbetter, A. J. Effect of preparation method on the structure of amorphous solids in the system As-S. *J. Non-Cryst. Solids* **71**, 295-302 (1985).

[47] Mikhailov, M. D., Kryzhanowsky, I. I., Petcherizin, I. M. Structure and properties of ion-beam sputtered As_xS_{1-x} films. *J. Non-Cryst. Solids* **265**, 1-8 (2000).

[48] Špalt, Z., Alberti, M., Peña-Méndez, E., Havel, J. Laser ablation generation of arsenic sulfide clusters. *Polyhedron*, **24**, 1417-1424 (2005).

[49] Zakery, A. et al. Low-loss waveguides in ultrafast laser-deposited As_2S_3 chalcogenide films. *J. Opt. Soc. Am. B* **9**, 1844-1852 (2003).

[50] Choi, D-Y. et al. Nano-phase separation of arsenic tri-sulphide (As_2S_3) films and its effect on plasma etching. *J. Non-Cryst. Solids* **353**, 953-955 (2007).

[51] White, K., Kumar, B., Rai, A. K. Effect of deposition rate on structures and properties of As_2S_3 film. *Thin Solid Films* **161**, 1390147 (1988).

[52] Petkov, K., Vlchek, M., Frumar, M. Photo- and thermo-induced changes in the properties of thin amorphous As-S films. *J. Mat. Sci.*, **27**, 3281-3285 (1992).

[53] Zoubir, A. et al. Direct femtosecond laser writing of waveguides in As_2S_3 thin films. *Opt. Lett.* **29**, 7, 748-750, (2004).

[54] Wong, S. et al. Direct laser writing of three-dimensional photonic crystals with a complete photonic bandgap in chalcogenide glasses. *Adv. Mater.* **18**, 265-269 (2006).

[55] Nemanich, R.J., Connell, G. A., Hayes, T. M., Street, R.A. Thermally induced effects in evaporated chalcogenide films. I. Structure. *Phys. Rev. B* **18**, 12, 6900-6914 (1978).

[56] Keneman, S. A., Bordogona, J., Zemel, J. N. Evaporated films of arsenic trisulfide: Physical model of effects of light exposure and heat cycling. *J. Appl. Phys.,* **49**, 9, 4663-4673 (1978).

[57] Špalt, Z., Alberti, M., Peña-Méndez, E., Havel, J. Laser ablation generation of arsenic sulfide clusters. *Polyhedron*, **24**, 1417-1424 (2005).

[58] Chiavari, G., Fabbri, D., Galletti, G.C. Pyrolysis/gas chromatography/mass spectrometry of arsenic inorganic compounds. *Rapid Comm. Mass. Spec.* **9**, 559-562 (1995).

[59] Janai M., Rudman, P. S., Mandelbaum, A. Mass spectrometric analysis of arsenic trisulfide. *J. Non-Cryst. Solids* **27**, 67-73 (1978).

[60] Aio, L.G., Efimov, A.M., Kokorina, V.F. Refractive index of chalcogenide glasses over a wide range of compositions. *J. Non-Cryst. Solids* **27**, 299-307 (1978).

[61] Nemanich, R.J., Connell, G. A., Hayes, T. M., Street, R.A. Thermally induced effects in evaporated chalcogenide films. I. Structure. *Phys. Rev. B* **18**, 12, 6900-6914 (1978).

[62] Mikla, V. I. Photoinduced structural changes and related phenomena in amorphous arsenic chalcogenides. *J. Phys. Condens. Matter.* **8**, 429-448 (1996).

[63] De Neufville, J. P., Moss, S. C., Ovshinsky, S. R. Photostructural transformations in amorphous As_2Se_3 and As_2S_3 films. *J. Non-Cryst. Solids* **13**, 191-223 (1973/74).

[64] Schulte, A. et al. Bulk-film structural differences of chalcogenide glasses probed in situ by near-infrared waveguide Raman spectroscopy. *Optics Comm.* **198**, 1-3, 125-128 (2001).

[65] Maruno, S., Noda, M. Microstructure of glasses in the system As_2S_x with $x<3$. *J. Non-Cryst. Solids* **7**, 1-11 (1972).

[66] Strom, U., Martin T. P. Photoinduced changes in the infrared vibrational spectrum of evaporated As_2S_3. *Solid State Comm.* **29**, 527-530 (1979).

[67] Tikhomirov, V. K., Barj, M., Turrell, S. Three-dimensional direct optical writing and Raman characterization of reslting structural changes in As_2S_3 glasses. *Phil. Mag. Lett* **85,** 7, 325-330 (2005).

[68] Koblinska, R. J., Solin, S. A. Temperature dependence of the Raman spectrum and the depolarization spectrum of amorphous As_2S_3. *Phys. rev. B* **8**, 2, 756-768 (1973).

[69] Ward, A. T. Raman spectroscopy of sulfur, sulfur-selenium, and sulfur-arsenic mixtures. *J. Phys. Chem.* **72**, 12, 4133-4139 (1968).

[70] Wong. S. H., Thiel, M. Brodersen, P., Fenske, D., Ozin, A. G., Wegener, M., von Freymann, G. Highly selective wet etch for high-resolution three-dimensional nanostructures in arsenic sulfide all-inorganic photoresist. *Chem. Mater.* **19**, 4213-4221 (2007).

[71] Stec, W. J., Morgan, W. E., Albridge, R. G., van Wazer, J. R. Measured binding energy shifts of the "3p" and "3d" electrons in arsenic compounds. *Inorg. Chem.* **11**, 2, 219-225 (1972).

[72] Pratt, A. R., Nesbitt, H. W. Core level electron binding energies of realgar (As_4S_4). *Amer. Minerologis*, **85**, 619-622 (2000).

[73] Tachibana, A. et al. Electronic behavior of amorphous Chalcogenide models. *J. Phys. Chem.* **82**, 3, 272-277(1978).

[74] Fritzche, H. The origin of reversible and irreversible photostructural changes in chalcogenide glasses. *Phil. Mag. B* **68**, 4, 561-572 (1993).

[75] Fritsche, H. Toward understanding the photoinduced changes in the chalcogenide glasses. *Semiconductors* **32**, 8, 850-854 (1998).

[76] Greenwood, N., Earnshaw, A. Chemistry of the elements, Second Edition. (Butterworth-Heinemann, Oxford, England, 1997).

[77] Street, R. A., Mott, N. F. States in the gap in glassy semiconductors. *Phys. Rev. Lett.* **35**, 19, 1293-1296 (1975).

[78] Lyubin, V., Klebanov, M., Tikhomirov, V. K. Photoinduced anisotropy of photoconductivity in chalcogenide amorphous films. *J. Non-Crst. Solids* **299-302**, 2, 945-948 (2002).

[79] Kastner, M., Adler, D., Fritzsche, H. Valence-alternation model for localized gap states in lone-pair semiconductors. *Phys. Rev. Lett.* **37**, 22, 1504-1507 (1976).

[80] Uchino, T., Clary, D.C., Elliot, S. R. Mechanism of photoinduced changes in the structure and optical properties of amorphous As_2S_3. *Phys. Rev. Lett.* **85**, 15, 3305-3308 (2000).

[81] Bollé, N. et al. Copper-induced changes in the properties of arsenic chalcogenides. *Semiconductors* **32**, 8, 873-878 (1998).

[82] Street R. A. Non-radiative recombinationin Chalcogenide glasses. *Solid State Comm.* **24**, 5, 363-365 (1983).

[83] LaFratta, C. C., Fourkas, J. T., Baldacchini, T., Farrer, R.A. Multiphonon fabrication. *Angew. Chem. Int. Ed.* **46**, 6238-6258 (2007).

[84] Török, P., Varga, P., Booker, G. R. Electromagnetic diffraction of light focused though a planar interface between materials of mismatched refractive indicies: structure of the electromagnetic field. I. *J. Opt. Soc. Am A* **12**, 10, 2136-2144 (1995).

[85] Ho, K. M., Chan et al. Photonic band gaps in three dimensions: New layer-by-layer periodic structures. *Solid State Comm.* **89**, 5, 413-414 (1994).

[86] Meisel, D. C., Diem, M., Deubel, M., Pérez-Willard, F., Linden, S., Gerthsen, D., Busch, K., Wegener, M. Shrinkage precompensation of holographic three-dimensional photonic crystal templates. *Adv. Mater.* **18**, 22, 2964-2968 (2006).

[87] Sheppard, C. J. R., Gu, M. Aberration compensation in confocal microscopy. *Appli. Opt.* **30**, 3563-568 (1991).

[88] Booth, M. J. Adaptive optics in microscopy. *Phil. Trans. R. Soc. A* **365,** 2829-2843 (2007).

[89] Whittaker, D. M., Culshaw, I. S. Scattering-matrix treatment of patterned multilayer photonic crystal structures. *Phys. Rev. B* **60**, 2610-2618 (1999).

[90] Martínez-Corral, M., Ibañez-López, C., Saavedra, G. Axial gain resolution in optical sectioning fluorescence microscopy by shaded-ring filters. *Opt. Exp.* **11**, 15, 1740-1745 (2003).

[91] Ibañez-López, C., Saavedra, G., Boyer, G. Quasi-isotropic 3D resolution in two-photon scanning microscopy. **13**, 16, 6168-6174 (2005).

[92] Zenkin, S. A. et al. Mechanism for interaction of amine solutions with monolithic glasses and amorphous films in the As-S system. *Glass Phys. And Chem.* **5**, 393-399 (1997).

[93] Mamedov, S. On the macromolecular mechanism of dissolution of As_2S_3 films in the organic solutions. *Thin Solid Films* **226**, 215-218 (1993).

[94] Voronkov, M. G.; Pizey, J. S. *Reaction of Sulfur with organic compound.*; (Consultants Bureau, New York, NY, 1987).

[95] Oae, S. *Organic Chemistry of Sulfur.* Ch. 1(Plenum Press: New York, NY, 1977).

[96] Davis, R. E. Nakshbendi, H. F. Sulfur in amine solvents. *J. Amer. Chem. Soc.* **84**, 2085-2090 (1962).

[97] Daly, F. P., Brown, C. W. Raman spectra of sodium tetrasulfide in primary amines. Evidence for S_4^{2-} and S_8^{n-} in rhombic sulfur-amine solutions. *J. Phys. Chem.* **79**, 4, 350-354 (1975).

[98] Daly, F. P., Brown, C. W. Raman spectra of Rhombic sulfur dissolved in secondary amines. *J. Phys. Chem.* **80**, 5, 480-482 (1976).

[99] Hodgson, W. G.; Buckler, S. A.; Peters, G. Free radicals in amine solutions of elemental sulfur. *J. Amer. Chem. Soc.* **85**, 543-546 (1963).

[100] Mayer, R., Gewald, K. Die entwirkung von schwefelkohlenstoff und schwefel auf enamine ketimine (Schiffsche basen) und CH-acide verbindungen. *Angew. Chem.* **79**, 298-311 (1967).

[101] Chen, G. C., Lauks, I. Spin-coated amorphous chalcogenide films. *J. Appl. Phys.* **53**, 10, 6979-6982 (1982).

[102] Chen, G. C., Lauks, I. Spin coated amorphous chalcogenide films: Structural characterization. *J. Appl. Phys.* **54**, 5, 2701-2705 (1983).

[103] Guiton, T. A., Pantano, C. G. Solution/gelation of arsenic trisulfide in amine solvents. *Chem. Mater.* **1**, 1, 558-563 (1989).

[104] Szargan, R., Schaufuβ, A., Roβbach, P. XPS investigation of chemical states in monolayers recent progress in adsorbate redox chemistry on sulphides. *J. Electon Spectrosc. Relat. Phenom.* **100**, 357-377 (1999).

[105] Schmitz, P. J. Characterization of the surface of $BaSO_4$ powder by XPS. *Surf. Sci. Spec.* **8**, 3, 195-199 (2001).

[106] Littlejohn, D., Chang, S.-G. An XPS study of nitrogen-sulfur compounds. *J. Electron Spectrosc. Relat. Phenom.* **17**, 71, 47-50 (1995).

[107] Steudel, R. Mechanism for the formation of elemental sulfur from aqueous sulfide in chemical and microbiological desulfurization process. *Ind. Eng. Chem. Res.* **35**, 1417-1423 (1996).

[108] Nesbitt, H. W. et al. Monitoring fundametnal reactions at NiAsS surfaces by synchrotron raditaion X-ray photoelectron spectroscopy: As and S air oxidation by consecutive reaction schemes. *Geochim. Cosmochim. Acta* **67**, 5, 845-858 (2003).

[109] Incorvia, M. J., Contarini, S. X-ray photoelectron spectroscopy studies of metal/inhibitor systems: Structure and bonding at the iron/amine interface. *J. Electrochem. Soc.* **136**, 9, 2439-2498 (1989).

[110] Balimann, G., Pregosin, P.S., Arsenic-75 nuclear magnetic resonance. A study of some arsenic salts. *J. Mag. Res.* **26**, 283-289 (1969).

[111] Hattori, M., Ogasawara, T., Heats of immersion of amorphous As_2S_3, As_2S_5 and As_2Se_3 in organic liquids. *Thermochimica Acta* **63**, 51-58 (1983).

[112] Hattori, M., Ogasawara, T., Jie, L. Hydrophobic properties of amorphous arseic trisulfide. *J. Coll. Inter. Sci.,* **107**, 1, 267-268 (1985).

[113] Reyes, A., Scott, R. M. Specific effects of dimethyl sulfoxide on the relative basicities of aliphatic amines. *J. Phys. Chem.* **84**, 3600-3603 (1980).

[114] Maiman, T. H. Stimulated optical radiation in ruby. *Nature* **187**, 493-494 (1960).

[115] Albers, P., Stark, E., Huber G. Continuous-wave laser operation and quantum efficiency of titanium-doped sapphire. *JOSA B* **3**, 1, 134-139 (1986).

[116] Desurvire, E., Simpson, J. R. Evaluation of $^4I_{15/2}$ and $^4I_{13/2}$ Stark-level energies in erbium-doped aluminosilicate glass fibers. *Optics Lett.* **15**, 10, 547-549 (1990).

[117] Cowan, R. D. *The Theory of Atomic Structure and Spectra.* University of California press, California, 1981. Page 4-18.

[118] Kenyon, A. J. Recent developments in rare-earth doped materials for optoelectronics. *Prog. Quant. Electr.* **26**, 225-284 (2002).

[119] Goff, D. R. *Fiber Optic Reference Guide, 3rd Edition.* (Focal Press Woburn, Massachusetts, 2002).

[120] Kumba, P. N., Risbud, S. H. Rare-earth chalcogenides – an emerging class of optical materials. *J. Mat. Sci.* **29**, 1135-1158 (1994).

[121] Quimby, R.S., Aitken, B.G. Multiphonon energy gap law in rare-earth doped chalcogenide glass. *J. Non-Cryst. Solids* **320**, 100-112 (2003).

[122] Iovu, M., Andriesh, A., Culeac, I. Fluorescence properties of As_2S_3 glass doped with rare-earth elements. *J. Opto. Adv. Mater.* **7**, 5, 232-2331 (2005).

[123] Harada, H, Tanaka, K. Photoluminescence from Pr^{3+}-doped chalcogenide glasses excited by bandgap light. *J. Non-Cryst. Solids* **246**, 189-196 (1999).

[124] Fick, J. et al. High photoluminescnce in erbium-doped chalcogenide thin films. *J. Non-Cryst. Solids* **272**, 200-208 (2000).

[125] Menehgini, C. et al. Luminescence from neodynium-ion-implanted As_2S_3 waveguides. *J. Opt. Soc. Am. B* **15**, 2, 1305-1308 (1998).

[126] Lyubin, V., Klebanov, M., Sfez, B., Askinadze, B. Photoluminescence and photodarkening effect in erbium-doped chalcogenide glassy films. *Mater. Lett.* **58**, 1706-1708 (2006).

[127] Kudoyarova, V. Kh., Kozyukhin, S. A., Tsendin, K. D., Lebedev, V. M. Photoluminescence and composition of amorphous As_2Se_3 films modified with Er(*thd*)$_3$ complex compound. *Semiconductors* **41**, 914-920 (2007).

[128] "Kurt J. Lesker Company, Deposition Techniques: Material name A – E". (2004) Kurt J. Lesker Company, 1515 Worthington Avenue, Clariton, Pennsylvania, U.S.A.
<http://www.lesker.com/newweb/deposition_materials/MaterialDeposition.cfm?pgid=0#e >

[129] Bigot, L., Jurdyc, A.-M., Jacquier, B., Adam, J.-L. Inhomogenous linewidthes in Er^{3+}-doped chalcogenide glasses. *Opt. Mater.* **24**, 97-102 (2003).

[130] Huang, Y. D., Portier, M., Auzel, F. Stark level analysis for Er^{+3D}oped oxide glasses: germinate and silicate. *Opt. Mater.* **15**, 243-260 (2001).

[131] Gu, S. Q. et al. Photoluminescnce and excitation spectroscopy of Er-doped As_2S_3 glass: novel broad band excitation mechanism. *J. Appl. Phys.* **77**, 3365-3371 (1995).

[132] Nipun, V. Busch, K., John, S. Theory of fluorescence in photonic crystals. *Phys. Rev. A* **65**, 043808 (2002).

[133] Bogaerts, W., Bienstman, P., Baets, R. Scattering at sidewall roughness in photonic crystal slabs. *Opt. Lett.* **28**, 9, 689-691 (2003).

[134] Tikhomirov, V.K. et al. The role of van der Waals bonding in photosensitivity of chalcogenide glasses. *J. Non-Cryst. Solids* **326-327**, 205-208 (2003).

[135] Kolobov, A. V., Elliot, S.R., Steel, A. T. Structure of photodoped and thermally Zn-doped glassy arsenic sulfide films. *Phys. Rev B* **41**, 4, 9913-9921 (1990).

[136] Liu, J. Z., Taylor, P.C. Effect of Cu alloying on the metastable photoinduced absorption in $Cu_x(As_{0.4}Se_{0.6})_{1-x}$ and $Cu_x(As_{0.4}S_{0.6})_{1-x}$ glasses. *Phys. Rev. B* **41**, 5, 3163-3171 (1990).

[137] Simidyankin, S. I. et al. Influence of copper on the electronic properties of amorphous chalcogenides. *Phys. Rev B* **72**, 020202(R) (2005).

[138] Fick, J. et al Thermally activated silver diffusion in chalcogenide tin films. *Thin Solid Films* **418**, 215-221 (2002).

[139] Newton, R. G., Davison, S. Conservation of Glass - Heinemann series in conservation and museology. (Butterworths, London 1989).

[140] Wágner, T. et al. Kinetics of optically- and thermally-induced diffusion and dissolution of silver in spin-coated $As_{33}S_{67}$ amorphous films; their properties and structure. *J. Non-Cryst. Solids* **326&327**, 233-237 (2003).

[141] Iovu, M.S. et al. Spectroscopic study of As_2S_3 glasses doped with Dy, Sm and Mn. *J. Non-Cryst. Solids* **326 & 327**, 306-310 (2003).

[142] Iovu, M. S. et al. Raman spectra of As_xSe_{100-x} and $As_{40}Se_{60}$ glasses doped with metals. *Chalcogenide Lett.* **2**, 4, 21-26 (2005).

[143] Seitz, M., Oliver A. G., Raymond, K.N. The lanthanide contraction revisted. *J. Am. Chem. Soc.* **129**, 11153-11160 (2007).

[144] Schleid, T., Lissner, F. Einkristalle von A-Nd_2S_3, U-Ho_2S_3, D-Er_2S_3 und E-Lu_2S_3 durch oxidation reduzierter chloride der lanthanide mit schwefel. *Z. anorg. allg. Chem.* **615**, 19-26 (1992).

[145] Van, T. T., Barger, J. R., Chang, J. P. Er coordination in Y_2O_3 thin films studied by extended x-ray absorption fine structure. *J. Appl. Phys.* **100**, 023115 (2006).

[146] Houde-Walter, S. N., Peters, P.M. X-ray absorption fine structure determination of the local environment of Er^{3+} in glass. *Appl. Phys. Lett.* **70**, 5, 541-543 (1997).

[147] Liu, J. Z., Taylor, P. C. Absence of photodarkening in bulk, glassy As_2S_3 and As_2Se_3 alloyed with copper. *Phys. Rev Lett.* **59**, 17, 1938-1941 (1987).

[148] Lyubin, V. et al. Photoinduced diffusion of Zn in chalcogenide glassy films. *J. Non-Cryst. Solids* **326&327**, 189-192 (2003).

[149] Rokitski, R., Tetz, R. A., Fainman, Y. Propagation of femtosecond surface plasmon pulses on the surface of a nanostructures metallic film: Space-time complex amplitude characterization. *Phys. Rev. Lett.* **95**, 177401 (2005).

[150] Butterfield, A. W. The optical properties of vitreous As_xSe_{1-x} thin films. *Thin Solid Films* **21**, 287-296 (1974).

[151] Role of S/Se ratio in chemical bonding of As-S-Se glasses investigated by Rman, x-ray photoelectron, and extended x-ray absorption fine structure spectroscopies. *J. Appl. Phys.* **98**, 5, 053503.

[152] Lyubin, V. et al. Photostructural transformations induced by IR radiation in As-Se-Te glassy films. *Mat. Lett.* **30**, 79-82 (1997).

[153] Lezal, D. Pedlikova, J., Zavadil, J. Chalcogenide glasses for optical and photonics applications. *Chalcogenide. Lett.* **1**, 1, 11-15 (2004).

[154] Popescu, M. Chalcogenides – Past, present, future. *J. Non-Cryst. Solids.* **352**, 887-891 (2006).

[155] Andriesh, A. M. Chalcogenide glass in optoelectronics. *Semiconductors* **32**, 8, 867-872 (1998).

[156] Ta'eed, V. G. et al. Ultrafast all-optical chalcogenide glass photonic circuits. *Opt. Express* **15**, 5, 9205-9221 (2007).

[157] Zakery, A., Hatami, M. Design of an ultra-fast all-optical dark soliton switch in a nonlinear directional coupler (NLDC) made of chalcogenide glasses. *J. Phys. D* **40**, 1010-1017 (2007).

[158] The MIT photonic bands package is freely available on the Internet. Details of the method can be found in Johnon, S. G., Joannopoulous, J. D. Block iterative frequency-domain methods for Maxwell's equations in a planewave basis. *Opt. Expr.* **8**, 3, 173-190 (2001).

[159] Doolittle, L. R. A semiautomatic algorithm for Rutherford Backscattering analysis. *Nucl. Instrum. Methods Phys. Res., Sect. B* **15**, 227-231 (1986). (Computer code available at www.genplot.com)

[160] Sheldrick, G. M. A short story of *SHELX. Acta. Cryst. A* **61**, 1, 112-122 (2008).

[161] Blair, K. W. et al. (1-pyrenylmethyl)amino alcohols, a new class of antitoumor DNA intercalators. Discovery and intitial amine side chain structure-activity studies. *J. Med. Chem.* **33**, 2385-2393 (1990).

[162] Anastasi, C. et al. Potent nonclassical nucleoside antiviral drugs based on the N,N-diarylforamidine concept. *J. Med. Chem.* **47**, 1183-1192 (2004).

[163] Ashton, P. R. et al. Hydrogen-bonded complexes of aromatic crown ethers with (9-anthracenyl)methylammonium derivatives. Supramolecular photochemistry and

photophysics. pH-controllable supramolecular switching. *J. Am. Chem. Soc.* **119**, 10641-10651 (1997).

[164] Hutton, R. C., Stephen, W. I. Organic reagents for the precipitation of nitrate ion. Part II. Di(napthylmethyl)amines and some derivatives of 2-napthylmethylamine. *J. Chem. Soc. A* 1426 (1967).

[165] Paventi, M., Hay, A. S. Novel synthesis of *N,N*-diarylmethanamines from *N*-(arylmethylene)arenamines and (arylmethoxy)arenes. *J. Org. Chem.* **56**, 20, 5875-5882 (1991).

[166] Miriyala, B., Bhattacharyya, S., Williamson, J. S. Chemoselective reductive arylation of ammonia with carbonyl compounds: synthesis of primary and symmetrical secondary amines. *Tetrahedron* **60**, 7, 1463-1471 (2004).

[167] Samec, J. S. M., Bäckvall, J.-E. Ruthenium-catalyzed transfer hydrogenation of imines by propan-2-ol in benzene. Chem.- Eur. J. 8, 13, 2955-2961 (2002).

[168] Kim, S. S., Jung, H. K. Oxidative *N*-debenzylation of *N*-benzyl-*N*-substituted benzylamines catalyzed by horseradish peroxidase. *J. Phys. Org. Chem.* **16**, 8, 555-558 (2003).

[169] Yu, Z. et al Ketoester methacrylate resin, secondary amine clean-up in the presence of primary amines. *J. Chem. Soc. Perkin Trans.* **16**, 1947-1952 (2001).

[170] Jellison Jr., G. E., Modine, F.A. Parameterization of the optical functions of amorphous materials in the interband region. *Appl. Phys. Lett.* **69,** 371-373 (1996).

[171] Rothe, J., Denecke, M. A., Dardenne, K., Fanghänel, Th. The INE-beamline for actinide reasech at ANKA. *Radiochim. Acta* **94**, 691-696 (2006).

[172] Ressler, T. Hagelstein, U., Hatje, U., Metz, W. In situ XAS investigations of chemical oscillations in the oxidation of Co on supported Pd catalysts. *J. Physique IV* **7-C2** 731-733 (1997).

[173] Stern, E. A. et al. The UWXAFS analysis package: philosophy and details. *Physica B* **208&209**, 117-120 (1995).